Tailoring of Optical Response for Sensing: Simulations, Roughness Effect, and Raman

Doctoral Thesis

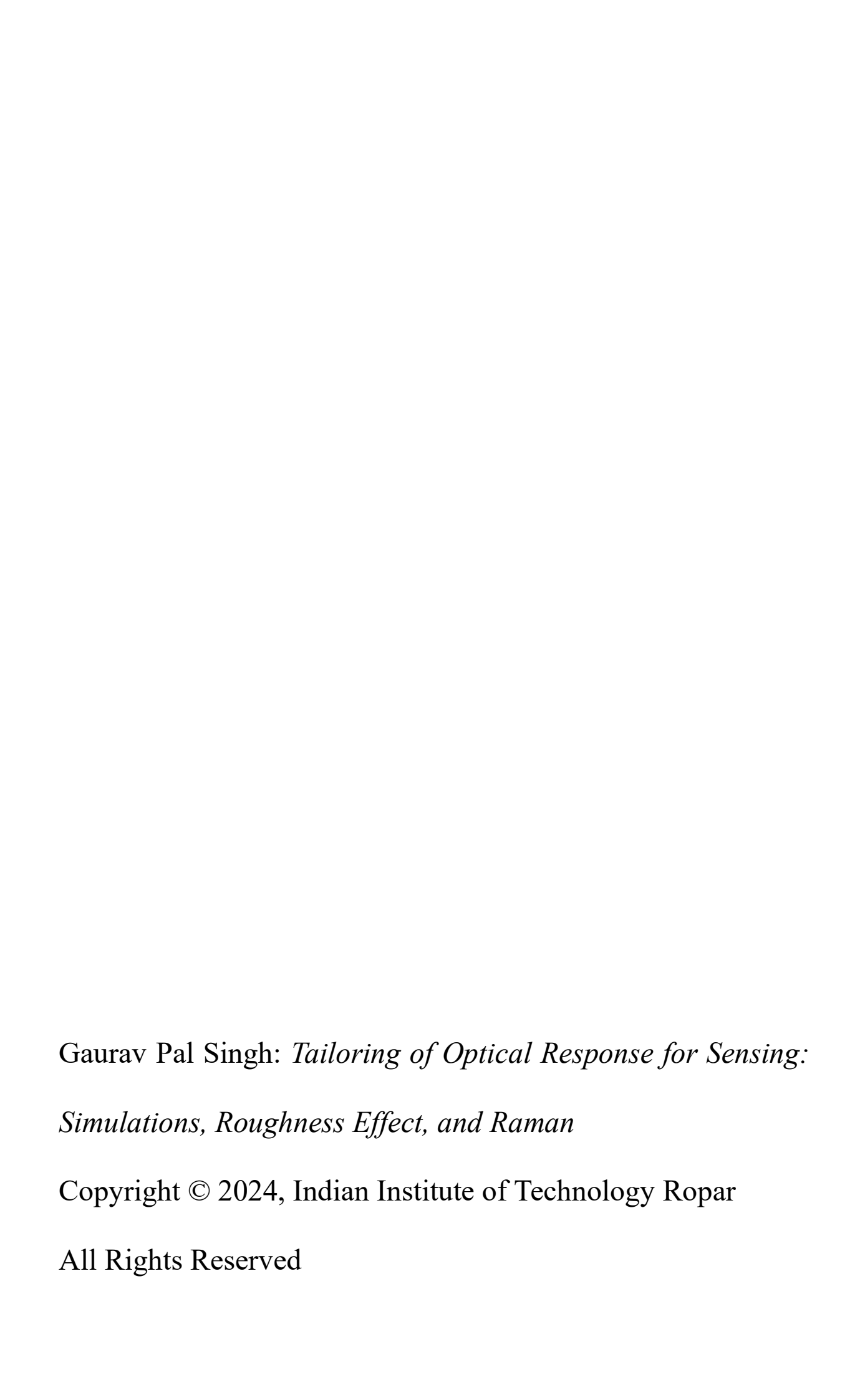
by

GAURAV PAL SINGH 2019MMZ0003



DEPARTMENT OF METALLURGICAL AND MATERIALS ENGINEERING

INDIAN INSTITUTE OF TECHNOLOGY ROPAR
September, 2024



This thesis is dedicated to my parents, for your endless love and unwavering support.

Declaration of Originality

I, Gaurav Pal Singh, hereby declare that the work which is being presented in the thesis entitled

"Tailoring of Optical Response for Sensing: Simulations, Roughness Effect, and Raman" has been

solely authored by me. It presents the result of my own independent investigation/research conducted

during the time period from July 2019 to September 2024 under the supervision of Dr. Neha Sardana

(Associate professor, PhD). To the best of my knowledge, it is an original work, both in terms of research

content and narrative, and has not been submitted or accepted elsewhere, in part or in full, for the award

of any degree, diploma, fellowship, associateship, or similar title of any university or institution.

Further, due credit has been attributed to the relevant state-of-the-art and collaborations (if any) with

appropriate citations and acknowledgments, in line with established ethical norms and practices. I also

declare that any idea/data/fact/source stated in my thesis has not been fabricated/ falsified/

misrepresented. All the principles of academic honesty and integrity have been followed. I fully

understand that if the thesis is found to be unoriginal, fabricated, or plagiarized, the Institute reserves

the right to withdraw the thesis from its archive and revoke the associated Degree conferred.

Additionally, the Institute also reserves the right to appraise all concerned sections of society of the

matter for their information and necessary action (if any). If accepted, I hereby consent for my thesis to

be available online in the Institute's Open Access repository, inter-library loan, and the title & abstract

to be made available to outside organizations.

Signature

Name: Gaurav Pal Singh

Entry Number: 2019MMZ0003

Program: PhD

Department: Metallurgical and Materials Engineering

Indian Institute of Technology Ropar

Rupnagar, Punjab 140001

Date:

ii

Certificate

This is to certify that the thesis entitled "Tailoring of Optical Response for Sensing: Simulations, Roughness Effect, and Raman", submitted by Gaurav Pal Singh (2019MMZ0003) for the award of the degree of Doctor of Philosophy of Indian Institute of Technology Ropar, is a record of bonafide research work carried out under my (our) guidance and supervision. To the best of my knowledge and belief, the work presented in this thesis is original and has not been submitted, either in part or full, for the award of any other degree, diploma, fellowship, associateship or similar title of any university or institution.

In my (our) opinion, the thesis has reached the standard fulfilling the requirements of the regulations relating to the Degree.

Dr. Neha Sardana
Associate professor
Department of Metallurgical and Materials Engineering
Indian Institute of Technology Ropar
Rupnagar, Punjab 140001

Date:

Acknowledgements

First and foremost, I want to thank my parents, Dr. Jaspreet Kaur and Dr. Bhupinder Pal Singh, and my supervisor Dr. Neha Sardana. My parents allowed me the freedom to pursue my dreams with their unwavering support. The passion for their respective professions set an example and motivated me to always work hard to achieve my goals regardless the results. None of this work would have been possible without the efforts and encouragement of Neha ma'am. She instilled confidence in me to aim for ideas out of my domain fearlessly. I have learnt countless things from her and am grateful to her for always being reachable and providing me with opportunities and resources throughout my PhD.

I am thankful to my doctoral committee, Dr. Ravi Mohan Prasad (Chairperson), Dr. Pratik K Ray (Head of Department, Metallurgical and Materials Engineering), Dr. Atharva Poundurik, Dr. Brajesh Rawat, and Dr. Priya Ghatwai (previous member) for their valuable inputs and support.

I want to thank the current Director, Prof. Rajeev Ahuja, and Ex-Director, Prof. Sarit Kumar Das, IIT Ropar and the Department of Metallurgical and Materials Engineering for providing me the opportunity to pursue my PhD and provide me all the basic research facilities. I would like to thank the Ministry of Education India (MIE) for providing the PhD stipend.

I was lucky to get the opportunity to go to the Martin-Luther-University Halle-Wittenberg, Germany, to fabricate my samples. I am grateful to Dr. Joerg Schilling for inviting me to Germany despite my limited knowledge of physics. I am thankful to IIT Ropar for the travel grant and MLU Halle for the financial support for accommodation and food. No samples would have been made without the training and support of Dr. Bodo Fuhrmann. I am also grateful to Stefan Schweizer for teaching me how to take Raman measurements, Ms. Claudia for providing me with chemicals and consumables, and Frank Syrowatka for giving me the FE-SEM images of my samples at a moment's notice.

I am thankful to Central Research Facility (CRF) IIT Ropar for providing the characterization instruments; I thank Dr. Ravi Mohan Prasad for allowing me to access the Raman instrument under the supervision of Mr. Damninder. I am also thankful to Mr. Harsimran and Mr. Kamlesh for AFM and XRD measurements. I would also like to thank Dishant sir, for optimizing my XRD parameters when I needed quick results.

I would like to thank Neha ma'am and Dr. Ananth Venkatesan for providing me with the data for the roughness analysis of thin films during COVID-19.

Although this work could not be included in the thesis, I really appreciate the help of Dr. Durba Pal and the Biomedical Engineering Department for giving me access to their facilities. I would especially like to thank Mr. Soumyajit for teaching me microbiology experiments and Mr. Ankit, Ms. Bhavya, and Mr. Palla Ramprasad for providing access to their lab every day (and sometimes night) for more than 3 months. I would also like to thank Dr. Suruchi for assisting me in analysing the biological experiments. I am also very grateful to Mr. Raj Harsh, an intern from Punjab Engineering College, Chandigarh, for

going above and beyond to help me with the biology experiments. I was delighted when Raj's simulation work was published and was on the cover of a good journal.

I would like to thank all my PhD seniors, especially Kushagra sir, Vishnu sir, and Rajesh sir, for creating a helpful and encouraging work environment. I would like to thank my lab mates, Heena, Ayush, Atul, and new members Shambhu and Ravinder. I would especially like to thank Atul for helping me find a needle in a haystack while performing SEM measurements of biological samples. I want to thank Sheshang and Nishant sir for introducing me to and teaching me basketball, which was crucial for my physical and mental fitness. I want to thank the one who cannot be named for supporting me when I needed it the most. I would also like to thank Sheshang, Atul, Ayush, Jay Hind, Abhinav Maurya, Sagarika, Maninder, Rishab, and Sambit for always being there to help during working hours and fun after it. Again, I thank Neha ma'am for her anime and movie recommendations. Finally, I would like to thank the doggo outside my hostel, Sheru, who always greeted me with a smile, wagging tail, and sometimes a big hug throughout my PhD.

Last but not least, I would like to thank God, who I only remembered during the toughest of times but still was kind enough to give me the strength to tackle every obstacle head on.

Lay summary

Agrochemicals are important in improving crop yield and preventing contamination of crops by insects, weeds, and microorganisms. However, continued consumption of these chemicals can lead to allergies, dermatological effects, respiratory issues, neurological disorders, and even cancer. The agricultural sector has been excessively using these agrochemicals to increase their profits, which has caused contamination of drinking water sources near the crops and the crop itself. The food safety agencies in India and around the world are not able to regulate the use of these agrochemicals. Therefore, quick and accurate monitoring of these chemicals is critical to ensure safe water and food.

Raman spectroscopy is a technique which can be used for agrochemical detection. The instrumentation includes a laser of the selected wavelength, collimation optics to focus the laser on the sample, an optical filter to cut out the laser wavelength after it is incident on the sample, and a detector to capture the wavelength dependent intensity from the vibrational modes of the sample. The advantages of Raman spectroscopy include a fingerprint response of each chemical, quick measurements and minimal sample preparation. However, the low signal strength from the target chemical is a major problem in Raman spectroscopy, which limits its commercial usage. Surface enhanced Raman spectroscopy (SERS) is an excellent solution to enhance the Raman signal strength. SERS substrates use the nano sized features on plasmonic materials (gold, silver, etc.) to trap the incident Raman laser light and, therefore, increase the amount of signal from the vibrational modes of the sample.

In the current thesis, simulations were first used to study the effect of shape, size, and material on nano-sized particles and periodic arrays. It was determined that square symmetric arrays of gold disks of diameter in the range of 100 nm to 250 nm have resonances wavelength in the visible to near infrared range. The resonance was due to the coupling of the resonance wavelength of the single disc and resonance wavelength due to the symmetry of the structures in the array. These nano disk arrays were then experimentally fabricated using laser interference lithography (LIL). The resonance wavelength of 300 nm diameter nano disk array matched the Raman excitation wavelength, which led to a massive enhancement in Raman signal. It was also determined that decreasing the surface roughness of nano sized structures and films improves their performance. The optimized SERS substrate was used to detect the most commonly used agrochemicals, herbicide (Atrazine), fungicide (Mancozeb), acaricide (Clofentezine), weedicide (Metribuzin) and insecticides (Chlorantraniliprole, Thiamethoxam, Taufluvalinate, and Flubendiamide) in water. Furthermore, density functional theory (DFT) was used to theoretically confirm Raman spectra of the agrochemicals.

Abstract

The manipulation and control of light is on the forefront of sensing technology. Humans have taken inspiration from nature (vibrant colours of butterfly's wings, iridescence in peacock feathers, camouflage of squid skin, etc.) to create periodic structures that are able to confine light in micro and even nano sized structures. The incorporation of plasmonic material into periodic structures produces sharp and strong resonances due to a combination of near field and far field effects. These nanostructures can be used as surface enhanced Raman spectroscopy (SERS) substrates to significantly enhance the intensity of the Raman signal. In this thesis, nanostructures optimized for Raman signal enhancement were used for sensing agrochemicals, which are causing food and water contamination due to their excessive use.

The plasmonic response of nanostructures from single nanoparticles to periodic nanoarrays was studied using finite element method (FEM) simulations. The geometric parameters of the arrays were optimized for fabrication. An experimental study was performed to establish the effect of roughness on the optical response of thin gold films. Gold nanodisk arrays of various periods were fabricated using laser interference lithography (LIL). Thermal annealing was performed to tune the geometric parameters and decrease the roughness of the nanodisks to enhance their plasmonic response. Annealing the arrays improved the coupling effect of the near filed and far field resonance. The simulations strongly supported the experimental results. The period of the nanodisk arrays fabricated using the LIL technique was optimized for Raman sensing. The overlap of the resonance wavelength of the nanodisk array and the Raman excitation created the highest SERS enhancement. The most commonly used agrochemicals, herbicide (Atrazine), fungicide (Mancozeb), acaricide (Clofentezine), weedicide (Metribuzin) and insecticides (Chlorantraniliprole, Thiamethoxam, Tau-fluvalinate, and Flubendiamide) were collected for testing their limit of detection (LOD) in water using the optimized LIL sample as a SERS substrate. Density functional theory (DFT) was used to theoretically confirm Raman spectra of the agrochemicals. DFT is quantum mechanical method which can be used to calculate and visualize the vibrational modes of molecules. The optimal basis set was selected at the B3LYP level theory which provided a good compromise between accuracy and computational cost. The DGDZVP basis set was used to perform the vibrational mode analysis and validate the Raman spectra of the agrochemicals.

List of publications

Chapter 2. Background

1. **G. P. Singh** and N. Sardana, "Smartphone-based Surface Plasmon Resonance Sensors: a Review," *Plasmonics*, vol. 17, no. 5, pp. 1869–1888, Oct. 2022, doi: 10.1007/s11468-022-01672-1.

Chapter 4. Simulating the Geometric Dependence of Plasmonic Responses

- 2. **G. P. Singh** and N. Sardana, "Plasmonic response of metallic nanoparticles embedded in glass and a-Si," *Bull. Mater. Sci.*, vol. 45, no. 4, p. 241, Dec. 2022, doi: 10.1007/s12034-022-02812-3.
- 3. **G. P. Singh**, R. Harsh and N. Sardana "Tuning of the Plasmonic Response Gold and Aluminum Nanoarrays for Sensing Applications" *Indian J. Pure Appl. Phys.*, vol. 62, pp. 77-86, Feb. 2024, doi: 10.56042/ijpap.v62i2.7709

Chapter 5. Probing the Plasmonic Response

- 4. **G. P. Singh**, S. Samanta, A. Pegu, S. S. Yadav, U. Singhal, A. Venkatesan and N. Sardana, "Enhancement of Plasmonic Response by Piezoelectrically Deposited Gold Films" *Indian J. Phys.*, Oct. 2023, doi: 10.1007/s12648-023-02974-8.
- 5. **G. P. Singh**, B. Fuhrmann, F. Syrowatka, J. Schilling, N. Sardana, "Plasmonic Coupling Effect of Annealed Gold Nanoarrays" (under review in Physica Scripta)

Chapter 6. Gold Nanodisk Arrays: A Promising Platform for Enhanced Agrochemical Detection

- G. P. Singh, B. Fuhrmann, F. Syrowatka, J. Schilling, N. Sardana, "Tuning the Plasmonic Response of Periodic Gold Nanodisk Arrays for Urea Sensing" *J. Mater. Sci.* vol. 59, pp. 6497–6508, April 2024, doi: 10.1007/s10853-024-09599-0
- 7. **G. P. Singh**, N. Sardana, "Vibrational Modes of Metribuzin: A Theoretical and Experimental Comparison" (accepted in Chemistry Select)
- 8. **G. P. Singh**, J. Schilling, N. Sardana, "Gold Nanodisk Arrays as SERS Substrate for Agrochemical Sensing" (2 under preparation)

Publications not related to thesis work:

- 1. Paper: G. P. Singh and N. Sardana, "Affordable, Compact and Infection-Free BiPAP Machine," Trans. Indian Natl. Acad. Eng., vol. 5, no. 2, pp. 385–391, 2020, doi: 10.1007/s41403-020-00134-6.
- 2. Paper: **G. P. Singh**, A. Pandey and N. Sardana, "MXene coupled surface plasmon resonance (SPR) sensors for sensitivity enhancement: a theoretical study," *(under review in Optics Communications)*
- 3. Patent: G. P. Singh and N. Sardana, "A system and method for measuring burst pressure for an adhesive," 202111032081, Indian patent filed, 2021
- 4. Book chapters:
 - **G. P. Singh** and N. Sardana, "Graphene-Based Tunable Metamaterial-FSS RAS BT Handbook of Metamaterial-Derived Frequency Selective Surfaces," Springer Nature Singapore, 2022, pp. 1–39.
 - **G. P. Singh** and N. Sardana, "Graphene Metamaterials Recent Advances in Graphene and Graphene-based technologies," IOP Publishing, 2023, pp. 17–38.
 - G. P. Singh and N. Sardana, "Auxetic Materials for Biomedical and Tissue Engineering Materials for Biomedical Simulation: Design, Development and Characterization," Springer Nature Singapore, 2023, pp. 1–36.

Table of Contents

Declaration of Originality	ii
Certificate	iii
Acknowledgements	iv
Lay summary	vi
Abstract	vii
List of publications	viii
List of Figures	xi
List of Tables	xvi
Abbreviations	xvii
Chapter 1. Introduction	1
Chapter 2. Background	5
2.1 Plasmonics	5 7
2.2 Localized Surface Plasmon Resonance (LSPR)	
2.3 Surface Plasmon Polaritons (SPPs)	9
2.3.1 Prism coupling	11
2.3.2 Grating coupling	12
2.4 Fabrication of periodic nanostructures	14
2.4.1 Laser Interference Lithography	15
2.4.2 Thermal annealing of Nanostructures	16
2.5 Raman sensing	16
2.6 Surface enhanced Raman Spectroscopy (SERS) Chapter 3. Theoretical and Experimental Framework	18
Chapter 3. Theoretical and Experimental Framework 3.1 Finite element method (FEM) simulations	21 21
3.1.1 Loretz Drude model	22
3.1.2 Single nanoparticle simulation methodology and validation	22
3.1.3 Nanoarray simulation methodology and validation	24
3.2 Modelling the effect of roughness	25
3.2.1 Impact of roughness on plasmonic response	25
3.2.2 Bruggeman effective medium theory to calculate SPR response	26
3.3 Density functional theory (DFT) for Raman	27
3.3.1 Basis sets for B3LYP level of theory	28
3.3.2 Equations to calculate vibrational modes	28
3.4 Laser interference lithography (LIL)	31
3.5 Thermal deposition	32
3.6 Transmission spectroscopy	33
3.7 Surface Plasmon Resonance (SPR)	34
3.8 Other characterization techniques	35
Chapter 4. Simulating the Geometric Dependence of Plasmonic Responses	37
4.1 Single nanoparticles	37
4.1.1 Simulation parameters and validation	37
4.1.2 Effect of size change	39
4.1.3 Effect of change in shape	40
4.1.4 Effect of nanoparticle embedding in dielectric	43
4.1.5 Effect of change of material	44
4.2 Nanoarrays	46
4.2.1 Simulation parameters and validation	46
4.2.2 Effect of geometric parameters (thickness, diameter, and periodicity)	48
4.2.3 Effect of change of material	50
4.2.4 Effect of change of shape	52
4.2.5 Sensitivity comparison	55 57
4.3 Chapter summary Chapter 5 Probing the Plasmonia Pospores	57 5 0
Chapter 5. Probing the Plasmonic Response 5.1 Effect of roughness on thin films	59
5.1 Effect of roughness on thin films 5.1.1 Experimental and simulation parameters	59 59
5.1.1 Experimental and simulation parameters 5.1.2 Experimental SPR response of thin films deposited with and without a quartz base	60
5.1.2 Experimental SPK response of thin films deposited with and without a quartz base 5.1.3 Confirmation using simulation results	63
5.1.5 Committation using simulation results 5.2 Effect of thermal annealing of gold nanodisk arrays	63

5.2.1 Experimental and simulation parameters	64
5.2.2 General impact of annealing	64
5.2.3 Plasmonic resonances in unannealed and 10 minute annealed samples in detail	69
5.2.4 Plasmonic resonances in unannealed and 20 minute annealed samples in detail	73
5.3 Chapter summary	76
Chapter 6. Gold Nanodisk Arrays: A Promising Platform for Enhanced Agrochemical Detection	77
6.1 Selection of the optimal SERS substrate	77
6.1.1 Experimental and simulation parameters	77
6.1.2 SERS response of gold nanodisk arrays	79
6.1.3 Understanding the plasmonic response	80
6.1.4 Confirmation for agrochemical sensing by detecting urea	82
6.2 Theoretical calculations of Raman spectra of agrochemicals	84
6.2.1 Vibrational response of Metribuzin	87
6.2.1.1 Confirmation of structure	88
6.2.1.2 Vibrational response (DFT and experimental)	88
6.2.2 Basis set comparison	92
6.2.3 Vibrational response (DFT and experimental) of agrochemicals	95
6.2.3.1 Atrazine	96
6.2.3.2 Mancozeb	97
6.2.3.3 Clofentezine	99
6.2.3.4 Chlorantraniliprole	100
6.2.3.5 Thiamethoxam	102
6.2.3.6 Tau-fluvalinate	104
6.2.3.7 Flubendiamide	105
6.2.4 Error analysis of the calculated wavenumbers	106
6.3 Testing of various agrochemicals using the optimized substrate	107
6.4 Chapter summary	109
Chapter 7. Conclusion and Future Scope	111
7.1 Conclusion	111
7.2 Future Scope	113
Appendix	115
Appendix A. MATALB codes	115
Appendix A.1. Lorentz Drude model	115
Appendix A.2. Effective dielectric function using Bruggeman model	117
Appendix A.3. Toolbox to calculate angle resolved SPR plots	118
Appendix B. Additional parameters for FEM simulations	119
Appendix C. Extinction cross-section plots of nanoparticles calculated using FEM	120
Appendix D. Transmission plots of nanoarrays calculated using FEM	124
Appendix E. DFT/B3LYP calculated Raman spectra of metribuzin using various basis sets.	126
Appendix F. DFT/B3LYP calculated Raman spectra of metribuzin using various basis sets.	127
Appendix G. Commercial agrochemicals tested in this thesis	129
Appendix H. Nomenclature of vibrational modes (Wilson notation)	131
Appendix I. Permission for figures	132
References	135

List of Figures

Figure 1.1 Use of pesticides worldwide from 1990 to 2021 according to a survey by the food and agriculture organization of the United Nations [1]	1
Figure 1.2 Thesis outline.	3
Figure 2.1 The d) real and e) imaginary part of the dielectric function of gold, copper, silver, and aluminium.	5
Figure 2.2 Schematic of the dipole created due to oscillations of electrons created in the LSPR effect.	7
Figure 2.3 a) Kretchmann configuration and b) Dispersion relation for prism coupling	11
Figure 2.4 a) Grating coupling and b) Dispersion relation for grating coupling.	12
Figure 2.5 Brief schematic of the LIL process to fabricate gold nanodisk array using the Lloyd's mirror setup.	15
Figure 2.6 Basic principle of Raman spectroscopy and Jablonski diagram along with Raman shifted response [170]. Reprinted with permission from <i>Nanotechnol. Environ. Eng.</i> 2023, 8, 41–48, Copyright 2018 Springer Nature.	16
Figure 2.7 Raman spectra of natural fingerprints of a human and fingerprints contaminated with aspirin, diclofenac, ketoprofen, ibuprofen and naproxen tablets in the "fingerprint" region of 500 cm ⁻¹ to 1800 cm ⁻¹ [176]. Reprinted with permission from <i>Sci. Rep.</i> 2022, 12, 3136. Copyright 2022 Springer Nature.	18
Figure 3.1 Schematic representation of the simulation domain of a single nanoparticle	23
Figure 3.2 Simulation domain of the plasmonic nanoarray with periodicity (P), thickness (t), and diameter (d)	24
Figure 3.3 Schematic illustration of a) Maxwell Garnett and b) Bruggeman effective medium theory.	26
Figure 3.4 Schematic of the layers used for transfer matrix method (TMM) calculations	27
Figure 3.5 Schematic of the thermal evaporation process.	32
Figure 3.6 Ray diagram presenting the components of the transmission spectroscopy setup. Inset has the image of the tabletop setup at IIT Ropar	33
Figure 3.7 a) Image of the tabletop SPR setup at IIT Ropar. b) Schematic of the Kretschmann configuration for excitation of the SPR condition. c) Ray diagram explaining all the components of the SPR setup.	34
Figure 4.1 Measured scanning transmission electron microscopy—cathodoluminescence (STEM-CL) unpolarized photon-emission intensity spectra collected for dipole position (solid black line with circular markers) [250] for gold nanoprism of side 266 nm and height 50 nm and FEM simulation extinction cross section of the nanoprism of the same dimensions (red dashed line with square markers).	38
Figure 4.2 (a-d) Measured monochromatic photon maps for nanoprism of side 266 nm and height 50 nm for the dipole (D) (a and b) and quadrupole (Q) (c and d) modes at the peak energies for s (a and c) and p polarized (b and d) emission. Each pixel is associated with a different position of the electron beam [250]. (Figures adapted with permission from <i>ACS Nano</i> 2018, 12, 8436–8446. Copyright 2018 American Chemical Society). (e-f) The normalized electric field (V/m) using FEM simulation for the same nanoprism for the D (e and f) and Q (g and h) modes when the electric field is perpendicular (e and g) and parallel (f and h) to the side of the nanoprism.	38

Figure 4.3 Plots of the extinction cross-section for gold (black), copper (blue), silver (red), and aluminium (orange) in air (solid line), glass (dashed line), and a-Si (dotted line) environment, of spherical nanoparticles, nanobars and nanoprisms (left to right), and volumes equal to spheres of diameter 50 nm, 100 nm, 150 nm, and 200 nm (top to bottom). 1, 2, and 3 represent the dipole, quadrupole, and octupole peaks, respectively	40
Figure 4.4 The normalized electric field (V/m) of silver nanoparticles in air with volume equal to sphere of diameter 200 nm. From left to right, the dipole, quadrupole, and octupole configurations of spherical nanoparticle (570 nm, 390 nm, and 360 nm), nanobar (1090 nm, 558 nm, and 453 m), and nanoprism (1394 nm, 704 nm, and 611 nm).	42
Figure 4.5 Quantitative peak shift upon increase in size for nanoparticles in a) air, b) glass, and c) silicon. Dipole shift compared to the equivalent nanoparticle in air for d) glass and e) a-Si surrounding.	45
Figure 4.6 Simulation transmission plot comparing a single nanodisk (diameter 200 nm and thickness 45 nm) and the same nanodisk placed in an array of period 400 nm (diameter of the disk was 200 nm and thickness 45 nm)	46
Figure 4.7 (a) Simulation domain showing the ports, periodicity and the shapes that were analyzed. The periodicity (P), thickness (T), diameter (d), and sides (s and t) were varied. (b) Real and imaginary part of the dielectric function of gold and aluminium according to Lorentz Drude model.	47
Figure 4.8 Comparison of simulation and experimental results of 400 nm period gold nanodisk array with diameter 187 nm and thickness 45 nm with surrounding material air and water. The inset shows the experimental gold nanodisk array	47
Figure 4.9 Simulated transmission spectra for gold disc nanoarray at air glass interface. (a-d) Thickness variation and (e-f) variation of d/P. The vertical dashed lines represent lattice resonance, (1 0) diffraction edge, and the number beside is the refractive index for the lattice resonance. No number pertains to the resonance due to glass environment (n = 1.5). Solid line represents the single disc resonance.	48
Figure 4.10 Extinction cross section of single nanostructures (disc, square, and triangle) with volume equivalent to a nanodisk of diameter 200 nm and thickness 30 nm of a) gold and b) aluminium.	50
Figure 4.11 Simulated transmission spectra for aluminium disc nanoarray at air glass interface. (a-d) thickness variation and (e-f) variation of d/P. The vertical dashed lines represent lattice resonance, (1 0) diffraction edge, and the number beside is the refractive index for the lattice resonance. No number pertains to the resonance due to glass environment (n = 1.5). Solid line represents the single disc resonance.	51
Figure 4.12 Comparison of gold (a-d) and aluminium (e-h) nanoarray simulated transmission spectra of square (a, c, e, and g) and triangle (b, d, f, and h). (a, b, e, and f) shows the height variation and (c, d, g, and h) shows the respective t/P and s/P ratios. The side of square and triangle were kept as 177.25 nm and 269.35 nm to keep the volume equal to the disc of diameter 200 nm. The nanoarray was at air glass interface for $\theta = 0^{\circ}$. The vertical dashed lines represent lattice resonance, (1 0) diffraction edge, and the number beside is the refractive index for the lattice resonance. No number pertains to the resonance due to glass environment (n = 1.5). Solid line represents the single disc resonance	53
Figure 4.13 a) Simulation domain of nanodisk array. b) Various shapes analyzed and the direction of polarization. (c-e) Normalized electric filed in (V/m) contours for the nanoarrays showing c) lattice and single particle resonances, d) Dipole and Octupole in disc nanoarray, e) Dipole and Quadrupole in triangle nanoarray, and Dipole and Quadrupole in square nanoarray	54

Figure 4.14 Refractive index (n1) variation in gold (a-c) and aluminium (a-c) nanoarray for disc (a, e), square, (b, f), and triangle (c, g) shapes. The sloid vertical line represents the single particle resonance. The side of square and triangle were kept as 177.25 nm and 269.35 nm to keep the volume equal to the disc of diameter 200 nm. The square lattice periodicity was equal to the coupling condition of the single particle resonance at air glass interface	55
Figure 4.15 Sensitivity comparison of gold and aluminium nanoarray of disc, square and triangle nanoarrays (at the optimal coupling condition). Volume equal to disk of diameter 200 nm and thickness 30 nm.	56
Figure 5.1 Reflectance spectra as a function of angle of incidence of gold films for various thicknesses deposited with and without a quartz base.	60
Figure 5.2 a) Experimental normalized reflectivity plots. b) Experimental slope of the angle and wavelength dependent resonance curve and c) AFM images of 40 nm thick gold films deposited with and without a quartz base.	62
Figure 5.3 TMM calculated reflectance spectra as a function of angle of incidence of gold films for 40 nm thickness gold film with RMS roughness corresponding to the film deposited with and without a piezoelectric base.	63
Figure 5.4 a), e) Experimental transmission response of gold nanodisk samples with period 400 nm (red) and 500 nm (blue). SEM images of b), f) unannealed sample (solid line) c), g) sample annealed at 500 °C for 10 minutes (dashed line) (d) sample annealed at 500 °C for 20 minutes (dotted line).	65
Figure 5.5 a) Average thickness for 400 nm and 500 nm period unannealed and samples annealed at 500 °C for 10 and 20 minutes. The error bars represent the standard error of the peak thickness. b) XRD measurements of 400 nm period sample (unannealed and annealed at 500 °C for 10 minutes). The inset shows the measurements for the main peak with an increased acquisition time which was used to calculate the grain size	67
Figure 5.6 AFM images of gold nanodisk samples with a) period 400 nm and c) 500 nm samples unannealed. Nanodisk samples with b) period 400 nm and d) 500 nm samples annealed at 500 °C for 10 minutes. Nanograting samples with e) period 400 nm and g) 500 nm samples unannealed. Nanograting samples with f) period 400 nm and h) 500 nm samples annealed at 500 °C for 10 minutes. i) AFM images of gold nanodisk sample of 400 nm period annealed at 500 °C for 20 minutes.	68
Figure 5.7 Simulated extinction cross-section spectrum for a) single gold nanodisk of dimeter 187 nm, 156 nm, and 156 nm broken (corresponding to unannealed and 10 min and 20 min annealed samples of 400 nm period), and 220 and 191 nm (corresponding to unannealed and 10 min annealed samples of 500 nm period) in non-homogenous medium (gold disk at air (n = 1) glass (n = 1.5) interface). a) Single gold nanodisk of 156 nm, 156 nm broken (corresponding to 10 min and 20 min annealed samples of 400 nm period), and broken structures with outer boundary of diameter 280 nm and 360 nm in homogenous medium (n = 1.5). The vertical lines represent the respective single disc resonances	69
Figure 5.8 Effect of variation of period on the simulated transmission spectra of a nanodisk array (disk diameter 156 nm and thickness 54.1). The nanodisks were placed in a) non-homogenous medium (air (n = 1) glass (n = 1.5) interface and b) homogenous medium (oil (n = 1.5) glass (n = 1.5) interface). λ_D and λ_G represent the single particle resonance and (1 0) grating resonance. The solid vertical lines are the single particle resonance and dashed vertical lines are (1 0) grating resonances.	70
Figure 5.9 Experimental and FEM simulation transmission response of gold nanodisk arrays with period a) 400 nm (red lines) and b) 500 nm (blue lines) when they are unannealed (solid lines) and annealed at 500 °C for 10 minutes (dashed lines). The solid and dashed vertical lines are the single particle resonances for unannealed and annealed samples, respectively.	71

Figure 5.10 a) Real and b) imaginary part of dielectric function of gold used in simulation of the unannealed and 10 minute annealed samples with corresponding modified Lorentz-Drude parameters listed in Figure 5.9.	72
Figure 5.11 (a, b) Experimental (solid lines) and (d, e) FEM simulation (dashed lines) transmission response of gold nanodisk arrays with period 400 nm when they are annealed at 500° C for 20 minutes. a) and d) is the transmission spectra in a non-homogenous medium, the nanodisks are placed in air (n = 1) and glass (n = 1.5) interface. b) and e) is the transmission spectra in a homogeneous medium, the nanodisks are placed in oil (n = 1.5) and glass (n = 1.5) interface. c) SEM image of the broken nanodisk array. f) Geometry of the broken nanodisks used for the FEM simulations.	73
Figure 5.12 a) Simulated extinction cross-section spectrum for single gold nanodisk of diameter 34 nm and height 39 nm. b) Simulated transmission spectra of the nanodisk placed in an array of period 400 nm. Both are in a homogenous medium (n = 1.5). The solid vertical lines are the single particle resonance and dashed vertical lines are (1 0) grating resonances.	75
Figure 5.13 Simulation transmission response of gold nanodisk array with a) unbroken discs (solid lines) and b) broken discs (dotted lines) of period 700 nm (green) and 900 nm (orange) in a homogenous medium of n = 1.5. The solid vertical lines are the single particle resonance and dashed vertical lines are (1 0) grating resonances.	75
Figure 6.1 SEM images of gold nanodisk arrays fabricated using LIL of period (a) 250 nm, (b) 300 nm, (c) 344 nm, (d) 395, and (g) 446 nm. (f) 3D representation of the AFM measurements of the 395 nm period array	79
Figure 6.2 Raman response to the chemical Rhodamine 6G of the LIL substrates of various periods and a bare glass substrate. (b) Intensity of the 612 cm ⁻¹ peak of Rhodamine 6G for the LIL substrates of various periods. The error bars represent the standard deviation between 3 measurements.	80
Figure 6.3 (a) Experimental and (b) simulated transmission specturm of the LIL substrates of various periods. (c) Simulated normalized electric field for the 300 nm period substrate at the resonance wavelength.	82
Figure 6.4 Raman response of the 300 nm LIL substrate and bare glass substrate to the varying concentration of urea.	82
Figure 6.5 (a) Raman spectrum of 99 % pure urea powder. (b) Plot of the Intensity of the main Raman peak (1010 cm ⁻¹) of urea for the 300 nm period LIL substrate vs the urea concentration in the log (base 10) scale. The error bars represent the standard deviation between 3 measurements	84
Figure 6.6 a) Ellipsoidal plot of the molecule metribuzin at the 50% probability level and at room temperature (298 K). b) Theoretical structure of metribuzin. Hydrogens have been removed for clarity. c) Comparison of the experimental and theoretical bond length. Theoretical structure was calculated using aug-cc-pVTZ B3LYP level of theory	87
Figure 6.7 Comparison of experimental a) Raman and b) FTIR spectra of Metribuzin with the calculated c) Raman and d) IR spectra calculated using aug-cc-pVTZ basis set	88
Figure 6.8 Raman a) shift and b) intensity error for the various basis sets compared to the experimentally observed values. The intensity for all the plots was normalized with respect to the vibrational mode 4 (the major experimental Raman shift of 660.5 cm ⁻¹)	92
Figure 6.9 Total error in a) Raman shift and b) Raman intensity of the various basis sets compared to the experimental vibrational modes. The absolute values of errors were used in calculating both (a) and (b).	94
Figure 6.10 Computational cost of the basis sets for calculating Raman spectra. The computation cost of all the basis sets was normalized with respect to aug-cc-pVTZ	94

Figure 6.11 Comparison of the experimental and calculated (at the DGDZVP B3LYP level of theory) Raman spectra of all the agrochemicals tested in this thesis	95
Figure 6.12 Optimized structure of Atrazine	96
Figure 6.13 Optimized structure of Mancozeb.	97
Figure 6.14 Optimized structure of Clofentezine	99
Figure 6.15 Optimized structure of Chlorantraniliprole	100
Figure 6.16 Optimized structure of Thiamethoxam	102
Figure 6.17 Optimized structure of Tau-fluvalinate	104
Figure 6.18 Optimized structure of Flubendiamide	105
Figure 6.19 Comparison of the Raman shift error for the vibrational modes in the tested agrochemicals	106
Figure 6.20 Comparison of the average of the absolute error in Raman shift for the tested agrochemicals	106
Figure 6.21 The limit of detection (LOD) of the agrochemicals testing using the optimized sample fabricated using LIL	107
Figure 7.1 Conclusion of the thesis	111
Figure E.1 Reflectivity plots for samples of various thicknesses deposited with and without a quartz base	126

List of Tables

Table 2.1 Applications of plasmonic sensors	6
Table 2.2 Applications of LSPR based sensors	8
Table 2.3 Brief collection of application of SERS based agrochemical sensors.	19
Table 3.1 Loretz Drude model parameters for gold in Rakic' et al. [203]. Units of Γ and ω are eV.	22
Table 4.1 Sensitivity comparison of nanopatterns in the literature	57
Table 5.1 FWHM calculations for 40N, 40Q, 60N and 60Q samples. Where 40N (and 60 N) and 40Q (and 60 Q) are gold films of thickness deposited with and without quartz base, respectively.	61
Table 6.1 Laser interference lithography (LIL) laser exposure parameters	
Table 6.2 Comparison of the detection limit of urea in the literature	83
Table 6.3 Applications of the commercial agrochemicals tested in this thesis	85
Table 6.4 Details of the agrochemicals tested in this thesis	86
Table 6.5 Comparison of experimental and calculated (using aug-cc-pVTZ) wavenumbers of the main peaks of Metribuzin with its vibrational mode assignment. Vibrational modes common for both Raman and IR are in bold. The vibrational modes are as follows: v is stretching (v_s is symmetric stretching and v_{as} is antisymmetric stretching), δ is bending (δ_s is symmetric bending and δ_{as} as is antisymmetric bending), ω is wagging, ρ is rocking, and τ is twisting. The ring mode assignments are from the Wilson nomenclature (Appendix G) [316]. Henceforth, these conventions were used throughout this thesis.	91
Table 6.6 Comparison of experimental and calculated wavenumbers of the main peaks of Atrazine and Mancozeb (bold text indicates vibrational modes with major contribution from Zineb) with their vibrational mode assignment	98
Table 6.7 Comparison of experimental and calculated wavenumbers of the main peaks of Clofentezine and Chlorantraniliprole with their vibrational mode assignment.	101
Table 6.8 Comparison of experimental and calculated wavenumbers of the main peaks of Thiamethoxam and Flubendiamide with their vibrational mode assignment	103
Table 6.9 Comparison of experimental and calculated wavenumbers of the main peaks of Tau-fluvalinate with its vibrational mode assignment.	104
Table 6.10 Comparison of the detection limit of the tested agrochemicals in the literature	108

Abbreviations

SERS Surface-Enhanced Raman Spectroscopy

LIL Laser Interference Lithography

DFT Density Functional Theory

FEM Finite Element Method

TMM Transfer Matrix Method

LOD Limit of Detection
EM Electromagnetic

LSPR Localized Surface Plasmon Resonance

SPR Surface Plasmon Resonance SPP Surface Plasmon Polariton

ε Dielectric function

 ϵ' Real part of

ε" Imaginary part of

UV Ultraviolet
NIR Near Infrared

a-Si Amorphous silicon
ppm Parts per million

M Molar

FDTD Finite-Difference Time-Domain
PDE Partial Differential Equation

PML Perfectly Matched Layer

RMS Root Mean Square

B3LYP Becke, 3-parameter, Lee—Yang—Parr STO-3G Slater Type Orbital - 3 Gaussian

cc-pVDZ Correlation-Consistent Polarized Valence Double Zeta cc-pVTZ Correlation-Consistent Polarized Valence Triple Zeta

FWHM Full Width at Half Maxima

n Refractive index λ Wavelength

 λ_D Resonance wavelength of single nanodisk

 λ_G (10) Grating resonance of nanodisk array

Q factor Quality factor R6G Rhodamine 6G

EF Enhancement factor

Chapter 1. Introduction

The modernization of agriculture demands high crop yields, which is causing the increasing use of agrochemicals to protect plants from insects, fungi, rodents, weeds, etc. This increasing trend was also surveyed by the food and agriculture organization of the United Nations [1], shown in Figure 1.1. Although these agrochemicals are intended to eliminate harmful organisms, their use in unregulated and excessive amounts is causing contamination of food and water. The frequency and quantity of use of these chemicals are causing their seepage into groundwater, nearby drinking water sources, and the crop produce itself. The chemical intake in our diet is increasing at an alarming rate due to the excessive use of agrochemicals [2]. The consumption of these chemicals over the recommended quantities can cause nausea, vomiting, diarrhoea, and positioning in the short term [3]. Continued consumption can lead to allergies, dermatological effects, respiratory issues, neurological disorders, and even cancer [4]. As per a report by the pollution monitoring lab of India on pesticide residues in bottled water in the Delhi region, even bottled water contains traces of pesticides [5]. The health concerns due to excessive use of pesticides is a massive problem in the world. The US Environmental Protection Agency (EPA) has banned the use of several pesticides, including chlorpyrifos, diazinon, ethoprop, phosmet, etc. [6]. In India, the Ministry of Agriculture & Farmers Welfare (MoA & FW) has also banned diazinon and other pesticides such as alachlor, chlorobenzilate, phosphamidon, etc. [7]. The Bureau of Indian Standards has listed the allowable limit of 14 commercial pesticides in drinking water, but numerous chemicals commonly used are absent [8]. Out of the 8 commonly used agrochemicals in the current thesis, the US EPA has quantified regulations for 2 (atrazine and metribuzin) and the MoA & FW in India has restricted the use of Mancozeb (banned for use on Guava, Jowar and Tapioca) [9]. Therefore, the regulation and monitoring of agrochemicals is essential to ensure that we are consuming safe and healthy food and water. This thesis aims to improve the monitoring of agrochemicals.

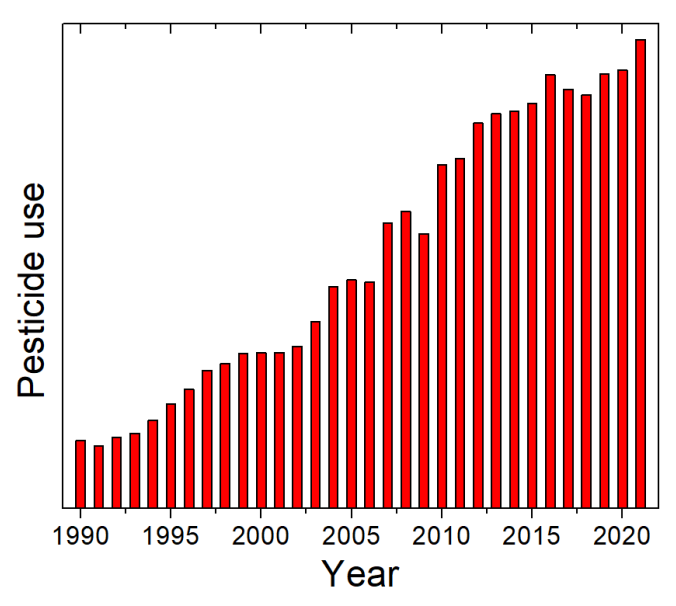


Figure 1.1 Use of pesticides worldwide from 1990 to 2021 according to a survey by the food and agriculture organization of the United Nations [1].

Vibrational spectroscopy uses the unique vibrational modes of these chemicals to identify and quantify their composition with high sensitivity, selectivity, speed, and accuracy. The basic principle of Raman spectroscopy is that the interaction of incoming photons and molecular vibrations of the target chemical causes inelastic scattering of the photons, and the energy shift of the scattered photons is unique to the polarizable vibrational modes of the chemical; hence, the Raman spectra act as a fingerprint of the chemical [10]. However, even after the optimization of all the instrumentation parameters, the probability of Raman scattering is very low. Therefore, engineers and scientists have been using surface enhanced Raman spectroscopy (SERS) to increase the Raman signal from the desired molecule. SERS uses periodic [11, 12] or non periodic [13, 14] structures with dimensions comparable to or smaller than the laser excitation wavelength and are generally fabricated using plasmonic materials (gold, silver, copper, aluminium, palladium, etc.) due to their resonant modes creating a large SERS enhancement. Plasmons are collective oscillations of electrons created at the interface of a metal and dielectric in response to an electromagnetic field at certain excitation conditions. The plasmonic response of periodic nanostructures create electromagnetic enhancement due to two effects: the near field and the far field response of the structures fabricated on the SERS substrate [15, 16]. The electromagnetic field experiences local confinement due to the size of the plasmonic structures being smaller than the incident wavelength. The confinement creates electric field hotspots majorly in the form of dipole and in some case multipoles. Thus, the massive field experienced by the target molecules helps increase its Raman signal. The Raman signal is amplified when the resonance wavelength is close to the Raman peak of the target molecule and the laser wavelength selected for the analysis [17]. Hence, optimising the plasmonic response of nanostructures can create highly sensitive and selective SERS substrates. However, the Raman "fingerprint" spectrum for many commercial agrochemicals is not prevalent in the literature. Density functional theory (DFT) can accurately model the vibrational response of these agrochemicals, which is crucial for researchers to develop more efficient SERS based substrates. In this thesis, plasmonic nanostructures were optimized using simulations and fabricated using laser interference lithography (LIL) technique. The effect of roughness on the plasmonic response on plasmonic thin films and nanostructures was experimentally studied. The LIL sample with the highest Raman enhancement was selected as a SERS substrate. Various agrochemicals used by the farmers were procured, and their Raman spectra were calculated using DFT. The optimized LIL sample was used to test the limit of detection (LOD) of 8 agrochemicals.

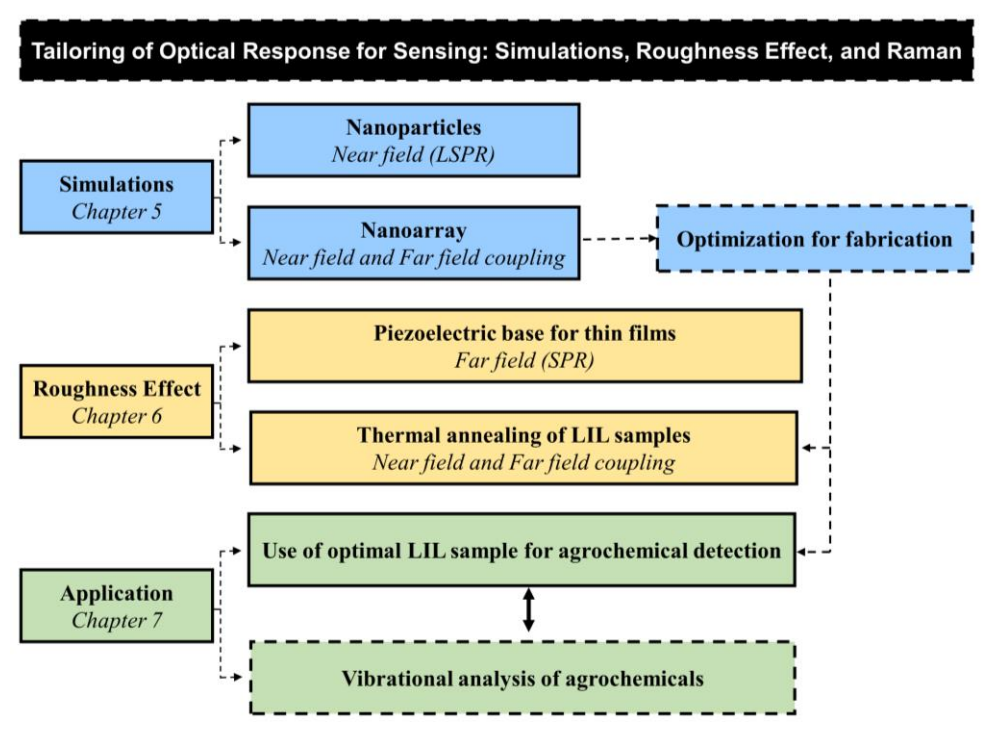


Figure 1.2 Thesis outline.

This thesis is divided into 8 chapters:

Chapter 1 briefly introduces the application of the work, the main principles involved, with a description of the work included in the various chapters.

Chapter 2 introduces the scientific principles and techniques discussed in this thesis. Plasmonic materials and structures along with their excitation and fabrication techniques were explained in detail. An introduction to Raman sensing, vibrational analysis and SERS substrates was also provided.

Chapter 3 explains the theoretical techniques used throughout this thesis. Finite element method (FEM) simulations were used to predict and optimize the response of single nanoparticles and nanoarrays. The combination of Bruggeman effective medium theory and transfer matrix method (TMM) was selected to model the roughness effect in thin plasmonic films. The Density functional theory (DFT) was used to calculate the Raman spectra of the various agrochemicals tested in this thesis. The vibrational analyses of the majority of these agrochemicals were not prevalent in the literature.

Chapter 4 presents the experimental procedures and characterization techniques. Laser interference lithography (LIL) and thermal deposition were used to fabricate gold nanodisk arrays. Transmission spectroscopy and surface plasmon resonance (SPR) techniques were used to analyse the plasmonic response. Characterization techniques that were used were SEM, AFM, XRD, SC-XRD, FTIR and Raman spectroscopy.

Chapter 5 discusses the simulations of plasmonic nanoparticles and nanoarrays. FEM was used to study the effect of shape, size, material, and surrounding environment on the plasmonic response. The coupling effect of the single nanostructure resonance and the array resonance was analysed in detail. The optimized material and geometry were selected to be fabricated.

Chapter 6 was focused on experimentally studying the roughness effect on plasmonic structures. An oscillating piezoelectric base was used during deposition to vary the roughness of gold thin films. To improve the surface morphology and control the dimensions of nanoarrays (which is difficult for the LIL technique), thermal annealing was performed at 500 °C for 10 and 20 minutes.

Chapter 7 discusses the applications of the gold nanodisk arrays as a SERS substrate. The optimized substrate was selected among samples with varying periods (period to diameter ratio was ~2.2) using the dye Rhodamine-6G. Its practical use was confirmed by detecting urea in water. Vibrational analysis of 8 agrochemicals was performed using DFT, and their LOD was experimentally tested using the optimized substrate.

Chapter 8 summaries and concludes the thesis.

Chapter 2. Background

2.1 Plasmonics

A plasmon refers to the collective excitation of electrons in response to an electromagnetic (EM) wave [18]. In practical applications, this collective excitation is generally obtained as localized plasmons in nano sized structures or particles, the resonance condition is called localized surface plasmon resonance (LSPR). In thin films, the collective excitation is in the form of surface plasmon polaritons (SPPs), the resonance condition in this case simply called surface plasmon resonance (SPR). The resonance condition used in sensing applications in nano sized structures or particles (localized plasmons) is called localized surface plasmon resonance Metals show a good plasmonic response due to the availability of free electrons on their surface [19]. The LSPR condition is satisfied in structures that are comparable to or smaller than the wavelength of the incoming EM wave. The electrons on the surface of these structures collectively oscillate to oppose the incoming EM wave; further, in the resonance condition, the oscillation frequency matches the incident EM wave [20]. SPR is observed in metallic films with thickness in tens of nanometres; however, SPR condition is not fulfilled directly by a thin metal film. The momentum of the incoming EM wave must match the momentum of the surface plasmons. The simplest method of satisfying the SPR condition is by using the Kretschmann configuration, which uses a prim that creates an evanescent wave via total internal reflection to satisfy the coupling condition [21]. Another method to obtain the momentum matching is by creating a grating like structure on the thin film, which is called grating coupling/resonance [22]. The plasmons in the case of thin films are no longer confined as in LSPR, but propagate as surface plasmon polaritons SPPs. At the resonance condition, the frequency of oscillation of the polariton is equal to the frequency of the incoming EM wave.

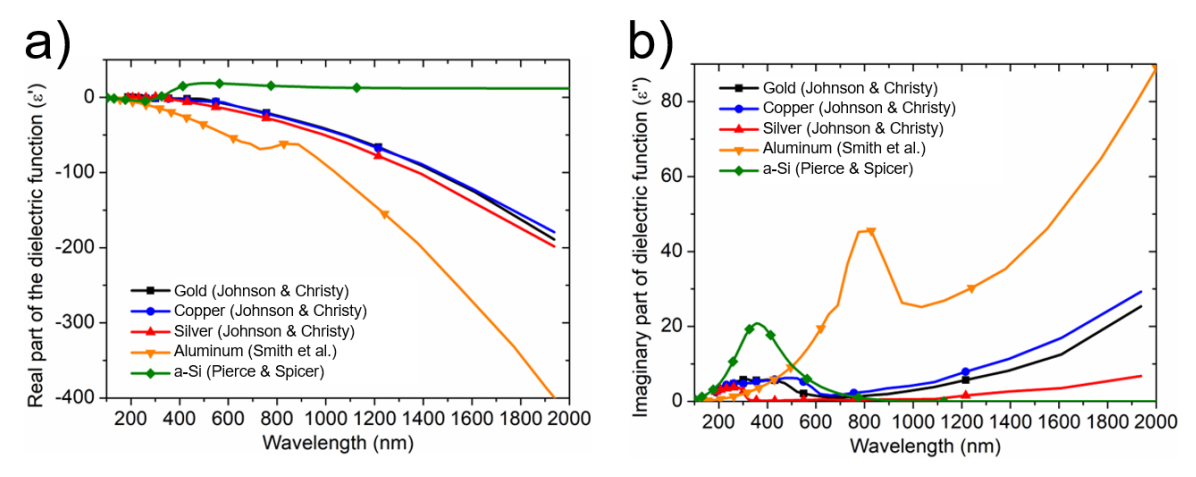


Figure 2.1 The d) real and e) imaginary part of the dielectric function of gold, copper, silver, and aluminium.

The dielectric function of a material determines the intensity and wavelength range of its plasmonic response [23]. Silver and gold have the best plasmonic response among the commonly available

materials; however, silver is highly prone to corrosion [24]. Hence, gold is highly prevalent as a plasmonic material throughout research and commercial applications. The research community is on the hunt for new economic materials that can replace gold, and the best candidates are copper and aluminium. Comparison of the dielectric function and LSPR response of silver, gold, copper and aluminium in Figure 2.1 shows that the wavelength of the plasmonic response of silver, gold, and Cu was similar and in the visible range. However, owing to the lower magnitude of the imaginary part of the dielectric function in the visible range for silver, it has the strongest plasmonic response, followed by gold and copper. A higher magnitude of the imaginary part of the dielectric function leads to more losses in the material, thereby causing a weaker plasmonic response. Aluminium, in comparison, shows plasmonic behaviour in the UV and visible wavelength, but it also had high losses similar to copper [25]. Apart from the material effect, the size, shape, and periodicity of the structure have a critical impact on its overall plasmonic response. The applications of plasmonic sensors are shown in Table 2.1.

Table 2.1 Applications of plasmonic sensors

Field	Detection	Species
Food safety	Bacteria	E.coli [26], Salmonella [27], Listeria monocytogenes [28], Campylobacter jejuni [29]
Mycotoxin Botulinum [30], Deoxy		Botulinum [30], Deoxynivalenol [31], Nivalenol [31]
	Exotoxin	Staphylococcal enterotoxin B [32]
Medical Cancer marker		Prostate specific antigen [33], Interleukin 6 [34], Interleukin 8 [35]
diagnostics	Cardiac marker	Myoglobin [36], Troponin I [37]
	Virus marker	Ebola [38], Influenza [39], Hepatitis B virus [40], DENV E-protein (Dengue) [41]
	Drug	Morphine [42], Interferon-γ [43], Warfarin [44]
Environmental	Metal ion	$Hg^{2+}[45], Pb^{2+}[46], Cu^{2+}$
monitoring	Pesticide	Atrazine [47], Dichlorophenoxyacetic acid [48], Thiabendazole [49], Phenol [50]
	Explosive	RDX [51], Trinitrotoluene [52]

The structure of metals is generally described as positive ions surrounded by a sea of electrons. Metals are charge neutral, but the electrons surrounding the positive ions are charged mobile species; hence, metals can be considered as plasma in electromagnetic terms. The plasma frequency of a bulk material can be calculated by the following equation [53]:

$$\omega_p = \sqrt{\frac{ne^2}{\epsilon_0 m}}$$
 2.1

where m, n, and e are the mass, concentration, and charge of the charged mobile species respectively, and ϵ_0 is the relative permittivity of free space. The most frequently used metals for SPR sensors are gold, silver, and aluminium; whose bulk plasma frequency lies in the UV region. Moreover, visible light being a transverse wave, cannot directly excite the surface plasmon wave, which is longitudinal in nature. Therefore, certain conditions have to be applied so that visible light can excite the surface plasmons on the metal-dielectric interface. In plasmon based sensors, the plasmons can be excited as

the LSPR mode or SPP mode. The excitation in SPP mode can be achieved by prism, waveguide, and grating coupling techniques.

2.2 Localized Surface Plasmon Resonance (LSPR)

The metal particles of size smaller than or comparable to the wavelength of incident electromagnetic radiation are excited in the LSPR mode. When an electromagnetic wave strikes metallic nanoparticles in a colloidal solution, the free electrons experience a force that causes the particles to displace, which induces a dipole movement to oppose the charge created; this leads to oscillation of the free electrons. The confinement of the electrons prevents their propagation, and at the resonance condition, the frequency of the oscillating electrons coincides with the incident photons. At the resonance frequency, a dip in the reflectance spectrum is observed, which is sensitive to the surrounding refractive index. The behaviour of the material of the nanoparticles is generally modelled using the Drude model. The plasmonic response of the nanoparticles is dependent on the dielectric constant of the metal (ε_m) and the surrounding (ϵ_d). Furthermore, $\epsilon_m = \epsilon' + i \; \epsilon''$, where ϵ' and $\; \epsilon''$ are the real and imaginary parts of the refractive index of the metal. ε' describes how much a material can store or permit the electric field incident upon it and ε'' takes into account the dissipation effect on the electric field in the metal [54, 55]. The radius of the nanoparticle is r, and N is the electron density, λ is the wavelength of the incoming radiation. The extinction cross-section defines the rate at which the incident energy per unit area is scattered and absorbed [56]. The resonance condition is satisfied when $2\varepsilon_d = -\varepsilon'$; for silver and gold nanoparticles, the resonance wavelength lies in the visible spectrum [57]. The particle size and shape also influence the resonance wavelength [58, 59].

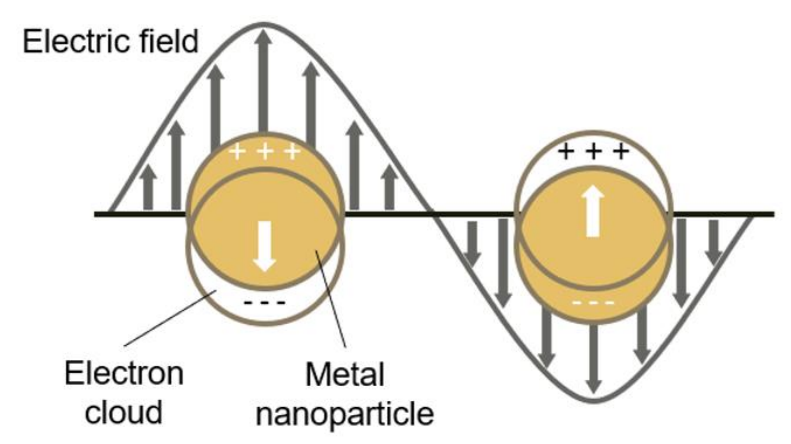


Figure 2.2 Schematic of the dipole created due to oscillations of electrons created in the LSPR effect.

The requirements of the material properties of the material to excite the plasmons in the propagating or LSPR (Fröhlich condition [6]) is derived by using Mie theory which uses the Drude model to model the complex dielectric function of the metal [61]. In the Drude model, it is assumed that the response of the nanoparticle due to induced EM field is damped by various phenomena including interactions of electron-electron, electron-lattice, defects, etc. However, in modelling the optical response of the

nanoparticles, the interband transitions is the most important factor, which describes the wavelength dependent damping rate [62]. For a plasmonic response, the real part dielectric function of the material should have a large negative real part and imaginary part should be positive and small. Additionally, the real part determines position of resonance wavelength and the imaginary part pertains to the losses. Noble metals, particularly gold and silver comply to these conditions, hence, they are commonly used in plasmonic based devices. However, more economical materials such as copper and aluminium are also being explored for various applications [63–65].

One of the earliest applications of the LSPR effects was in the Roman empire, where gold and silver nanoparticles were embedded in glass to decorate cups that displayed different colours depending upon whether the cup was lit from the inside or outside [66]. The LSPR effect observed in the plasmonic nanoparticles solution is extensively used in sensing applications. The LSPR does not require any special excitation condition compared to the SPP based thin film SPR sensors which will be discussed in the later sections. Hence, the instrumentation of the LSPR based sensors is very simple, therefore, economical devices can be developed using metallic nanoparticle solutions. LSPR sensors generally use a white light source, collimation optics to focus the light into the solution containing nanoparticles and the target chemical which is to be detected, the transmitted light is then focussed onto a spectrometer. A dip in the transmission spectrum is observed at the LSPR wavelength [67]. The LSPR wavelength is dependent on the surrounding (solution) refractive index of the nanoparticles. When target chemicals are added to the nanoparticle solution, the refractive index of the solution changed, which shifts the resonance wavelength. This shift in LSPR wavelength is correlated to the concentration of the target chemical. This forms the basis of the LSPR based sensing devices. Generally, the surface of the nanoparticle is immobilized to trap the target chemicals and enhance the selectivity as well as the sensitivity of the device. The Table 2.2 lists a few LSPR based sensors for food safety, biomarker, and water pollutants. LSPR based sensors can be optimized to detect nanomolar levels of concentrations of the target chemical.

Table 2.2 Applications of LSPR based sensors

Field	Detection	Sensor Performance (LOD)	Ref
Food safety	E. coli	0.47 CFU/mL	[68]
	Thiram	5 nM	[69]
	ethion	9 ppm	[70]
Biomarker	Cholesterol	25.5 nM	[71]
	Creatinine	128.4 uM	[72]
Pollutant	Pb2+	50 pM	[73]

The advanced applications of metallic nanoparticles extend over a plethora of domains, which includes light manipulation [74], light emitters [75], spectroscopy [76, 77], photodetection [78], surface-enhanced Raman spectroscopy (SERS) [79–81] and solar cells [82]. Gold and silver have excellent

plasmonic properties and generally have applications in the visible and NIR range. Among metals displaying good plasmonic response, aluminium is the only one that displays the resonance wavelength in the deep UV and NIR region for sizes up to 200 nm [83]. The active deep UV region is a new region of interest for SERS applications [84], however, it has limited applications due to the requirement of expensive lasers and degradation of certain materials due to the high energy. Nanoparticles of copper have applications in catalysis [85] and electronic circuits [86] (because of the high conductivity of copper).

Fabrication techniques such as electron beam lithography [87, 88], nanoimprinting [89], laser interference lithography [90] have increased the ease of fabrication of metallic nanoparticles of complex shapes. Arrays are being employed that include nanostructures of various shapes, which enhance the performance of plasmonic devices. The triangular and square cross-sections are useful because their sharp features enhance the optical response due to the formation of electric field hotspots near the sharp edges [91, 92]. Copper and silver are highly prone to surface oxidation; hence, metal nanoparticles are being embedded in various media to achieve stable nanoparticles which are protected from environmental effects [93, 94]. The media generally used are glass [95, 96] and silicon [97, 98], and the major applications include solar cells, SERS, biosensing, and photovoltaics. In SERS and other sensing applications, the embedding of nanoparticles in a glass or another dielectric matrix adds robustness to the substrate and prevents agglomeration as well as oxidation. Another application of metal nanoparticles in a glass environment is in the development of glasses that prevent the entry of UV and/or NIR light into cars/buildings [99]. Phenomenon such as nonlinear refraction, absorption and optical limiting are observed in metal nanoparticle implanted glasses [100, 101]. The enhanced electric fields around metal nanoparticles distributed in a dielectric in the LSPR condition can lead to third order nonlinear susceptibility creating nonlinear optical refraction and absorption when exposed to high energies [102]. The optical limiting using metallic nanoparticles is being used for protection against laser radiation by limiting its transmittance. The two photon absorption was deemed to be the major contributor to the optical limiting [103], the overlap of the LSPR band and two photon absorption can enhance the optical limiting performance. Furthermore, nonlinear effects created by implanting metal nanoparticles in glass medium have paved the way for new applications in telecommunications and magneto optical devices [93].

2.3 Surface Plasmon Polaritons (SPPs)

Surface plasmons are observed when an electromagnetic wave under suitable conditions excites the free electrons at a metal-dielectric interface, leading to collective charge (electron) oscillations. The excitation in the SPP mode leads to the creation of oscillating density wave of electrons which travels on the metal-dielectric interface, called SPPs. At the resonance condition, the momentum of the incoming photons matches that of the electrons present at the interface, which leads to the transfer of energy from the incoming photons to the free electrons. Thus, a dip can be observed in the reflectance

spectrum at this condition, which is dependent on the refractive index surrounding the metal-dielectric interface; this shift forms the basis of SPR based sensing [104]. Plasmons were first published in 1902 as anomalies that appeared as dark bands when light was incident on a metallic grating [105]; these anomalies were later proved to be associated with electromagnetic surface waves [106]. In 1968, Otto [107] and Kretschmann [108] independently reported techniques to excite the surface plasmons using a prism and a metallic thin film. The earliest practical application of the SPR effect was a gas sensor reported by Liedberg et al. in 1983 [109]. Since then, numerous SPR based sensors have been developed for medical diagnostics, food safety, water pollutant detection, etc., owing to the label free and real time detection of these sensors. SPR is able to measure changes in the refractive index of the order of 10⁻⁶ to 10⁻⁷ of its surrounding medium, which can be interpreted as the change in refractive index due to 0.01 to 0.001 °C variation in water temperature [110]. The advantages of SPR sensing over other conventional techniques are its sensitivity, selectivity, low background noise, lack of labelling requirement, immediate results, small sample volume requirement, reproducibility, and its ability to multiplex [111, 112]. Therefore, during the COVID-19 pandemic, SPR was explored as one of the options for quick and accurate detection of the virus SARS-CoV-2 [113-116]. SPR sensors' ability to detect viruses can be confirmed by its extensive use in the detection of the Ebola virus [38, 117].

Maxwell's equations are solved using appropriate boundary conditions to find the expression of the wavevector of the SPPs. Similar to LSPR calculations, the Drude model is used to model the behaviour of the metal. The wavevector of the SPPs (k_{SPP})is given by [118]:

$$k_{SPP} = k \sqrt{\frac{\varepsilon_{m} \varepsilon_{d}}{\varepsilon_{m} + \varepsilon_{d}}}$$
2.2

where k is the wavevector of the incoming radiation. $\varepsilon_m = \epsilon' + i\epsilon''$ and ε_d are the dielectric functions of the metal film and surrounding medium, respectively. SPR phenomenon is a combination of quantum mechanics and electromagnetism; the momentum of a quantum particle is analogous to the wavevector of a matter wave. In the above expression, the square root term is generally more than 1 and positive; hence, the wavevector or momentum of the incoming radiation has to be increased to match the wavevector of the SPPs, which is achieved via a coupling mechanism. The most popular methods of excitation of SPPs are prism, waveguide, and grating coupling. These coupling methods are explained later in this section. An additional conclusion that can be drawn when solving Maxwell's equation for SPP mode is that s-polarized (TE polarized) electromagnetic wave cannot induce SPPs as there is no electric field vector in the direction of the SPP wavevector; therefore, only the p-polarized (TM polarized) radiation is used for excitation of SPPs. Furthermore, while solving Maxwell's equations to obtain the propagation length and depth, the following conditions have to be satisfied [19]:

$$\varepsilon_{\rm m}\varepsilon_{\rm d} < 0$$
 2.3

$$\varepsilon_{\rm m} + \varepsilon_{\rm d} < 0$$
 2.4

These equations can be satisfied when one of the dielectric constants is negative and much greater in magnitude than the other. Therefore, ε_d being positive, the metal film should have a large negative dielectric constant. The metals generally used in SPR sensors have a large and negative ε' in the visible and NIR range. While ε'' is positive and small, which leads to low decay of the SPPs. The propagation length (L_{SPP}) and depth (δ_{SPP}) of SPP is defined as the distance at which the intensity of the polariton decays to 1/e of its initial value in the direction and perpendicular to the direction of propagation, respectively; they are calculated using the following expressions [119]:

$$L_{SPP} = \lambda \frac{(\varepsilon')^2}{2\pi \varepsilon''} \left(\frac{\varepsilon' + \varepsilon_d}{\varepsilon' \varepsilon_d} \right)^{\frac{3}{2}}$$
 2.5

$$\delta_{\text{SPP}} = \frac{\lambda}{2\pi} \left(\frac{\varepsilon' + \varepsilon_{\text{d}}}{\varepsilon_{\text{d}}^2} \right)^{\frac{1}{2}}$$
 2.6

The conclusions previously mentioned regarding ϵ' can be applied to obtain a large L_{SPP} . To achieve a higher selectivity of detections, the δ_{SPP} should be small. The LSPR mode works in a shorter range (15-50 nm) as compared to the SPP mode (250-500 nm) [120, 121]. Therefore, the selectivity of the LSPR mode is higher as compared to SPP mode because of the concentrated field enhancement, but the use of LSPR sensors is limited because of its much lower sensitivity [122]. However, the LSPR effect is less susceptible to inaccuracies caused by temperature variation and other minor changes in the surroundings [123]. Gold and silver are used as thin films for various coupling techniques because of their high SPR response. Silver is considered to produce the highest SPR response and sensitivity, but silver layer exposed to the surroundings is highly prone to oxidation [124, 125]. It has been reported that the SPR phenomenon can also be explained using Fano resonance and electromagnetically induced transparency [111, 126, 127]. Sensors based on the combination of LSPR and SPP modes are also being developed, which offer high selectivity and good sensitivity due to electric field enhancement. Reports of sensing using combined LSPR and SPP mode utilizing nanoarrays on metallic film are highly prevalent in the literature [110, 128].

2.3.1 Prism coupling

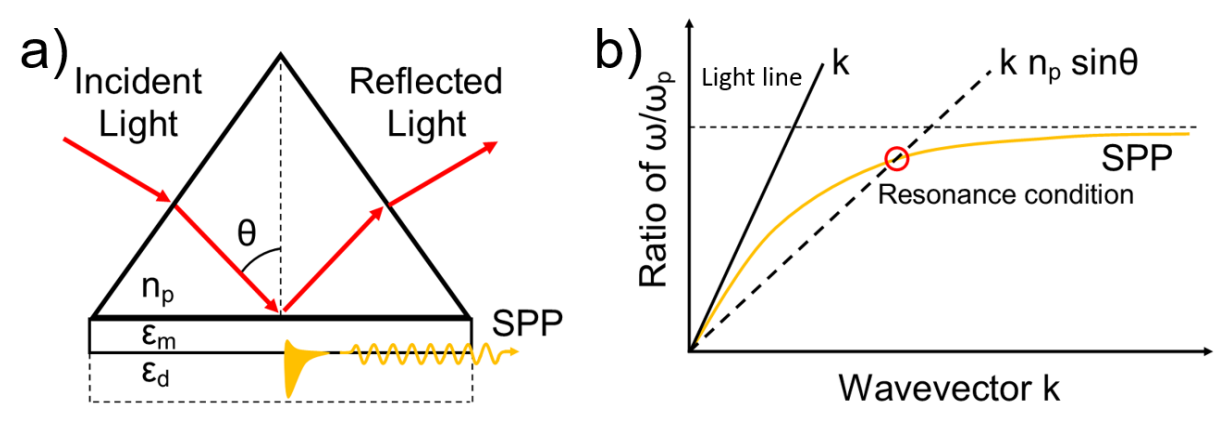


Figure 2.3 a) Kretchmann configuration and b) Dispersion relation for prism coupling.

Prism coupling is the most simple and easy to control coupling method and offers excellent sensitivity. The prism coupling can be achieved using the Otto and the Kretschmann configuration (Figure 2.3 (a)). The Otto configuration is not generally used because the air gap between the metal film and the prism is difficult to control. The basic working of the Kretschmann configuration is that a p-polarized light incident on a prism undergoes total internal reflection (TIR), creating an evanescent wave at the metal-dielectric interface. The evanescent wave is responsible for the coupling and creation of the SPPs at a critical angle. The coupling effect only takes place if the thickness of the metal film is less than 100 nm because of the exponential decay of the evanescent wave in the metallic film. However, if the thickness of the metal is too low (lower than 30 nm), the SPR signal strength will be low due to the lower number of charged electrons being available to absorb the incident energy [129]. Hence, the metal film thickness generally selected is between 40 and 50 nm. The coupling condition can be visualized by the dispersion relation shown in Figure 2.3 (b); by incorporating the prism refractive index, the wavevector is increased to fulfil the resonance condition. The resonance condition of prism coupling is given by the following equation [18]:

$$n_{p} \sin \theta = Re \left\{ \sqrt{\frac{\varepsilon_{m} \varepsilon_{d}}{\varepsilon_{m} + \varepsilon_{d}}} \right\} + Re \left\{ \frac{\Delta \beta \lambda}{2\pi} \right\}$$
 2.7

where n_p is the refractive index of the prism, θ is the angle of incidence, and $\Delta\beta$ takes into account the effect of the prism and thickness of the film. The $\Delta\beta$ term is commonly ignored while expressing the dispersion relation. At the critical angle, a dip in the reflectance spectrum is observed, which is dependent on the refractive index of the surrounding dielectric medium. The biggest drawback of the prism coupling technique is the relatively bulky nature of its components.

2.3.2 Grating coupling

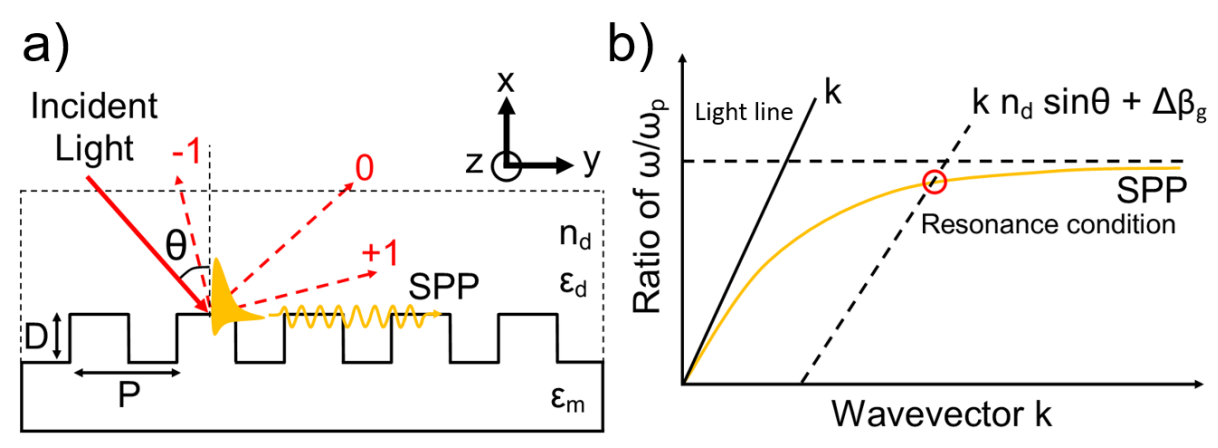


Figure 2.4 a) Grating coupling and b) Dispersion relation for grating coupling.

The basic principle of grating based coupling is shown in Figure 2.4; the incoming radiation is incident on a metallic grating, which leads to a diffraction wave consisting of various diffraction modes that are

coupled. The different modes produce a distinctive response to the SPR signal [130]. Generally, the mode that creates the sharpest SPR response is selected for investigation. When the incident wave with a wavevector k_z (in the z direction) is incident on a diffraction grating with pitch of P and depth D, a diffracted wave is formed with wavevector k_{zm} , which is given by [18]:

$$k_{zm} = k_z + m \frac{2\pi}{P}$$
 2.8

where m is the order of diffraction. The coupling expression can be written as:

$$n_{\rm d} \sin\theta + m \frac{\lambda}{P} = \pm \left(\text{Re} \left\{ \sqrt{\frac{\varepsilon_{\rm m} \varepsilon_{\rm d}}{\varepsilon_{\rm m} + \varepsilon_{\rm d}}} \right\} + \text{Re} \left\{ \frac{\Delta \beta_{\rm g} \lambda}{2\pi} \right\} \right)$$
 2.9

where $\Delta\beta_g$ represents the propagation constant, which causes a shift in the wavevector induced by the presence of the grating, and n_d is the refractive index of the surrounding dielectric medium. The resonance condition can be visualized by the dispersion relation shown in Figure 2.4 (b). There is an excellent potential for commercial metallic grating based sensors due to advanced manufacturing techniques, but the drawback of this method is its lower sensitivity and the noise and inaccuracies caused by the analyte molecules influencing the diffraction phenomenon [131]. A new technique that can be included in grating coupling method uses a thin metal film that is perforated with nanoscale holes or structures arranged in an array [132]. A combination of LSPR and SPP effect is observed, creating more sensitive and selective surfaces [128, 133]. The incident radiation is transmitted through the film, and because of the arrangement of the nanoholes, SPP Bloch wave (SPP-BW) is produced at Bragg's condition. The depth of the holes plays an important role in defining the sensitivity of the mechanism [134]. The resonance condition of a BW-SPP in a 2D array is given by [135]:

$$\left| k \sin \theta + iG_y + jG_z \right| = \text{Re} \left\{ k \sqrt{\frac{\varepsilon_m \varepsilon_d}{\varepsilon_m + \varepsilon_d}} \right\}$$
 2.10

where G_y and G_z represent the periodicity in the y and z direction. Apart from the periodicity effect, transmission from the nanohole pattern creates a diffraction effect which is known as the Rayleigh-Wood anomaly. This technique provides improved sensitivity; however, the cost of fabrication is increased due to the complexity of the nanohole array. Further, various studies have been performed to understand the effect of the symmetry of the array, as well as the shape and size of the constituents of the array, through simulations and experimentation. Schade et al. [90] studied the aforementioned effect using aluminium nanoparticles of various shapes in a parodic array. It was observed that increasing the diameter of the spherical nanoparticles as well as an increase in the distance between the particles in the array caused a red shift in the transmission spectrum. Further, introducing asymmetric particles (almost quadratic and ellipse particles) created a polarization vector dependence on the plasmonic

response. Sinibaldi et al. [136] reported that the SPP-BW based 1D photonic crystal performed better than the conventional plasmonic based sensors. Therefore, the periodic nanoparticle arrays have the potential to improve plasmonic sensing by introducing new concepts such as asymmetric shapes and novel structures [137, 138].

2.4 Fabrication of periodic nanostructures

Periodic arrays of metal nanostructures formed the centre of many studies in the area of metamaterials and metasurfaces. They were applied to increase the luminescence of attached molecules [139, 140], which led even to lasing [141, 142]. However, the intense local fields accompanying the resonances are also of special interest for SERS, as recent studies show[143–145]. However, the commercial application of these structured surfaces is still in its nascent stage due to the cost and time required for their fabrication. The fabrication methods employed by engineers and scientists to fabricate nanostructures include electron beam lithography (EBL) [146], UV lithography [147], laser interference lithography (LIL) [148], nanoimprint lithography [149], and templating methods which use nanospheres [150] and anodic aluminium oxide (AAO) arrays [151]. Nishijima et al. [152] presented the effect of periodicity on the plasmonic resonance of gold nanodisk arrays for applications in light harvesting and solar cells. EBL was used to fabricate the arrays on a glass substrate. EBL is the method with the highest resolution and is able to create periodic as well as non-periodic structures; however, the technique is slow and very expensive [153]. The remaining techniques use templates to create periodic structures, which can then be selectively deposited with the required material and thickness, and the excess material is etched away. These techniques can create arrays of nanosized shapes of plasmonic materials on the required substrate. The highly prevalent shapes for plasmonic applications include nanoarrays of disc, square and triangle shaped structures in a square lattice. As previously explained, the LSPR and SPR conditions have different excitation conditions. The nanoarrays display a combined effect of LSPR (due to the size of the individual shape being comparable to the incoming EM wave) and grating resonance. Therefore, nanoarrays have the potential to reap the benefits of both lattice and single structure resonance modes. Furthermore, the interference of the various resonance modes in metal and/or dielectric structures arranged in a periodic lattice can create exciting properties such as electromagnetically induced transparency (EIT) [154]. The applications of EIT are in optical communications and computation (increasing the speed and decreasing power compared to electronic switches), light delay and storage [155], enhanced non linear optics [156], biomedical imagining and new age sensing substrates. Another interesting property observed in nanoarrays is electromagnetically induced absorption (EIA) [157], as opposed to EIT, constructive inference enhances the absorption of light in a specific wavelength range. The applications include non linear spectroscopy, lasers and optical amplifiers.

2.4.1 Laser Interference Lithography

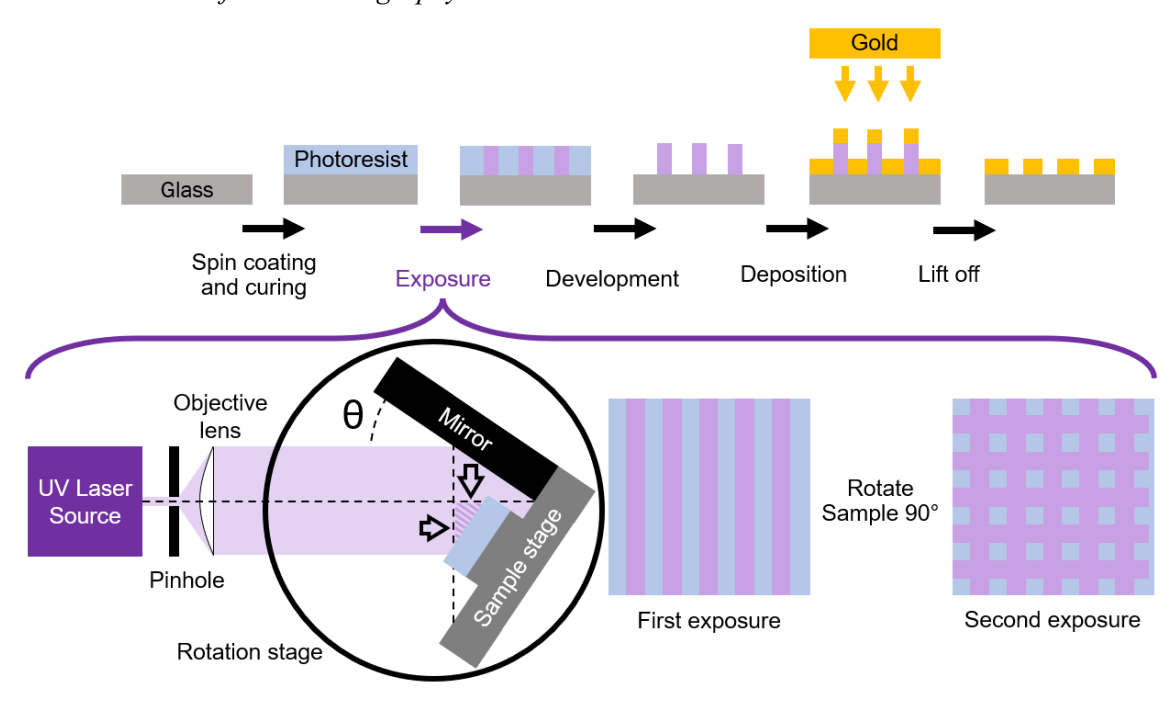


Figure 2.5 Brief schematic of the LIL process to fabricate gold nanodisk array using the Lloyd's mirror setup.

In most studies, the nanometer sized structures are fabricated using electron beam or UV lithography. Although electron beam lithography is very versatile and can produce highly complex structures with minimal defects whose size can be as small as tens of nanometers, the technique is expensive and extremely slow. Mask based UV lithography is faster, but it needs high quality masks and the minimum feature size is limited to a few hundred nanometers. LIL is a maskless fabrication technique that uses the interference of two or more laser beams to construct features from a few nanometers to micrometers [158]. A brief description of the LIL process using Lloyds mirror setup is shown in Figure 2.5. The detailed discussion of the LIL setup used in the fabrication of gold nanodisk arrays in the current thesis is discussed in section 3.4. Depending upon the type of setup selected, LIL can fabricate a wide variety of substrate sizes; hence, it has a high throughput [159]. Moreover, the fabrication time and setup cost of LIL setups are much lower than EBL. Additionally, since the interference of laser beams is used to create patterns on a photosensitive material, a wide range of materials can be selected for deposition. Although a wide variety of shapes and symmetries can be fabricated using LIL, they are limited by the number and angle of laser beams. Hence, highly complex and non periodic structures cannot be fabricated using LIL. Furthermore, LIL has been used to fabricate a few SERS substrates [160, 161].

2.4.2 Thermal annealing of Nanostructures

Gold is extensively used in plasmonic based devices for applications in sensing [88], SERS [162], catalysis [163], nonlinear photonics [164], etc. Thermal annealing is an effective method to improve the optical performance of plasmonic devices due to lowering of scattering losses [165]. Various groups have used thermal annealing as an effective tool to alter the response of nanoarrays. Potejanasak et al. [166] created gold nanodisks by chemically treating quartz substrate, deposited gold using chemical etching, and thermally annealed the surface for 15 minutes at a wide range of temperatures. It was observed that the nanodisk formation began when the surface was annealed at 500 °C due to the agglomeration of the gold film. Hulteen et al.[167] deposited gold nanoparticles in porous alumina via electrodeposition. The irregularly shaped nanoparticles were annealed at 400 °C for one hour to become dense and almost spherical in shape. The colour of the film changed from blue to pink after annealing due to the diffusion and coalescence of the nanoparticles. Cesca et al. [168] used thermal annealing to control the optical response of gold nanoarrays fabricated by nanosphere lithography, which is a low cost and high throughput fabrication technique that uses polystyrene spheres of diameters in hundreds of microns, but can only produce triangular prisms in a honeycomb lattice. The 30 nm thick nanoarray was heated at various temperatures from 200 °C to 800 °C, as the temperature was increased, the peak absorbance blue shift due to change in the shape of the nanosized structure from triangular progressively to circular, with an increase in thickness of the pattern. However, the intensity of the absorbance peak decreased drastically. Xu et al. [169] fabricated a silver and gold bimetallic nanodisks using LIL method. The nanodisks were annealed at 500 °C for 4 hours at a heating rate of 25 °C/min. It was observed the nanodisks broke down into several small parts which blue shifted the extinction peak from 872 nm to 508 nm due to the decrease in size of structures.

2.5 Raman sensing

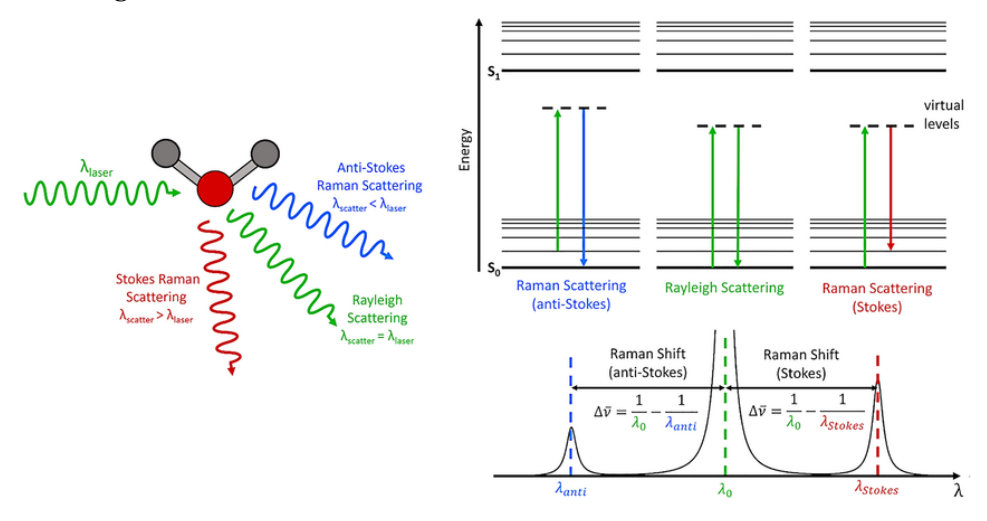


Figure 2.6 Basic principle of Raman spectroscopy and Jablonski diagram along with Raman shifted response [170]. Reprinted with permission from *Nanotechnol. Environ. Eng.* 2023, 8, 41–48, Copyright 2018 Springer Nature.

Vibrational spectroscopy is an excellent tool for detecting chemicals in food and water because of its excellent selectivity, minimal sample preparation requirement, non-destructive nature, and quick measurements. The most widely used vibrational spectroscopy techniques are Raman and infrared (IR) spectroscopy. The basic principle of Raman spectroscopy is that the interaction of incoming photons and molecular vibrations of the target chemical causes inelastic scattering of the photons, as shown in Figure 2.6. The molecular vibrations can absorb or transfer energy to the photons; thereby, the scattered photons have information of the vibrational modes of the chemical. The energy shift of the scattered photons is unique to the vibrational modes of the chemical; hence, the Raman spectra act as a fingerprint of the chemical [10]. Raman spectroscopy can only detect vibration modes that cause a change in the polarizability of the target chemical. The Raman activity can be explained using classical electromagnetic. The excitation source EM field E_{loc} with a frequency ω_{inc} creates a dipole moment μ in the target molecule which is related to its polarizability α_{mol} . The dipole moment is calculated as [171]:

$$\mu = \alpha_{\text{mol}} \cdot E_{\text{loc}}(\omega_{\text{inc}})$$
 2.11

The instrumentation of Raman spectroscopy usually includes a monochromatic light source (laser) and some optics to focus the light onto the sample and into the detector capable of recording the wavelength and intensity of the light. However, despite all the benefits of Raman spectroscopy, its major drawback is that the intensity of the scattered light is very low. Therefore, high quality optics and sensitive instrumentation are required for trace level of detection of chemicals, which significantly increases the cost of the technique. However, several techniques are being developed to enhance the Raman signal: Surface-Enhanced Raman Scattering (SERS) [172], Tip-Enhanced Raman Scattering [173], Coherent Anti-Stokes Raman Scattering [174], and Time-Gated Raman Spectroscopy [175] being some examples. Raman spectroscopy has massive potential for commercialization in the near future because of the advancement of the aforementioned techniques and the improvement in instrument manufacturing.

Raman spectroscopy is becoming prevalent in various industries such as pharmaceuticals, chemical, petrochemical, biotechnology, and forensics, for both quality control and material identification. Raman sensors can help identify and quantify the chemical composition of materials. An example of the practical use of Raman spectroscopy is shown in Figure 2.7. It was able to distinguish between human natural fingerprints and fingerprints contaminated with various chemicals. Furthermore, the information about chemical structure is also present in the "fingerprint" region of the Raman spectrum of 500 cm⁻¹ to 1800 cm⁻¹. Other techniques for material identification, mass spectroscopy, liquid chromatography, enzyme linked immune sorbent assay, etc., have drawbacks such as complicated sample preparation, requirement of chemicals for pre-treatment, destruction of the sample, and large time for completing the analysis[177]. Raman sensors offer high sensitivity, selectivity, speed, and accuracy. Furthermore, in most cases, Raman spectroscopy is non destructive and requires minimal sample preparation, which makes the technique perfectly suited for in situ measurements [178].

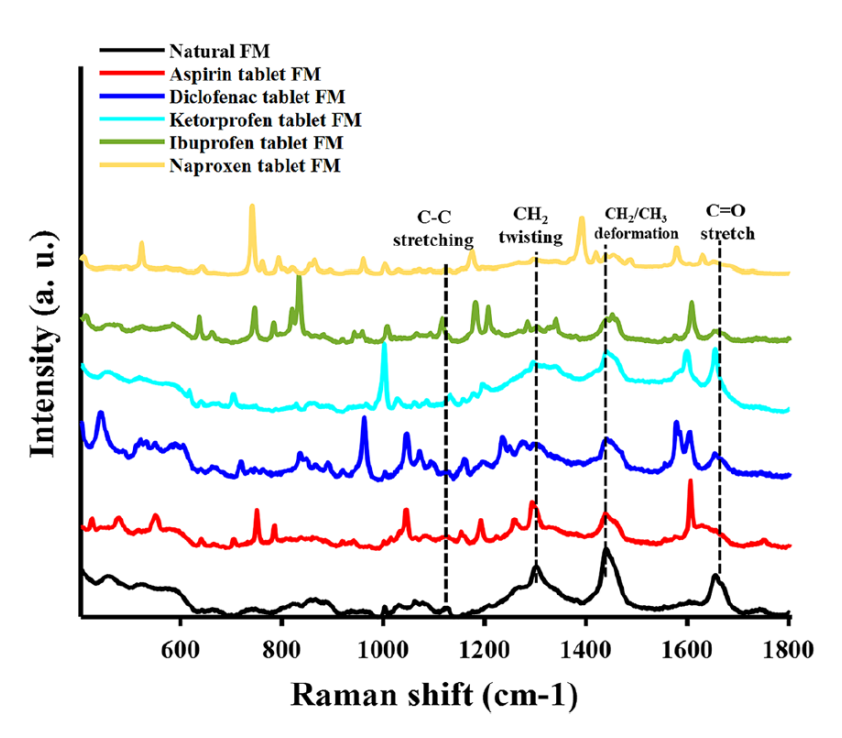


Figure 2.7 Raman spectra of natural fingerprints of a human and fingerprints contaminated with aspirin, diclofenac, ketoprofen, ibuprofen and naproxen tablets in the "fingerprint" region of 500 cm⁻¹ to 1800 cm⁻¹ [176]. Reprinted with permission from *Sci. Rep.* 2022, 12, 3136. Copyright 2022 Springer Nature.

2.6 Surface enhanced Raman Spectroscopy (SERS)

The SERS effect was first observed in 1974 by Fleischmann et al. [179], Raman enhancement due to roughened silver was noticed using the chemical Pyridine. The Raman signal of a molecule is due to the inelastic scattering of the incident laser light, which is proportional to the molecule's polarizability. The instrumentation parameters, laser wavelength, power, spot size, and exposure time have an impact on the Raman signal [180]. However, even after the optimization of the aforementioned parameters, the probability of Raman scattering is very low. Engineers and researchers have been using SERS to increase the Raman signal from the desired molecule. SERS uses periodic [11, 12] or non periodic [13, 14] structures with dimensions comparable to the laser excitation wavelength and are generally fabricated using plasmonic materials (gold, silver, copper, aluminium, palladium, etc.) due to their resonant modes creating a large SERS enhancement.

Recently, SERS has been used for food safety, medical diagnostics, drug detection, tissue imaging, forensic analysis, and in various other fields [181]. The most commonly used SERS substrates are roughened surfaces and nanoparticle solutions fabricated using plasmonic materials. However, these substrates have a random morphology; hence, they have a lot of variation in the Raman enhancement depending upon the analysis area selected [172]. Therefore, periodic SERS substrates are used to achieve a large enhancement consistently across the whole substrate.

The enhancement of SERS signals is due to two factors: chemical and electromagnetic. The chemical enhancement is due to the charge transfer and/or overlap of the ground state orbitals between the SERS

materials and the target molecule [182]. However, the contribution of chemical enhancement is much lower than electromagnetic enhancement. Electromagnetic enhancement is more than 5 orders of magnitude larger than chemical enhancement [183]. The electromagnetic enhancement is due to two effects: the near field and the far field response of the structures fabricated on the SERS substrate [15, 16]. The electromagnetic field experiences local confinement due to the size of the plasmonic structures being smaller than the incident wavelength. The confinement creates electric field hotspots majorly in the form of dipole and in some case multipoles. Thus, the massive field experienced by the target molecules helps increase its Raman signal. The phenomenon mentioned above for the near field results in a LSPR response in the far field. The Raman signal is amplified when the LSPR wavelength is close to the Raman peak of the target molecule and the laser wavelength selected for the analysis [17]. Thereby, the second mechanism of electromagnetic enhancement depends on the LSPR wavelength, along with the shape, size, thickness, and material of the structures [184, 185].

Table 2.3 Brief collection of application of SERS based agrochemical sensors.

Base	Agrochemical	Limit of detection (LOD)	Ref	
Water	Thiabendazole	4 ppm	[186]	
Water	Ricin B	50 ng/ml	[187]	
Water	Bacillus anthracis spores	$10^4 \mathrm{CFU}$	[188]	
Water	Chlorpyrifos	0.01 mg/L	[189]	
Water	Isocarbophos, Omethoate, Phorate, and	1, 5, 0.1 and 5 ppm	[190]	
	Profenofos			
Water	Theophylline	3.5 mM	[191]	
Water	Methomyl, acetamiprid-(AC) and 2,4-	$5.58 \times 10^{-4}, 1.88 \times 10^{-4}$ and	[192]	
	dichlorophenoxyacetic acid-(2,4-D)	$4.72 \times 10^{-3} \mu \text{g/mL}$		
Vegetable oil	α-tocopherol (α-Toc)	10 ppb	[193]	
Apple peel	Parathion-methyl, thiram, and	2.60 ng/cm ² , 0.24 ng/cm ² and	[194]	
	Chlorpyrifos	3.51 ng/cm^2		
Cucumber, Grapes, and	Thiram, Methyl parathion,	10 ng/cm^3	[195]	
Apple peels	Malachite green			
Plant leaves	Triazophos, Fonofos, and thiram	$10^{-7} \ M, \ 10^{-6} \ M \ and \ 10^{-6} \ M$	[196]	

Chapter 3. Theoretical and Experimental Framework

3.1 Finite element method (FEM) simulations

Over the years various methods have been used to model the response of the nanoparticles in the LSPR condition. The quasi static approximation assumes that the metallic object behaves like an electric dipole as a response to the incoming light and ignores any electrodynamic effects, however, the theory is only valid for spherical nanoparticles below 40 nm [197]. Mie theory further includes the polarization and retardation effects in the calculations of spherical nanoparticles [198, 199]. However, as the complexity in shape is introduced to the nanoparticle, Mie theory fails to accurately predict the plasmonic response [60]. The optical properties of complex shaped nanoparticles can be accurately calculated by methods such as discrete dipole approximation (DDA), boundary element method (BEM), finite difference time domain (FDTD) method, and finite element method (FEM), to name a few. DDA considers the nanoparticle as an array of dipoles, however, it is not very efficient for irregularly shaped particles [200]. Although BEM can accurately solve problems involving extreme aspect ratios and open regions because it only requires meshing on the surface, complex shapes and non linear problems are major limitations. FEM and FDTD are robust methods, both widely used in commercial software. Generally, for high frequency problems and harmonic fields, FEM is preferred [201, 202]. Therefore, FEM was selected for the analysis of the majority of the nanosized particles, films and structures throughout this thesis. The simulation analysis was performed on commercial software COMSOL, which works on the FEM that uses partial differential equations (PDEs) to solve Maxwell's equations. In the field of space and time dependent problems within the domain of physics, the governing laws are often described through PDEs. Unfortunately, the analytical solutions for these PDEs are elusive for the majority of geometries and scenarios. As a pragmatic alternative, approximations of these equations are formulated, typically employing various discretization techniques. These methods involve representing the continuous PDEs as numerical model equations, which can then be tackled using numerical methods. FEM out as a prominent approach for generating such approximations. By utilizing FEM, one can discretize the problem domain into finite elements, allowing for the creation of a system of algebraic equations. Solving these equations provides a numerical solution to the model, serving as an approximation to the actual solution of the original PDEs. This indispensable methodology plays a crucial role in tackling complex physical problems that resist analytical resolution, offering a practical means to obtain valuable insights into the behaviour of dynamic systems. Overall, the FEM stands out for its flexibility in discretization, allowing users to freely choose elements for spatial discretization and basis functions. FEM is widely used in the literature for obtaining accurate solutions for plasmonic structures [202].

3.1.1 Loretz Drude model

In the simulations, the input of dielectric functions of materials is essential for an accurate analysis. The dielectric function of air and glass were assumed to be constant in the targeted wavelength range and were input as 1 and 2.25, respectively. The Lorentz Drude model was used to model the dielectric function of gold [203]:

$$\varepsilon(\omega) = 1 - \frac{\Omega_{\rm p}^2}{\omega(\omega - i\Gamma_0)} + \sum_{\rm j=1}^{\rm k} \frac{f_{\rm j}\omega_{\rm p}^2}{\left(\omega_{\rm j}^2 - \omega^2\right) + i\omega\Gamma_{\rm j}}$$
 3.1

where, the plasma frequency is represented by ω_p , k is the number of oscillators with frequency, strength and lifetime represented by ω_j , f_j , and $1/\Gamma_j$, respectively. Further, $\Omega_p = \omega_p \sqrt{f_0}$ is the plasma frequency associated with intraband transitions, oscillator strength f_0 and damping constant Γ_0 . The Lorentz Drude model incorporates both the real and imaginary part of the dielectric function. Furthermore, the intraband as well as interband effects are considered in the model. The parameters reported by Rakic' et al. [203] are mentioned in Table 3.1. To quantify the effect of annealing on the material parameters and roughness, the oscillator strength (f_0) and damping constant (Γ_0) were adjusted to match the respective experimental transmission spectra, as explained later in section 5.2.3. The MATLAB code to vary the parameters in the Loretz Drude model is in Appendix A.1.

Table 3.1 Loretz Drude model parameters for gold in Rakic' et al. [203]. Units of Γ and ω are eV.

\mathbf{f}_0	Γ_0	$\mathbf{f_1}$	Γ_1^a	ω_1^a	\mathbf{f}_2	Γ_2	ω_2	f ₃	Γ_3	ω3
0.760	0.053	0.024	0.241	0.415	0.010	0.345	0.830	0.071	0.870	2.969

f ₄	Γ_4	ω4	f ₅	Γ_5	ω ₅
0.601	2.494	4.304	4.384	2.214	13.32

3.1.2 Single nanoparticle simulation methodology and validation

The scattering and absorption cross-section of nanoparticles was calculated using FEM simulations. The sum of which is called the extinction cross-section, was used to analyse their plasmonic response. Extinction cross-section represents the equivalent cross-sectional area of the object that scatters and absorbs the incoming light. In the simulation, the nanoparticle is placed in a surrounding material of dielectric function ϵ_s , and an electric field $\mathbf{E}_{inc}(\mathbf{r})$, of amplitude E_0 is incident upon it. The calculation of the scattering cross-section is achieved by integrating the flux of the Poynting vector of the field scattered (S_{sca}) over the nanoparticle surface, which is expressed as [204]:

$$\sigma_{\text{sca}} = \frac{1}{S_0} \iint_{\text{nanoparticle}} \mathbf{S}_{\text{sca}}(\mathbf{r}) \cdot \mathbf{n} \, dS$$
 3.2

where, **n** is the unit vector perpendicular to the surface S, the power density of the incident field, $S_0 = \frac{\sqrt{\epsilon_s}E_0^2}{2Z_0}$ and Z_0 is the characteristic impedance of vacuum. The absorption cross-section is evaluated by integrating the power dissipated over the volume of the nanoparticle:

$$\sigma_{abs} = \frac{1}{S_0} \iiint\limits_{nanoparticle} Q_h dV \eqno 3.3$$

$$\mathbf{E}_{\rm inc}(\mathbf{r}) = \mathbf{E}_0 \,\,\mathrm{e}^{\mathrm{i}(\mathbf{k}\cdot\mathbf{r} - \omega t)} \tag{3.4}$$

$$\mathbf{H}_{\text{inc}}(\mathbf{r}) = \mathbf{H}_0 \, e^{i(\mathbf{k} \cdot \mathbf{r} - \omega t)}$$
 3.5

where the power dissipation density, $Q_h = \frac{1}{2}\omega\epsilon_0 \text{Im}(\epsilon_m)|\mathbf{E}(\mathbf{r})|^2$, V is the volume, ω is the frequency, and ϵ_m is the dielectric function of the nanoparticle. The region in which the nanoparticle was placed was spherical in shape and was surrounded by perfectly matched layers (PMLs) which absorb all the outgoing waves [205]. The simulation was validated by comparing simulation [205] and experimental [206] of spherical nanoparticle results in the literature. The detailed validation was presented in Chapter 4.

The simulation domain is shown in Figure 3.1 (a), the metallic nanoparticle is placed in a surrounding dielectric medium. The surrounding domain was big enough to minimize the effect of reflections within the domain. The PML also contributes to decreasing the noise in the simulation due to reflections. Applying the symmetry leads to a decrease in computational cost. Additional details of the simulation parameters are in Appendix B.

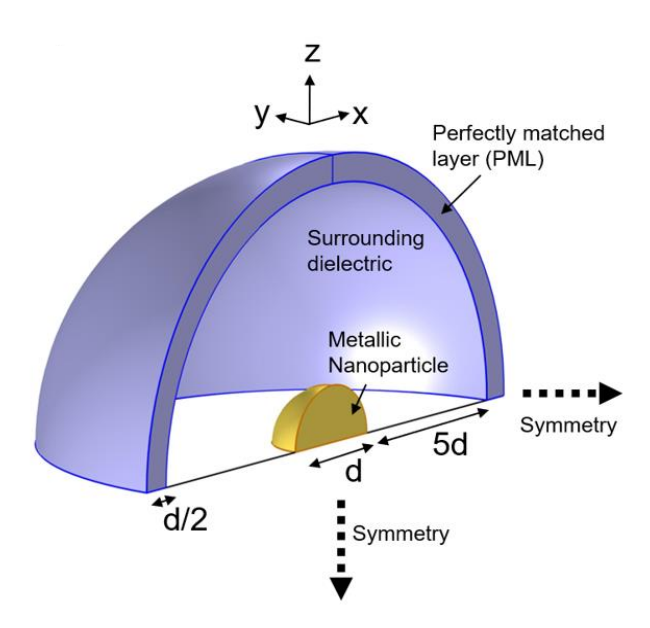


Figure 3.1 Schematic representation of the simulation domain of a single nanoparticle.

3.1.3 Nanoarray simulation methodology and validation

The simulation study was performed on commercial software COMSOL Multiphysics, which uses FEM to solve Maxwell's equations. The following wave equation is considered in the simulation domain:

$$\nabla \times \left(\frac{1}{\mu_{\rm r}} \nabla \times \mathbf{E}\right) - \mathbf{k}_0^2 \varepsilon_{\rm r} \mathbf{E} = 0$$
 3.6

where, ε_r and μ_r are the relative permittivity and permeability, respectively. \mathbf{k}_0 represents the incident wave vector and \mathbf{E} is the electric filed vector [207]. The above equation allows the calculation of the far field optical response. To quantify the near field electric field, the EM wave perpendicular to the nanoarray with the wave vector \mathbf{k}_0 is oriented parallel to the z axis. The electric field \mathbf{E} corresponds to linearly polarized light. The computation is performed in the wavelength domain, allowing the removal of the oscillation factor $\mathbf{e}^{i\omega t}$ from \mathbf{E} as:

$$\mathbf{E} = |\mathbf{E}_0| e^{i(\mathbf{k} \cdot \mathbf{r} - \omega t)} \hat{\mathbf{E}}$$
 3.7

where, the amplitude of the electric field is denoted by the absolute value of E_0 . $\hat{\mathbf{E}}$ is the unit vector pointing at the direction of polarization.

The 3D simulation domain consisted of a nanoarray placed at the interface of materials with refractive index n_1 and n_2 as show in Figure 3.2 (a). To induce the array effect, the floquet periodic condition was applied at the opposing faces [208]. The EM wave traveled from the top to the bottom of the simulation domain via two ports. The upper and lower boundaries of the simulated array domain were also equipped with perfect matching layer (PML) boundary conditions to absorb the unwanted scattered fields [209]. Glass was considered the substrate, thereby, the refractive index n_2 was 1.5. Additional details of the simulation parameters are in Appendix B.

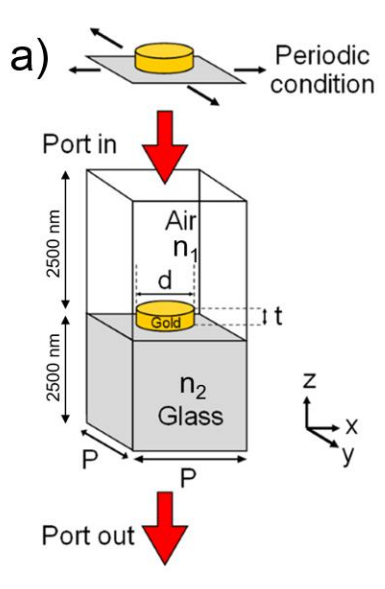


Figure 3.2 Simulation domain of the plasmonic nanoarray with periodicity (P), thickness (t), and diameter (d).

3.2 Modelling the effect of roughness

The FEM simulations were used to predict the plasmonic response of nanostructures and thin films. However, the roughness effect of the practical surfaces is not taken into account for the FEM simulations. In this section, we devise a method to incorporate the effect of roughness in thin films by modifying the dielectric function of gold.

3.2.1 Impact of roughness on plasmonic response

To understand the effect of roughness, we consider a metal and a surrounding dielectric (in this case, air) interface with dielectric function represented as ε_m ($\varepsilon_m = \varepsilon_m' + i \varepsilon_m''$) and ε_d , respectively. The metal and dielectric are approximated as semi-infinite and the equations are solved for low losses. Further, k_{zm} and k_{zd} are wavevectors in the z direction (direction of propagation of plasmons) for the metal and the surrounding dielectric. Solving Maxwell's equations, the dispersion relation D_0 can be written as:

$$D_0 = \frac{k_{zm}}{\varepsilon_m} + \frac{k_{zd}}{\varepsilon_d} = 0$$
3.8

It is considered that roughness causes scattering losses and ultimately deteriorates the SPR sensing performance. Raether [118] considered the effect of roughness similar to the effect of a grating and assumed a statistically rough interface with root mean square (RMS) height δ and thickness d. The new dispersion relation (D_r) was derived as:

$$D_{r} = \epsilon_{m} D_{0} - \delta^{2} k^{2} (\epsilon_{m} - 1)^{2} k^{2} \int d^{2} k'_{spp} g(k|k_{spp} - k'_{spp}|) H(k'_{spp})$$
 3.9

which is calculated when ϵ_d =1, where $g = 2\pi/a$ considers the grating effect of the rough surface, and a is the grating constant. $H(k'_{spp})$ is a complex function of the wavevectors parallel and perpendicular to the interface. The increased scattering due to roughness causes a decrease in the phase velocity of SPP [210]. Furthermore, an increase in roughness leads to a decrease of the effective ϵ'_m that ultimately leads to a lower enhancement factor of the SPR [11]. Further, Mills [211] had done rigorous analysis on the effect of rough surfaces on surface plasmon polaritons and calculated that for the condition that $|\epsilon| >> 1$. The attenuation length (1) due to roughness was calculated as:

$$l = \frac{3}{4} \frac{|\epsilon|^{1/2}}{(k)^5 (\delta A)^2}$$
 3.10

where A is the transverse correlation length of the rough surface, which approximately represents the mean distance between two peaks or valleys of the roughness. Thereby, an increase in surface roughness (both δ and A) cause a decrease in length over which the polariton can travel [212].

3.2.2 Bruggeman effective medium theory to calculate SPR response

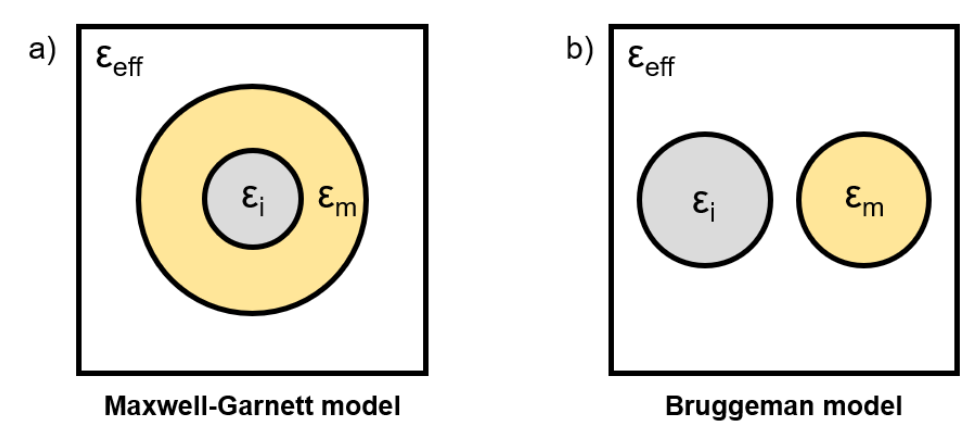


Figure 3.3 Schematic illustration of a) Maxwell Garnett and b) Bruggeman effective medium theory.

Maxwell Garnett and Bruggeman effective medium theory are two different approaches to model the effective dielectric properties of a composite material [213]. Maxwell Garnett effective medium theory calculates the effective dielectric function of a composite material with inclusions of another material. It is assumed that the inclusions are spherical, and their concentration is very low compared to the host medium. The model treats the inclusions as isolated entities surrounded by the host medium.

Bruggeman effective medium theory does not distinguish between the host and inclusion materials. Instead, it treats the composite as a homogeneous material with inclusions of both components embedded in an effective medium. The Bruggeman theory assumes that the inclusions are randomly distributed and can have any shape. To model the effect of roughness, non spherical shapes of the inclusion (air) embedded in gold medium have to be considered, and the Bruggeman effective medium theory was used to approximate the rough part of the gold film. Further, transfer matrix method (TMM) was used to calculate the reflectivity of the system. Bruggeman effective medium theory considers the dielectric function impurities (ϵ_{i}) in a matrix (ϵ_{m}) to approximate the effective dielectric function (ϵ_{eff}) of the overall system [214].

$$\frac{(\varepsilon_{i} - \varepsilon_{eff})f_{i}}{\varepsilon_{eff+}(\varepsilon_{i} - \varepsilon_{eff})A} + \frac{(\varepsilon_{m} - \varepsilon_{eff})(1 - f_{i})}{\varepsilon_{eff+}(\varepsilon_{m} - \varepsilon_{eff})A}$$
3.11

where f_i is the volume fraction of the impurity and A is the depolarization factor. The value of f_i of 0 and 1 can be varied from 0 to 1. Further, the shape of impurity determines the value of A. In equation 3.11, when A is 1/3, the impurities are considered spherical, and when A is 1, the impurities are considered as wire shaped. To approximate the rough surface air was treated as an impurity in a gold matrix to calculate the effective dielectric function of the rough surface. To select the parameters which simulated the rough surface, f_i was varied from 0.1 to 0.5 and A was varied from 0.4 to 0.9. The code for calculating the dielectric function is in the Appendix A.2. The total thickness of the film was kept constant, and the thickness of the rough part of the film was varied to incorporate the effect of roughness

increase. The thickness of the rough part was obtained from the root mean square (RMS) roughness calculated from the atomic force microscopy (AFM) data. TMM was used to calculate the reflectivity for the selected range of angle of incidence and wavelength. The details for the TMM calculations are in the Appendix A.3. FEM was also investigated for the calculations; however, TMM results were closer to the experimental data. The TMM calculates angle dependent transmission and reflection through multiple layers of materials for the selected polarization by solving Maxwell's equations [215]. TMM reduces the complexity in calculation by considering a transfer matrix for each layer; the transfer matrix of all the layers is multiplied to get the overall response of the multilayer system. The transfer matrix incorporates the thickness and the refractive index of the layer. The calculations of TMM were performed in MATLAB considering 4 layers. TM polarized light was input through a lossless glass layer into a rough gold layer and a solid gold later; the final layer (output layer) was air, as shown in Figure 3.4. The dielectric constant of air and glass layer was input as 1 and 2.25, respectively. The dielectric function of solid gold was calculated according to the Drude model, which was also used in the Bruggeman effective medium theory for approximating the rough surface.

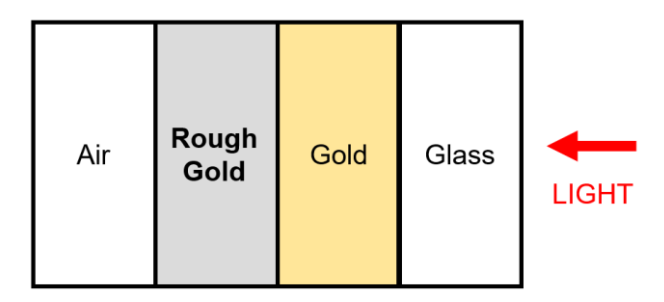


Figure 3.4 Schematic of the layers used for transfer matrix method (TMM) calculations.

3.3 Density functional theory (DFT) for Raman

Density Functional Theory (DFT) is a computational tool based on quantum mechanical methods for analyzing the electronic structure of atoms, molecules, crystals, and condensed phases. DFT is widely used to study electrical, optical, and mechanical properties of materials, molecular structure, reaction mechanics, and various other aspects of materials on the atomic and/or molecular level. DFT uses exchange correlation functional to account for the electron exchange and also electron-electron correlation. One of the most popular and robust functional is the B3LYP, which is a hybrid of Hartee-Fock exchange and a functional developed by Lee, Yang, and Parr [216]. Its hybrid nature allows accurate calculation of both short range and long range correlation effects. Thereby, B3LYP method can be used to accurately study a wide range of molecules at a moderate computational cost. The B3LYP level of theory has previously been reported to calculate the vibrational response of agrochemicals and their interaction with substrates, which is highly important for SERS sensing [217]. Castillo et al. [218] used the B3LYP method to calculate the Raman and IR spectra of a pesticide dieldrin in different media; both the Raman and IR spectra were in good agreement with the experimental spectra. James et al. [219]

compared the DFT calculated and experimental Raman and IR spectra of a herbicide, the Raman spectrum was very close for both wavenumber and intensity of the vibrational modes. However, inaccuracies were present in the IR spectrum. Hu et al. [220] detected the pesticide difenoconazole using Raman spectroscopy, and gold nanoparticles were used as SERS substrates. DFT was used to calculate the Raman spectrum; however, there were discrepancies with the experimental spectra due to the calculations being performed in the gas phase. Various basis sets are available in the Gaussian software for B3LYP level of theory.

3.3.1 Basis sets for B3LYP level of theory

Briefly discussing the various basis sets available, the smallest basis sets are the STO-3G and 3-21G [221, 222]. The "*" and "+" additions incorporates diffuse and polarization functions on the basis sets for improved accuracy with increased computational time. The 6-31G and 6-311G are medium sized basis sets and are most commonly used in the literature [223, 224]. The "(d)" additions to the basis set represent the addition of d-type polarization on non hydrogen atoms, and "(p)" addition represents p-type polarization functions on hydrogen atoms. "+" adds polarization function to non hydrogen atoms and "++" adds both polarization and diffuse functions. The cc-pVDZ refers to correlation-consistent polarized valence double zeta, and similarly, cc-pVTZ contains triple zeta functions [225]. Both these correlation consistent basis sets are very large and highly accurate. The "aug" stands for augmented, which adds diffuse functions to these basis sets. The "Lan" and "SDD" type basis sets are smaller datasets that are used for studying heavy atoms [226, 227]. They are included in the current study to because some of the agrochemicals also contain heavy elements on which these datasets will be useful. They are also used to study the SERS effect of chemicals with plasmonic materials. DGDZVP is a relatively new double zeta type split valence basis set with polarization functions [228]. The DGDZVP2 contains additional polarization functions for increased accuracy [229].

3.3.2 Equations to calculate vibrational modes

DFT is a tool to find solutions to the Schrödinger equation to study the properties of materials on the atomic level. The fundamental theorems by Kohn and Hohenberg and equations by Kohn and Sham form the basis of all DFT calculations. Kohn and Hohenberg stated that the ground state electron density exclusively governs the energy, wavefunction, and all other properties of the system in the ground state. Further, the energy from the functional of the aforementioned ground state electron density has to be minimized. Kohn and Sham provided a method to find the correct electron density, in which each set of self-consistent field equations involving a single electron. Thereby reducing the complexity of the solution to the Schrödinger's equation. Born Oppenheimer approximation is applied to further reduce the computational cost required for the calculations. The approximation allows for the separation of the degrees of freedoms related to the electrons and nuclei. The nuclei are considered quasi immobile and generate a quasi static field in which electrons obit "independently". The fundamental theorems and

equations mentioned above consider the material at 0 K. However, in real life conditions, vibrations also contribute to the material's energy. The frequency and intensity of these vibrations are the basis of vibrational spectroscopy techniques of Raman and FTIR [230].

To find the vibrational frequencies of a system of N atoms, we express their cartesian coordinates as a single vector with 3N components, $\mathbf{r} = (\mathbf{r}_1, \mathbf{r}_2, \dots, \mathbf{r}_{3N})$. Initially, the atoms are positioned at \mathbf{r}_0 , which is the local minimum of the atoms' energy. The position is given by the coordinates, $\mathbf{x} = \mathbf{r} - \mathbf{r}_0$. The Taylor expansion of the atom's energy (E) to the second order about \mathbf{r}_0 is [231]:

$$E = E_0 + \frac{1}{2} \sum_{i=1}^{3N} \sum_{j=1}^{3N} \left[\frac{\delta^2 E}{\delta x_i \delta x_j} \right]_{x=0} x_i x_j$$
 3.12

Where E_0 is the initial energy of the system and x_i and x_j are individual components of the displacement coordinate vector. The first derivative of equation 1 is exactly 0 because it is evaluated at minimum energy. The component $\left[\delta^2 E/\delta x_i \delta x_j\right]_{\mathbf{x}=0}$ in equation 1 is defined as the Hessian matrix (H_{ij}), which is a 3N x 3N matrix. The Hessian is used to define the equations of motion of the atoms in a way that is similar to classical dynamics. The Hessian is approximated using the finite difference method as:

$$H_{ij} = \left[\frac{\delta^2 E}{\delta x_i \delta x_j}\right]_{\mathbf{x}=0} \cong \frac{E(\delta x_i, \delta x_j) - 2E_0 + E(-\delta x_i, -\delta x_j)}{\delta x_i \delta x_j}$$
3.13

where $E(\delta x_i, \delta x_j)$ is the energy of the atoms when the coordinates are not 0, i.e., the atoms are slightly displaced from the equilibrium positions. The eigenvectors and eigenvalues of the mass-weighted Hessian matrix form the solution of the equations of motion. The 3N normal mode frequencies are provided by the 3N eigenvalues. Therefore, the motions of the atoms lead to specific vibrational frequencies.

Vibrational modes are divided into two, Raman active and Infrared (IR) active. The Raman activity involves the change in polarizability of the molecule and IR activity depends on the dipole moment of the molecule. The intensity and frequency of these vibrational modes help us get the system's complete vibrational response. The Raman intensity is calculated using the Placzek's classical theory of polarizability [232], and IR intensity is calculated using the first order time-dependent perturbation theory [233]. Taylor series expansion is used to approximate the polarizability $(\overline{\alpha})$ and dipole moment $(\overline{\mu})$ equations of the molecule in the mass weighted normal coordinates $\mathbf{R}^{(q)}$ over k nuclei [233]:

$$\overline{\alpha} = \overline{\alpha}^{(0)} + \sum_{k} \left[\frac{\delta \overline{\alpha}}{\delta R_{k}^{(q)}} \right]_{0}^{R_{k}^{(q)}} \qquad 3.14 \quad \overline{\mu} = \overline{\mu}^{(0)} + \sum_{k} \left[\frac{\delta \overline{\mu}}{\delta R_{k}^{(q)}} \right]_{0}^{R_{k}^{(q)}} + O(R_{k}^{(q)2}) \qquad 3.15$$

where $\overline{\alpha}^{(0)}$ and $\overline{\mu}^{(0)}$ is the polarizability and dipole moment at the equilibrium condition and $O(R_k^{(q)2})$ term representing the higher order terms from the quadratic and higher nuclear displacements. Now, to find the polarizability $\langle \alpha_{fi} \rangle$ and dipole moment $\langle \mu_{fi} \rangle$ matrix for a transition state from i to j, the following equations are used:

$$\langle \alpha_{fi} \rangle = \overline{\alpha}^{(0)} \langle \nu_f | \nu_i \rangle + \sum_k \left[\frac{\delta \overline{\alpha}}{\delta R_k^{(q)}} \right]_0 \langle \nu_f | R_k^{(q)} | \nu_i \rangle \qquad 3.16 \qquad \langle \mu_{fi} \rangle = \mu^{(0)} \langle \nu_f | \nu_i \rangle + \sum_k \left[\frac{\delta \overline{\mu}}{\delta R_k^{(q)}} \right]_0 \langle \nu_f | R_k^{(q)} | \nu_i \rangle \qquad 3.17$$

where the first term in the equations represents the initial polarizability (or dipole moment) matrix between the initial (v_i) and final vibration state (v_f) , and $\langle v_f | R_k^{(q)} | v_i \rangle$ signifies the vibrational matrix of the transition state involving the kth mass weighted normal coordinate. Simplifying the equations and using Hermite polynomials on the matrix elements, the amplitude of the polarizability and dipole moment is calculated for the vibrational state transition $|v_{k,i} + 1\rangle \leftarrow |v_{k,i}\rangle$

$$\langle \alpha_{fi} \rangle = b_{vk} \big(\nu_{k,i} + 1 \big)^{1/2} \left[\frac{\delta \, \overline{\alpha}}{\delta R_k^{(q)}} \right]_0 \qquad 3.18 \qquad \langle \mu_{fi} \rangle = b_{vk} \big(\nu_{k,i} + 1 \big)^{1/2} \left[\frac{\delta \, \overline{\mu}}{\delta R_k^{(q)}} \right]_0 \qquad 3.19$$

where $b_{vk}^2 = \hbar/4\pi v_k$

The aforementioned equations are used in the backend of the software Gaussian 09. The calculations were performed at the B3LYP level with various basis sets. The optimization of the geometry was performed, followed by calculation of the vibrational mode wavenumbers and intensity. To accommodate for the excitation wavelength of the Raman laser, the Raman intensity (I_i) was calculated as [234]:

$$I_{i} = C(\nu_{0} - \nu_{i})^{4}\nu_{i}^{-1}B_{i}^{-1}S_{i}$$
 3.20

$$B_{i} = 1 - \exp\left(-\frac{hcv_{i}}{kT}\right)$$
 3.21

where C is a constant, v_0 is the excitation frequency of the Raman laser, v_i is the frequency of the vibrational mode, S_i is the Raman scattering activity of the vibrational mode calculated in the Gaussian software, B_i represents Boltzmann distribution at a defined temperature (T). h, k, and c are Plank's constant, Boltzmann's constant, and speed of light, respectively. Since the article compares the various basis sets available for calculation, no scaling factor was used. The Raman and IR spectra were plotted using the Lorentzian band shape with full width at half maximum (FWHM) of 10 cm⁻¹. The visualization software GaussView was used to envision and assign the various vibrational modes to their corresponding wavenumbers. For the calculations, the structures were acquired from pubchem.ncbi.nlm.nih.gov in the ".mol" format.

3.4 Laser interference lithography (LIL)

The Lloyd's mirror interferometer setup was used to fabricate the nanodisks which is based on the division of wavefront method [235, 236]. The setup uses a mirror for two beam interference of coherent laser beams. The incident laser beam passes through a spatial filter to produce a spatially coherent beam that is incident on the substrate as well as on the mirror, which is placed at an angle of 90° to the substrate. Due to the standing wave created by the interference of the direct and reflected beams, a fringe pattern is formed on the surface of the substrate [237]. The difference in intensity of the fringes is recorded on the substrate which is covered with a photosensitive material. Hence, selective area can be chemically etched away to obtain a 1 D grating when a single exposure of the laser is applied. The period P of the interference fringes is dependent on the angle between the direct and the reflected beam θ and wavelength of the laser λ . The period d can be calculated by [238]:

$$P = \frac{\lambda}{2\sin\theta}$$
 4.1

As shown in Figure 2.5, the rotation stage rotates the Lloyd's mirror to vary the angle θ to produce fringes of various periods. A high coherence and similar intensity level of the direct and reflected is required to ensure a high intensity pattern. Thereby improving the sharpness of the features recorded in the photosensitive film. A high coherence can be achieved by selecting a laser source with a very narrow wavelength width. Although the setup is very compact and stable compared to other LIL methods, the degree of freedom of the setup is low [239]. The total area of the substrate exposed to the interfering beams varies with the angle θ ; hence, as the angle decreases, the exposed area decreases. Thus, creating a limitation on the period of the gratings that can be made.

Multiple exposure exposures can create more complex patterns on the substrate. Moreover, the size and period of the structures can be tuned slightly by varying the exposure and the development time. In the current article, a double exposure of a photoresist coated on a glass substrate was performed. Wherein, after the first exposure, the substrate was rotated by 90° for the second exposure. Due to the difference in refractive indices of the photosensitive material and the substrate, a second standing wave is formed on the walls of the photoresist [240]. Therefore, the exposure and development time have to be optimized to avoid defects in the pattern formed on the substrate. In the next step, a thin chromium layer (to ensure good adhesion of the gold layer [241]) and a gold layer of the required thickness were deposited on the substrate. The excess gold and photosensitive film were etched away to obtain an array of nanodisks on the glass substrate. Optimizing the exposure time was also necessary to ensure that the final etching step was successful.

3.5 Thermal deposition

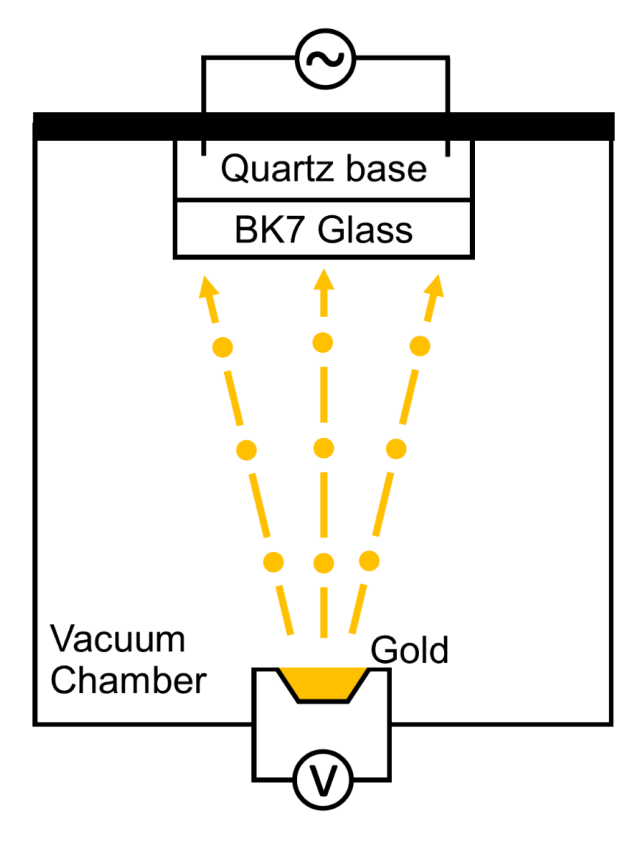


Figure 3.5 Schematic of the thermal evaporation process.

Thermal deposition was used to deposit a thin gold layer on the glass substrates. A thin layer of chromium, 5 nm to 10 nm, was used as an adhesive between the gold and glass. The samples were mounted on a holder with a quartz base and were placed inside the chamber of the thermal evaporator as shown in Figure 3.5. However, the quartz base was not used for the instrument used to deposit gold for the LIL samples. Pure solid gold and chromium were placed in ceramic boats. Vacuum greater than 10^{-5} torr was created in the chamber, following which chromium was heated, which led to its evaporation. Initially, a cover was applied to stabilize the evaporation rate. After the stabilization of the metal deposition at the selected deposition rate, the cover was slid to the side to expose the samples. A different second quartz thickness monitor (only one quartz base was used for the LIL samples) was used to ensure the targeted thickness was achieved. After the thin chromium layer, gold of the desired thickness was deposited on the samples.

3.6 Transmission spectroscopy

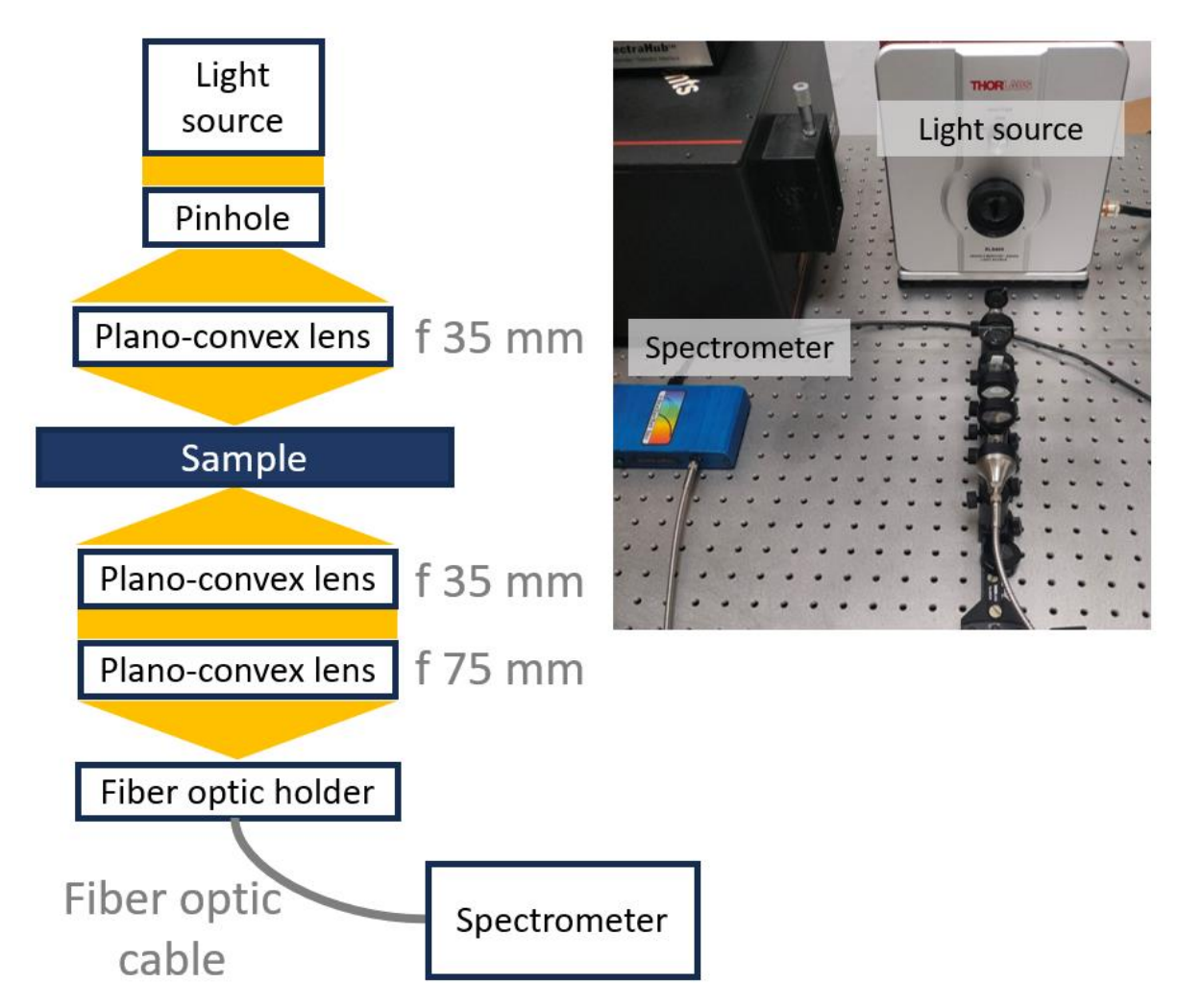


Figure 3.6 Ray diagram presenting the components of the transmission spectroscopy setup. Inset has the image of the tabletop setup at IIT Ropar.

The transmission response of the LIL samples was analysed using the method mentioned in Figure 3.6. A broadband light source using a xenon lamp was controlled using a pinhole and focussed on the sample using two collimating lenses. Another lens was used to guide the light to the fibre optic cable and eventually to the StellarNet spectrometer. Thereby, plots of the transmission intensity and wavelength (400 nm to 1000 nm) of the LIL samples were acquired to study their plasmonic response.

3.7 Surface Plasmon Resonance (SPR)

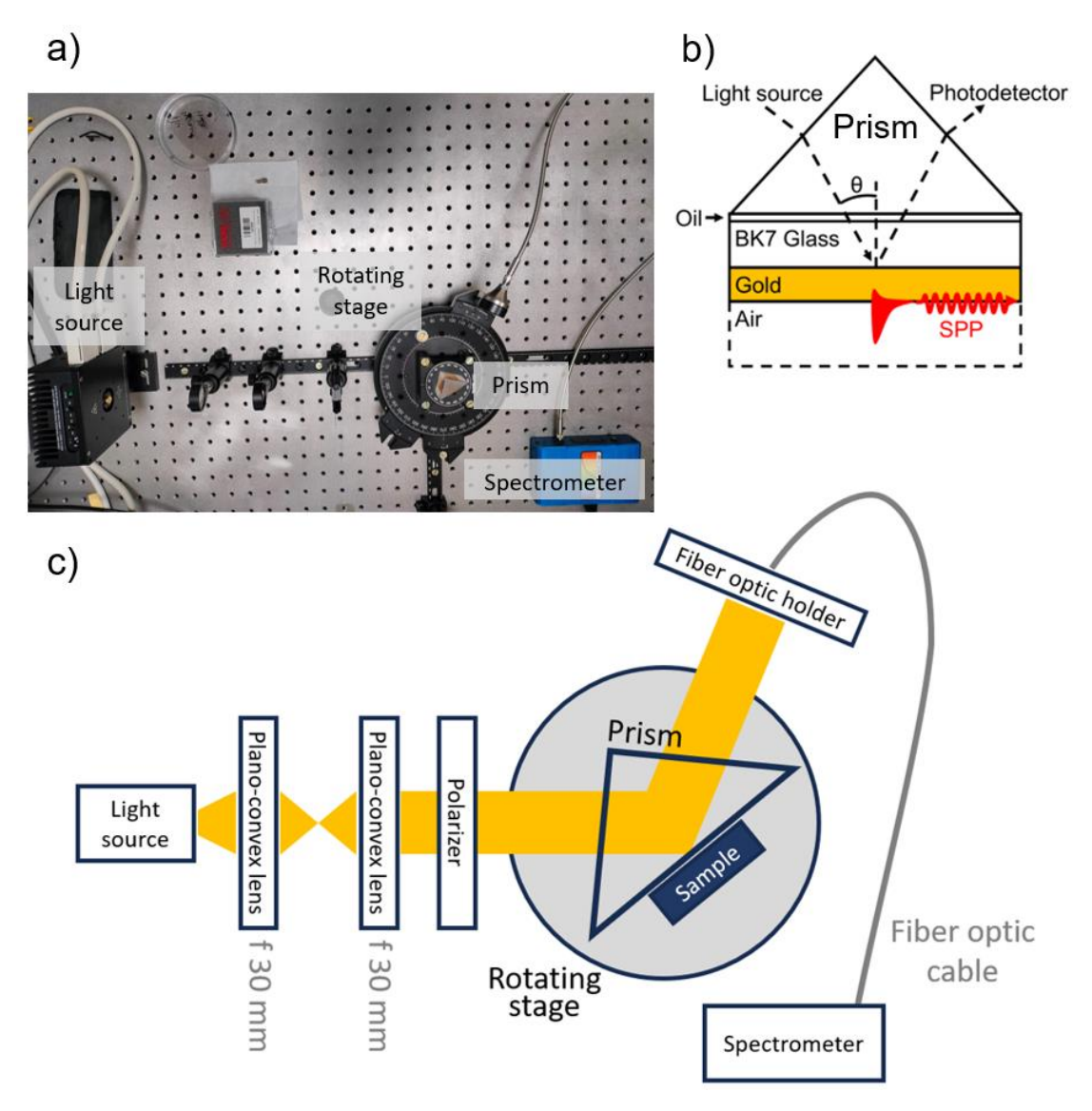


Figure 3.7 a) Image of the tabletop SPR setup at IIT Ropar. b) Schematic of the Kretschmann configuration for excitation of the SPR condition. c) Ray diagram explaining all the components of the SPR setup.

To analyse the SPR response of thin gold films, the method shown in Figure 3.7 was used. The light source was collimated using two plano-convex lenses of focal length 30 mm to achieve a sharp and coherent beam. A polarizer was used to select the desired mode (TM or TE) which was to be incident on the sample. The sample, which was deposited on a glass slide, was adhered to a prism using a refractive index matching oil. The prism was placed on a rotating stage for angle based reflectivity measurements. The incident light after total internal reflection was collected using a lens that was contained in the fibre optic holder. Fibre optic cable guided the light to the spectrometer, which provided the plot of the reflectivity and wavelength of the thin films.

3.8 Other characterization techniques

- **AFM**: The height of the nanodisks was confirmed by atomic force microscopy (AFM) using the Bruker Multimode AFM.
- FTIR: Bruker Tensor II was used for the FTIR measurements of the agrochemical.
- Raman: The Raman measurements were performed using the Horiba LabRAM HR via a 633 nm laser (Melles Griot) and 100x objective lens with 0.8 numerical aperture.
- **FE-SEM**: Field Emission Scanning electron microscopy (FE-SEM) images by Zeiss Gemini 500 SEM were used to measure the diameter of the nanodisk and the period of the array fabricated using LIL.
- SC-XRD: Single crystal x-ray diffraction (SC-XRD) was performed on the Bruker D8 venture with x-ray wavelength of 0.71073 Å to compare the experimental structures of molecules.
- **XRD**: The grain size of the gold nanodisks was calculated using x-ray diffraction (XRD) measurements (Malvern PANalytical) at an omega angle of 1°.

Chapter 4. Simulating the Geometric Dependence of Plasmonic Responses

This chapter aims to use FEM simulations to study the effect of size, shape, material, and surrounding environment on plasmonic response of nanoparticles and nanoarrays. Simulation is an excellent tool available to scientists and engineers to predict the response of their samples for specific applications. Thereby reducing the cost of experimental fabrication by optimizing the parameters using simulation results.

4.1 Single nanoparticles

The selection of material, size, shape, and the surrounding environment is essential for tailoring the response of the single nanoparticle. Although there are several works in the literature studying the properties of gold and silver nanoparticles of various shapes [242–244], the collective quantitative comparison of all the metals displaying the best plasmonic response, gold, silver, copper, and aluminium, of various shapes, sizes and embedding over a broadband range will be beneficial to the scientific community. The optical response of all the materials, shapes and surrounding medium from the UV to the NIR wavelength range is shown in Figure 4.3 (a-l). Initially, the response of silver will be used to establish the effect of size, shape, and embedding. In the last part of this section, the dipole and higher order peaks appearing in the extinction spectrum for all the materials will be analysed quantitively.

4.1.1 Simulation parameters and validation

The shapes of the nanoparticles and the direction of the incident light and its polarization are shown in Figure 4.4. The volumes of the nanoparticles being studied were equal to spheres of diameter 50 nm, 100 nm, 150 nm, and 200 nm, and the sides of the nanobars and nanoprisms were calculated as per section 3.1.2. The sides of the cross-sections and the edges of the nanobars and nanoprism were smoothened by filleting to construct shapes comparable to experimentally fabricated nanoparticles [245, 246]. The general rounding radius was selected to be 4 nm, and the fillet radius of the sides of the square and the equilateral triangle was chosen as side/20. Therefore, both the shapes would have the same rounding of the edges, and only the inherent effect of the shape of the nanobar and nanoprism can be observed. The thickness of the nanobar and nanoprism was selected to be 30 nm, to effectively observe the plasmonic effect in all the sizes.

The light was incident normal to the square and triangular face of the nanobar and the nanoprism. The electric field was parallel to the side of the square face of the nanobar and perpendicular to the side of the equilateral triangle of the nanoprism. Comparing the extinction cross-section of the nanoprism, when the electric field was perpendicular and parallel to the side of the equilateral triangle (configuration 1 and 2 in Figure 4.4); the peak wavelengths were similar with slightly decreased intensity (due to the decrease in the size in the direction of the electric field) for the case of electric field

parallel to the side. Hence, only the configuration with electric field perpendicular to the side was used to compare the response of the various nanoparticles. The optical properties of gold, silver, copper [247], aluminium [248], and a-Si [249] were obtained from the literature. The relative permittivity of the aforementioned materials is in complex form. The permittivity of air and glass contains only the real part and was set as 1 and 2.25, respectively.

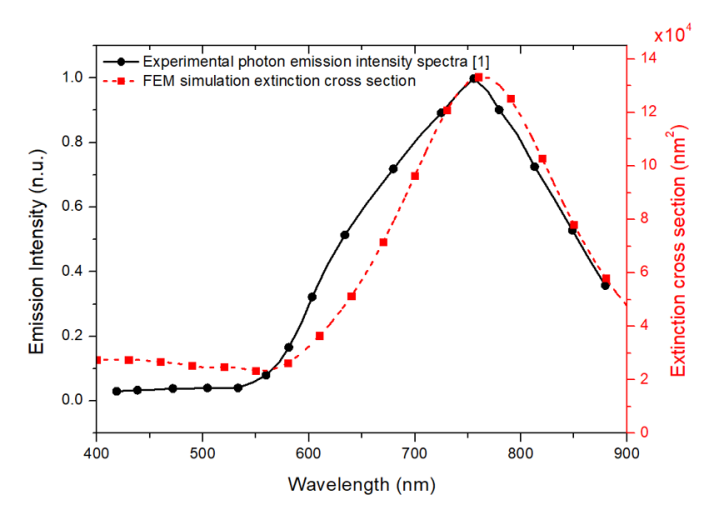


Figure 4.1 Measured scanning transmission electron microscopy—cathodoluminescence (STEM-CL) unpolarized photon-emission intensity spectra collected for dipole position (solid black line with circular markers) [250] for gold nanoprism of side 266 nm and height 50 nm and FEM simulation extinction cross section of the nanoprism of the same dimensions (red dashed line with square markers).

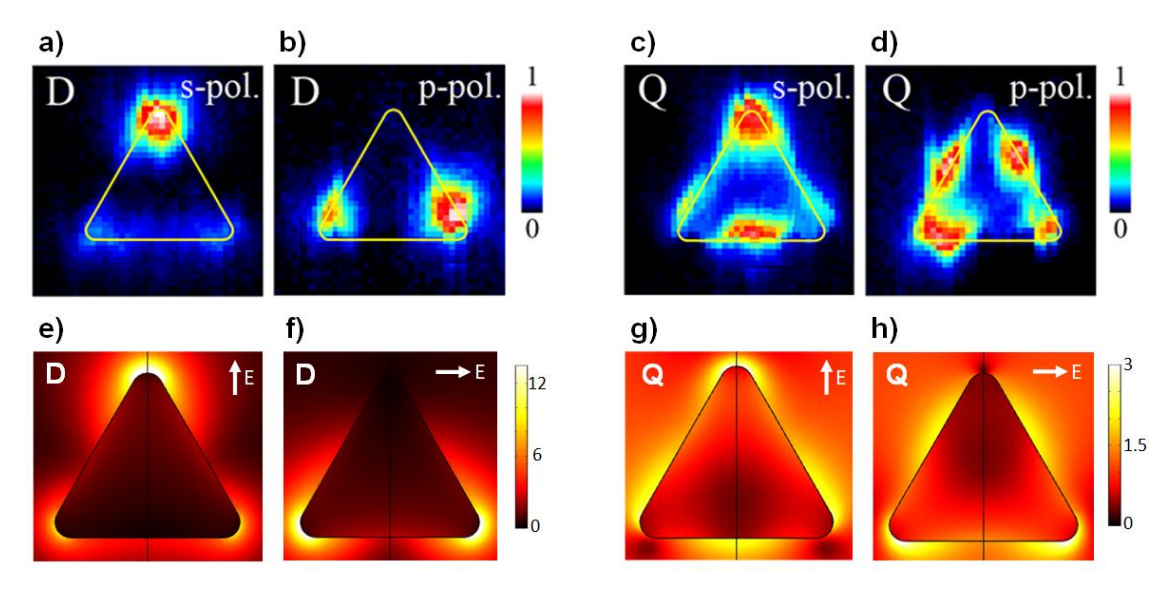


Figure 4.2 (a-d) Measured monochromatic photon maps for nanoprism of side 266 nm and height 50 nm for the dipole (D) (a and b) and quadrupole (Q) (c and d) modes at the peak energies for s (a and c) and p polarized (b and d) emission. Each pixel is associated with a different position of the electron beam [250]. (Figures adapted with permission from *ACS Nano* 2018, 12, 8436–8446. Copyright 2018 American Chemical Society). (e-f) The normalized electric field (V/m) using FEM simulation for the same nanoprism for the D (e and f) and Q (g and h) modes when the electric field is perpendicular (e and g) and parallel (f and h) to the side of the nanoprism.

To further establish the accuracy of the simulation results, the far field and near field simulation results of nanoprisms were compared with experiments performed by Myroshnychenko et al. [250] in Figure 4.2. The experimental photon emission intensity spectra and the hotspot created due to dipole and quadrupole modes of the gold nanoprism were in close agreement.

4.1.2 Effect of size change

Silver is considered the best material for plasmonic devices due to its low imaginary part of permittivity and lack of overlap of the plasmonic peaks and interband transitions. The real and imaginary components of permittivity for silver are very close to zero at around 320 nm. Hence, for all the shapes, sizes, and surrounding environments, a dip was observed in the extinction spectrum near the aforementioned wavelength. The spherical silver nanoparticle of volume 50 nm displayed a clear dipole at 363 nm when the surrounding medium was air as shown in the solid red line in Figure 4.3 (a)). The absorption component was higher than scattering in the dipole extinction peak. As the volume of the nanoparticle was increased to a sphere of diameter 100 nm, the dipole peak red shifted to 393 nm (solid red line Figure 4.3 (b)), and the increased size led to a much higher scattering component as compared to absorption [63].

The higher scattering and absorption caused an increase in the overall extinction cross section of the dipole peak. The red shift was observed because upon an increase in size causing a lower surface to volume ratio creates a lower surface charge density, thus, causing a lower restoring force (depolarization) leading to a decreased resonance frequency [251, 252]. Along with the red shift, the full width at half maxima (FWHM) of the dipole peak increased upon an increase in size due to radiation damping, causing a weakened dipole plasmon [253, 254]. Furthermore, a small quadrupole component was observed at 353 nm, since increasing the size enables higher multipole character due to the increased radiative damping [255, 256]. Upon increasing the diameter of the sphere to 150 nm, the dipole and quadrupole peaks were observed at 458 nm and 366 nm, respectively (solid red line Figure 4.3 (c)). The extinction cross section of the quadrupole peak was larger than the dipole peak. A small octupole component was observed in the extinction spectrum at 360 nm when the diameter of the silver sphere in air was increased to 200 nm, which is seen in the solid red line of Figure 4.3 (d)). The dipole and quadrupole peaks were red shifted to 570 nm and 390 nm, respectively, for the aforementioned plot. The effect of nanoparticle size on the plasmonic peaks of other metallic nanoparticles is similar qualitatively, the quantitative comparison of various metallic nanoparticles is discussed in section 4.1.5.

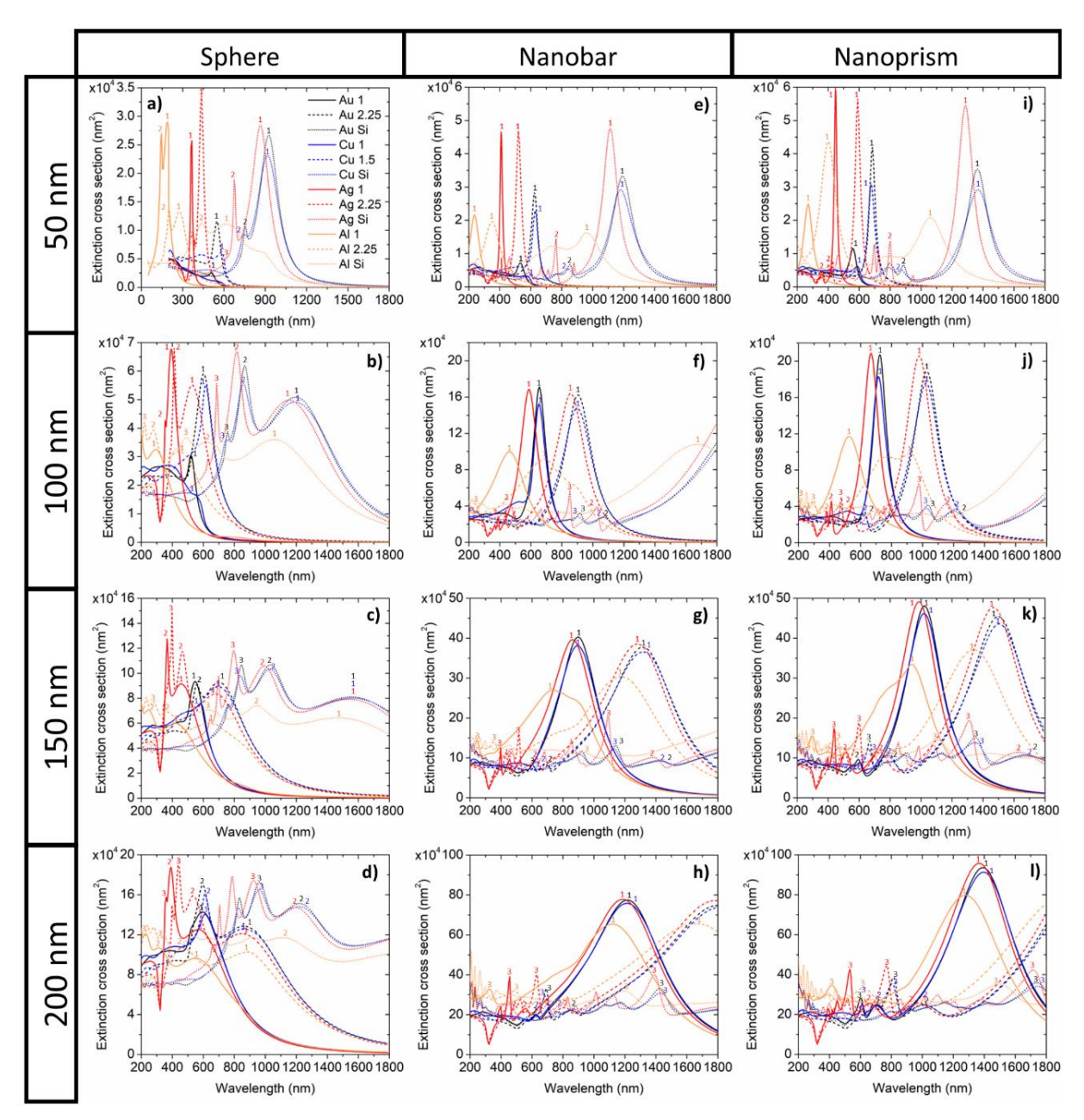


Figure 4.3 Plots of the extinction cross-section for gold (black), copper (blue), silver (red), and aluminium (orange) in air (solid line), glass (dashed line), and a-Si (dotted line) environment, of spherical nanoparticles, nanobars and nanoprisms (left to right), and volumes equal to spheres of diameter 50 nm, 100 nm, 150 nm, and 200 nm (top to bottom). 1, 2, and 3 represent the dipole, quadrupole, and octupole peaks, respectively.

4.1.3 Effect of change in shape

The dipole, quadrupole, and octupole electric field distribution for sphere [255, 257], nanobar [258], and nanoprism [259, 260] are displayed in Figure 4.4 (a-l) for silver nanoparticles in air of volume equal to sphere of diameter 200 nm. The shape of the square and triangular face of the nanobar and nanoprism causes hotspots creation (Figure 4.4 (d-l)). Hence, the intensity of the maximum electric field was much greater in nanobars and nanoprisms dipoles than the equivalent spherical nanoparticles. The quadrupole

electric field distribution for nanobar and nanoprism of volume equal to 50 nm diameter sphere was similar to the equivalent spherical nanoparticle due to the low aspect ratio. The maximum intensity of the electric field was similar for dipoles, quadrupoles, and octupoles in spheres. Further, in Figure 4.4 (a), dipole configuration was slightly asymmetrical due to the higher order pole (quadrupole, octupole, etc.) effects [255]. In the studied polarization direction, where the electric filed was perpendicular to the side of the triangle, the size of the triangle was greater than the square for the same volume. Hence, for the same volume, the aspect ratio of a nanoprism was greater than that of a nanobar. For the dipole electric distribution, the regions of high electric field were larger in nanoprisms than nanobars. Meanwhile, for quadrupole and octupole, the difference in maximum intensity was not very significant. The hotspot formation causes a significant increase in the dipole peak intensities in the extinction spectrum, which was also observed in the difference in the extinction cross section scales used for spherical nanoparticles, and nanobars and nanoprisms in Figure 4.3 (a-l). The electric field distribution for the nanoprism when the electric field was perpendicular and parallel to the side of the triangle (Figure 4.4 (j-l)) were compared. Although the dipole and multipoles configurations were considerably different, as previously explained, the extinction cross-section of both systems was similar in peak positions; however, the intensity of the peaks decreased slightly for the nanoprism with electric field parallel to the side of the triangle due to the decreased aspect ratio in the electric field direction.

When the volume was equal to sphere of diameter 50 nm, the dipole peaks for silver nanobar and nanoprism in air were at 408 nm (solid red line in Figure 4.3 (e)) and 447 nm (solid red line in Figure 4.3 (i)), respectively. A significant red shift was observed as compared to the spherical nanoparticle due to the change in shape from the equivalent spherical nanoparticle, for which dipole peak was present at 363 nm. The extinction cross section of the nanoprism was greater than the nanobar due to higher aspect ratio of the nanoprism. The higher intensity of the electric field hotspots in nanoprism (Figure 4.4 (g)) as compared to nanobar (Figure 4.4 (d) leads to an increased extinction cross section for the equivalent nanoparticles (Figure 4.3). Hence, correlating the near field enhancement (hotspots) with their far field response (extinction cross section). Furthermore, the lack of hotspot generation in spherical nanoparticles leads to the lower extinction cross section in spherical nanoparticles as compared to the equivalent nanobars and nanoprisms. It was observed that the dipole peaks were much higher in intensity than the quadrupole and octupole peaks due to the presence of high intensity hotspots in the dipole configuration, even when the volume of the nanobar and nanoprism was equal to sphere of diameter 200 nm (solid red line in Figure 4.3 (h and l)). Similar to the spherical nanoparticles, increasing the volume led to red shifting and increased FWHM of the dipole and other higher order peaks as seen in Figure 4.3 (f and j). For silver nanoparticle of volume equal to 100 nm diameter sphere in air, the dipole peak red shifted by 30 nm for spherical nanoparticle, 179 nm for nanobar, and 221 nm for nanoprism, as compared to nanoparticle of volume equal to 50 nm sphere. Further increase in size lead to an increased red shift and increased intensity of electric field hotspots, and hence a higher extinction cross section for all the shapes, although the electric field distribution of the dipole and higher order

poles remained similar. Silver, had the highest hotspot intensity and therefore, the highest extinction cross section for equivalent nanoparticles as compared to the other metals due to lowest losses as seen in the imaginary part of the dielectric function. The electric field distribution of hotspots was similar for all the metals, however, the intensity changed as a result of the variation of the dielectric functions. Comparing the red shift when the volume of the nanoparticle was varied from 50 nm diameter sphere to 100 nm diameter sphere in air, the dipole red shift for gold was 10 nm for spherical nanoparticle, 120 nm for nanobar, and 163 nm for nanoprism. The dipole red shift for copper was 79 nm for nanobar and 128 nm for nanoprism; for copper, no distinct dipole peak was present for spherical nanoparticle of diameter 50 nm. The dipole red shift for aluminium was 107 nm for spherical nanoparticle, 226 nm for nanobar, and 256 nm for nanoprism. The red shifts due to the change in material is studied in detail in section 3.4.

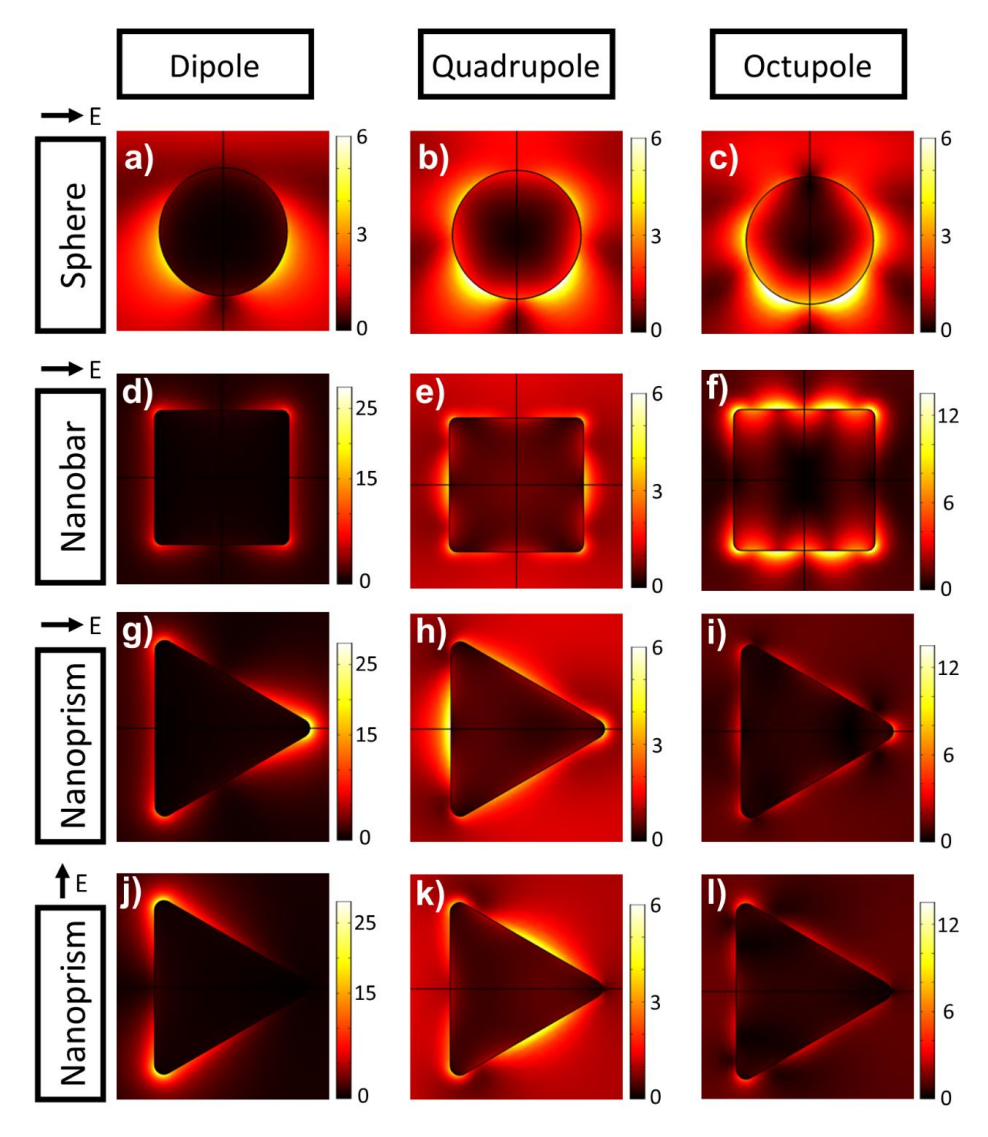


Figure 4.4 The normalized electric field (V/m) of silver nanoparticles in air with volume equal to sphere of diameter 200 nm. From left to right, the dipole, quadrupole, and octupole configurations of spherical nanoparticle (570 nm, 390 nm, and 360 nm), nanobar (1090 nm, 558 nm, and 453 m), and nanoprism (1394 nm, 704 nm, and 611 nm).

4.1.4 Effect of nanoparticle embedding in dielectric

Embedding a silver nanoparticle in glass and a-Si has a significant effect on the characteristics of the dipole and other higher order peaks. Glass is considered to only have a constant real permittivity of 2.25; a-Si, on the hand, has a real and imaginary competent which varies with wavelength. In the visible region, the real part of permittivity of a-Si is much higher than glass, and the imaginary part decreases from a finite value and tends to zero beyond 950 nm. The increase in the permittivity of the surrounding medium induces greater polarization of the medium, which attenuates the charge concentration in the resonance zone (decreased surface charge) that leads to decreased restoring force [261]; hence, the peak is red shifted as compared to air environment. Furthermore, the dip for silver nanoparticles near 320 nm is not very sharp for a-Si environment as compared to air and glass, due to higher absorption (dotted red lines in Figure 4.3 (a-l)). The dipole peak for the 50 nm diameter spherical silver nanoparticle was red shifted to 435 nm (dashed red line in Figure 4.3 (a)) and 864 nm (dotted red line in Figure 4.3 (a)) in glass and a-Si, respectively, as compared to air. Furthermore, the aforementioned peak broadens as the surrounding medium was changed from air to glass to a-Si due to the increased damping because the external field weakens due to the increase of the surrounding refractive index [262]. In glass and a-Si, quadrupole peaks were observed at 385 nm in the dashed red line in Figure 4.3 (a) and at 673 nm in the dotted red line in Figure 4.3 (a) for 50 nm diameter spherical nanoparticle. In a-Si, a small octupole component was also present at 615 nm for the 50 nm diameter silver sphere. Hence, multipole character was observed for smaller sizes as compared to nanoparticles in air, similar to the size effect, higher damping causes increased multipole character because of the increased retardation effects when the dielectric constant of the surrounding is increased [60, 263]. Increasing the diameter of the spherical nanoparticle to 100 nm in glass and a-Si environment, a red shift and broadening of the dipole and higher order poles were observed in the red dashed and dotted lines in Figure 4.3 (b). In a-Si medium, the dipole, quadrupole, and octupole peaks were clearly distinguishable for the aforementioned silver nanoparticle. The dipole peak was shifted beyond 1800 nm for spherical silver nanoparticle of diameter 200 nm in a-Si as observed for the dotted red line in Figure 4.3 (d)). Silver nanobar and nanoprism of volume equal to sphere of diameter 50 nm, had dipole peak in glass environment at 533 nm (dashed red line in Figure 4.3 (e)) and 603 nm, respectively; and in a-Si environment at 1125 and 1297 nm, respectively. Upon increase in volume to sphere of diameter 100 nm, the dipole peak of nanobar and nanoprism in a-Si shifted beyond 1800 nm due to the combined effect of the shape and surrounding environment. Additionally, for glass environment the dipole peak shifted beyond 1800 nm for silver nanobar and nanoprism of volume equal to sphere of diameter 200 nm (dotted red line in Figure 4.3 (h and l)). Hence, the analysis when the dipole was beyond the range of the simulation, the higher order poles were considered.

4.1.5 Effect of change of material

The previous parts of the results section discussed the optical response of silver nanoparticle due to change in size, shape, and surrounding environment. In the current part, the comparison of the response of spherical nanoparticles, nanobars, and nanoprisms of gold, copper, silver, and aluminium due to increase in size (Figure 4.5 (a-c)), and change in the surrounding environment (Figure 4.5 (d) & (e)) are presented. The separate plots for individual materials in Figure 4.5 are displayed in the Appendix C for gold, copper, silver, and aluminium.

Silver, gold, and copper have interband transitions at around 320 nm, 521 nm, and 590 nm, respectively. The interband transitions for gold and copper overlap with the plasmonic region; hence, multipole behaviour was not observed for smaller sizes in air as evident by the solid black and blue lines in Figure 4.3 (a-j)). Copper and gold display similar peak wavelengths, but the higher absorption of copper due to the larger imaginary part of the dielectric function leads to peaks of lower intensity. The dipole peak for copper sphere in air was not sharp for nanoparticles of volume lower than diameter 200 nm sphere (Solid blue line in Figure 4.3 (a-c)). Simulations were performed starting from 50 nm for aluminium nanoparticles to observe important peaks in the UV region. The dipole and quadrupole peaks were observed at 187 nm and 143 nm for aluminium sphere of diameter 50 nm as shown in the solid orange line in Figure 4.3 (a). The imaginary part of permittivity is close to zero up to 200 nm in aluminium, beyond which it increases; hence, the highly intense peaks are present in the UV region for aluminium for small sizes. The high imaginary part of permittivity leads to lower intensity peaks beyond the UV region for aluminium as compared to other materials. Additionally, the overlap of the interband and plasmonic peak at around 870 nm causes broad peaks for aluminium around this wavelength which can be observed in air by the solid orange lines in Figure 4.3 (g and k), in glass by the dashed orange lines in Figure 4.3 (f and j), and in a-Si by the dotted orange line in Figure 4.3 (a, e and i).

Figure 4.5 (a) shows that the dipole red shift in air due to increase in volume of the equivalent nanoparticles. When the surrounding was air, the dipole red shift for the spherical nanoparticle was the lowest. The dipole red shift for nanoprism was higher than the nanobar for gold, silver, and copper. Comparing the dipole red shift among materials, aluminium displayed the highest red shift upon increase for nanoparticles whose volume was increased from 50 nm to 100 nm diameter sphere. The massive shift can be attributed to the involvement of interband transitions of aluminium. As the peaks move away from the interband transitions, due to the increase in volume, the dipole red shift in aluminium gradually decreases as the volume of the nanoparticle was increased. Gold and copper display similar dipole red shift, and silver displayed slightly higher values than gold and silver. Furthermore, it was observed that the dipole red shift for increase in volume from diameter 100 nm to 150 nm was very similar (slightly lower) than increase in volume from diameter 150 nm to 200 nm. Furthermore, it can be observed from Figure 4.3 that for silver, gold, and copper, the dipole peaks for 200 nm diameter nanoparticles were very similar. Figure 4.5 (b) shows the dipole red shift due to an increase in size in glass environment. The values were significantly higher for gold, copper, and silver

spherical nanoparticles than the equivalent nanoparticles in air. The nanobars and nanoprisms showed slightly higher values than the equivalent nanoparticles in air for the aforementioned nanoparticles. Similar to air, aluminium displayed the highest dipole shift in glass environment, which was followed by silver. In a-Si environment, the dipole peak was not present for all the nanoparticles; hence, higher order poles were compared in Figure 4.5 (c). The higher order poles display lower peak shift as compared to dipole peaks. Similar to the previous cases, gold and copper have similar shifts, although, gold has slightly higher values. The broad peaks of aluminium lead to the lack of higher order peaks for some of the nanoparticles; however, spherical nanoparticle of aluminium had the largest shift due to increase in size.

To analyse the effect of only the surrounding environment, the red shifts of the dipole peaks in glass and a-Si environment were compared to the equivalent nanoparticles in air for the various sizes of the nanoparticles in Figure 4.5 (d) and (e). Aluminium dipole displayed the highest shift for all sizes of spherical nanoparticles in glass compared to air. In a-Si environment, the dipole shift compared to air was much greater as compared to glass environment. It was clearly observed that for all the shapes and sizes, aluminium displayed the highest dipole peak shift in a-Si compared to air, followed by silver, gold, and copper.

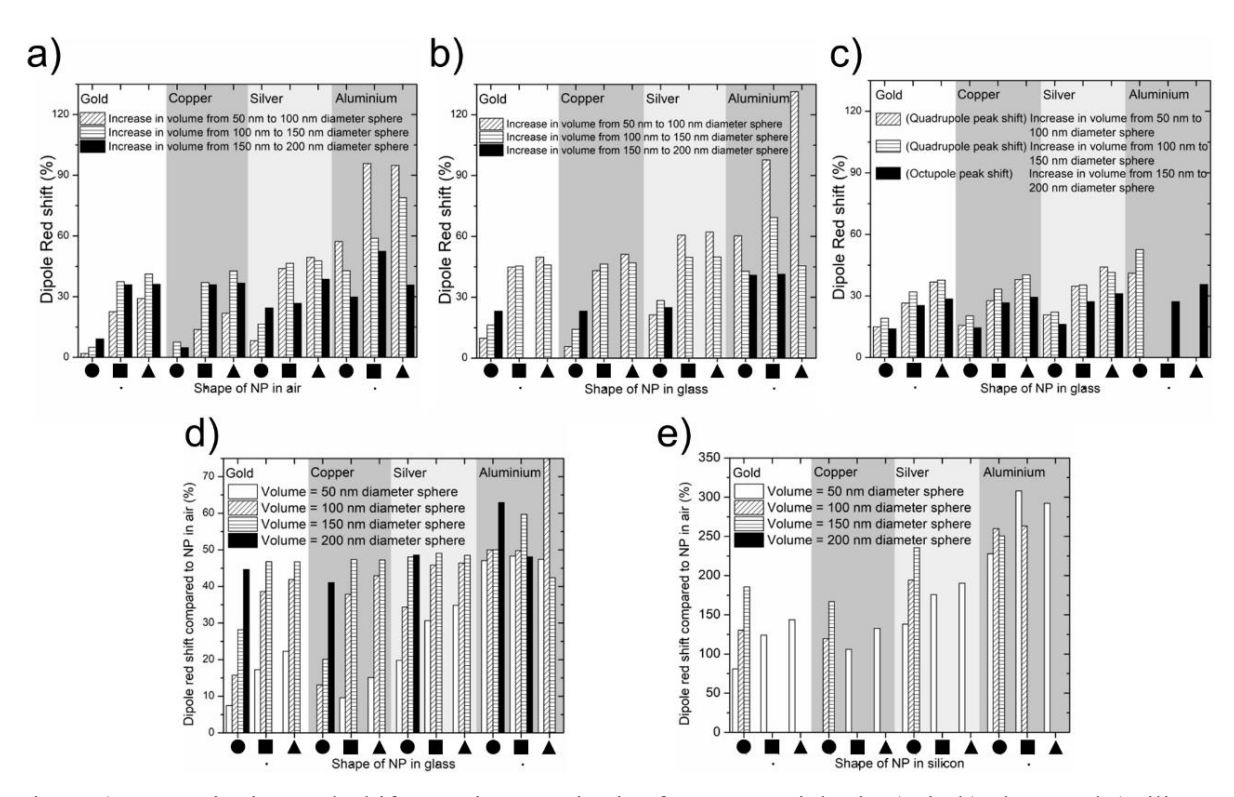


Figure 4.5 Quantitative peak shift upon increase in size for nanoparticles in a) air, b) glass, and c) silicon. Dipole shift compared to the equivalent nanoparticle in air for d) glass and e) a-Si surrounding.

4.2 Nanoarrays

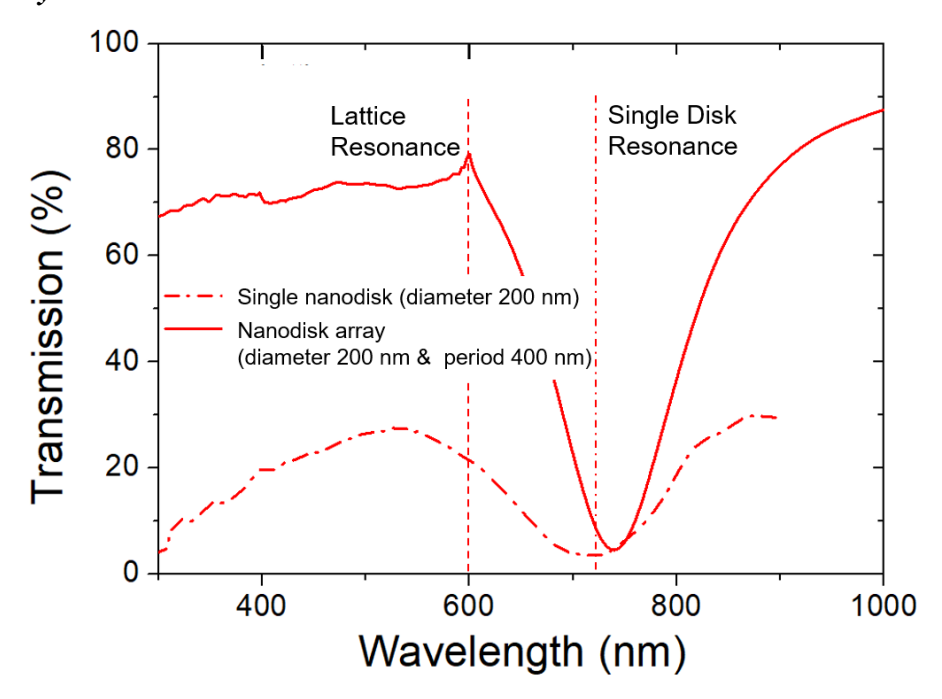


Figure 4.6 Simulation transmission plot comparing a single nanodisk (diameter 200 nm and thickness 45 nm) and the same nanodisk placed in an array of period 400 nm (diameter of the disk was 200 nm and thickness 45 nm)

To enhance the optical response of the nanoparticles, they were placed in a periodic array which added a resonance due to periodicity to the inherent LSPR of the nanoparticle as shown in Figure 4.6. Thereby unlocking the potential of nanostructures.

The current work aims to improve the understanding of the resonant modes in a nanoarray placed in a non-homogenous medium (air-glass interface) for sensing applications. Single structure resonance and grating resonance, as well as their coupling effect are presented. First, the effect of geometric parameters (diameter, thickness and periodicity) of gold nanodisk arrays of gold and aluminium are compared. Then, the disc shape is compared with square and triangle, to observe the effect of increased hotspot generation on their overall plasmonic response and sensitivity. Although the discussion of nanoarrays is prevalent in the literature, the discussion covering material effect, the single structure response, lattice and structure resonance coupling, and sensitivity analysis is lacking.

4.2.1 Simulation parameters and validation

The simulation was performed as per section 3.1.3 for nanopatterns with disc, triangular, and squares. To compare the three shapes, the volume of the shapes was kept the same. Figure 4.7 (a) shows the various shapes and the geometric parameters studied in the current article. To calculate the transmission spectra of the various nanoarrays, the simulation was performed from wavelength 200 nm to 1800 nm. Initially, the effect of thickness (10 nm to 150 nm) with diameter to period ratio of 0.5 for gold and

aluminium nanodisks of diameter 50 nm, 100 nm, 200 nm, and 300 nm was seen. Then, the effect of periodicity (diameter to periodicity ratio 0.2 to 0.8) for the aforementioned nanodisks with thickness 30 nm was calculated. The coupling effect was most clearly observed in 200 nm nanodisks (explained in results and discussion section); hence, it was selected for further analysis. Similar thickness and periodicity studies were performed for square and triangle shapes with volume equal to disc of diameter 200 nm and thickness 30 nm. Sensitivity analysis was performed for the optimal coupling periodicity. The simulation was validated using experimental results; the comparison is shown in Figure 3.2 (b). The nanodisks were fabricated using laser interference lithography (LIL) which is explained in section 3.4. The discrepancy in the resonance wavelength was less than 4 % and a stronger resonance was observed compared to the experimental spectrum. It was deemed to be due to the practical losses and imperfections in the experimental nanoarray.

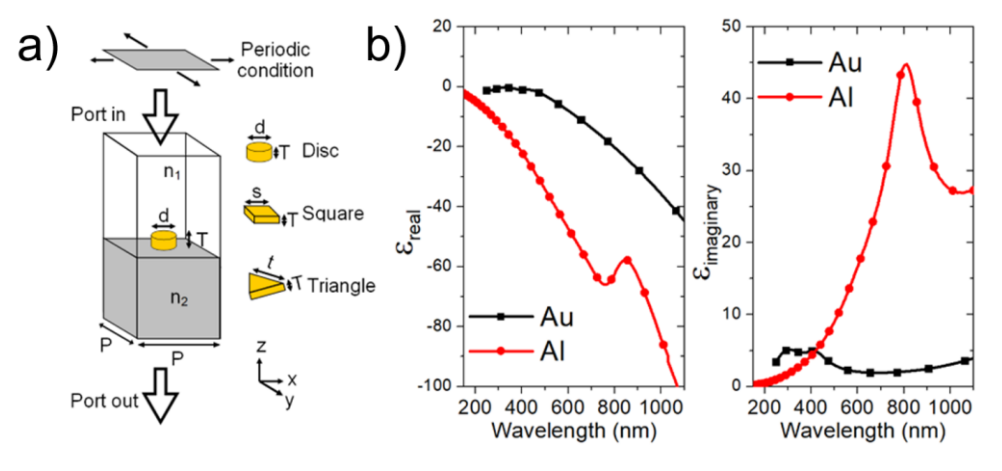


Figure 4.7 (a) Simulation domain showing the ports, periodicity and the shapes that were analyzed. The periodicity (P), thickness (T), diameter (d), and sides (s and t) were varied. (b) Real and imaginary part of the dielectric function of gold and aluminium according to Lorentz Drude model.

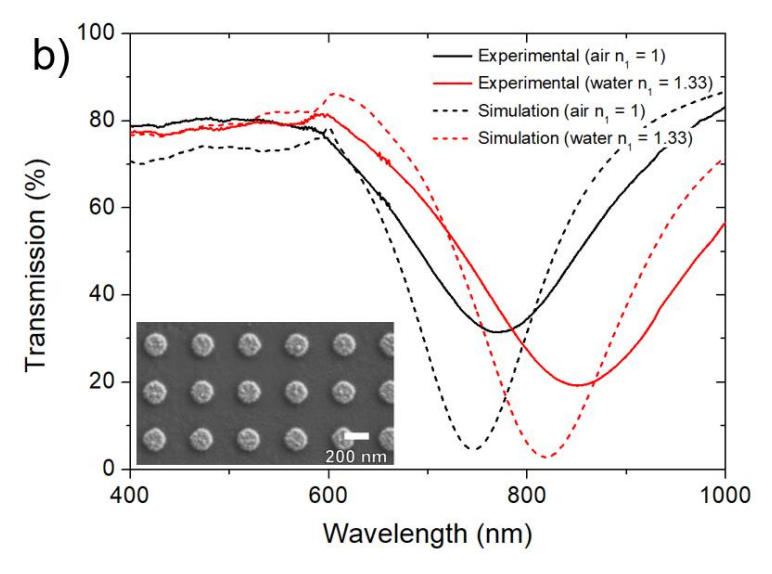


Figure 4.8 Comparison of simulation and experimental results of 400 nm period gold nanodisk array with diameter 187 nm and thickness 45 nm with surrounding material air and water. The inset shows the experimental gold nanodisk array.

4.2.2 Effect of geometric parameters (thickness, diameter, and periodicity)

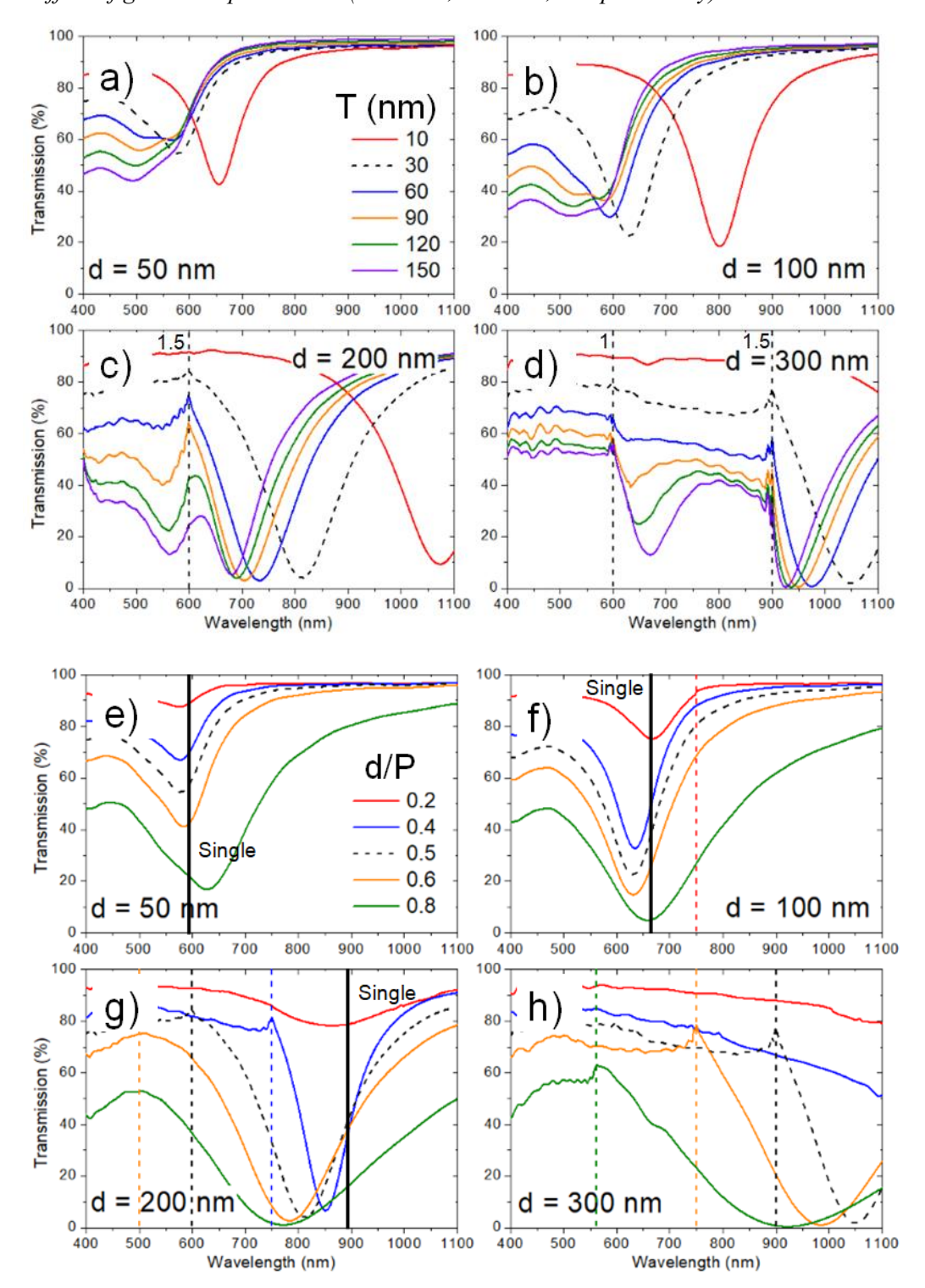


Figure 4.9 Simulated transmission spectra for gold disc nanoarray at air glass interface. (a-d) Thickness variation and (e-f) variation of d/P. The vertical dashed lines represent lattice resonance, (1 0) diffraction edge, and the number beside is the refractive index for the lattice resonance. No number pertains to the resonance due to glass environment (n = 1.5). Solid line represents the single disc resonance.

The selection of geometric parameters is a critical aspect for any plasmonic application. Generally, the disc nanoarray is the easiest to fabricate by the methods listed in the introduction section. Furthermore, in many of the techniques, the diameter to period ratio (d/P) is usually around 0.5. Therefore, the gold disk nanoarray on a glass air interface of diameters 50 nm, 100 nm, 200 nm, and 300 nm are compared with d/P 0.5 in the Figure 4.9 (a-d). A strong resonance in the transmission spectra was observed in Figure 4.9 (a) and (b). In the near field, the creation of a dipole was observed in the electric field contour, as shown in Figure 4.13 (d). Increasing the thickness leads to a blue shift in the transmission dip, this is due to an increase in the surface charge of the nano sized disc [264]. The increase in size diameter causes a red shift of the transmission dip. The larger size creates a lower surface charge density, which leads to a weaker restoring force of the oscillating dipole and hence, a decreased resonance frequency [251, 252]. Further, the increase in size also increases the size of the localized plasmon, which is comparable to the size of nanodisk [253]. Therefore, the increased size also causes higher radiation damping that increases the full width at half maxima (FWHM) of the dipole resonance [253]. Now, for the 200 nm diameter disc, a Fano like resonance can be clearly observed at 600 nm for all the thicknesses that are plotted in the Figure 4.9 (c). This Fano resonance is due to a lattice effect in the surrounding refractive index, which can be approximated using the following general equation [265].

$$\lambda = n P 5.1$$

where λ represents the resonance wavelength, n is the refractive index of the surrounding. The 600 nm lattice resonance is due to the 1.5 refractive index of the glass substrate. Increasing the thickness creates a higher conferment of the EM wave; therefore, for larger thicknesses, along with a dipole at larger wavelengths, an octupole resonance [197] can be observed at the shorter wavelengths as shown in Figure 4.13 (d). Moving to an even greater diameter of 200 nm, along with the lattice resonance due to glass surrounding at 900 nm, another lattice resonance can be observed at 400 nm due to the refractive index of air (n=1).

The effect of periodicity is observed by varying the d/P ratio for the various diameters of the disc nanoarray as shown in Figure 4.9 (e-h). It was observed that at smaller d/P (for very large periodicity), the resonance intensity was very low, and it increased as d/P was increased (the periodicity becomes closer to the diameter of the disc). For larger d/P, the higher confinement of the EM wave creates a strong plasmonic response. The dashed lines represent the lattice resonance for the respective coloured d/P. An interesting observation can be made for 200 nm diameter disc nanoarray (Figure 4.9 (g)). The major transmission dip had a very strong resonance for the d/P ratio of 0.4. It was noted that the single particle resonance for 200 nm diameter gold disc is at 895 nm, represented by the solid black line. It was observed that the strongest resonance (had the lowest transmission dip) for the d/P ratio for which the lattice resonance was the closest to the single particle resonance. As the lattice resonance moved further away from the single particle resonance, the intensity of the major resonance decreased. Hence, it can be concluded that the coupling of the single particle and lattice resonance creates a highly intense

transmission dip [266]. For a 300 nm diameter disc nanoarray, the single particle resonance was at 1152 nm (far away from the lattice resonance), and the lattice resonance dominates the single particle resonance. Meanwhile, for 50 nm and 100 nm diameter, the single particle resonance (at 592 nm and 664 nm, respectively) dominates the transmission spectra. Therefore, to observe the coupling effect in other shapes (square and triangular nanoarrays), where the volume is kept equal to the diameter 200 nm disc. The comparison of the various shapes is presented after the discussion of aluminium disc nanoarray.

4.2.3 Effect of change of material

To study the effect of the change in material to the response of the nanopattern array, the extinction cross section spectrum of single nanostructures of volume equivalent to disc of diameter 200 nm and thickness 30 nm (shown in Figure 4.10). Considering a nanodisk of gold and aluminium, it was clearly observed that a strong dipole resonance was seen for both. However, for aluminium, the resonance was blue shifted, had a higher FWHM, and was of lower intensity. To explain this change in the response of the nanodisk, the dielectric function of gold and aluminium, shown in Figure 4.7 (b) will be used. The blue shift was due to the large negative real part of the dielectric function achieved for shorter wavelength in aluminium as compared to gold. The broader and less intense resonance was due to the large positive imaginary part of the dielectric function.

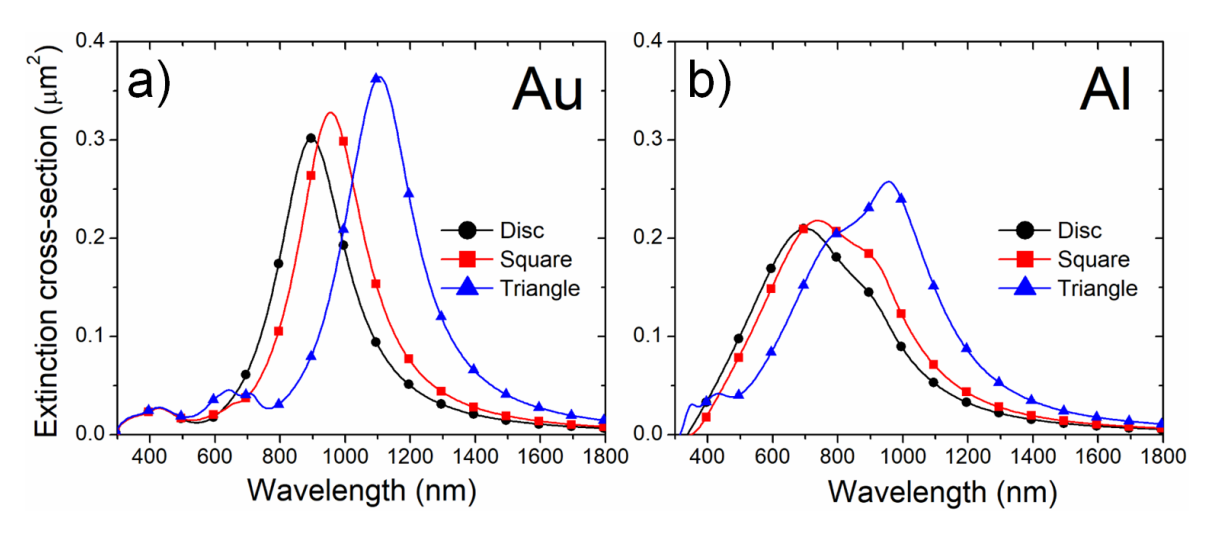


Figure 4.10 Extinction cross section of single nanostructures (disc, square, and triangle) with volume equivalent to a nanodisk of diameter 200 nm and thickness 30 nm of a) gold and b) aluminium.

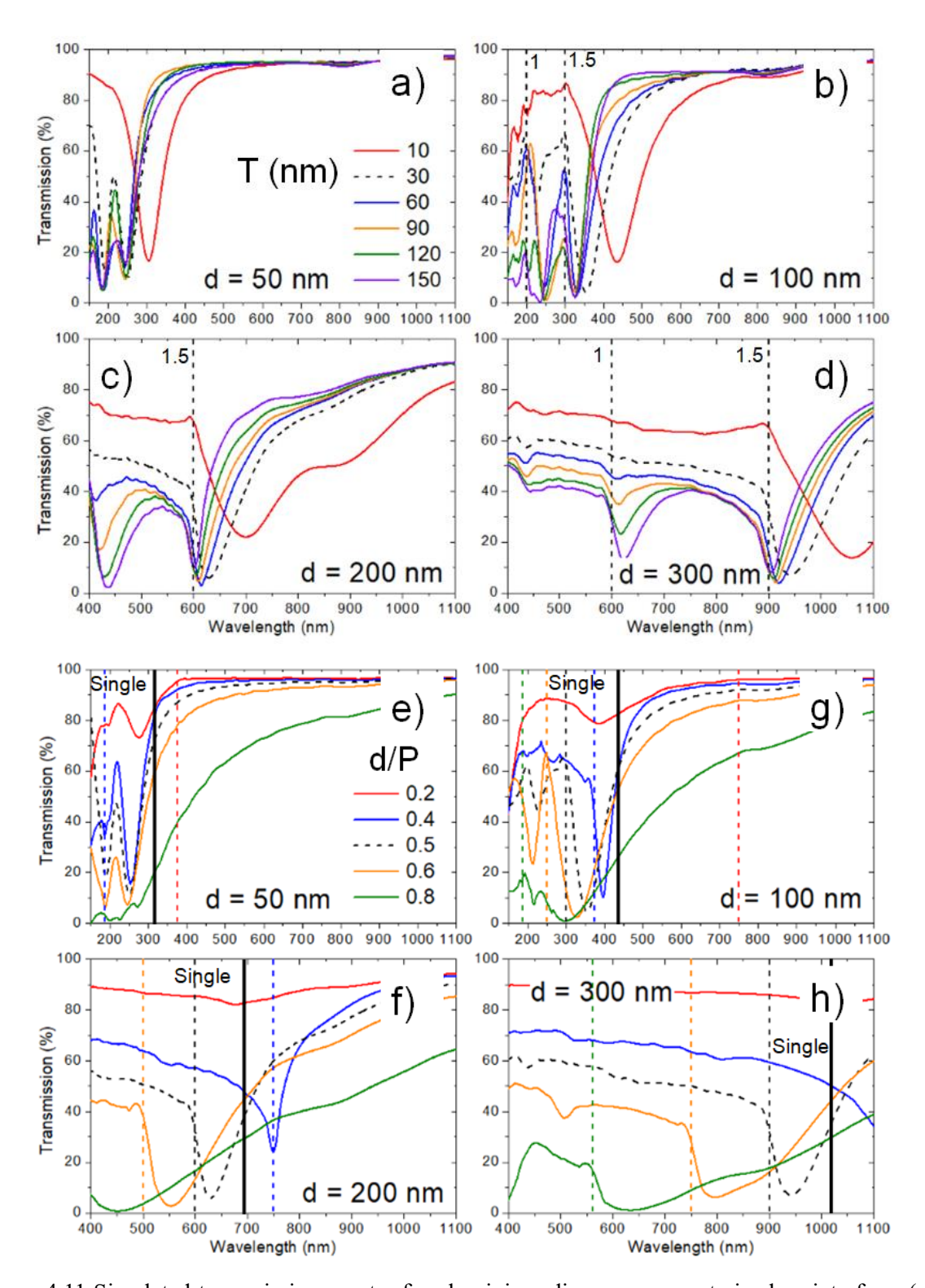


Figure 4.11 Simulated transmission spectra for aluminium disc nanoarray at air glass interface. (a-d) thickness variation and (e-f) variation of d/P. The vertical dashed lines represent lattice resonance, (1 0) diffraction edge, and the number beside is the refractive index for the lattice resonance. No number pertains to the resonance due to glass environment (n = 1.5). Solid line represents the single disc resonance.

Now, when the nanodisks were arranged in a square lattice, it was observed that the dipole resonance of aluminium for similar sizes was blue shifted, and a strong resonance in the transmission spectra was also observed in the UV region as shown in Figure 4.11 (a-h). This can be easily observed for 50 nm and 100 nm diameter disc nano array in Figure 4.11 (a) and Figure 4.11 (b). The distinguishable resonances in the UV region in aluminium can be explained due to the lower imaginary part of the dielectric function in the UV region (shown in Figure 4.7 (b)). However, at larger wavelengths, the transmission dip is broader and less intense in aluminium because of the increased losses, as compared to gold. The Fano resonance due to lattice effect was seen for diameter 100 nm disc nanoarray also. The other observations for aluminium disc nanoarray were similar to that of gold nanoarray. For the diameter 200 nm aluminium disc nanoarray, the single particle resonance for aluminium was at 691 nm. The highest coupling effect was observed for the d/P of 0.4, for which the lattice resonance was at 750 nm. The red shifted lattice resonance (for d/P 0.5 and d/P 0.6) led to a weaker resonance (higher FWHM), and for the red shifted resonance (d/P = 0.2), the resonance almost disappeared. Also, due to the low losses in the UV region, a big coupling effect was also observed for d/P ratio of 0.4 for diameter 100 nm disc nanoarray (which was absent for gold nanodisk array). Therefore, the material and the geometric parameters play a critical role in determining the plasmonic response of the nanoarray.

4.2.4 Effect of change of shape

To analyse the effect of the shape of the particle in the nanoarray, square and equilateral triangle shapes were simulated. The sides s (for square) and t (for triangle) were kept at 177.25 nm and 269.35 nm to keep the volume equal to the disc with a diameter of 200 nm. The size was chosen in order to observe the coupling effect clearly in the selected shapes. The polarization direction for the simulated plots can be seen in Figure 4.13 (θ was 0° for the plots in the current article). The extinction cross section plots in the Figure 4.10 present the effect of the change in optical response for disc, square and triangle of volume equal to nanodisk of diameter 200 nm and thickness 30 nm. A red shifted and increased dipole intensity in the extinction cross section spectrum can be observed as the shape of the nanostructure was changed from disc to square to triangle. The red shift was majorly due to the increase in size of the structure (both square and triangle) in the polarization direction (the direction is same as for 4.13) when the volume was kept equal to the disc. The increase in intensity was due to the creation of electric field hotspots near the sharp corners in square and triangle [25]. The asymmetry in the dipole resonance in aluminium structures was because of the increased effect of higher order poles.

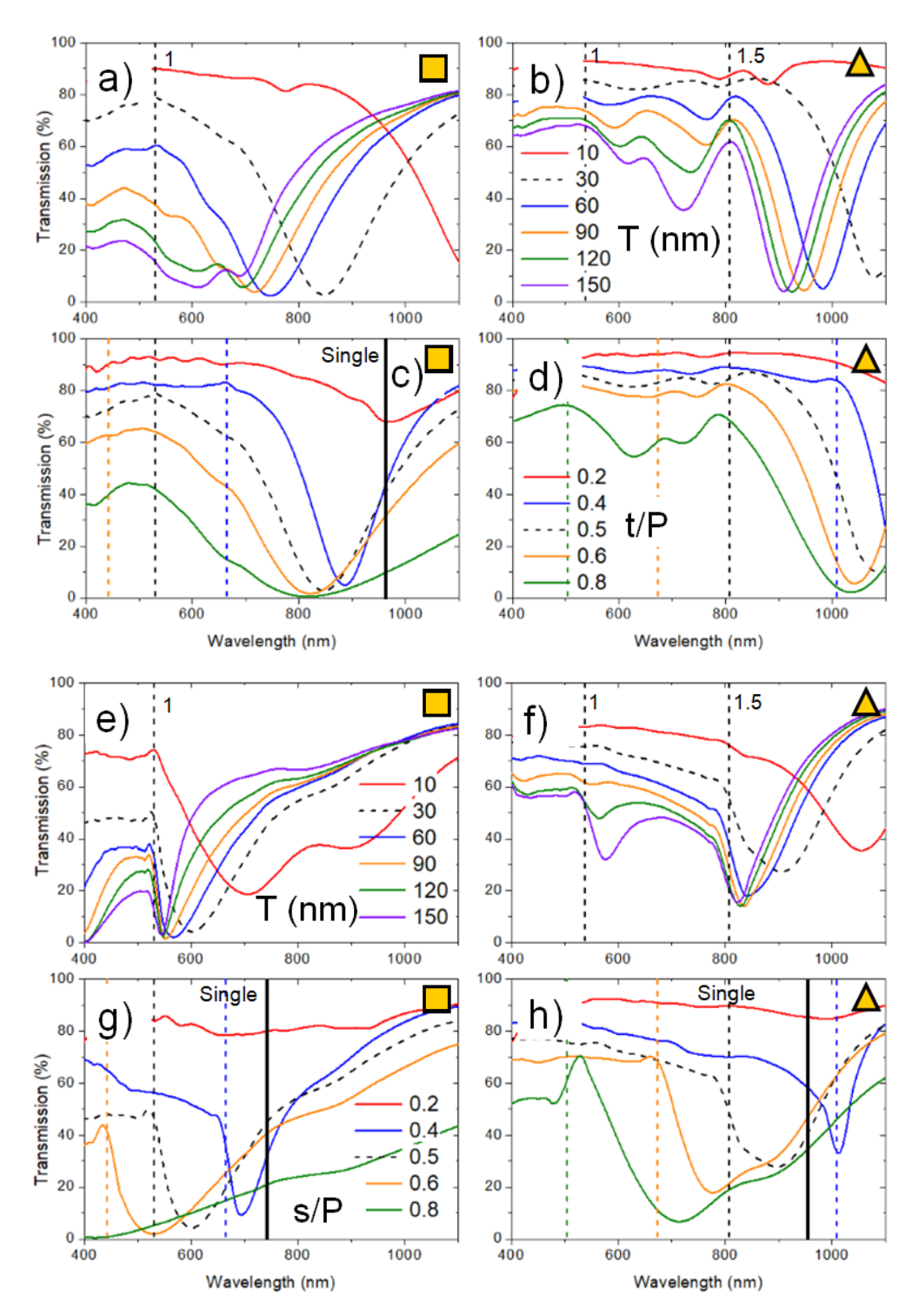


Figure 4.12 Comparison of gold (a-d) and aluminium (e-h) nanoarray simulated transmission spectra of square (a, c, e, and g) and triangle (b, d, f, and h). (a, b, e, and f) shows the height variation and (c, d, g, and h) shows the respective t/P and s/P ratios. The side of square and triangle were kept as 177.25 nm and 269.35 nm to keep the volume equal to the disc of diameter 200 nm. The nanoarray was at air glass interface for $\theta = 0^{\circ}$. The vertical dashed lines represent lattice resonance, (1 0) diffraction edge, and the number beside is the refractive index for the lattice resonance. No number pertains to the resonance due to glass environment (n = 1.5). Solid line represents the single disc resonance.

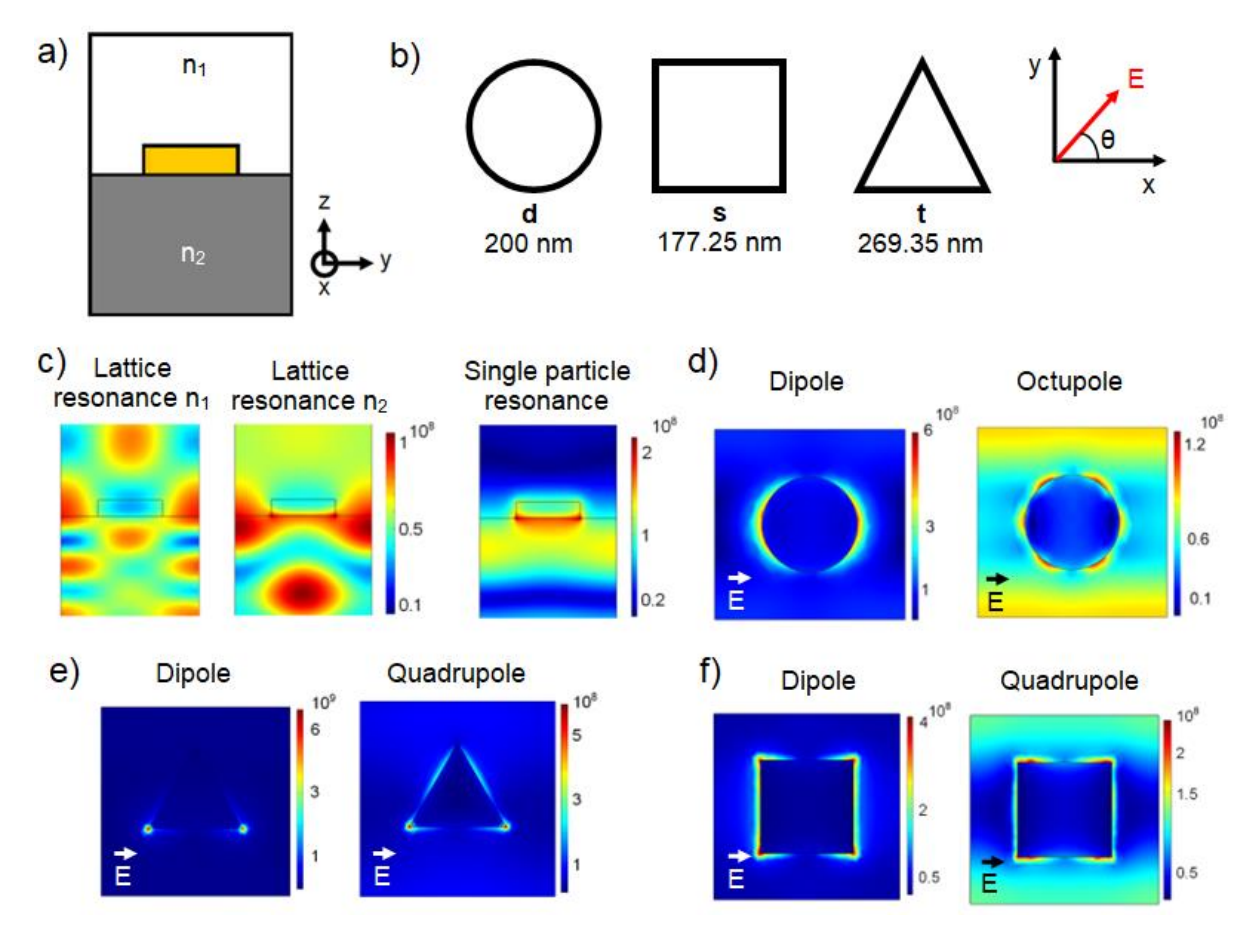


Figure 4.13 a) Simulation domain of nanodisk array. b) Various shapes analyzed and the direction of polarization. (c-e) Normalized electric filed in (V/m) contours for the nanoarrays showing c) lattice and single particle resonances, d) Dipole and Octupole in disc nanoarray, e) Dipole and Quadrupole in triangle nanoarray, and Dipole and Quadrupole in square nanoarray

Simulations were performed for both gold and aluminium nanoarrays to observe the effect of thickness and periodicity, as shown in Figure 4.12 (a-h). The plots displayed a similar trend to that discussed for disc nanoarray. It was observed that for comparable sizes, the major resonances were red shifted due to single particle resonance being at longer wavelengths for both square and triangle. Furthermore, the increased confinement of the EM wave due to the hotspot generation was confirmed by the increased intensity of the resonances. Similar to the disc nanoarray, higher order poles were observed for larger thicknesses which are shown in Figure 4.12 (e) and (f). Comparing gold and aluminium, it can be inferred from Figure 4.12 b) and f), the lattice resonance due to air (n = 1) was more clearly observed for aluminium. The lower losses in the UV region, as seen in Figure 4.7 (c) was the clear contributor to the aforementioned phenomenon. A similar trend was also seen in Figure 4.12 (a) and (e). Furthermore, for similar sizes, the coupling effect was observed more clearly for aluminium square and triangle in the Figure 4.12 (g) and (h) due to the increased proximity of the single particle resonance to the lattice resonance. The effect of polarization was also checked using refractive index variation plots in

Appendix D; it was observed that the shift in the resonance wavelengths was not very significant for the respectively comparable cases for $\theta = 45^{\circ}$ for square nanoarray and $\theta = 60^{\circ}$ and 90° for triangle nanoarray as compared to the $\theta = 0^{\circ}$ polarization.

4.2.5 Sensitivity comparison

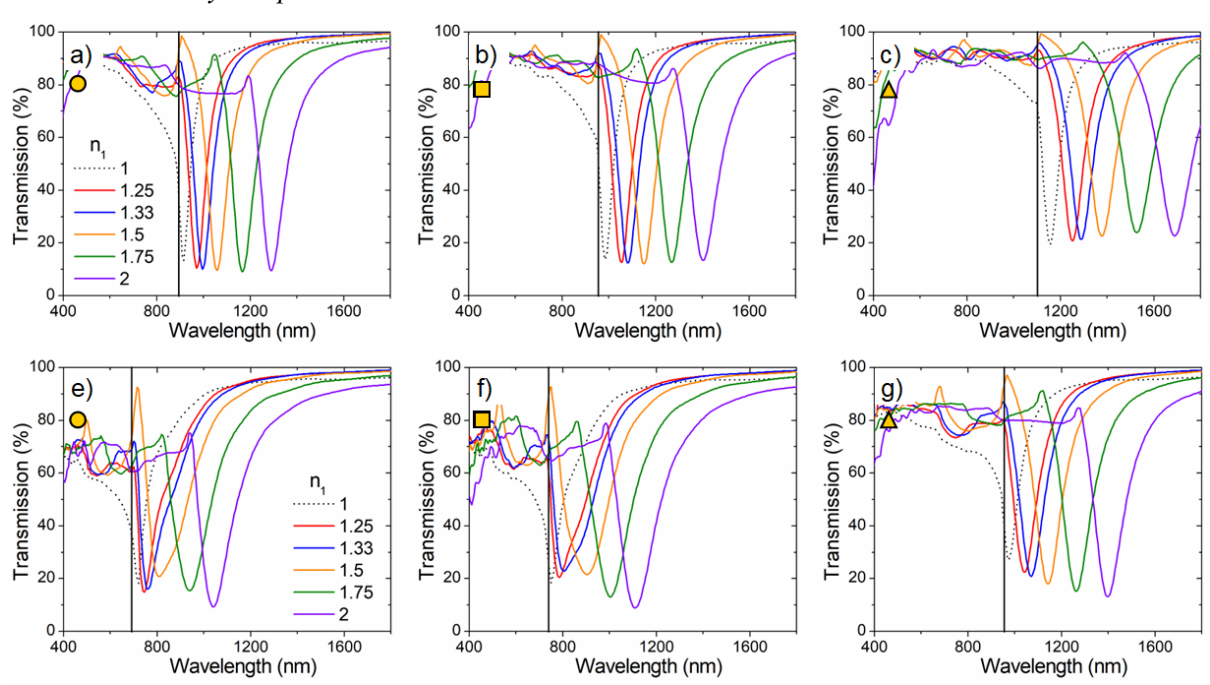


Figure 4.14 Refractive index (n1) variation in gold (a-c) and aluminium (a-c) nanoarray for disc (a, e), square, (b, f), and triangle (c, g) shapes. The sloid vertical line represents the single particle resonance. The side of square and triangle were kept as 177.25 nm and 269.35 nm to keep the volume equal to the disc of diameter 200 nm. The square lattice periodicity was equal to the coupling condition of the single particle resonance at air glass interface.

The effect of the material and the shape of the nanoarray were quantified using a parameter that had numerous practical applications. Nanoarrays are often used as chemical and biosensors, and they work on the principle that a change in the surrounding refractive index is created by the targeted molecule. This change in refractive index leads to shift in the resonance wavelength which can be observed in the transmission spectrum. The refractive index based sensing has already been used for the detection of bacteria [267], viruses [268], biomarkers [269], heavy metals [270], pesticides [271] etc. The sensitivity of these sensors is defined as the ratio of change in wavelength to the variation refractive index. Therefore, simulations were performed by varying n_1 from 1 to 2, the volume of the particle in the array being equal to a disc with a diameter of 200 nm and a thickness of 30 nm. To compare the best performing structures, the refractive index variation was performed when the periodicity of the lattice was equal to the single particle resonance of the structure. The single particle resonance of the structures was measured from the Figure 4.10, thereby, the sensitivity comparison was performed for the optimal

coupling condition as shown in Figure 4.14 (a-g). It was observed that, when the surrounding of the nanostructures became homogeneous ($n_1 = n_2 = 1.5$), the largest Fano like resonance was observed. As expected, the resonance wavelength was at shorter wavelengths for aluminium as compared to gold. Comparing the sensitivity, the triangle displayed the highest sensitivity, followed by the square and the disc nanoarray, as shown in Figure 4.15. Furthermore, gold showed better sensitivity than aluminium due to the larger losses in aluminium. The sensitivity comparison was also performed for the nanostructures with periods equivalent to d/P = 0.5 (not at the optimal coupling condition) as shown in the Appendix D. The sensitivity was much lower than for the structures at optimal coupling condition.

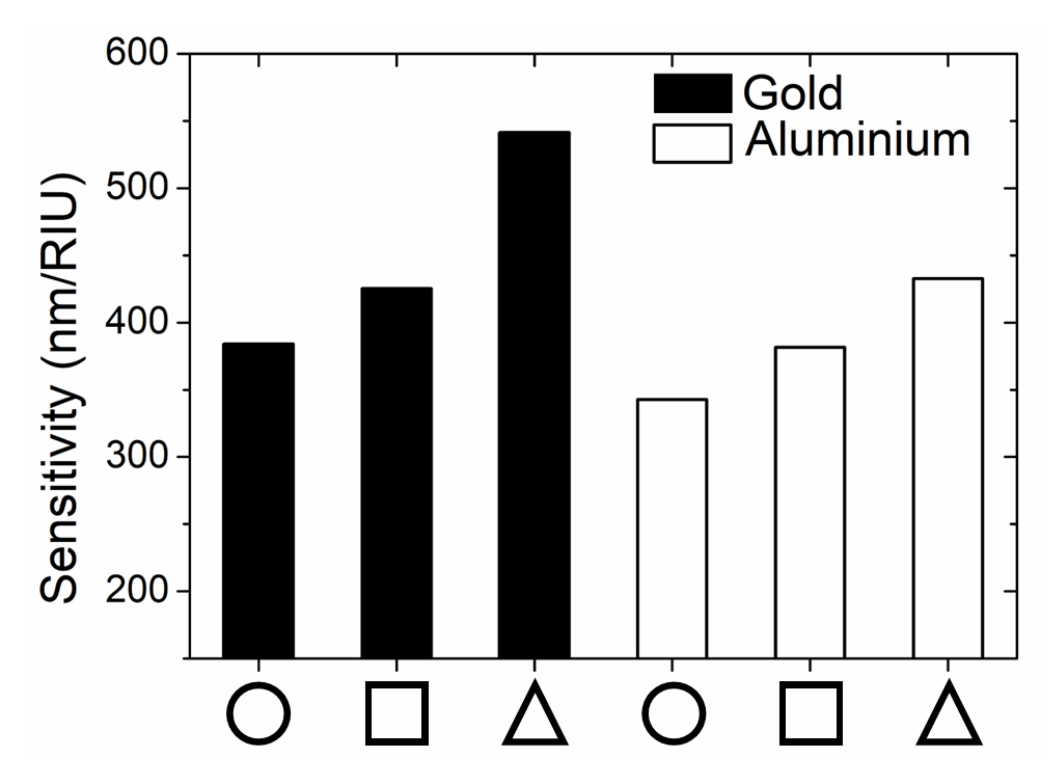


Figure 4.15 Sensitivity comparison of gold and aluminium nanoarray of disc, square and triangle nanoarrays (at the optimal coupling condition). Volume equal to disk of diameter 200 nm and thickness 30 nm.

Table 4.1 shows the sensitivity comparison of the various nanopatterns available in the literature. The sensitivity of the triangle nanoarray was comparable to the configurations in the literature. Furthermore, from table 1, it can be inferred that more complicated geometries (crescent shaped array [272], sinusoidal grating [273], and C shaped nanorod array [274]) had higher sensitivities than the conventional shaped arrays. Therefore, this confirms that geometries with more potential for hotspots are highly suitable for sensing applications.

Table 4.1 Sensitivity comparison of nanopatterns in the literature.

Configuration	Sensitivity (nm/RIU)	Reference
Nanograting	73	[275]
Nanodisks array	116	[276]
Plus shaped rod array	250	[277]
Elliptical nanodisk array	327	[278]
Nanocone array	450	[279]
Nanohole array	481	[280]
Nanoellipsoid array	484	[281]
Triangle nanoarray	541	This work
C shaped nanorod array	600	[272]
Sinusoidal nanograting	717	[273]
Nanocrescent array	879	[274]

4.3 Chapter summary

In this chapter, FEM simulations were used to understand the effect of shape, size, material and surrounding environment on the plasmonic response of nanoparticles and nanoarrays.

For the single nanoparticles, it was observed that aluminium had very low losses in the UV region and interband transitions are at around 870 nm. Hence, a strong plasmonic response was observed in the UV region, and broad peaks were observed near the interband transition region. The sudden change in the response of aluminium leads to an increased rate of dipole and multipole peak shift as compared to other materials. The positioning of the interband transitions in the UV region and low losses make silver the optimal plasmonic material in the visible and NIR region. As a result of the aforementioned reason, silver had the most intense peaks and displayed the highest multipole character among all the materials. Gold and copper showed a similar response; however, the high losses in copper leads to reduced intensity of the peaks as compared to gold. As the size of the nanoparticles was increased, the shape and size factor dominated more than the material. Aluminium and copper displayed good plasmonic response for larger sized particles; therefore, they have the potential to be used as alternatives to gold and silver.

The nanoarrays improve the plasmonic response of the nanoparticles. The geometry and material parameters of nanoarrays on a glass substrate were studied. The coupling effect of the lattice resonance with the single nanostructure resonance was observed for larger sized structures (disk of diameter greater 100 nm). The coupling of the aforementioned resonances resulted in stronger resonance in the transmission spectra. The increase in thickness of the structures led to increased confinement of the EM wave and created higher order poles along with the major dipole response. Aluminium nanoarrays displayed resonance at shorter wavelengths than gold; similar to the nanoparticles, resonance in the UV region was also observed in nanoarrays of aluminium. However, in the visible region, the resonances

were weaker due to increased material losses. The refractive index variation with resonance wavelength (sensitivity) was studied to study the practical use of these nanoarrays. The overlap of the lattice resonance with the single structure resonance was considered the optimal coupling condition. Sensitivity at the coupling condition was the highest. The best sensitivity was observed for the gold triangle nanoarray (541 nm/RIU), which was high compared to conventionally shaped sensing substrates in the literature. Higher sensitivity was observed in the literature for unconventional shapes, such as creset shaped nanoarrays and C shaped nanorods.

This work confirms that nanoarrays of large sizes (diameter greater than 100 nm for applications in the visible region) at the optimal coupling condition are highly suitable for sensing applications. Hence, gold nanodisk arrays of diameter greater than 100 nm were selected to be fabricated using LIL.

Chapter 5. Probing the Plasmonic Response

The simulation results in Chapter 4 assume that the nanostructures are perfect i.e., there are no rough edges, imperfections or any other material defects. However, in experimentally fabricated films and nanostructures, these imperfections are always present. This chapter aims to initially study the effect of roughness on thin gold films. The change in roughness was achieved by introducing a piezoelectric quartz base oscillating at a specific frequency during the gold deposition. Then, it was targeted to enhance the plasmonic response of gold nanodisk arrays by annealing the structures. It was envisioned that annealing would cause a change in the geometric parameters and surface morphology of the nanostructures, leading to stronger resonances.

5.1 Effect of roughness on thin films

The current work presents gold films of various thicknesses (10 nm, 20 nm, 40 nm, 60 nm, and 80 nm) deposited on a glass slide (BK7) under two conditions, with and without an oscillating quartz base. The piezoelectric base oscillated with a frequency of 6 MHz. The presence of the piezoelectric base was expected to change the surface roughness of the resulting gold film, thus affecting its sensing performance. The simultaneous comparison of thickness and roughness on the SPR response of gold films is essential to determine their plasmonic performance.

5.1.1 Experimental and simulation parameters

Gold was thermally evaporated at a rate of 1.5 to 2.0 Å/sec by passing current in Tungsten boats. The samples were glued to a quartz crystal used in thickness monitors vibrating in a fundamental shear mode at approximately 6 MHz as shown in Figure 3.5. Samples without the quartz base were prepared with similar deposition parameters. A second quartz thickness monitor was used to measure the sample thickness. The Kretschmann configuration was selected to observe the SPR response of the gold films. Light was incident on a prism with a gold coated glass slide adhered to it via a refractive index matching oil. The prism assembly was transferred to the UV-Vis spectrometer (Agilent technologies, Cary series) stage, which had a birefringent crystal polarizer to linearly polarize the light incident on the prism. The incident angle was varied from 42.5° to 50.0° for s and p polarized light, and the wavelength range was 350 nm to 1050 nm. The obtained reflectivity spectrum for p polarized light was divided by the s polarized light to suppress the noise of the plot. The roughness of the thin films was characterized using AFM (Bruker Multimode Atomic Force Microscopy). Gwyddion software was used to calculate the RMS roughness of the surfaces.

The simulation methodology in the section 3.2 was used to simulate the gold thin film (Bruggeman Model to calculate effective dielectric constant and TMM calculations for the SPR response). The values of f_i and A that closely represented the experimental reflectance data were 0.25 and 0.5, respectively.

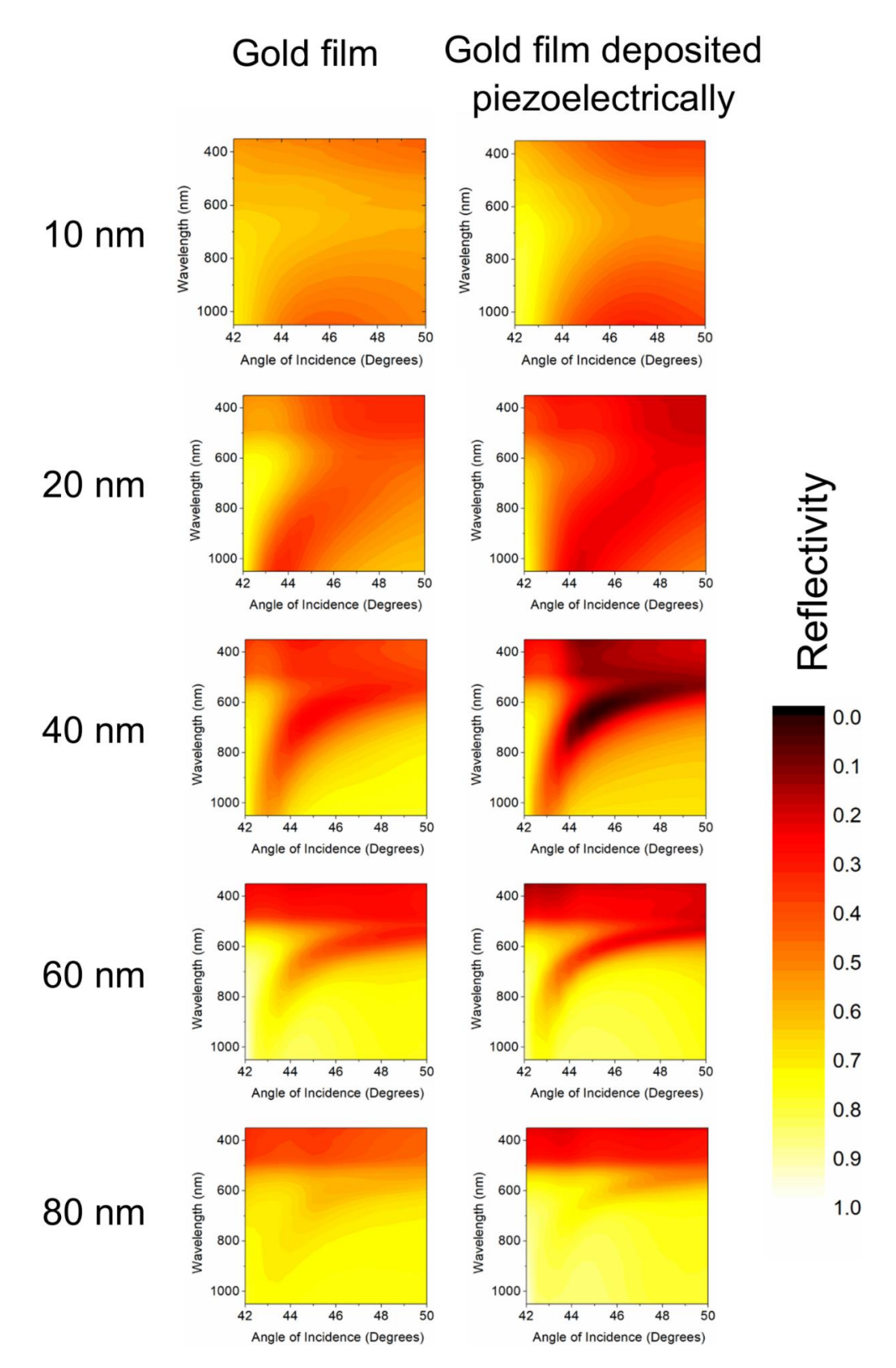


Figure 5.1 Reflectance spectra as a function of angle of incidence of gold films for various thicknesses deposited with and without a quartz base.

The reflectance spectra as a function of angle of incidence for various thicknesses of gold films deposited with and without quartz are shown in Figure 5.1. The plots were calculated using reflectivity plots which are shown in Figure E.1. The dips in reflectivity correspond to the respective SPR wavelengths and incidence angles. A narrow region of low reflectivity indicates a highly sensitive sensing surface due to increased confinement of plasmons [282]. The narrow region can be seen clearly for 40 nm thick films from wavelength 550 nm to 1050 nm. At wavelengths less than 550 nm, the imaginary part of the dielectric of gold is very high; hence, most of the energy is absorbed in this region [283]. Therefore, the optimal performance for a gold film of 40 nm thickness lies in the visible region. Although the 60 nm thick film produced a narrow region of low reflectivity, the dip in reflectivity is not as deep as the 40 nm thick samples. The 10 nm and 20 nm films do not show a sharp dip, and beyond 60 nm, the low reflectivity was barely present, which is in agreement with the literature [284]. For a thickness below 30 nm, the number of charged electrons are too low to absorb the incident energy [129]. Beyond 60 nm thickness, the exponential decay of the evanescent wave prohibits any significant plasmonic response.

Table 5.1 FWHM calculations for 40N, 40Q, 60N and 60Q samples. Where 40N (and 60 N) and 40Q (and 60 Q) are gold films of thickness deposited with and without quartz base, respectively.

	Angle of	FWHM		Angle of	FWHM		
	incidence (°)			incidence (°)			
	44.0	212.48		44.0	199.91		
	44.5	178.26		44.5	165.08		
40N	45.0	153.42	40Q	45.0	143.57		
	45.5	142.67		45.5	129.95		
	46.0	128.43		46.0	124.20		
	44.0	146.35		44.0	112.83		
	44.5	115.71		44.5	91.32		
60N	45.0	103.59	60Q	45.0	81.03		
	45.5	92.54		45.5	68.91		
	46.0	76.48		46.0	71.48		

It is known that mechanical stress, which is due to the oscillation of quartz base in this case, can cause the formation of gold nano islands in thin films [285]. Below 10 nm thickness, these nano islands can create holes in the film [286]; however, beyond 10 nm, the oscillatory motion can cause preferential lateral growth [287]. Hence, the oscillatory motion creates a smoother film for low thickness films. The surface roughness for 40 nm thick films was calculated from the AFM images (Figure 5.2 (c)); it was observed that the RMS surface roughness of the piezoelectrically deposited film (7.3 nm) was much

lower than the film not deposited piezoelectrically (25.5 nm). The 40 nm film piezoelectrically deposited was observed to have a lower reflectivity as shown in Figure 5.2 (a). The full width at half maxima (FWHM) for the reflectivity dip were calculated for 40 nm and 60 nm thick films (shown in Table 5.1); it was inferred that the films deposited with quartz base displayed a smaller FWHM. The slope of the angle and wavelength dependent resonance curve can help determine the SPR sensitivity of the film. The resonance curve was plotted by considering the lowest reflectivity regions in the Figure 5.1. The film of 40 nm thickness piezoelectrically deposited displayed a significant increase in the slope of the resonance curve, as shown in Figure 5.2 (b). Thereby confirming the increased sensitivity of the piezoelectrically deposited film.

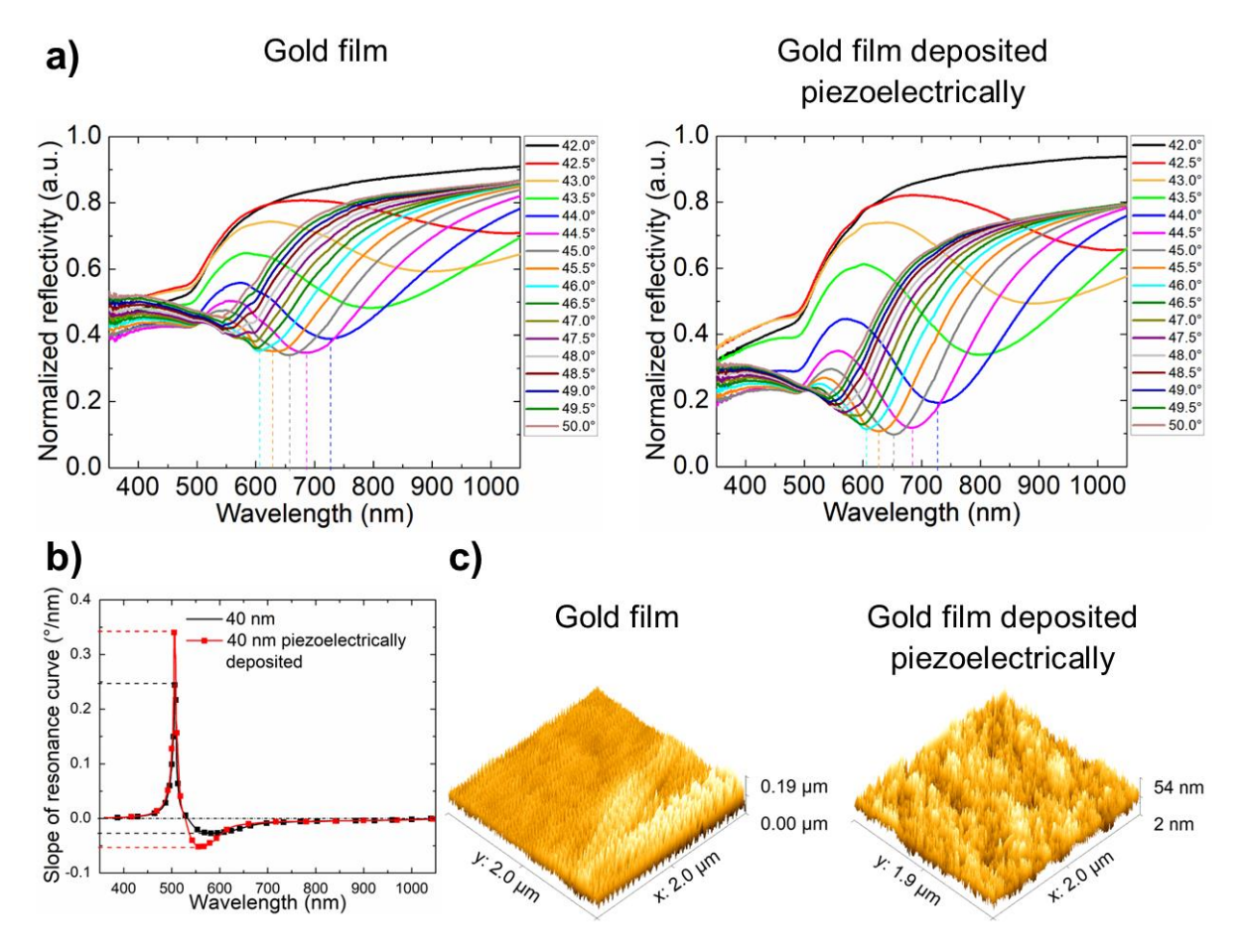


Figure 5.2 a) Experimental normalized reflectivity plots. b) Experimental slope of the angle and wavelength dependent resonance curve and c) AFM images of 40 nm thick gold films deposited with and without a quartz base.

5.1.3 Confirmation using simulation results

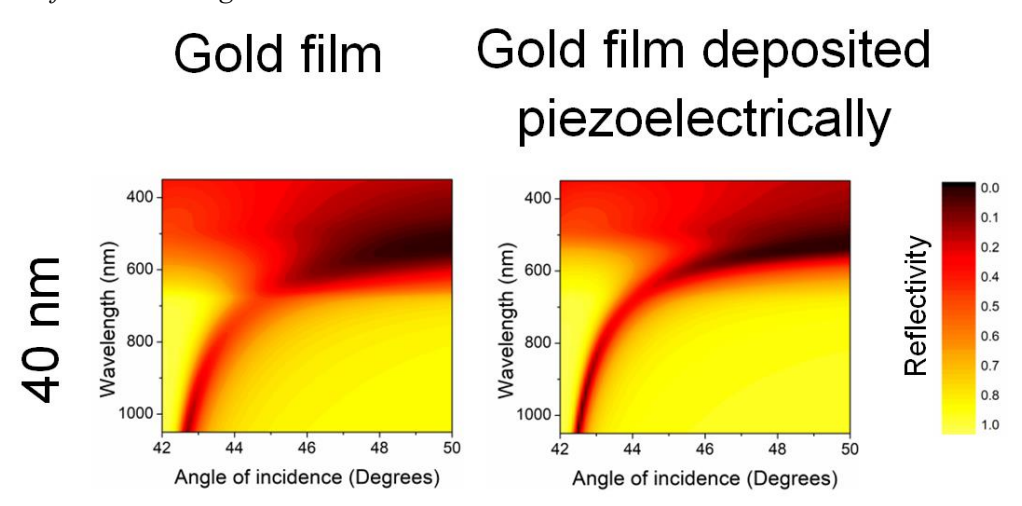


Figure 5.3 TMM calculated reflectance spectra as a function of angle of incidence of gold films for 40 nm thickness gold film with RMS roughness corresponding to the film deposited with and without a piezoelectric base.

To support the experimental data, TMM calculations were performed for 40 nm thickness film was divided into two layers. The thickness of the upper layer was equal to RMS roughness and its refractive index was calculated from Bruggeman effective medium theory. The lower layer was considered as solid gold, the total thickness of the system was 40 nm. The reflectance spectra for various angles of incidence showed that the piezoelectrically deposited gold film had a narrower low reflectivity region, further, the minimum reflectance value was lower as shown in Figure 5.3. There was no significant change in the angle of incidence corresponding to the low reflectivity regions. The observations of the TMM calculations were similar to the experimental data.

5.2 Effect of thermal annealing of gold nanodisk arrays

In this work we report on the fabrication of gold nanodisk arrays on a glass substrate via LIL with different periods and their structural changes following thermal annealing. Subsequently, their plasmonic response was studied by transmission measurements revealing the impact of the structural changes on the optical properties. Although there has been substantial work on LIL nanoarrays, the coupling of the various resonance modes and tuning the resonance wavelength by heating to alter the dimensions and surface morphology of the patterns has not been sufficiently explored. We present a method to improve the coupling effect in gold nanodisk arrays using thermal annealing. The resonances were in visible and NIR regions near commonly used Raman laser wavelengths for potential SERS applications.

5.2.1 Experimental and simulation parameters

The gold nanoarrays were created by LIL method using a Lloyd's mirror setup to create a nanosized structures as explained in section 3.4. A UV laser of wavelength 266 nm with power of 30 mW was incident on BK7 glass substrate 1 mm thick which was spin coated with a negative photoresist. The spin coated substrate was exposed to the laser beam which was reflected off the mirror; hence, the incident and reflected beams interfered. A double exposure, first exposure of 110 s and a second exposure of 110 s after 90° rotation of the sample led to the creation of nanodisks. The sample was developed, and about 40 nm gold was deposited on the substrate via a thermal evaporator. A 5 nm chromium layer was deposited on the substrate prior to the gold deposition for better adhesion with the glass substrate. The gold was lifted off the areas where photoresist was present using ultrasonication in acetone. A period of 400 nm and 500 nm were created by varying the angle at which the laser beam was incident on the Lloyd's mirror calculated by equation 4.1. The transmission spectrum was measured by StellarNet spectrometer on which light was incident via a Halogen and Deuterium source. The images of the gratings and disks were captured by a Zeiss Gemini 500 Field Emission Scanning Electron Microscope (FE-SEM). The atomic force microscopy (AFM) data was acquired using an atomic force microscope (AFM) (Bruker). The grain size of the gold nanodisks was calculated using x-ray diffraction (XRD) measurements (Malvern PANalytical) at an omega angle of 1°. To perform thermal annealing, the samples were placed on a hotplate at 500 °C for the selected time and then cooled in air. The transmission, SEM, AFM, and XRD data were used to compare and understand the change in the optical response of the annealed samples due to changes in the dimensions and morphology of the patterns. The simulation for the nanoarrays was performed on COMSOL software as per section 3.1.3, and the parameters of the Lorentz-Drude model were varied to support the experimental results as explained in section 3.1.1

5.2.2 General impact of annealing

The effects of heat treatment/annealing first the square lattice of gold nanodisks with period 400 nm and 500 nm is considered in Figure 5.4. Figure 5.4 (a) and (e) shows the transmission spectra of the sample at 3 different stages:

- Unannealed (right after lift off process)
- Annealed at 500°C for 10 minutes
- Annealed at 500°C for 20 minutes

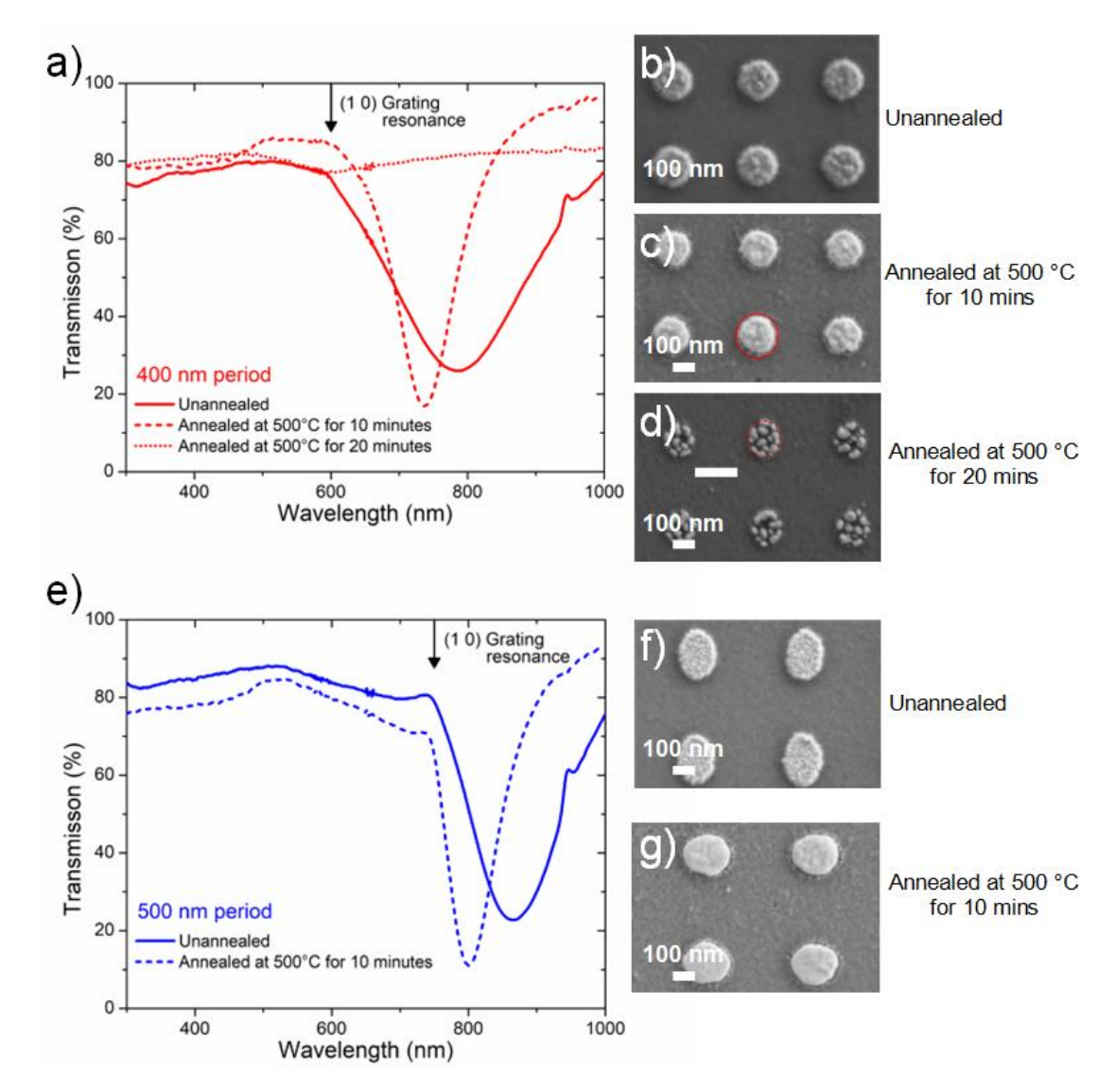


Figure 5.4 a), e) Experimental transmission response of gold nanodisk samples with period 400 nm (red) and 500 nm (blue). SEM images of b), f) unannealed sample (solid line) c), g) sample annealed at 500 °C for 10 minutes (dashed line) (d) sample annealed at 500 °C for 20 minutes (dotted line).

In the first case for 400 nm period nanodisk array, a strong plasmonic resonance dip is observed at 786 nm, which after 10 minutes of annealing (second case) shifts to 736 nm. For the last case only a very shallow and broad valley around 600 nm is observed (easier to see in the detailed view in Figure 5.10 (a)). The shape of the transmission dips of the unannealed sample and the 10 minute annealed sample resemble Lorentzian line shapes, and the FWHM of these resonances amounts to 214 nm and 94 nm, resulting in Q factors of 3.6 and 7.8, respectively. This increase in Q factor after annealing already demonstrates that the annealing at 500°C for 10 minutes leads to a reduction in losses, which is in agreement with the results reported in the literature earlier [288]. A similar increase in Q factor from 6.2 to 11.5 was seen when the 500 nm period sample was annealed for 10 minutes.

Observing the SEM images in Figure 5.4 b) and c) (for 400 nm period) and f) and g) (for 500 nm period) supports the argument that the heat treatment leads to a reduction in surface roughness. The nanoscopic roughness on top of the disk at the unannealed sample was significantly reduced after 10 minutes of annealing.

For circular cylinders/disks of a fixed volume, the minimum surface is obtained when the disk diameter matches the disk thickness. Indeed, a tendency of this form change can already be observed in the sample annealed for 10 minutes. Evaluating the size of the 400 nm period nanodisks from the SEM images in Figure 5.4 (b) and (c) a reduction of disk diameter after annealing is obvious. The reduction is represented by the transition of the diameter of the disk from the solid line to the dotted line in Figure 5.4 (c). While the unannealed disks have an average diameter of 187 nm, the diameter is reduced by 16.5 % to 156 nm after 10 minutes annealing at 500°C. In a similar way, the diameter of the disks in the array with period of 500 nm decreases from initially 220 nm by 12.3 % to a diameter of 193 nm after 10 minutes of annealing as shown in Figure 5.4 (f) and (g). AFM measurements of the same samples confirm these lateral size reductions, and further show that the thickness of the disks increases after the annealing on average by 6.4 nm from 47.7 nm to 54.1 nm for the sample with 400 nm period and by 9.6 nm from 37.1 nm to 46.6 nm for the sample with 500 nm period (Figure 5.5 (a)). The full AFM images are shown in Figure 5.6. This supports the idea of a rearrangement of the gold atoms to reduce the overall surface of the disks. So, gold atoms are effectively removed from the outer rim of the disks and pile up at the top of the disks, reducing the disks' diameter and increasing their thickness. However, the removal of the gold at the outer diameter is not complete. Since the adhesion (promoted by the chromium) seems to be strong, a few gold atoms remain at their original place, resulting in a ring of very small remaining spherical gold particles surrounding the annealed disks (see space between solid and dashed circles in Figure 5.4 (c)) and hinting at the original extend of the disks before annealing. Hence, annealing at 500 °C caused a decrease in the diameter of the disks, increase in the thickness, and decreasing the surface roughness. This smoothening process is basically driven by the disks' tendency to reduce their surface energy by assuming their minimum surface area and trying to conglomerate into a sphere. The mobility of the gold surface atoms at elevated temperatures is strongly increased due to their lower activation energy [289, 290]. Hence, annealing enabled the gold atoms to diffuse into their lowest energy state, reducing the overall surface area of the gold disk and thereby smoothening the gold surface. The reduced surface roughness then leads to less light scattering in the transmission measurements, reducing the radiation losses and resulting in the increased Q factor resonance for the sample annealed for 10 minutes. In addition, the annealing also leads to a growth of the gold grains in the polycrystalline gold disks, as shown in the XRD measurements in the Figure 5.6 (b). The grain size of the samples increased from 20.4 nm to 23.4 nm after annealing for 10 minutes. The increase in grain size reduces interface scattering/damping of the oscillating electrons at the grain boundaries, supporting a longer lifetime of the local plasmon oscillation. This leads to a reduction of intrinsic (ohmic) losses in the gold and contributes to the increase of the Q factor.

The drive to lower surface energy should ultimately lead to the formation of a gold sphere out of the deposited gold disk (or rather, a hemisphere if the strong bonding to the substrate is taken into account). However, the extension of the annealing time has however a rather detrimental effect on the overall structure. The disks disintegrate into a collection of individual small round gold particles of varying sizes separated by small gaps of a few nanometers width (Figure 5.4 (d)). This agglomeration of much smaller gold particles also has a reduced thickness, which hints to increased loss of gold during extended annealing at high temperatures maybe by evaporation or diffusion into the substrate. In addition, the plasmonic response of the structure changes dramatically, so that the strong plasmonic resonance is effectively destroyed.

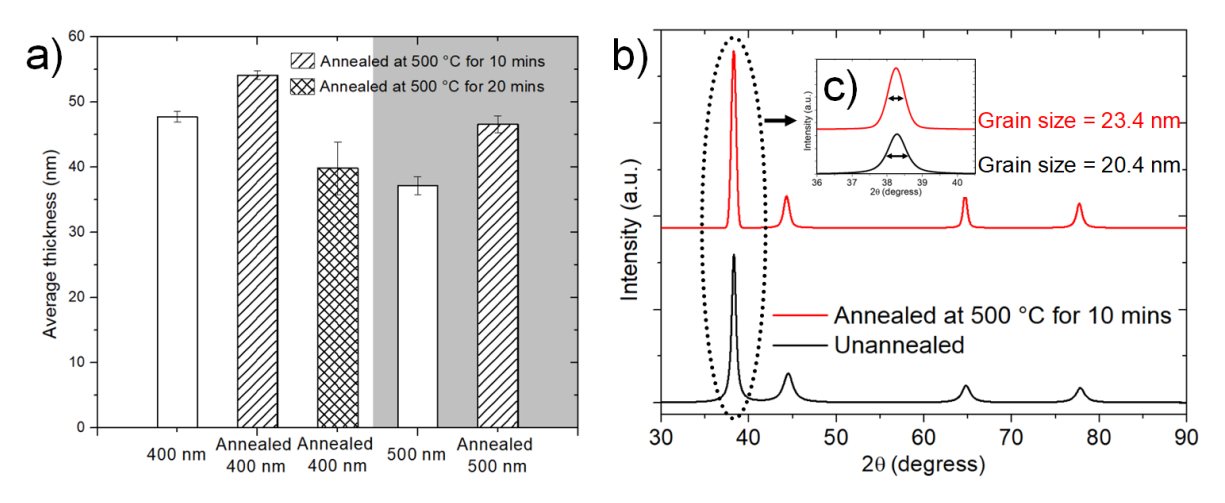


Figure 5.5 a) Average thickness for 400 nm and 500 nm period unannealed and samples annealed at 500 °C for 10 and 20 minutes. The error bars represent the standard error of the peak thickness. b) XRD measurements of 400 nm period sample (unannealed and annealed at 500 °C for 10 minutes). The inset shows the measurements for the main peak with an increased acquisition time which was used to calculate the grain size.

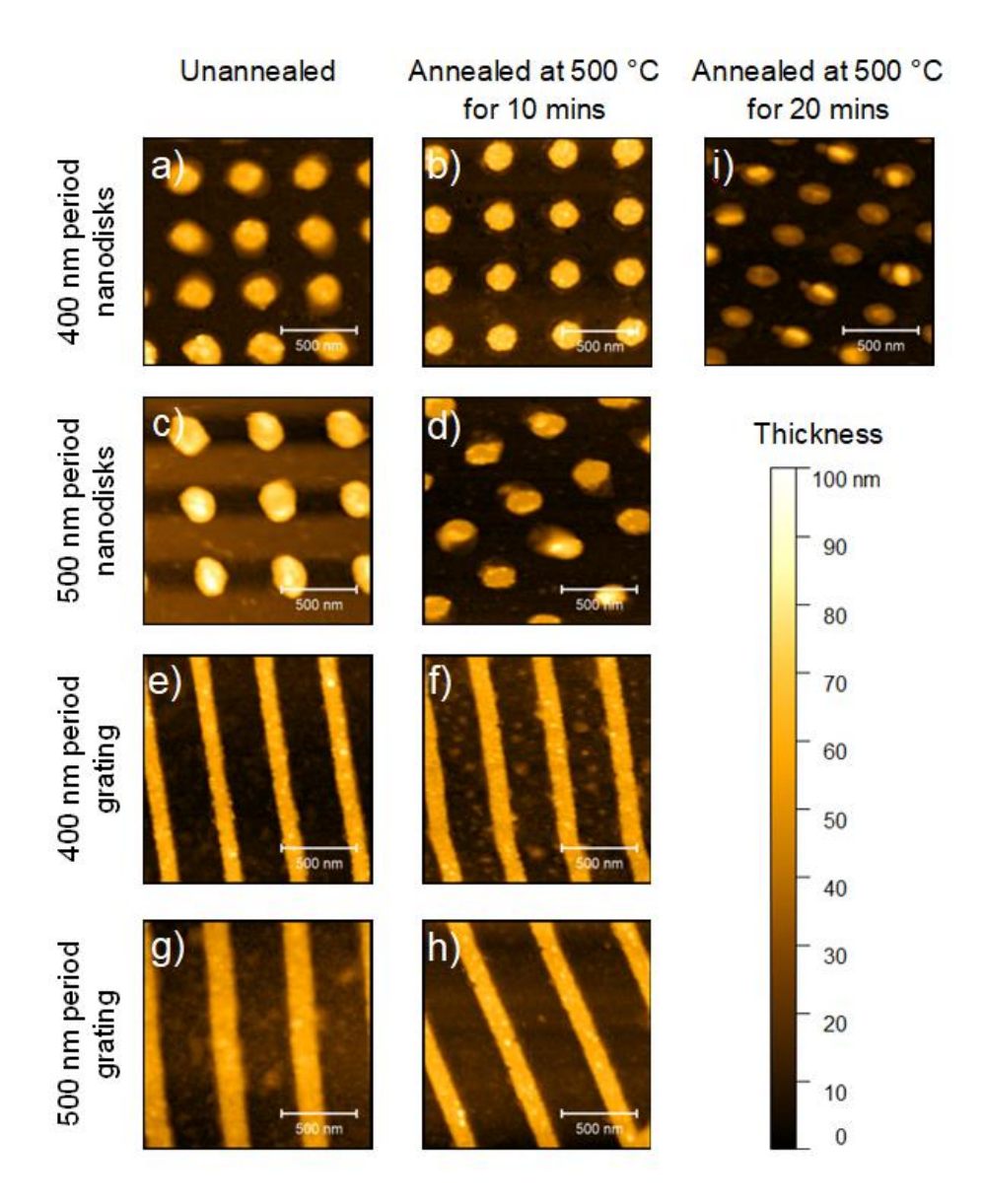


Figure 5.6 AFM images of gold nanodisk samples with a) period 400 nm and c) 500 nm samples unannealed. Nanodisk samples with b) period 400 nm and d) 500 nm samples annealed at 500 °C for 10 minutes. Nanograting samples with e) period 400 nm and g) 500 nm samples unannealed. Nanograting samples with f) period 400 nm and h) 500 nm samples annealed at 500 °C for 10 minutes. i) AFM images of gold nanodisk sample of 400 nm period annealed at 500 °C for 20 minutes.

In the following formation, spectral shift and structural dependence of the plasmonic resonances in the unannealed and annealed sample structures are investigated in more detail and compared with FEM simulations. First, the strong plasmonic resonances appearing in the unannealed and 10 minutes annealed structures are discussed. Afterwards, the plasmonic response of the disintegrated disks (20 minutes annealed) is investigated in more detail.

5.2.3 Plasmonic resonances in unannealed and 10 minute annealed samples in detail

To understand the formation of the observed strong plasmonic resonances in the array of gold disks, lets first consider the local plasmonic dipole resonances of a single isolated disks. Figure 5.7 (a) shows the extinction spectra for single gold cylinders with the same dimensions as they also appear in the periodic arrays: 187 nm diameter and 220 nm for unannealed case (solid lines) and 156 nm and 191 nm for the annealed case (broken lines). Reducing the diameter of the nanodisk from 187 nm to 156 nm (and enlarging the thickness from 47.7 nm to 54.1 nm) due to annealing leads to a blue shift of the single particle resonance from $\lambda_D = 945$ nm to $\lambda_D = 839$ nm as shown by the transition from broad to a narrow extinction peak in the red curves in Figure 5.7 (a). Similar blue shift of the resonance was also observed when the size of the nanoparticles was reduced in the simulation plot of Figure 4.3 in section 4.1. The reduction of diameter from 220 nm to 191 nm results in a resonance blue shift from $\lambda_D = 1010$ nm to λ_D = 945 nm (blue curves in Figure 5.7 (a)). Overall, this demonstrates that the resonance wavelength of the single disks is crucially dependent on their diameter with larger diameters leading to longer resonance wavelengths. This can be intuitively explained in the following way: an increased disk diameter leads to a lower surface charge density, which is due to a weaker restoring force of the oscillating dipole and, hence, a decreased resonance frequency [251, 252]. Furthermore, the increased size also causes higher radiation damping that increases the full width at half maxima (FWHM) of the dipole resonance [253].

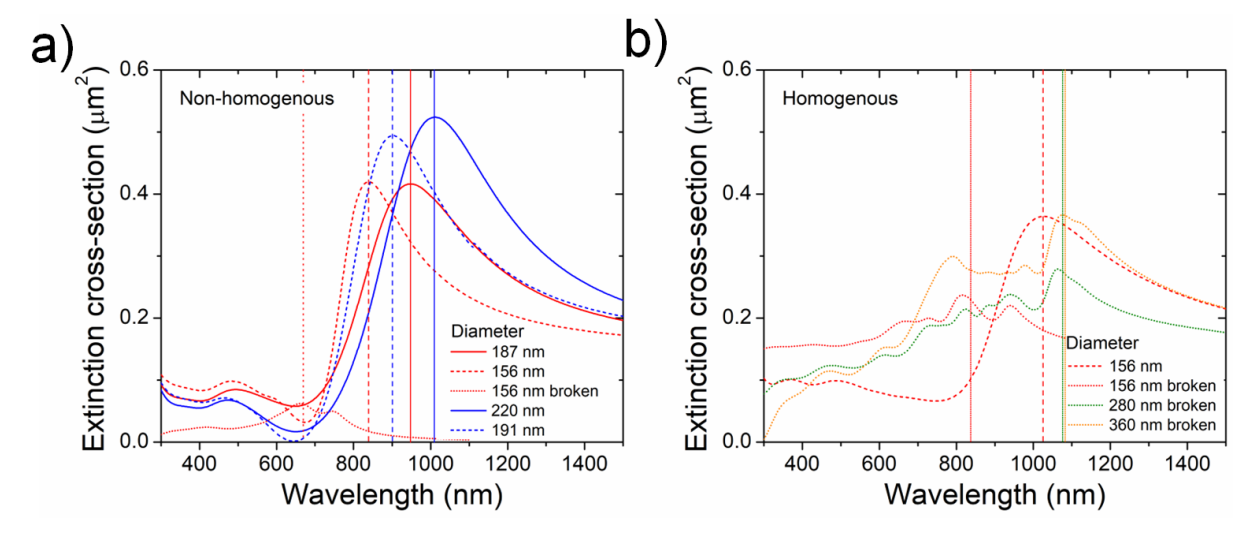


Figure 5.7 Simulated extinction cross-section spectrum for a) single gold nanodisk of dimeter 187 nm, 156 nm, and 156 nm broken (corresponding to unannealed and 10 min and 20 min annealed samples of 400 nm period), and 220 and 191 nm (corresponding to unannealed and 10 min annealed samples of 500 nm period) in non-homogenous medium (gold disk at air (n = 1) glass (n = 1.5) interface). a) Single gold nanodisk of 156 nm, 156 nm broken (corresponding to 10 min and 20 min annealed samples of 400 nm period), and broken structures with outer boundary of diameter 280 nm and 360 nm in homogenous medium (n = 1.5). The vertical lines represent the respective single disc resonances.

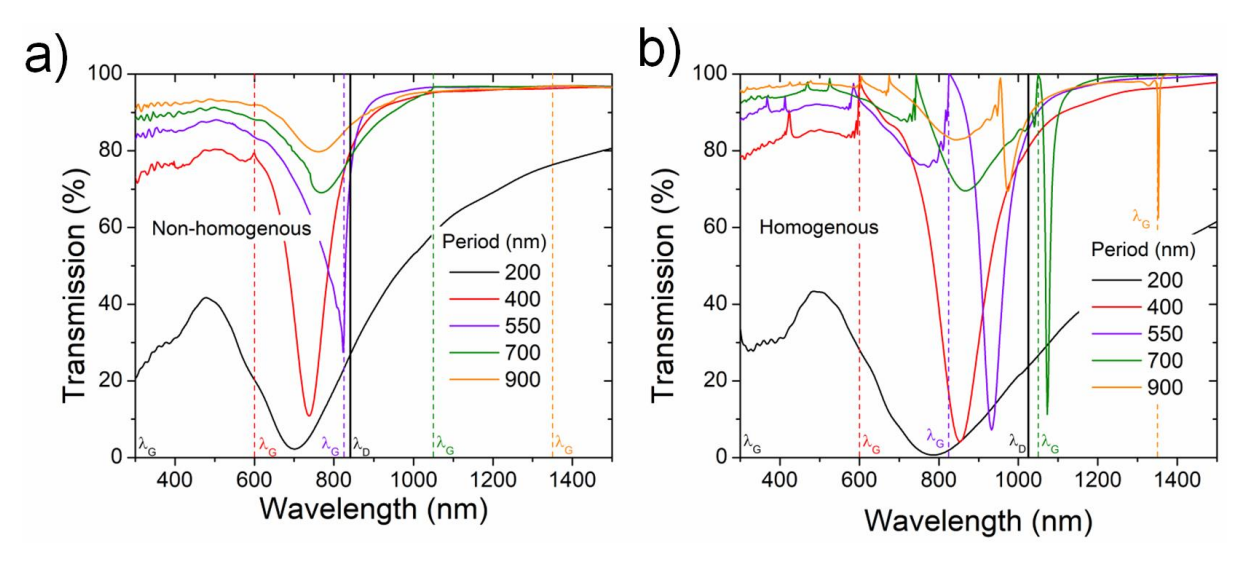


Figure 5.8 Effect of variation of period on the simulated transmission spectra of a nanodisk array (disk diameter 156 nm and thickness 54.1). The nanodisks were placed in a) non-homogenous medium (air (n = 1) glass (n = 1.5) interface and b) homogenous medium (oil (n = 1.5) glass (n = 1.5) interface). λ_D and λ_G represent the single particle resonance and (1 0) grating resonance. The solid vertical lines are the single particle resonance and dashed vertical lines are (1 0) grating resonances.

Arranging disks of the same size now in a periodic pattern adds an additional grating resonance to the picture and the optical response of the overall structure is determined by the interplay between this grating resonance, λ_G , with the individual disk resonance (single particle resonance), λ_D . The grating resonance occurs just at wavelengths slightly larger than the Woods anomaly, which is defined as the wavelength, where the first propagating diffraction order just vanishes i.e. when (for normal incidence) the period p of the grating is equal to the wavelength [265]:

$$\lambda_G = n p$$
 6.1

where λ_G represents the resonance wavelength, n is the refractive index of the surroundings, and p is the periodicity of the lattice. Since each disk can be modelled as an oscillating plasmonic dipole [291], each disk acts as a source of a scattered wave, which interacts with the neighbouring disks. If the primary incident wave and the scattered wave of the neighbouring disks are in phase (which is the case when the disks are about a wavelength apart), an effective increase in the field driving the plasmonic oscillation of the disk under consideration can be created leading to an overall enhanced plasmonic resonance [266]. For relatively sparse square 2D arrays, where small metal particles with single particle resonances in the visible wavelength range are arranged in relatively large periods, the (1 0) grating resonance wavelength λ_G is shifted to the red or even IR and occurs on the long wavelength side of the single particle resonance ($\lambda_G > \lambda_D$). In this case, the interplay of the resonances leads to very sharp Fanotype resonances of high Q factors in a homogeneous medium [141, 142]. However, for a non-homogenous medium (where the refractive index of the surrounding medium and substrate is different),

the resonance for the case where $\lambda_G < \lambda_D$ is not very strong. This is studied using FEM simulation transmission spectra of nanodisk arrays with varying periods in Figure 5.8 (a) and (b). In the case where the medium is homogenous, sharp resonances are seen when $\lambda_G > \lambda_D$, also reported by Auguie´ and Barnes [292]. However, in the case of a non-homogenous medium, the sharp resonance is observed when $\lambda_G \approx \lambda_D$, but it drastically weakens when $\lambda_G > \lambda_D$ due to inhomogeneity causing diminished coupling. When however, the period is reduced or the size of the particles is enlarged, where the grating resonance occurs at the short wavelength side of the single particle resonance, $\lambda_G < \lambda_D$ can occur. Although, in this case the combined resonance is usually not as strong and the Q factors are also lower in a homogenous medium. Moreover, in a non-homogenous medium, the decay rate of the resonance due to the disparity between λ_G and λ_D (when $\lambda_G < \lambda_D$) is much lower as compared to the case when $\lambda_G > \lambda_D$. In our samples with periods of 400 nm and 500 nm, the major dip in the transmission spectrum is for a non-homogenous medium and $\lambda_G < \lambda_D$. The sharpest resonance is achieved for the nanodisk array in a non-homogenous medium when $\lambda_G > \lambda_D$.

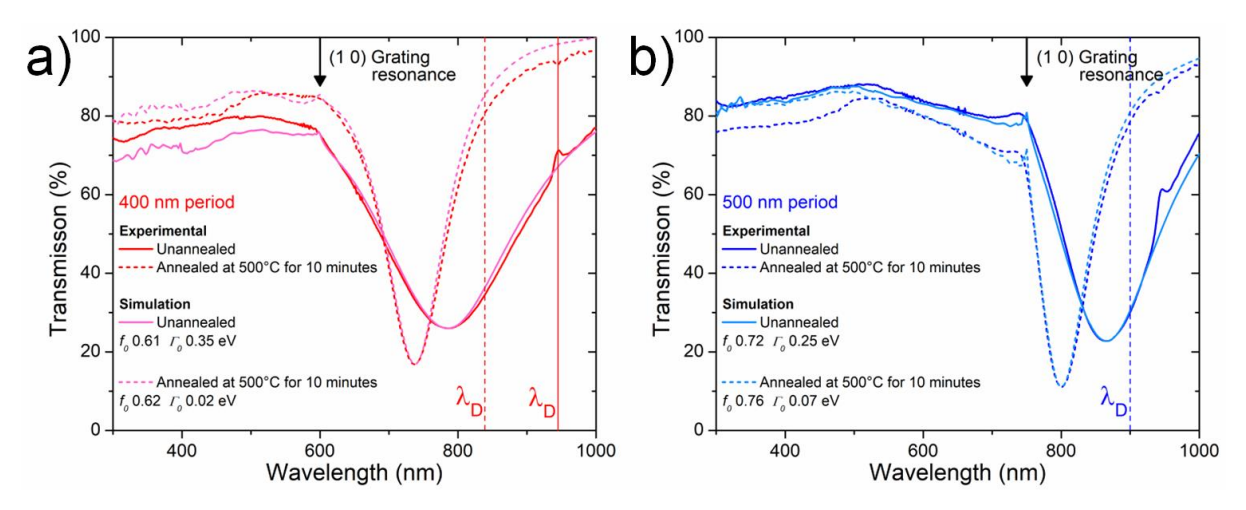


Figure 5.9 Experimental and FEM simulation transmission response of gold nanodisk arrays with period a) 400 nm (red lines) and b) 500 nm (blue lines) when they are unannealed (solid lines) and annealed at 500 °C for 10 minutes (dashed lines). The solid and dashed vertical lines are the single particle resonances for unannealed and annealed samples, respectively.

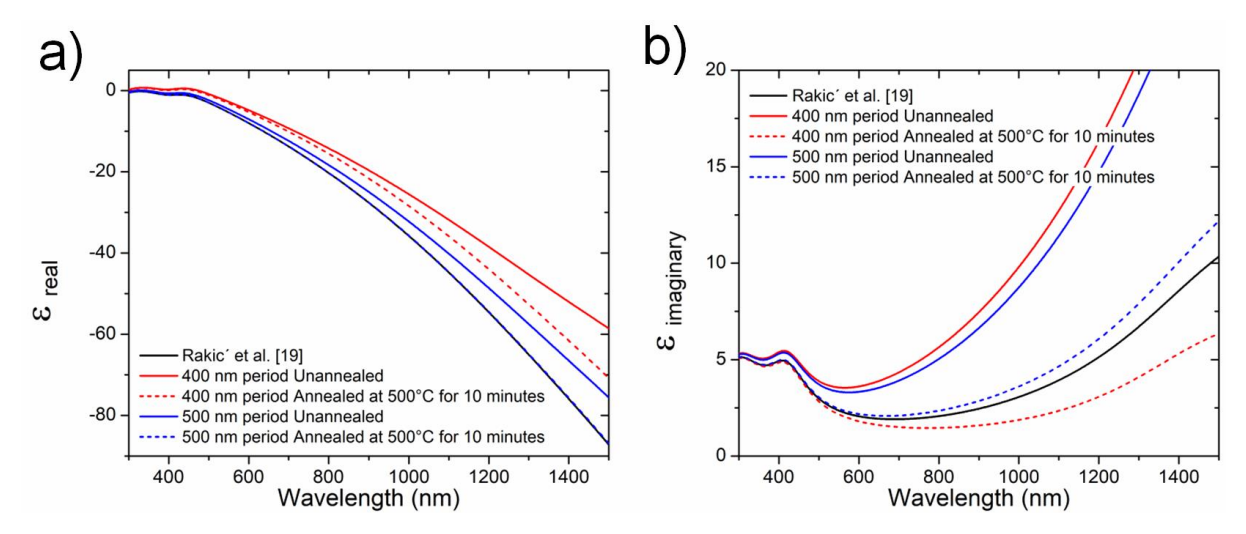


Figure 5.10 a) Real and b) imaginary part of dielectric function of gold used in simulation of the unannealed and 10 minute annealed samples with corresponding modified Lorentz-Drude parameters listed in Figure 5.9.

Figure 5.9 quantifies the effect of annealing on the plasmonic response of the gold nanodisk arrays. As explained previously, annealing causes a decrease in the diameter, increase in thickness, smoothening of the surface and increase in grain size of the nanodisks. The change in geometric parameters causes λ_D to decrease from 945 nm to 839 nm for the 400 nm period sample ($\lambda_G = 600$ nm) and from 1010 to 900 nm for the 500 nm period sample ($\lambda_G = 750$ nm). Thereby, decreasing the discrepancy between λ_D and λ_G . As previously explained, this causes a decrease in the FWHM and increase in Q factor of the resonance. The Q factor increases from 3.6 to 7.8 for 400 nm period sample and from 3.2 to 11.5 for the 500 nm period sample. Now, to include the effect of roughness and material properties of the nanodisks, the major parameters in the Lorentz-Drude model (f_0 and Γ_0) were adjusted in FEM simulations to match the experimental curves which is shown in Figure 5.9. The resonance wavelength and FWHM is controlled by f_0 and Γ_0 , respectively. The Lorentz-Drude model parameters used for the annealed and unannealed samples are also reported in Figure 5.9. The optical losses in annealed samples have drastically been reduced which can be clearly seen by the lowering of the damping constant (Γ_0) from 0.35 to 0.02 for the 400 nm period sample and from 0.25 to 0.07 for the 500 nm period sample. Furthermore, an increase in the oscillator strength (f_0) confirms that a stronger plasmonic response is displayed from the material in annealed state. Since the geometric parameters were accounted for in the FEM calculations, the improvement in the optical response not considering the geometric parameters is due to a combination of smoother surfaces and increased grain size of the annealed gold nanodisks. Both these factors were targeted to include in the new dielectric functions. The modified dielectric function of the unannealed and samples annealed for 10 minutes along with the comparison with dielectric function reported by Rakic' et al. [203] is shown in Figure 5.10. The large decrease in losses due to annealing can be clearly observed in the imaginary part of the dielectric function. The curves of the real part of the dielectric function showed a steeper slope for the annealed samples, confirming their stronger plasmonic response. Furthermore, for both the real and imaginary part of the dielectric function, the curves of the annealed samples move closer to the curve of Rakic' et al. [203] which is widely used in the literature to simulate the plasmonic response of gold structures. Hence, thermal annealing for shorter time led to smoother structures and increased grain size leading to stronger resonances due to increased coupling effect between λ_G and λ_G .

5.2.4 Plasmonic resonances in unannealed and 20 minute annealed samples in detail

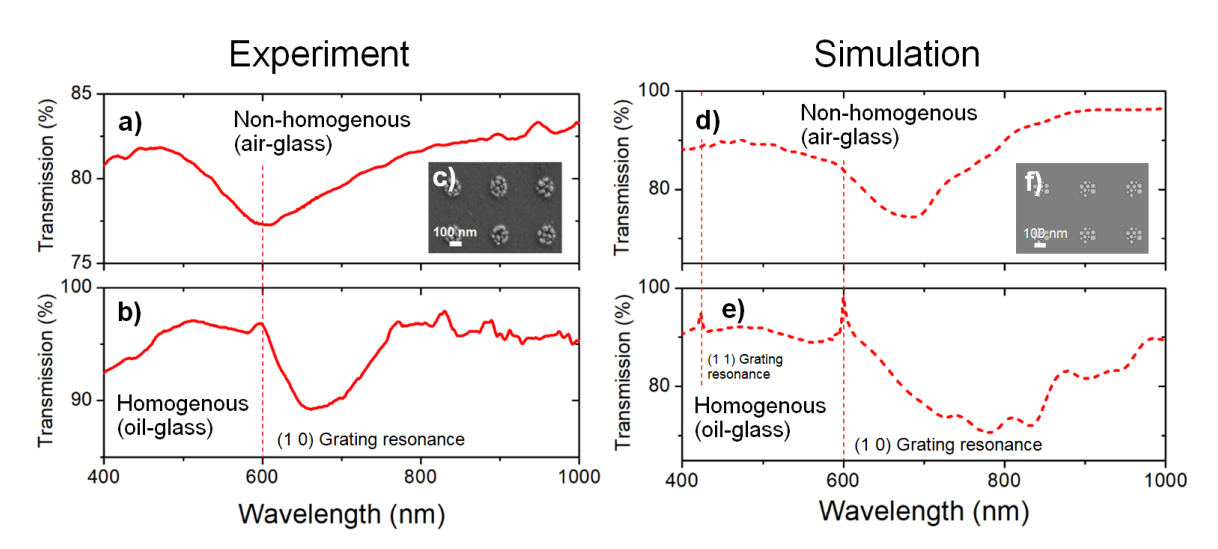


Figure 5.11 (a, b) Experimental (solid lines) and (d, e) FEM simulation (dashed lines) transmission response of gold nanodisk arrays with period 400 nm when they are annealed at 500 °C for 20 minutes. a) and d) is the transmission spectra in a non-homogenous medium, the nanodisks are placed in air (n = 1) and glass (n = 1.5) interface. b) and e) is the transmission spectra in a homogeneous medium, the nanodisks are placed in oil (n = 1.5) and glass (n = 1.5) interface. c) SEM image of the broken nanodisk array. f) Geometry of the broken nanodisks used for the FEM simulations.

Although annealing for 10 minutes improved the plasmonic response of the nanodisks, but the condition of the sharpest resonance ($\lambda_G \approx \lambda_D$) was not achieved for the non-homogeneous case. Therefore, annealing for additional time was performed. However, it was observed that the nanodisks disintegrated into several smaller disks of varied sizes while maintaining its periodicity. Annealing at high temperatures and/or long time leads to the destruction of the shape and material loss in nanostructures [169, 293]. Additionally, a very weak plasmonic dip was observed at around 600 nm, as shown in Figure 5.11 (a).

To understand the response, simulations were performed by recreating the small disks using the SEM and AFM data, the geometry of which is shown in Figure 5.11 (f). Both experimental and simulation transmission spectra of the broken disks showed the absence of the Fano like (1 0) grating resonance expected at 600 nm (λ_G) (Figure 5.11 (a) and (d)). To confirm the absence of the effect of the λ_G

resonance, transmission measurements were performed by surrounding the gold nanodisk pattern by refractive index matching oil which had n=1.5 (similar to the glass substrate). The transmission measurements, both in experimental and simulation spectra confirmed that in a homogenous medium, the λ_G resonance was present at 600 nm for (1 0) grating resonance due to stronger coupling. Additionally, the simulation spectra also showed a Fano like resonance at 424 nm for the (1 1) grating resonance. Figure 5.8 (a) also shows the absence of the effect of the λ_G resonance when a small disk in a lattice with very large period was placed in a non-homogenous environment, but, clear resonances were seen in the homogenous medium. However, the resonance for the broken disk sample in a homogenous medium was still not as strong as observed for the case of small disk in a large period, as seen in the Figure 5.8 (b). It was seen that the single particle resonance (λ_D) for the broken disk structure was at about 669 nm for non-homogenous medium and 835 nm for homogenous medium (Figure 5.7). Although it was closer to λ_G as compared to 10 minute annealed sample, it was still in the condition of $\lambda_G < \lambda_D$. Thereby, the weak resonance of the broken disk was due to the lower size of the smaller nanodisks while still being in the condition of $\lambda_G < \lambda_D$.

The limitation of the LIL technique is that the diameter to period ratio of the fabricated nanodisks is always close to 0.5. It was shown in the current article that annealing for 10 minutes could reduce the ratio only to 0.4, which upholds the condition $\lambda_G < \lambda_D$. To achieve the condition of $\lambda_D < \lambda_G$, simulations were performed for a very small disk of diameter 34 nm (average of the diameter of the broken structures) in a 400 nm period which are shown in Figure 5.12. However, λ_D was 672 nm for the single disk in a homogenous medium and still the condition $\lambda_G < \lambda_D$ was maintained. Therefore, sharp resonance was still not seen in the transmission spectra for the aforementioned disk in a 400 nm period lattice (Figure 5.12 (b)). Upon annealing for longer duration, the nanodisks disintegrated in smaller pieces (which is also reported in the literature [169, 293]). The disintegrated nanodisk structures in larger periods had the potential to achieve sharp resonances by fulfilling the condition ($\lambda_D < \lambda_G$). To analyse this hypothesis, simulations were performed for broken structures similar to Figure 5.11 (f). However, the ratio of the diameter (of boundary of the broken pieces) to period was kept 0.4, the number of pieces were increased keeping the size of the pieces similar to Figure 5.11 (f). The simulation geometry can be seen in the inset of Figure 5.13 (b). Figure 5.13 also shows the simulated transmission plots of 700 nm and 900 nm period nanodisk arrays with unbroken disks (Figure 5.13 (a), diameter to period ratio of 0.4) and corresponding broken disc arrays, both were in a homogenous (n = 1.5). The λ_G of 700 nm and 900 nm period was 1050 nm and 1350 nm, respectively. As previously seen for the 400 nm and 500 nm period nanoarrays, the unbroken disks of periods 700 nm and 900 nm have broad resonances (due to $\lambda_G < \lambda_D$) as shown in Figure 5.13 (a). However, replicating the structures achieved after annealing for long duration, broken disc structures show sharp resonances in Figure 5.13 (b) (especially for 900 nm period). This response was explained using the simulation response of the single structures in Figure 5.7 (b). The λ_D for the broken structures with outer boundary diameter 280 nm (corresponding to diameter to period ratio of 0.4 for period 700 nm) and 360 nm (corresponding to

diameter to period ratio of 0.4 for period 900 nm) was at 1176 nm and 1183 nm, respectively. Hence, for 700 nm period, the condition $\lambda_G \approx \lambda_D$ created a sharp resonance, and for 900 nm period, the condition $\lambda_G > \lambda_D$ created an even sharper resonance. The Q factor of the unbroken discs of period 700 nm and 900 nm was 7.2 and 8.6, respectively. The Q factor was increased significantly for broken discs of period 700 nm and 900 nm to 38 and 260, respectively. Keeping the ratio of the diameter of the outer boundary to period as 0.4, the λ_D increase when the period was increased from 700 nm to 900 nm was lower because of the small size of the individual broken pieces being maintained. Therefore, for smaller periods (400 nm and 500 nm) the size of the small individual nanodisks was not sufficient to create the condition $\lambda_G > \lambda_D$, however, increasing the period fulfilled this condition. Hence, the phenomenon of thermal annealed for longer time/duration could be used to create sharper resonances (condition $\lambda_G > \lambda_D$) in nanoarrays which are fabricated by techniques where the diameter to period ratio is fixed.

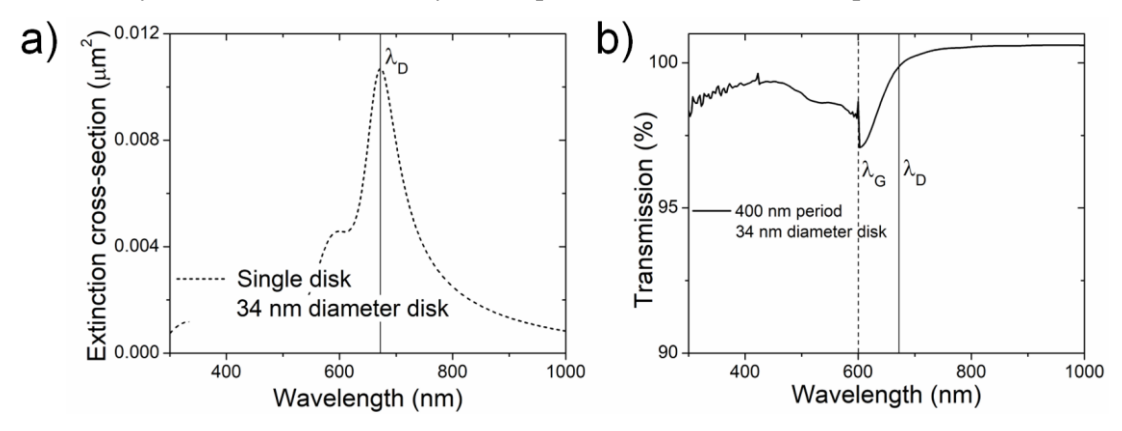


Figure 5.12 a) Simulated extinction cross-section spectrum for single gold nanodisk of diameter 34 nm and height 39 nm. b) Simulated transmission spectra of the nanodisk placed in an array of period 400 nm. Both are in a homogenous medium (n = 1.5). The solid vertical lines are the single particle resonance and dashed vertical lines are (1 0) grating resonances.

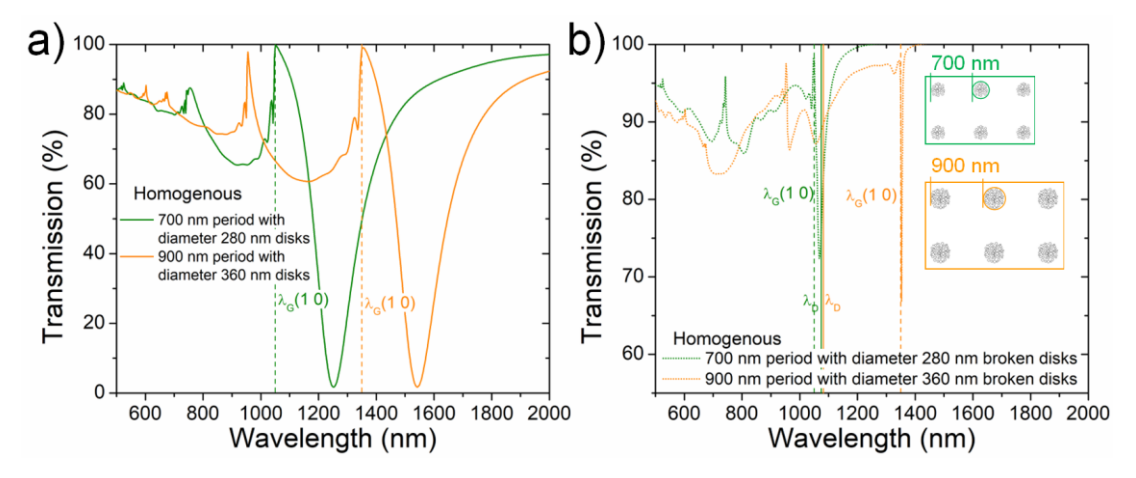


Figure 5.13 Simulation transmission response of gold nanodisk array with a) unbroken discs (solid lines) and b) broken discs (dotted lines) of period 700 nm (green) and 900 nm (orange) in a homogenous medium of n = 1.5. The solid vertical lines are the single particle resonance and dashed vertical lines are (1 0) grating resonances.

5.3 Chapter summary

The SPR response of gold films of various thicknesses deposited with and without an oscillating quartz base were compared. The presence of the piezoelectric base resulted in gold films of lower surface roughness. The 40 nm thick film had the highest plasmonic response. A sharper SPR response was established by the lower FWHM of the SPR peak near the optimal angle of incidence (45.5°) and increased slope of the angle and wavelength dependent resonance curve of the piezoelectrically deposited film of thickness 40 nm compared to its counterpart. The experimental claims were supported by TMM calculations. This work confirmed that smoother gold films have a stronger and sharper plasmonic response for enhanced sensing.

The smoothening effect for enhanced plasmonic response was expanded to gold nanodisk arrays fabricated on a glass substrate using the LIL method. Annealing was performed by placing the samples on a hot plate at 500 °C for 10 minutes and 20 minutes and then cooling them in air. The annealing was effective in changing the shape and the morphology of the samples. Annealing for 10 minutes caused the gold to conglomerate and decrease the diameter of the nanodisks and increase their thickness. Furthermore, a decrease in surface roughness and increase in grain size was observed for the annealed samples. The transmission response of the nanoarrays comprised of a single particle resonance (λ_D) and grating resonance (λ_G). The grating resonance was dependent on the period of the nanoarray and the single particle disk resonance was dependent on the diameter and thickness of the disks. The proximity of the aforementioned resonances created a coupling effect which led to a sharp and intense transmission dip. For the nanodisks, annealing the samples for 10 minutes decreased discrepancy between λ_G and λ_G , thus improving the Q factor along with increasing the magnitude of the transmission dip. The improvement in the material properties and roughness due to annealing were quantified by the decrease in the damping constant and increase in oscillator strength used in the Lorentz-Drude model for the annealed sample to match the experimental plots. However, the samples were still in the condition of $\lambda_G < \lambda_D$. The limitation of LIL is that the diameter to period ratio even after annealing was about 0.4. To achieve sharper resonances using the condition $\lambda_D < \lambda_G$, annealing was performed for 20 minutes which led to disintegration of the nanodisk into several smaller sized disks. A very small transmission dip was observed in the transmission spectra due to the small size and $\lambda_G < \lambda_D$ condition for 400 nm and 500 nm period samples. However, simulating the response for larger periods of the broken nanodisk arrays (keeping diameter of the boundary of the broken structures to period ratio as 0.4), the condition $\lambda_D < \lambda_G$ was achieved. A 30.2 times increase in Q factor was achieved for the simulated annealed (broken discs) nanoarray compared to the unannealed (unbroken discs) nanoarrays of period 900 nm.

Therefore, annealing the gold nanodisks for 10 minutes led to a strong and sharp resonance due to decrease in diameter and increase in thickness of the nanodisks which decreased the difference between λ_D and λ_G . Lower roughness and increased of the grain size also contributed to the improved response. Annealing for longer duration disintegrated the nanodisks which could lead to even sharper resonances because the condition $\lambda_D < \lambda_G$ was satisfied.

Chapter 6. Gold Nanodisk Arrays: A Promising Platform for Enhanced Agrochemical Detection

This chapter presents the application of the nanodisk array fabricated using LIL method explained in section 3.4. Samples of varying periods were fabricated and the optimized sample with the highest Raman enhancement was selected. The use of the optimized sample was confirmed by detecting the fertilizer urea. The application of the optimized sample was envisioned to be various types of agrochemicals. However, the Raman spectrum of most of these agrochemicals was not available. Therefore, DFT was used to calculate the Raman spectra and it was compared with experiments to assign vibrational modes to the agrochemical molecules. Initially, the structural study and vibrational mode assignment was performed for the weedicide Metribuzin. The basis set comparison using the B3LYP level of theory was analysed for Metribuzin to select the basis set with good accuracy and low computational cost. Finally, the vibrational mode assignment was performed for all the selected agrochemicals. The optimized LIL substrate was used to check the limit of detection (LOD) of the agrochemicals.

6.1 Selection of the optimal SERS substrate

In the current work, an optimal SERS substrate was selected among gold nanodisk arrays of various periods. Gold nanodisk arrays were fabricated on glass substrates with periods 250 nm, 300 nm, 344 nm, 395 nm, and 446 nm. The period to diameter ratio of the nanodisk arrays was close to 2.2. The Raman signal of the nanodisks was compared using Raman active dye Rhodamine 6G. Further, to understand the optical response of the nanodisks, transmission spectra were analysed experimentally and using finite element method (FEM) simulations. The practical use of the nanodisks was confirmed by selecting the optimized nanodisk array as a SERS substrate to detect urea in water.

6.1.1 Experimental and simulation parameters

A brief description of the LIL process used for the fabrication of the gold nanodisks is discussed in section 3.4. The substrate was square shaped BK7 glass with an of area 25 mm² and thickness of 1 mm. A thin layer of adhesion promoter (Allresist AR 300-80) was applied on the RCA cleaned glass substrate by spin coating at 500 rpm for 15 seconds and 4000 rpm for 90 seconds and curing at 180 °C for 3 minutes. The promoter layer ensures proper adhesion of the photoresist on the substrate. A negative photoresist (Allresisit AR-N 4200) layer was deposited on the developer layer by spin coating at 500 rpm for 15 seconds and 4000 rpm for 90 seconds and curing at 85 °C for 10 minutes. Further, a customized Lloyd's mirror setup was used for exposure of the photoresist coated glass substrates. A highly stable UV laser source of wavelength 266 nm was expanded using an objective lens and pinhole for spatial coherence. The beam was incident on a highly polished mirror and the sample. The power of the incident laser beam was 32 mW. The laser beam, after reflecting from the mirror, interfered with the

incident beam on the sample to create a standing wave which created a grating like structure on a single exposure. The sample was rotated by 90° for the second exposure. The angle between the direct and the reflected beam determines the period of the gold nanodisk array, which can be calculated from equation 1. The angle between the direct and the reflected beam was varied by rotating the stage of Lloyd's mirror setup. The angles at which the exposure was performed are shown in Table 6.1. The exposed sample was developed by dipping in a developer (Allresist AR 300-475) for 30 seconds and cleaning using deionized water. After cleaning, the substrate was immediately baked at 95 °C for 5 minutes. The developed substrate was placed in a thermal evaporator, where 10 nm of chromium and about 45 nm of gold were deposited on the substrate. The excess gold and photoresist were lifted off the substrate by ultrasonication for 1 minute in an acetone bath. The substrate was finally cleaned using acetone, isopropyl alcohol, and deionized water. The ratio of period and the diameter of the nanodisks was close to 2.2 for the various angles tested.

Table 6.1 Laser interference lithography (LIL) laser exposure parameters.

Angle between direct	Time of 1st	Time of 2 nd	Diameter of the	Period of the gold
and reflected beam	exposure	exposure	gold nanodisk	nanodisk array
(Degree)	(s)	(s)	(nm)	(nm)
17.19	120	120	198	446
19.40	120	120	182	395
22.33	120	120	159	344
26.32	110	110	140	300
32.14	110	110	110	250

The diameter of the nanodisk and the period of the array were calculated by scanning electron microscopy (SEM) images (Zeiss Gemini 500 SEM), as shown in Figure 6.1 (a-d, and f). The height of the nanodisk was confirmed by atomic force microscopy (AFM) (Bruker Multimode AFM) for the 395 nm period nanodisk using open source software Gwyddion. The total height of the nanodisk was 57.7 nm, which consisted of 10 nm of chromium and 47.7 nm of gold. The measurements for Rhodamine 6G (99% Sigma Aldrich) were performed at 1.7 mW with an accumulation time of 2 seconds with 3 acquisitions. 10 µL of R6G solution was drop cased on 5 mm² substrate and was allowed to dry naturally. Similarly, for the detection of urea (commercially available 99 % pure), 10 µL of the urea solution was drop casted on the substrate and allowed to dry. The measurements were performed for an accumulation time of 18 seconds with 3 acquisitions.

To understand the optical response, simulations were performed in COMSOL software as discussed in 3.1.3. The dielectric constant of air and glass was input as 1 [294] and 2.25 [295], respectively. The Lorentz Drude model was selected to model the dielectric function of gold (epsilon infinity = 1 and plasma frequency: $1.369 \times 10^{16} \text{ rad/s}$) [203].

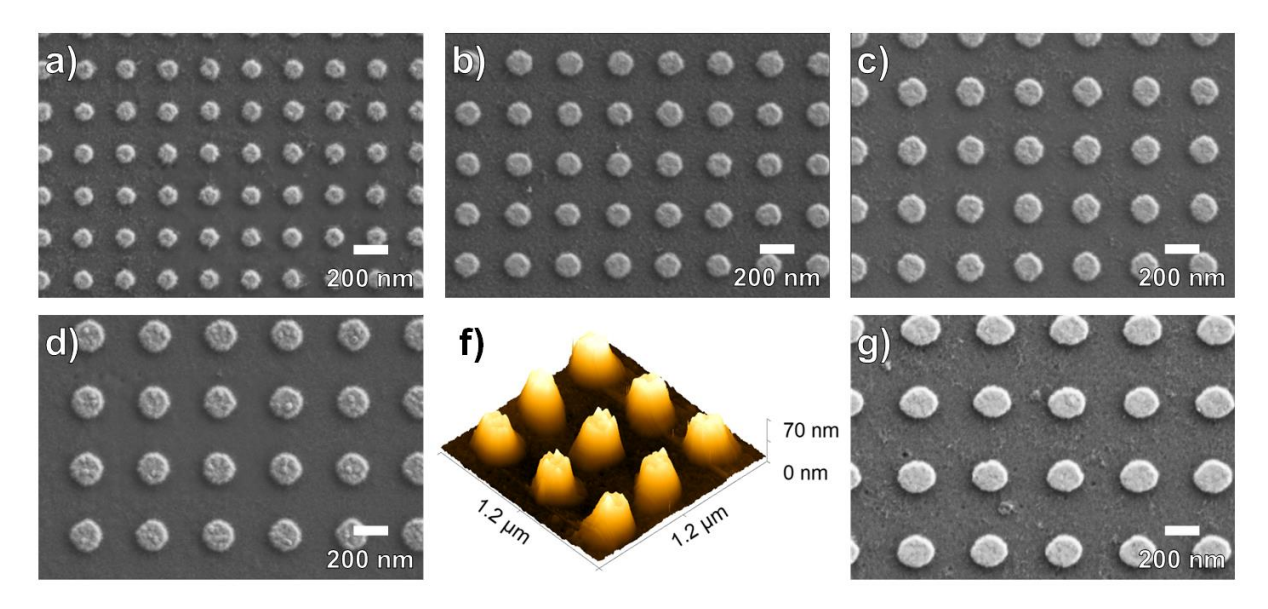


Figure 6.1 SEM images of gold nanodisk arrays fabricated using LIL of period (a) 250 nm, (b) 300 nm, (c) 344 nm, (d) 395, and (g) 446 nm. (f) 3D representation of the AFM measurements of the 395 nm period array

The gold nanodisk substrates fabricated by the LIL process were envisioned to be SERS substrates. The Raman enhancement of the nanodisks was tested by performing measurements on the Raman active dye Rhodamine 6G (R6G), whose peaks are observed for Raman shifts of 612, 774, 1127, 1183, 1310, 1362, 1508, 1574, and 1675 cm⁻¹ [296]. R6G molecule is highly Raman active and its signal is even expected to be seen for SERS substrates with low enhancement factors. Hence, it is an excellent tool to compare different SERS substrates. For the instrument used and the selected substrates, the peak at 612 cm⁻¹ was well resolved and had a high intensity, hence was selected for further analysis. The aforementioned peak corresponds to the C C ring in plane bending in the xanthene/phenyl type rings of R6G. The results of the measurements are shown in Figure 6.2 (a). The Raman measurements of the LIL substrates was performed for 10 µM concentration. For the selected concertation no resolvable peak was observed for bare glass substrate and the 450 nm period substrate. The highest Raman signal for 10 μM concentration was observed for the 300 nm period substrate, followed by the 395 nm and 344 nm period substrates which had similar enhancement, as shown in Figure 6.2 (b). The 612 cm⁻¹ peak of the 300 nm period substrate was 4.1 and 3.7 times higher than the 395 nm and 344 nm period substrates. Further, the Raman response of the 250 nm period substrate was 12.6 times lower than the 300 nm substrate. To calculate the average enhancement factor (EF) of the optimized substrate, the signal for 1M Rhodamine 6G was measured on bare glass substrate. The measurements on all the substrates were performed for the same instrument parameters and substrate size. Hence, the average EF can be calculated by the equation [297, 298]:

$$EF = \frac{I_{SERS}C_{REF}}{C_{SERS}I_{REF}}$$
 7.1

where I and C are the intensity of the 612 cm⁻¹ peak and concentration of the Rhodamine 6G used, respectively. The subscripts SERS and REF represent the SERS active substrate and bare glass reference substrate, respectively. The average EF of 2.3 x 10⁶ was experimentally calculated for the 300 nm period substrate. The EF of the substrate showing the best response was comparable to the other nanostructured SERS substrates of comparable sizes available in the literature [161, 299, 300]. The current study aims to determine the optimal SERS substrate among LIL substrates of various periods for practical use.

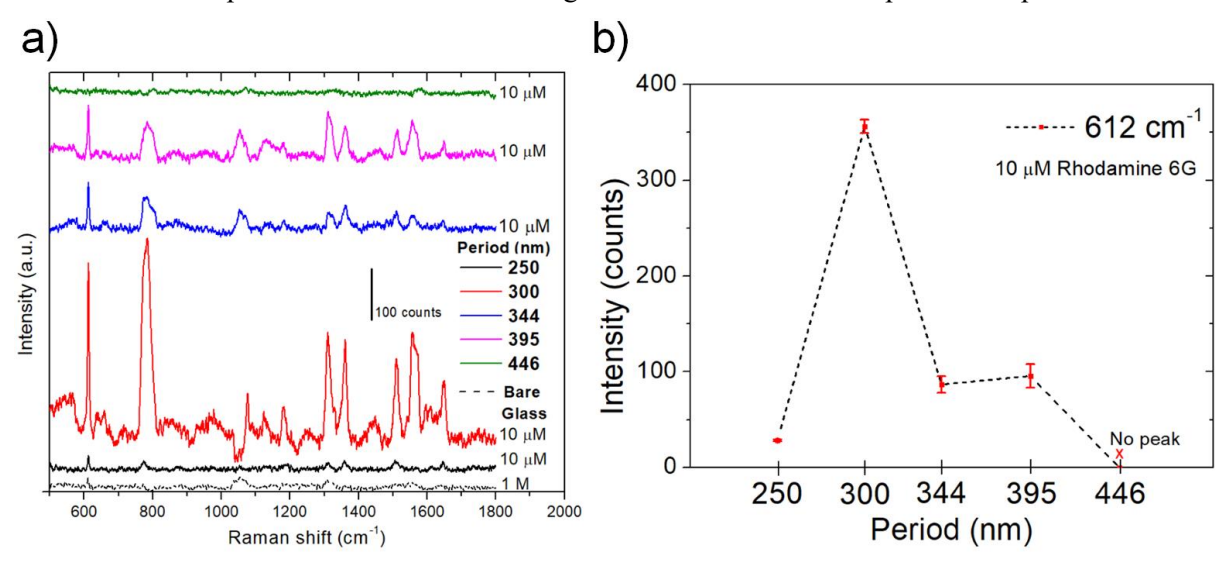


Figure 6.2 Raman response to the chemical Rhodamine 6G of the LIL substrates of various periods and a bare glass substrate. (b) Intensity of the 612 cm⁻¹ peak of Rhodamine 6G for the LIL substrates of various periods. The error bars represent the standard deviation between 3 measurements.

6.1.3 Understanding the plasmonic response

To understand the aforementioned phenomenon, transmission measurements were performed experimentally and confirmed by FEM simulations, shown in Figure 6.3 (a) and Figure 6.3 (b). It was observed in the transmission measurements that the resonance wavelength was observed in the visible region for the LIL substrates. A single highly intense dip was observed due to the plasmonic dipole created to oppose the incoming electric field by the nanodisk along. Moreover, the neighbouring nanodisks also have a major effect on the plasmonic response of the nanodisk array. The arrangement of the nanodisks in the form of a symmetric array greatly increases its resonance due to the coupling effect of the incident field and the scattered field of the nanodisks, which is in phase with incident field. FEM simulations shown in Figure 6.3 (c) were used to visualize the plasmonic dipole created when light at the resonance wavelength and polarized in x direction was incident on the 300 nm period substrate. The structure was confirmed to be polarization independent when light was incident normally, hence, other polarization directions will have the same transmission response. However, the direction

of the dipole will be parallel with the direction of the incident electric field, similar to Figure 6.3 (c). The normalized electric field contour shows that in regions near the edges of the nanodisk, the electric field was much higher than in the surrounding regions. Thereby, confirming the presence of regions of high electric field as a result of the enhanced electron oscillations due to the LSPR and array effect. Comparing the nanodisks, the resonance shifts towards a higher wavelength when the diameter of the nanodisks is increased due to the weakening of the restoring force of the oscillating dipole as the net surface charges are further apart when the size of the particle is increased [251]. Further, as the diameter of the nanodisks is increased, the bottom of the transmission dip occurred at a lower value. The increase in the size of the nanodisk results in a more intense plasmon due to the increase in the size of the dipole [253]. Higher order multipoles were not observed in the nanodisk arrays due to the dominance of the dipole resonance [25]. The transmission spectra calculated using FEM simulations were in close agreement with the experimental plots, as shown in Figure 6.3. The maximum deviation of the simulation and experimental resonance wavelengths of the gold nanodisk arrays was less than 5 %. The lower position of the transmission dip and the sharper resonance in the simulated spectrum is due to the practical limitations of the experimental nanodisk array including roughness, blunt edges, and other imperfections, which contribute to damping of the plasmonic effect.

The aforementioned results show that the increase in Raman intensity for the LIL substrates was dependent upon the transmission response as well as the electric field enhancement created due to the confinement of the electric field. The electric field enhancement leads to an increase in the Raman signal for all LIL substrates. The resonance wavelength of the 300 nm period substrate was 674 nm. The laser excitation wavelength used for the Raman measurements was 633 nm, and the wavelength of the Raman shift for the 612 cm⁻¹ peak of Rhodamine 6G was 658.5 nm. The excitation wavelength of the laser has an important role in the signal enhancement. It has been reported that when the excitation wavelength is near the resonance wavelength [145, 265] or slightly blue shifted [301] in comparison to the resonance wavelength, the highest Raman enhancement is expected. The response of 300 nm period LIL substrate confirms the aforementioned condition. The vicinity of the resonance wavelength of the 300 nm period substrate to the Raman peaks of the target molecule also contributes to the enhancement of the SERS signal [302]. Therefore, the vicinity of the Raman excitation wavelength and the wavelength of the Raman peaks of the target molecule to the resonance wavelength, and the intense plasmon created by the 300 nm period substrate (lower transmission dip) signal, contributed to its highest Raman signal among the LIL substrates. The higher position of the transmission dip (weaker plasmon) of 250 nm substrate and highly red shifted (compared to the excitation wavelength) resonance of the larger period substrates lead to their lower SERS enhancement. Thereby, the 300 nm period LIL substrate was considered optimal among the various substrates tested.

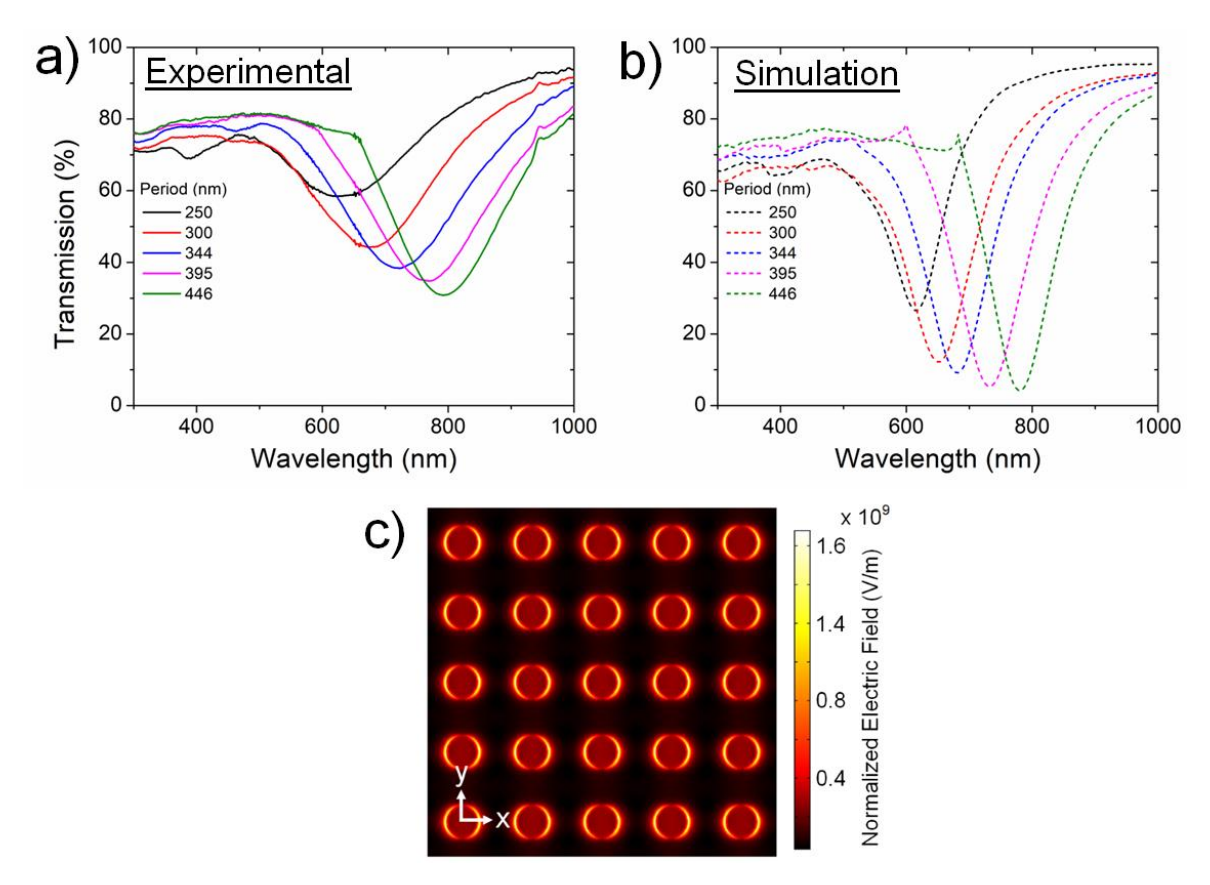


Figure 6.3 (a) Experimental and (b) simulated transmission specturm of the LIL substrates of various periods. (c) Simulated normalized electric field for the 300 nm period substrate at the resonance wavelength.

6.1.4 Confirmation for agrochemical sensing by detecting urea

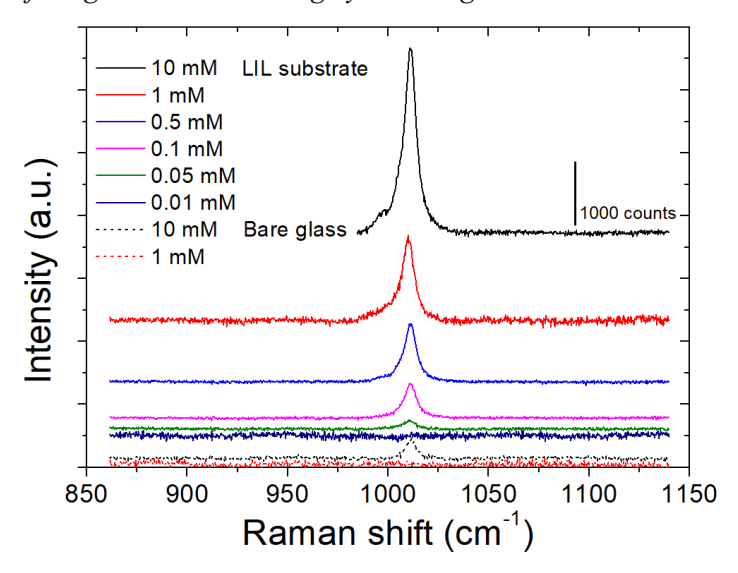


Figure 6.4 Raman response of the 300 nm LIL substrate and bare glass substrate to the varying concentration of urea.

To confirm the effectiveness of the gold nanodisks as an effective SERS substrate, the 300 nm period substrate was used to detect urea. Urea was selected because it is a widely used agrochemical and is a

good starting point to showcase the practical use of the optimal SERS substrate. Urea is commonly used as a fertilizer; however, its excessive use can lead to very high nitrogen content in the soil, which can have a negative effect on plant growth. Furthermore, it can cause skin problems, eye irritation, and mild toxicity in humans [303]. The detection limit for the 300 nm LIL substrate was analysed by performing Raman measurements for 10 mM, 1 mM, 0.5 mM, 0.1 mM, 0.05 mM, and 0.01 mM of urea in water. The Raman signal for a 99 % pure solid urea powder is shown in Figure 6.5 (a). The prominent peak for urea is the symmetric C N stretching vibration at a Raman shift of 1010 cm⁻¹, which was used for further analysis [304]. The comparison of the Raman signal of various concentrations of urea on the 300 nm period LIL substrate and a bare BK7 glass substrate is shown in Figure 6.4. 10 mM urea was detected on both the LIL substrate and bare glass. The 1010 cm⁻¹ Raman peak of urea showed an 18.8 times enhancement the LIL substrate compared to the bare glass substrate. Moreover, 1 mM urea showed no peak on bare glass. The lowest detectable urea concentration was 0.05 mM on the 300 nm period LIL substrate. The comparison of the intensity of the 1010 cm⁻¹ peak for various concentrations of urea on the LIL substrate is shown in Figure 6.5 (b). The obtained response shows a good linear fit of the intensity of the Raman peak to concentration of urea in the logarithmic scale. Hence, the 300 nm period LIL substrate can detect urea much lower than the required detection concentration in biological fluids in the human body, which varies from 1 mM to 20 mM [305]. Also, the obtained detection limit was comparable to the SERS substrates available in the literature as shown in Table 6.2.

Table 6.2 Comparison of the detection limit of urea in the literature

SERS substrate	Detection limit	Ref	
	(mM)		
Gold capped pyramid shaped arrays	30	[306]	
Silver capped Nanodome array	25	[307]	
Silver capped Nanodome array	12.5	[308]	
Gold nanoprism array	3	[309]	
Silver-TiO ₂ nanocage	1	[310]	
Silver nanoparticles modified with bovine serum albumin	1	[311]	
Silver nanoparticles and porous gold nanoclusters	1	[305]	
3D silver nanorod	0.05	[312]	
Gold nanodisk array	0.05	This work	
Photoinduced silver-TiO ₂ nanostructures	0.01	[313]	
Floating type silver nanoparticles-graphene based nanosheets	0.001	[314]	
Nanoporous gold	0.000001	[315]	

The listed the literature with SERS structures optimized for only hotspot formation [307, 309–311], structure with very weak plasmonic response [306], and structures with resonance wavelength far away from the Raman excitation wavelength [305, 308] showed lower performance than the 300 nm period

LIL substrate presented in the current article. Liu et al. [312] developed a silver nanorod based SERS substrates whose resonance was dependent on the length of the nanorods. The resonance of the substrate was tuned to match the Raman excitation wavelength and displayed a similar detection limit as the 300 nm period LIL substrate. Improving the analyte and nanostructure interaction by using pre irradiation of silver-TiO₂ nanostructures with UV light [313] and using floating type silver nanoparticles-graphene based nanosheets [314] resulted in a better detection limit of urea.

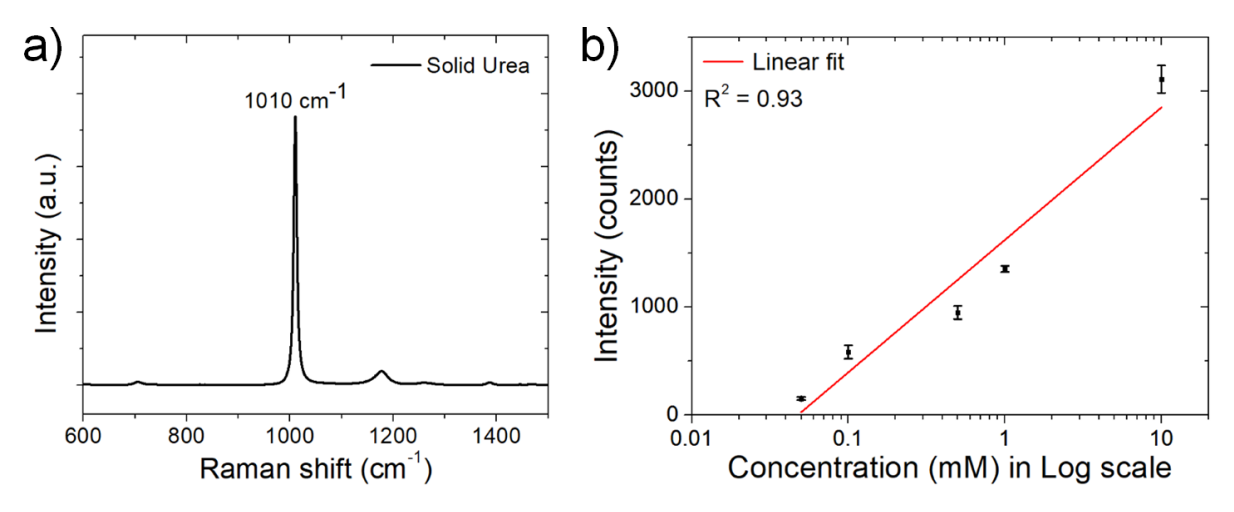


Figure 6.5 (a) Raman spectrum of 99 % pure urea powder. (b) Plot of the Intensity of the main Raman peak (1010 cm⁻¹) of urea for the 300 nm period LIL substrate vs the urea concentration in the log (base 10) scale. The error bars represent the standard deviation between 3 measurements

6.2 Theoretical calculations of Raman spectra of agrochemicals

This chapter first lists the various types of agrochemicals tested in the current work. Then, the structure and vibrational modes of the weedicide Metribuzin were studied and confirmed using experimental results. Metribuzin is a widely used agrochemical, but the study of its vibrational modes is lacking in the literature. The comparison of basis sets using B3LYP level of theory were studied using the calculated and experimental Raman response of Metribuzin, which allows for the selection of the optimal basis set for the remaining agrochemicals. Then, the vibrational modes of a herbicide (Atrazine), fungicide (Mancozeb) and acaricide (Clofentezine) were discussed, followed by the vibrational mode assignment and comparison of four insecticides (Chlorantraniliprole, Thiamethoxam, Tau-fluvalinate, and Flubendiamide). The calculations were performed in the GAUSSIAN software using the methodology mentioned in section 3.3

Table 6.3 Applications of the commercial agrochemicals tested in this thesis

Agrochemical	Sprayed	Sprayed directly	Application on crops
	on soil?	on crops?	
Atrazine	Yes	No	Corn, sorghum, sugarcane, wheat,
			mustard, cotton, tobacco, sunflowers
Mancozeb	No	Yes	Tomatoes, potatoes, cucumbers, peppers,
			lettuce, and cruciferous vegetables
Metribuzin	Yes	Yes	Wheat, potatoes, tomatoes, soy bean, and
			sugarcane
Clofentezine	No	Yes	Apples, pears, stone fruit, nuts,
			ornamentals
Chlorantraniliprole	Yes	Yes	Sugarcane, rice, and soybean, lettuces, Cabbage
Thiamethoxam	Yes	Yes	Apple, tomato, cabbage
Tau-fluvalinate	Yes	Yes	Cabbage, Brussels sprouts, broccoli,
			crucifer greens, collards, kale and
			mustard greens
Flubendiamide	No	Yes	Rice, Brinjal, Cabbage, corn, cotton, tobacco, tree fruit, tree nuts, vine crops and vegetable crops

The ever increasing use of agrochemicals to improve the crop yield is causing rampant contamination of food and drinking water. Scientists and engineers are developing solutions to reduce and monitor the use of these chemicals. In this thesis, the focus was on the monitoring of agrochemicals using Raman sensing. As discussed in section 2.6, the SERS technique is an excellent to monitor minuscule quantities of target chemicals quickly. Moreover, the Raman spectra of each chemical being unique makes the sensing highly selective. Therefore, researchers are able to optimize the instrumentation and substrate of the sensors using the unique Raman spectra of the target chemicals. Therefore, knowing the vibrational response (Raman spectra in the context of the current work) is critical for developing highly efficient sensors for detection of agrochemicals. DFT calculations provide a very accurate estimation of the Raman spectra of various systems. Hence, this section uses DFT calculations to present the Raman vibrational modes of widely used commercial agrochemicals. In the next section, these agrochemicals were detected using the optimized LIL substrate for SERS sensing, as discussed in section 6.1.

Agrochemicals widely used by farmers were procured from the market, it was ensured that different types of agrochemicals were analyzed. The crops on which these chemicals are effective also depend upon the chemistry of the product. Hence, the use of these agrochemicals is mentioned in Table 6.3. Table 6.4 shows the type of agrochemical and the main chemical along with its chemical structure and

molecular weight. The detailed chemical structure of the various agrochemicals is shown in Figure G.1. The different types of agrochemicals, herbicide, fungicide, weedicide. acaricide, and insecticides are used at various stages of the crop production.

Table 6.4 Details of the agrochemicals tested in this thesis

Main chemical	Chemical structure	Molecular weight g/mol	Commercial product
Atrazine	C ₈ H ₁₄ ClN ₅	215.7	SA-
			CROPGYM
Mancozeb	$[C_{8}H_{12}MnN_{4}S_{8}]_{x}[C_{8}H_{12}ZnN_{4}S_{8}]_{y} \\$	541.1	M-45
Metribuzin	$C_8H_{14}N_4OS$	214.3	Sencor
Clofentezine	$C_{14}H_8Cl_2N_4\\$	303.1	SENTO
Chlorantraniliprole	$C_{18}H_{14}BrCl_2N_5O_2 \\$	483.1	Cover
Thiamethoxam	$C_8H_{10}ClN_5O_3S$	291.7	Apterra Plus
Tau-fluvalinate	$C_{26}H_{22}ClF_3N_2O_3$	502.9	KAY 24EW
Flubendiamide	$C_{23}H_{22}F_{7}IN_{2}O_{4}S \\$	682.4	FAME
	Atrazine Mancozeb Metribuzin Clofentezine Chlorantraniliprole Thiamethoxam Tau-fluvalinate	$\begin{array}{cccc} A trazine & C_8H_{14}ClN_5 \\ \\ Mancozeb & [C_8H_{12}MnN_4S_8]_x[C_8H_{12}ZnN_4S_8]_y \\ \\ Metribuzin & C_8H_{14}N_4OS \\ \\ Clofentezine & C_{14}H_8Cl_2N_4 \\ \\ Chlorantraniliprole & C_{18}H_{14}BrCl_2N_5O_2 \\ \\ Thiamethoxam & C_8H_{10}ClN_5O_3S \\ \\ Tau-fluvalinate & C_{26}H_{22}ClF_3N_2O_3 \\ \\ \end{array}$	

The major component in Atrazine's structure is the triazine type ring. The ring has three groups attached to it, two starting with nitrogen, ethylamine and propylamine groups; and a chlorine atom is attached to the ring. Mancozeb is a complex molecule comprising of a non systematic dithiocarbamate, structure comprising of N and S atoms. It is a combination of two dithiocarbamates, Maneb (plomeric complex with Mn) and Zineb (plomeric complex with Zn). The metribuzin molecule comprises a triazinone type ring with methanethiolate, carbonyl, amino, and isobutane groups. Clofentezine has a tetrazine type structure in hydrogens are substituted by o-chlorophenyl groups. As seen in the structure, it has a ring dominated structure. Coming to the insecticides, which have more complicated and larger structures than the agrochemicals discussed above. Chlorantraniliprole has three rings, a dimethylbenzamide ring with a methyl group and chlorine atom, a chloropyridine ring, and a 5 member pyrazole ring with a bromine atom. Thiamethoxam contains an ozadiazine type ring with a nitramide group along with 5 member chloro chlorothiazol ring. Tau-fluvalinate also has 3 ring type structures, 2 phenyl type rings in the phenoxyphenyl group (which has methylbutanoate and cyano type groups) and an anilino ring with chlorine atom and trifluoromethyl group. Flubendiamide consists a phenyl type ring with methyl and perfluoropropan groups and a phthalimide ring containg methylsulfonyl group.

6.2.1 Vibrational response of Metribuzin

The complete vibrational response of the weedicide of Metribuzin has not been studied. In the current work, Metribuzin's complete vibrational mode assignment was presented using experimental Raman and FTIR spectra in conjunction with aug-cc-pVTZ B3LYP calculations. The structure was confirmed by comparing the experimental and calculated bond lengths. Also, the major basis sets available in the Gaussian software for B3LYP level of theory were compared with the experimental Raman spectrum. Although various articles discuss the application of some of these basis sets, a thorough analysis of the same was not performed comparing the individual and total error in the wavenumber and intensity of the various basis sets.

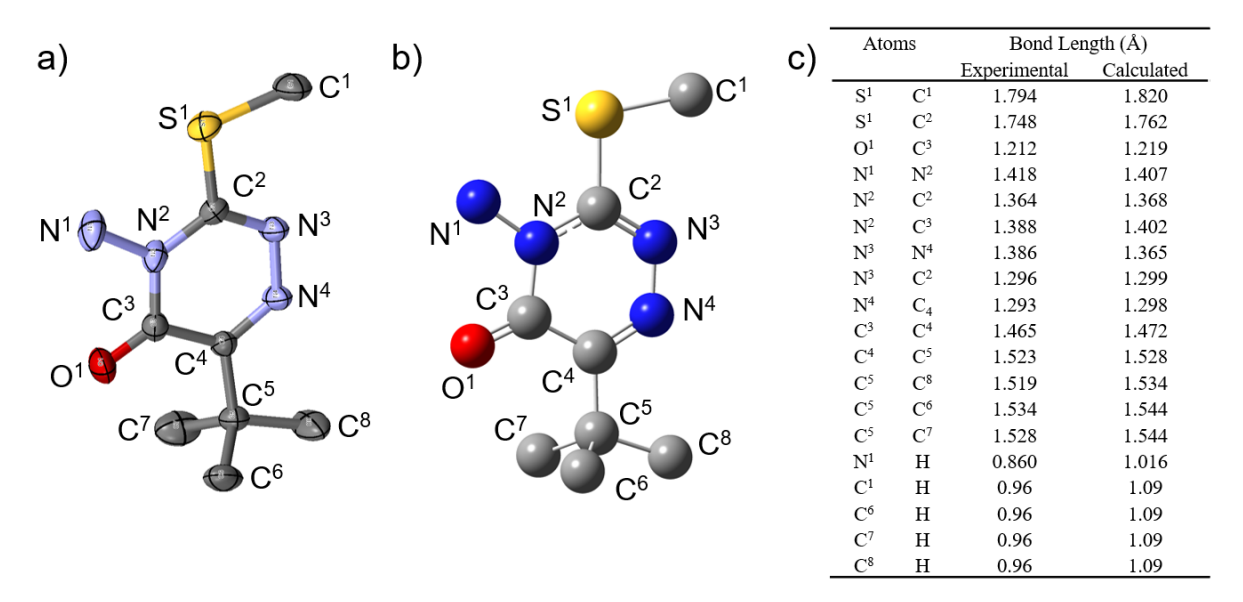


Figure 6.6 a) Ellipsoidal plot of the molecule metribuzin at the 50% probability level and at room temperature (298 K). b) Theoretical structure of metribuzin. Hydrogens have been removed for clarity. c) Comparison of the experimental and theoretical bond length. Theoretical structure was calculated using aug-cc-pVTZ B3LYP level of theory.

Single crystal x-ray diffraction (SC-XRD) was performed on the Bruker D8 venture with x-ray wavelength of 0.71073 Å to compare the experimental structure of Metribuzin. The Metribuzin powder was dissolved in ethanol and allowed to dry in air to get the crystals required for the SC-XRD. Bruker Tensor II was used for the FTIR measurements of the metribuzin powder. The scan resolution was 4 cm⁻¹ and the spectra was averaged over 16 scans. The Raman measurements on the metribuzin powder were performed using the Horiba LabRAM HR with the 633 nm laser (Melles Griot) and 100x objective lens with 0.8 numerical aperture. The resolution of the Raman spectra was 0.33 cm⁻¹, the laser accumulation time was 6 seconds and spectra was averaged over 12 scans.

6.2.1.1 Confirmation of structure

Prior to the study of the vibrational modes of Metribuzin, the SC-XRD was used to obtain the structure of Metribuzin, as shown in Figure 6.6 (a). The chemical formula of Metribuzin was confirmed to be $C_8H_{14}N_4OS$, and the molecular weight was 214.29. The crystallized Metribuzin has a Monoclinic system with space group P21/c. The dimensions of the unit cell were, a = 14.2204 Å, b = 9.3048 Å, and c = 8.7365 Å. The corresponding angles were $\alpha = 90^\circ$, $\beta = 104.335^\circ$, and $\gamma = 90^\circ$. There were 4 metribuzin molecules in the unit cell, and the volume of the unit cell was 1220 Å³. The density of Metribuzin was calculated to be 1.271 g/cm⁻¹.

The theoretical structure of Metribuzin calculated using aug-cc-pVTZ basis set is shown in Figure 6.6 (b). The metribuzin molecule comprises of a triazinone type ring with methanethiolate, carbonyl, amino, and isobutane groups. The comparison of the metribuzin molecule's experimental and calculated bond lengths is shown in Figure 6.6 (c). The discrepancy between the bond lengths of the experimental and calculated structures was less than 1.5 % when not considering the hydrogen atoms. However, when the hydrogen atoms were included to calculate the discrepancy, the error increased to 20 %. The inaccurate calculation of the N-H and C-H bonds was because the calculations were performed in the gas phase with only one metribuzin molecule. However, the experimental Metribuzin was surrounded by other Metribuzin molecules, and therefore, the experimental bond lengths were lower.

6.2.1.2 Vibrational response (DFT and experimental)

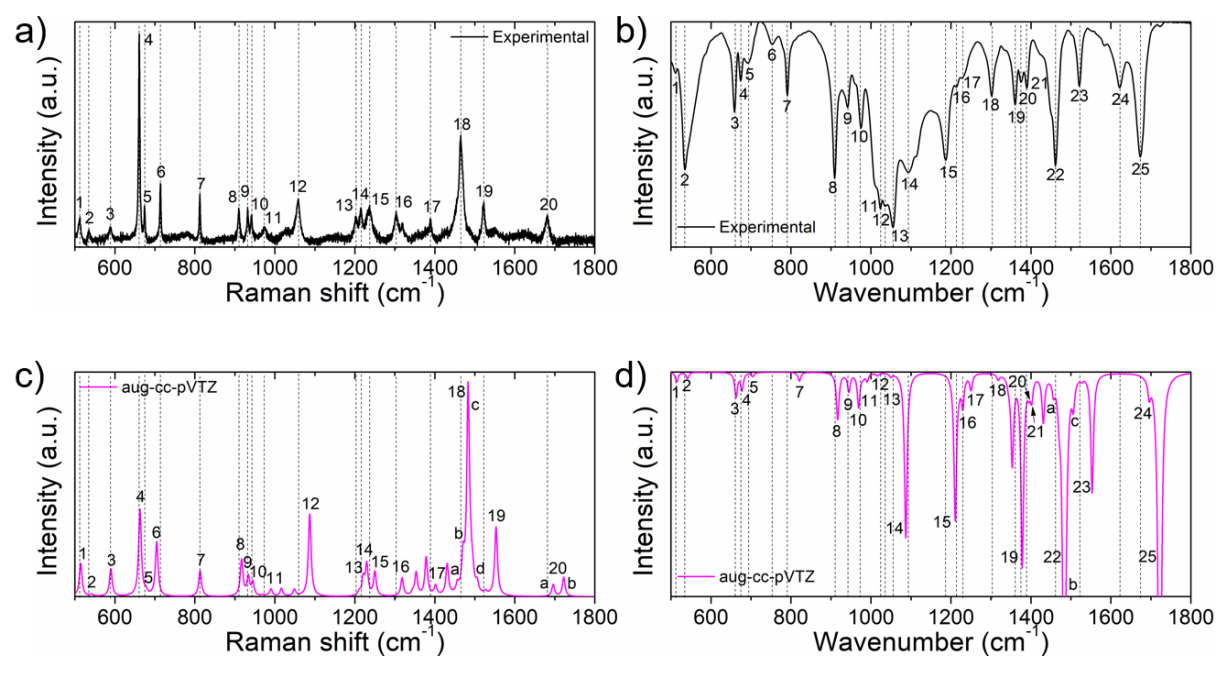


Figure 6.7 Comparison of experimental a) Raman and b) FTIR spectra of Metribuzin with the calculated c) Raman and d) IR spectra calculated using aug-cc-pVTZ basis set.

The comparison of the experimental and calculated (using aug-cc-pVTZ basis set) Raman and IR spectra is shown in Figure 6.7. The experimental Raman and IR spectra show 20 and 25 major vibrational modes, respectively. The plots in Figure 6.7 are labelled with the vibrational modes, and the vertical lines correspond to their equivalent experimental wavenumbers. Only the vibrational modes present in the experimental spectra are discussed. Some of the vibrational modes in the calculated spectra were not present in the experimental spectra due to practical restrictions on vibrations, lattice strain, and surface effects. The wavenumbers of the calculated vibrational modes were in good agreement; however, the intensity had a higher discrepancy. One of the main reasons for this is the lack of surrounding molecules in the calculated structure, which is also discussed in the bond length comparison. Due to the lack of restriction on the hydrogen atoms, they are free to vibrate, and hence, higher intensities were observed for the vibrational modes involving hydrogen atoms. The assignment of the vibrational modes, along with a comparison of the experimental and calculated wavenumbers is presented in Table 6.5. The calculated vibrational modes were at slightly higher wavenumbers, which is consistent with the literature. The vibrational modes were visualized in the GaussView software, and then they were assigned to their corresponding wavenumbers. The vibrational modes in the fingerprint region of 500 cm⁻¹ to 1800 cm⁻¹ are discussed in the current article because this region is generally used for detecting agrochemicals. The wavenumbers mentioned henceforth are the calculated wavenumbers to avoid the slight deviation wavenumbers of the vibrational modes common to both Raman and IR spectra.

Ring Vibrations

The ring modes in the triazinone type ring are assigned according to the Wilson nomenclature [316] (Appendix G). The visualization of the ring modes can be interpreted easily using the standard nomenclature. At the lower part of the spectrum 500 to 1000 cm⁻¹ the ring modes dominate the vibrational modes in the Raman and IR spectrum for a single ring type molecule [317, 318]. At lower wavenumbers, the calculated spectra are very close to the experimental spectra. Ring modes 3 and 17a corresponding to 514.41 cm⁻¹ and 541.38 cm⁻¹ are present in both Raman and IR spectra, however, their intensity in the IR spectra is much larger due to the dominance of the dipole nature of the vibrational modes. The main Raman vibrational mode of Metribuzin is at 662.72 cm⁻¹ (ring mode 6a), corresponding to Raman mode 4. It is also present in the IR spectrum but at a lower intensity. Similarly, ring mode 3 at 677.36 cm⁻¹ has higher intensity in the Raman spectra as compared to IR spectra. The ring mode 5 is only present in the IR spectrum at 821.25 cm⁻¹. The degenerate ring modes, 18a and 18b were present in both the spectra at 909 cm⁻¹ and 1087.12 cm⁻¹. At larger wavenumbers, due to prevalence of C N and N N stretching at around 1200 to 1400 cm⁻¹ [319], ring mode 8a and 9a are located at 1250.09 cm⁻¹ and 1483 cm⁻¹ for both the spectra. The ring modes 1 and 13 were observed at 1016.33 cm⁻¹ and 1210.75 cm⁻¹ only in the IR spectra. Due to the presence of strong C=N vibrational mode at about 1500 cm⁻¹ [320], an intense ring mode 9b is present at 1553.03 cm⁻¹ in both the vibrational spectra.

Combining the individual vibrational modes prevailing in the ring mode contributes to their high intensity.

C H vibrations

The C-H bond is present in the methanethiolate and isobutane groups. For C⁵C₃H₉, the isobutane group, the symmetric bending and symmetric stretching vibrational mode are present in the Raman spectrum at 589.86 cm⁻¹ and 812.94 cm⁻¹. As previously reported for a pesticide, the C-H bond vibrational modes are the majority modes in the spectral range of 1000 to 1500 cm⁻¹ [321]. For Metribuzin, antisymmetric bending of C⁶H₃, C⁷H₃, and C⁸H₃ groups was highly prevalent, and it was seen in the vibrational modes at wavenumber 944.78 cm⁻¹, 1229.64 cm⁻¹, and 1318.07 cm⁻¹ for both Raman and IR spectra. Also, it was present in the IR spectra at 1049.66 cm⁻¹. Symmetric bending (umbrella type) of C⁶H₃, C⁷H₃, and C⁸H₃ groups were observed at 1401.73 cm⁻¹ for both spectra. Antisymmetric stretching of the isobutane group was located at 944.78 cm⁻¹. Stretching of C⁴ C⁵ bond was seen at 1318.07 cm⁻¹. For the Raman spectra, isobutane group antisymmetric stretching along with twisting of C⁸H₃ group was present at 933.43 cm⁻¹ and 1221.08 cm⁻¹, respectively. The C H twisting of the type vibrational modes were also previously reported around 900 cm⁻¹ and 1200 cm⁻¹ [322]. The twisting vibrational mode for C⁶H₃ and C⁷H₃ was observed in both the spectra at 1505.62 cm⁻¹. For the IR spectra, antisymmetric and symmetric bending of C⁶H₃ and C⁷H₃ were present at 1048.17 cm⁻¹ and 1394.87 cm⁻¹, respectively. For the methanethiolate group, C¹H₃ antisymmetric bending, twisting, and symmetric bending modes were observed at 990 cm⁻¹, 1456.4 cm⁻¹, and 1470.49 cm⁻¹, respectively.

The vibrational mode 18 for the Raman spectra is the most intense in the calculated Raman spectra. It is mixture of the following vibrational modes: Ring mode 9a, C¹H₃ twisting, C¹H₃ symmetric bending and twisting of C⁶H₃ and CૃH₃ groups. All of these combined to attain the strong Raman response; however, the experimental intensity of mode 18 was not the highest in the Raman spectra. The reason was that the metribuzin powder had closely packed molecules in the practical condition, while the calculations were performed for a single molecule. The absence of any restriction allowed intense vibrations of the C-H bonds, leading to an overestimation of the intensity of the vibrational mode.

Table 6.5 Comparison of experimental and calculated (using aug-cc-pVTZ) wavenumbers of the main peaks of Metribuzin with its vibrational mode assignment. Vibrational modes common for both Raman and IR are in bold. The vibrational modes are as follows: ν is stretching (ν s is symmetric stretching and ν as is antisymmetric stretching), δ is bending (δ s is symmetric bending and δ as as is antisymmetric bending), ω is wagging, ρ is rocking, and τ is twisting. The ring mode assignments are from the Wilson nomenclature (Appendix G) [316]. Henceforth, these conventions were used throughout this thesis.

	Raman				Infrared (IR)			
Mode	Experimental Raman shift	Calculated Raman shift	Assignment	Mode	Experimental Wavenumber	Calculated Wavenumber	Assignment	
1	(cm ⁻¹)	(cm ⁻¹)	Ring mode 3 and C ⁵ C ₃ H ₉ δ ₈	1	(cm ⁻¹) 512.5	(cm ⁻¹) 514.41	Ring mode 3 and C ⁵ C ₃ H ₉ δ _s	
2	535	541.38	Ring mode 17a	2	535	541.38	Ring mode 17a	
			_				_	
3	588	589.86	$C^5C_3H_9$ δ_s and S1 C2 ν	3	660.5	662.72	Ring mode 6a	
4	660.5	662.72	Ring mode 6a	4	674	677.36	Ring mode 3 and C ¹ S ¹ v	
5	674	677.36	Ring mode 3 and C ¹ S ¹ v	5	693.5	704.58	C1 S1 v	
6	714	704.58	$C^1 S^1 v$	6	754	-	-	
7	812	812.94	$C^5C_3H_9 \nu_s$	7	791.5	821.25	Ring mode 5	
8	909	916.83	Ring mode 18b, N^1 N^2 v, and $C^5C_3H_9$ v_{as}	8	909	916.83	Ring mode 18b, N^1 N^2 v, and $C^5C_3H_9$ v_{as}	
9	931	933.43	$C^5C_3H_9~\nu_{as},~C^8H_3~\tau,~C^6H3~\delta_{as},$ and $C^7H_3~\delta_{as}$	9	943	944.78	$C^5C_3H_9$ vas, and C^6H_3 δ_{as} , C^7H δ_{as} , and C^8H_3 δ_{as}	
10	943	944.78	$C^5C_3H_9$ v_{as} , and C^6H_3 δ_{as} , C^7H_3 δ_{as} , and C^8H_3 δ_{as}	10	976.5	969.21	N^1H_2 ω and Ring mode 8a	
11	974	990.33	$C^{1}H_{3}\delta_{as}$	11	1024.5	1016.33	Ring mode 1, N^1H_2 ω , and C^1H δ_{as}	
12	1058	1087.12	Ring mode 18a and $N^1\omega$	12	1034.5	1048.17	$C^6H_3~\delta_{as},C^7H_3~\delta_{as},$ and $C^8H_3~\tau$	
13	1203	1221.08	$C^5C_3H_9~\nu_{as},~C^8H_3~\tau,~C^6H_3~\delta_{as},$ and $C^7H_3~\delta_{as}$	13	1055.5	1049.66	$C^6H_3~\delta_{as},C^7H_3~\delta_{as},$ and $C^8H_3~\delta_{as}$	
14	1214.5	1229.64	N ² v _{as} , C ⁵ C ₃ H ₉ v _{as} , C ⁶ H ₃ δ_{as} , C ⁷ H ₃ δ_{as} , and C ⁸ H ₃ δ_{as}	14	1095	1087.12	Ring mode 18a and $N^1H_2\ \omega$	
15	1236	1250.09	Ring mode 8a, $C^5C_3H_9$ vas, C^6H_3 δ_{as} , C^7H_3 δ_{as} , and C^8H_3 δ_{as}	15	1186.5	1210.75	Ring mode 13	
16	1303	1318.07	C^4 C^5 v, C^6 H ₃ δ_{as} , C^7 H ₃ δ_{as} , and C^8 H ₃ δ_{as}	16	1214.5	1229.64	N^2 v _{as} , $C^5C_3H_9$ v _{as} , C^6H_3 δ_{as} C^7H_3 δ_{as} , and C^8H_3 δ_{as}	
17	1389	1401.73	C^6H_3 δ_s , C^7H_3 δ_s , and C^8H_3 δ_s	17	1228.5	1250.09	Ring mode 8a, C ⁵ C ₃ H ₉ v _{as} , C ⁶ H δ _{as} , C ⁷ H ₃ δ _{as} , and C ⁸ H ₃ δ _{as}	
18	1464.5	1456.4	C¹H ₃ τ	18	1303	1318.07	C^4 C^5 v, C^6 H ₃ δ_{as} , C^7 H ₃ δ_{as} , and C^8 H ₃ δ_{as}	
		1470.49	$C^1H_3 \delta_s$	19	1359.5	1378.35	$N^2 \nu_{as}$, $C^1 H_3 \delta_{as}$, and $N^1 H_2 \delta_s$	
		1483.19	Ring mode 9a, C^1H_3 δ_s , and C^8H_3 δ_s	20	1376	1394.87	$C^6H_3~\delta_s$ and $C^7H_3~\delta_s$	
		1505.62	$C^6H_3 \tau$ and $C^7H_3 \tau$	21	1389	1401.73	$C^6H_3 \delta_s$, $C^7H_3 \delta_s$, and $C^8H_3 \delta_s$	
19	1522	1553.03	Ring mode 9b	22	1464.5	1456.4	C¹H ₃ τ	
20	1680.5	1695.75	$N^1H_2 \delta_s$			1483.19	Ring mode 9a, C^1H_3 δ_s , an C^8H_3 δ_s	
		1722.09	C^3 O^1 v and N^1H_2 δ_s			1505.62	C ⁶ H ₃ τ and C ⁷ H ₃ τ	
				23	1522	1533.05	Ring mode 9b	
				24	1622	1695.75	N¹H ₂ δ _s	
				25	1674	1722.09	$C^3 O^1 v$ and $N^1 H_2 \delta_s$	

C S, CO, C S, and N N vibrations

C¹ S bond stretching was observed at 704.58 cm⁻¹ in both Raman and IR spectra which is the reported range in the literature (700 to 750 cm⁻¹) [323]. The wagging mode of N¹H₂ was seen for the IR spectra at 969.21 cm⁻¹ which is slightly blue-shifted to the reported wavenumber of around 800 cm⁻¹ [324]. N¹H2 in plane symmetric bending (scissoring mode) was observed at 1695.75 cm⁻¹ which is very similar to the previously established range of around 1650 cm⁻¹ [324]. The stretching of the amino group (N-N) was also seen for both spectra at 916.83 cm⁻¹. The C N stretching was reported to be around 1250 cm⁻¹ [325]. A complex vibrational mode comprising of antisymmetric stretching of the amino group and the triazinone ring was located at 1229.61 cm⁻¹ and 1378.35 cm⁻¹. The C=O stretching vibrational mode is usually seen around 1750 cm⁻¹ [326]. The most intense IR vibrational mode in the calculated spectrum was for mode 25, which is the stretching of the C³=O¹ bond at 1722.09 cm⁻¹. The experimental IR spectrum has a mixture of vibrational modes 10, 11, 12, 13 and 14 contributing to the most intense mode. Practical effects and imperfections in the structure causes a complex vibrational response. Similar to the Raman spectra, the unrestricted movement of the C³=O¹ bond in the calculated spectrum causes the overestimation of the IR intensity.

6.2.2 Basis set comparison

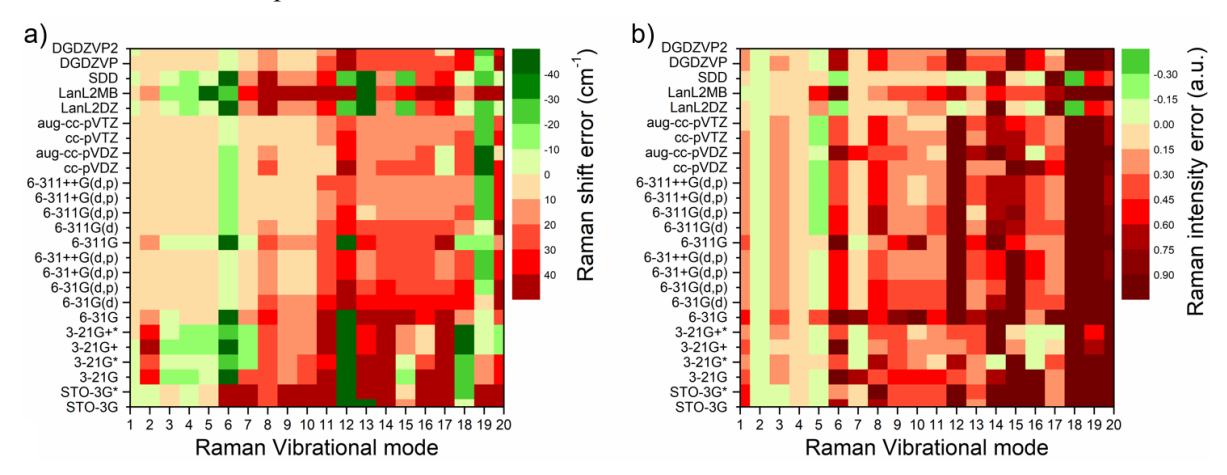


Figure 6.8 Raman a) shift and b) intensity error for the various basis sets compared to the experimentally observed values. The intensity for all the plots was normalized with respect to the vibrational mode 4 (the major experimental Raman shift of 660.5 cm⁻¹)

Researchers use several basis sets to calculate vibrational modes at the B3LYP level of theory. The comparison of all the major basis sets available for calculation in the Gaussian software is presented in this section. No scaling factor was applied to the corresponding wavenumbers of the vibrational modes to compensate for the experimental error. Applying a single scaling factor does not often provide an accurate assignment to the vibrational modes throughout the fingerprint spectrum region [327]. Either individual scaling factors are used for the different vibrational modes, or scaling factors are used for a specific wavenumber range [328]. The current article presents the accuracy of the wavenumber and

intensity of the vibrational modes for the various basis sets. Thereby, a suitable basis set can be chosen based on the compromise between accuracy of the calculation and its computational cost.

As discussed previously, the aug-cc-pVTZ basis set provided accurate calculations; however, its computational cost is very high compared to other basis sets. The comparison of the computational cost of all the basis sets is shown in Figure 6.10, the values were normalized to the total computation time of the aug-cc-pVTZ basis set. It can be seen that the next most computationally expensive basis sets are aug-cc-pVDZ and cc-PVTZ, with computational costs of 0.028 and 0.015. The remaining basis sets are all lower than 0.006.

The experimental Raman spectrum was selected for the comparison because of the presence of sharp and distinguishable peaks. The Raman spectra of Metribuzin calculated using all the basis sets are shown in the Appendix F. The 20 vibrational modes in the experimental spectra are shown in Figure 6.7 (a). They were used to calculate the errors in the wavenumber and intensity of the various basis sets. The error in wavenumber was calculated simply by subtracting the calculated and experimental wavenumbers. The error in intensity was calculated by first normalizing the intensity to the major vibrational mode 4 for all the other modes, both for the experimental and calculated plots. The error in intensity was then calculated by subtracting the calculated normalized intensity from the experimental normalized intensity for all the 20 vibrational modes. The error in the wavenumber and intensity are compared for all the basis sets in Figure 6.8 (a) and (b). It can be observed in Figure 6.8 (a) that the error in wavenumber is lower for smaller wavenumbers (500 cm⁻¹ to 1000 cm⁻¹), beyond which the error increases. Generally, the calculated wavenumbers are shifted towards larger wavenumbers, i.e., the error is positive. The sum of the absolute Raman shift error is shown in Figure 6.9 (a). It can be seen that the smaller basis sets (STO-3G, 3-21G, 6-31G) and basis sets for heavy atoms (LanL2DZ, LanL2MB, and SDD) have large total errors. The total error in the 6-31G and 6311-G decreases as additional polarization, diffuse, and other functions are added. The DGDZVP basis sets, whose computational cost is comparable to small to medium sized basis sets, perform on par with larger basis sets, 631++G(d,p), 6311G(d,p), and cc-pVDZ. Furthermore, the performance of 6311++G(d,p) basis set is comparable to the much larger aug-cc-pVDZ and ccPVTZ basis sets. The intensity error comparison in Figure 6.8 (b) shows that calculated intensity is generally overestimated, i.e., the error is positive. The error is slightly lower for the smaller wavenumbers, and it increases significantly beyond 1000 cm⁻¹ as the effect of hydrogen atoms on the vibrational modes increases. Comparing the absolute total error in intensity (Figure 6.9 (b)), the smaller basis sets (STO-3G, 3-21G, 6-31G, and 6-311G) have large errors. The error in the 6-311G(d) basis set increases as additional functions are added due to the overestimation of the effect of hydrogen atoms. Similar overestimation is seen for aug-cc-pVDZ compared to cc-pVDZ basis set. Most of the medium to large sized basis sets have comparable total errors in intensity. However, the lowest total error was observed in LanL2DZ and SDD basis sets due to the lack of polarization functions for the hydrogen atoms. However, these basis sets have a very high error in

wavenumber. Hence, the DGDZVP basis set at the B3LYP level of theory was used for all the agrochemicals.

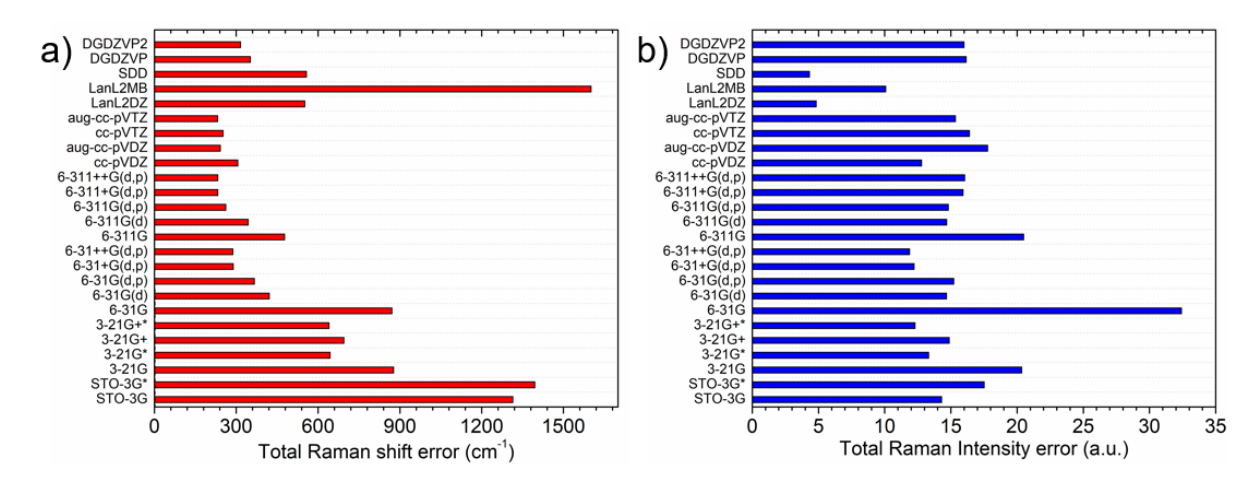


Figure 6.9 Total error in a) Raman shift and b) Raman intensity of the various basis sets compared to the experimental vibrational modes. The absolute values of errors were used in calculating both (a) and (b).

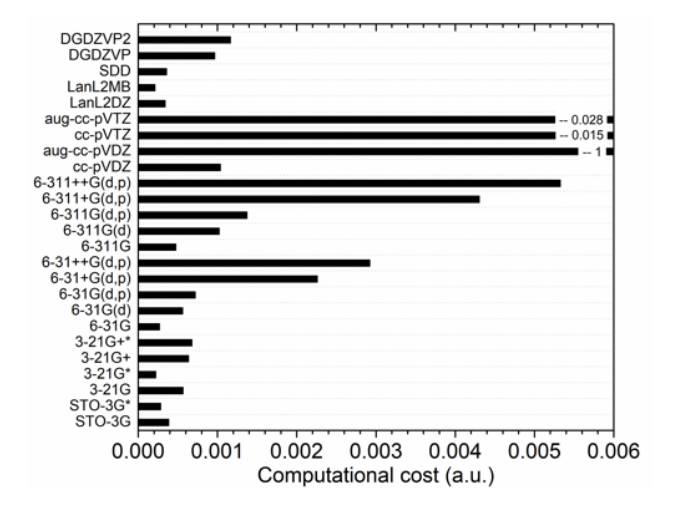


Figure 6.10 Computational cost of the basis sets for calculating Raman spectra. The computation cost of all the basis sets was normalized with respect to aug-cc-pVTZ.

6.2.3 Vibrational response (DFT and experimental) of agrochemicals

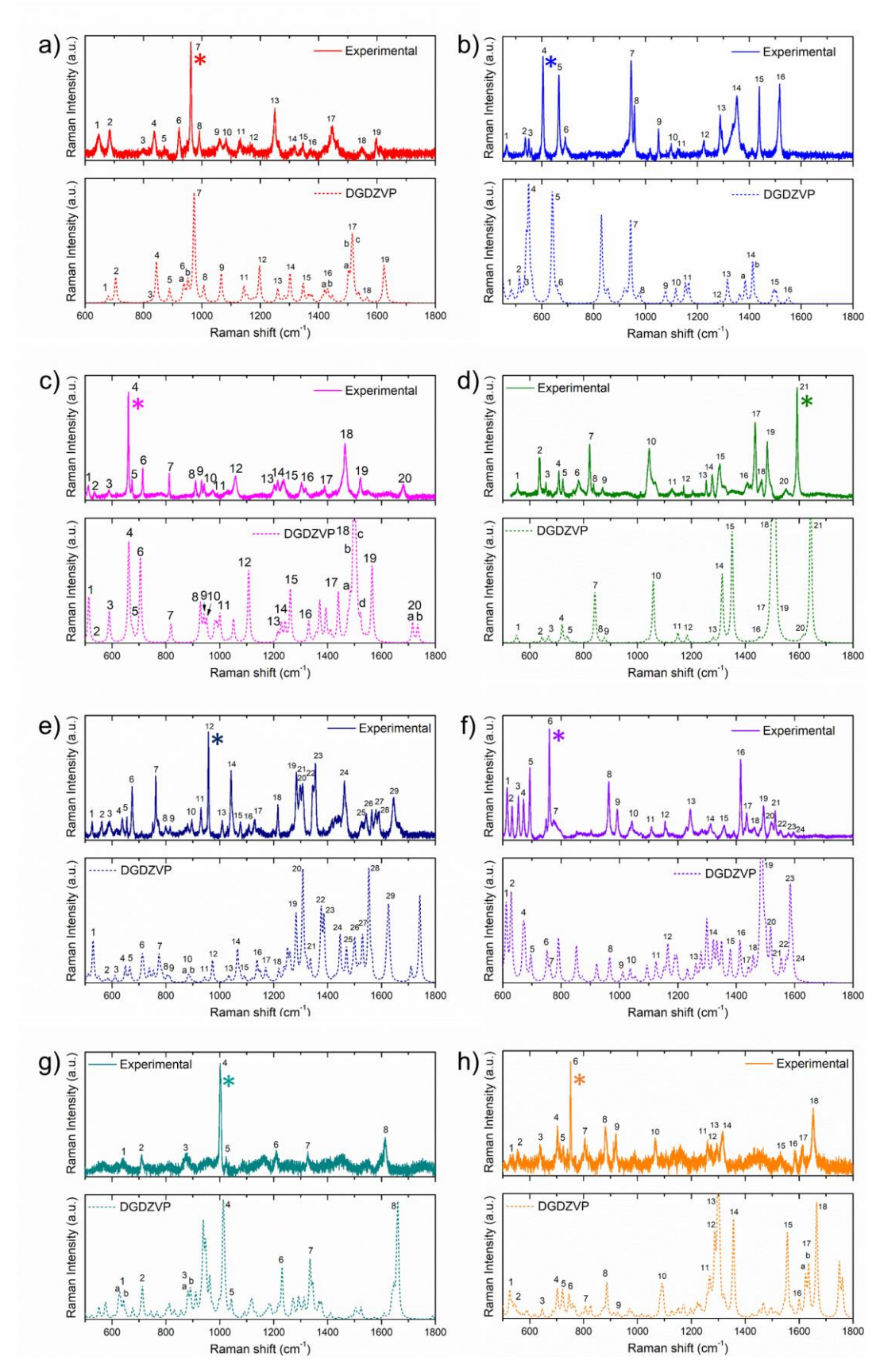


Figure 6.11 Comparison of the experimental and calculated (at the DGDZVP B3LYP level of theory) Raman spectra of all the agrochemicals tested in this thesis.

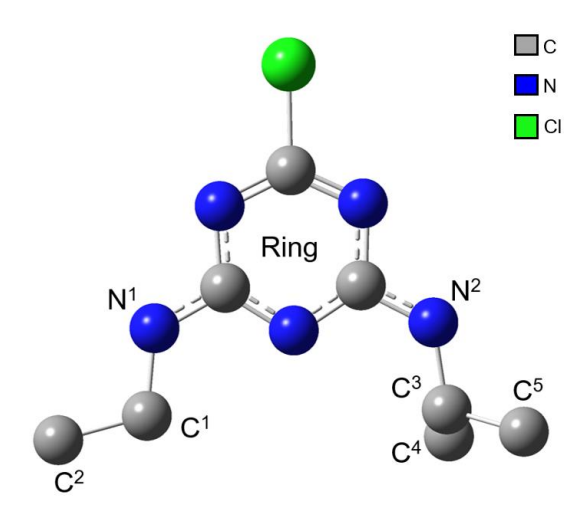


Figure 6.12 Optimized structure of Atrazine

Atrazine is a herbicide which is highly studied in the literature. The comparison of the experimental and theoretical Raman spectra is shown in Figure 6.11 (a). The vibrational mode number and their corresponding experimental and calculated wavenumbers are shown in 6.6. At the lower wavenumbers (500 to 1000 cm⁻¹), the ring modes dominated the Raman spectrum, which is consistent with the results in the literature for a single ring type molecule [317, 318]. Vibrational modes 1 to 8 are dominated by the vibration of the triazine type ring, although the modes were influenced by the heavy chlorine atom. The ring mode 18a type of vibration is present at 646 cm⁻¹. The ring mode 6a dominated the vibrational mode at 683 cm⁻¹, 837.5 cm⁻¹, and 872 cm⁻¹, in the latter two modes, the involvement of ethyl and propyl group was also seen. The ring mode 4 with out of plane vibrations was seen at 800.5 cm⁻¹. The most intense vibrational mode of atrazine was the ring mode 7, which was at 962 cm⁻¹, corresponded to the ring mode 12. The ring mode 12 was also a major element in the vibrational mode at 991 cm⁻¹. Also, at higher wave numbers, ring mode 18b was observed at 1250.5 cm⁻¹ and 8b was seen at 1373 cm⁻¹ and 1599 cm⁻¹. The reason pertains to the reported C N stretching around 1250 cm⁻¹ [325]. The C C and C H bonds in the ethyl and propyl groups also create major vibrational modes in the Raman spectrum. The combination of twisting of C⁴H₂ and C⁵H₂ groups and antisymmetric stretching of C³C₃H₆ group led to the vibrational mode at 921.5 cm⁻¹. The antisymmetric of C³C₃H₆ group also causes the vibrations at 1131.5 cm₋₁. The stretching of C¹ C² bond led to the vibrational mode at 1060 cm₋₁. Further, the twisting of C²H₃ led to Raman mode at 1317.5 cm₋₁. The mode 17, which was of very high intensity in the calculated Raman spectrum, was a combination of twisting and scissoring of C⁴H₃, C⁵H₃ and C²H₃. As mentioned previously, the unrestricted vibration of the hydrogen containing groups caused their much higher intensity in the calculated spectrum compared to the experimental. The symmetric bending (umbrella type) of the C²H₃, C⁴H₃, and C⁵H₃ contributed to Ring mode 8b in the 16 Raman mode at 1446.5 cm⁻¹. The bending of the C³ H bond caused the Raman mode at 1346.5 cm⁻¹. Similar to the reported range of 1250 cm₋₁ [325], C³ N² stretching was observed at 1170.5 cm⁻¹. N¹ H bond bending was the major contributor for 1549 cm⁻¹ mode and minor contributor to the mode at 1599 cm⁻¹.

The validation of the calculation was confirmed by comparing the assigned vibrational modes with the literature [329]. All the major vibrational modes were consistent with the literature. This confirms that the DGDZVP basis set provides an accurate calculation of the vibrational mode of agrochemicals.

6.2.3.2 Mancozeb

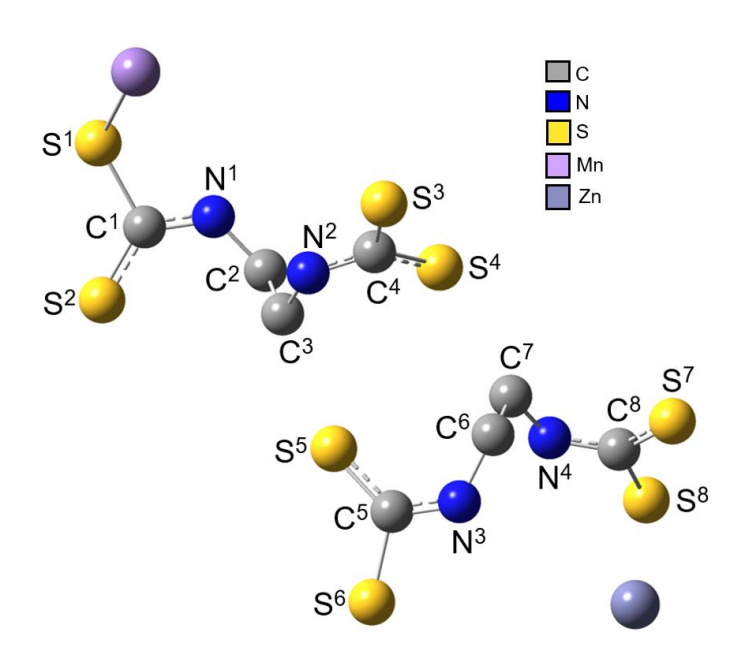


Figure 6.13 Optimized structure of Mancozeb

Mancozeb is a complex molecule of a non systematic dithiocarbamate type structure comprising of N and S atoms. It is a combination of two structures, Maneb (with Mn) and Zineb (with Zn); therefore, simulations were performed on two structures, as shown in Figure 6.13. Although similar vibrational modes were obtained for both at close proximity of wavenumbers, the asymmetric structure of the Maneb due to the proximity of Mn atom to the S¹ atom caused a considerable increase in some of the vibrational modes. The Zineb part of the optimized structure was very symmetric. The Maneb part of the structure dominated the spectrum, as observed in the vibrational modes in Table 6.6. The symmetric bending of the C¹ (at centre) along with S¹S²N¹ was the major vibrational mode at 536 cm⁻¹. The symmetric counterpart of the Zineb was at 550.5 cm⁻¹. The S¹ H bending was the main vibrational mode at 945 cm⁻¹. The stretching of the C N bonds in Maneb was the dominant vibrational mode at 1099 cm⁻¹ ¹. The N² H bending and N¹ H bending were the major modes at 464.5 cm⁻¹ and 605 cm⁻¹, respectively. The Zineb part with N³ H bending was present at 1517.5 cm⁻¹. The stretching of the central carbons in the Maneb and Zineb was the major mode at 957 cm⁻¹ and 1124.5 cm⁻¹, respectively. Moving to the modes with the C H bonds, similar vibrational modes were present for both Maneb and Zineb at a similar range of wavenumbers. The rocking of the central CH₂ bonds was observed at 667 cm⁻¹ and 1051 cm⁻¹. The twisting of the central CH₂ bonds was seen at 691.5 cm⁻¹ and 1224.5 cm⁻¹. Twisting of

the central CH₂ bonds was present for Maneb at 1289 cm⁻¹ with movement of one hydrogen only dominating the vibrational mode. The wagging of the central CH₂ bonds in Maneb and Zineb dominated the vibrational mode at 1352.5 cm⁻¹. The in plane symmetric bending (scissoring mode) of the central CH₂ bonds was the major mode at 1438.5 cm⁻¹. The vibrational modes 4 and 5 were the major vibrational modes for both experimental and simulation Raman spectra.

Table 6.6 Comparison of experimental and calculated wavenumbers of the main peaks of Atrazine and Mancozeb (bold text indicates vibrational modes with major contribution from Zineb) with their vibrational mode assignment.

	Atrazine					Mancozeb		
Mode	Experimental Raman shift (cm ⁻¹)	Calculated Raman shift (cm ⁻¹)	Assignment	Mode	Experimental Raman shift (cm ⁻¹)	Calculated Raman shift (cm ⁻¹)	Assignment	
1	646	680.65	Ring mode 18a	1	464.5	482.06	$N^2 H \delta$, $N^1 H \delta$ (smaller)	
2	683	704.85	Ring mode 6a	2	536	514.04	$C^1 S^1 S^2 N^1 \delta s, C^2 H2 \rho, C^3 H_2 \rho, N^2 H$ $\delta \& C^4 S^3 S^4 N^2 \delta s$	
3	800.5	820.97	Ring mode 4	3	550.5	530.19	$C^5 S^5 S^6 N^3 \delta s, C^8 S^7 S^8 N^4 \delta s, N^4 H \delta,$ $C^6 H_2 \rho \& C^7 H_2 \rho$	
4	837.5	844.44	Ring mode 6a, $C^3C_2H_6 \nu_s$ & $C^2H_3 \delta_{as}$	4	605	540.71	$N^1 H \delta$, $C^1 S^1 S^2 N^1 \delta s \& C^4 S^3 S^4 N^2 \delta s$	
5	872	889.35	Ring mode 6a, $C^{3}C_{2}H_{6} \nu_{s}$, $C^{1}H_{2} \delta_{as} \& C^{2}H_{3} \delta_{as}$			549.53	N^1 H δ & N^2 H δ (smaller)	
6	921.5	936.47	$C^{4}H_{3}\tau,C^{5}H_{3}\tau,\&C^{3}H\delta$	5	667	640.64	$C^{2}H_{2} \rho$, $C^{3}H_{2} \rho$, $C^{1} S^{1}S^{2} \nu s \& C^{2}$ $S^{3}S^{4} \nu s$	
		952.53	$C^3C_2H_6\nu_{as}$			644.16	$C^{6}H_{2} ho, C^{7}H_{2} ho, C^{5} S^{5}S^{6} vs \& C^{8}$ $S^{7}S^{8} vs$	
7	962	973.63	Ring mode 12	6	691.5	658.73	$C^{2}H_{2} au, C^{3}H_{2} au, C^{2} S^{3}S^{4} vs \& C^{1}$ $S^{1}S^{2} vs$	
8	991	1006.83	Ring mode 12, C^1 C^2 ν , C^4H_3 , δ_{as} & C^5H_3 δ_{as}			670.02	$C^{6}H_{2} \tau, C^{7}H_{2} \tau, C^{6} S^{5}S^{6} vs \& C^{8}$ $S^{7}S^{8} vs$	
9	1060	1066.3	C^1 C^2 v	7	945	942.79	S^1H δ , S^4H δ (smaller), C^3H_2 ρ & C^4H_2 ρ	
10	1083.5			8	957	973.71	C^2 C^3 v, C^4 S^3 S^4 vas, S^3 H δ & N^2 H δ	
11	1131.5	1143.92	$C^3C_2H_6 \ \nu_{as}$			978.89	C ⁶ C ⁷ v, C ⁶ S ⁵ S ⁶ vas, C ⁸ S ⁷ S ⁸ vas, S ⁶ H δ, S ⁸ H δ, N ³ H δ & N ⁴ H δ	
12	1170.5	1197.56	$C^3 N^2 \nu$	9	1051	1073.22	$C^{2}H_{2} \rho, C^{3}H_{2} \rho, C^{2} C^{3} \nu, C^{2} N^{1} \nu \& C^{3} N^{2} \nu$	
13	1250.5	1260.11	Ring mode 18b			1078.31	$C^{6}H_{2} \rho, C^{7}H_{2} \rho, C^{6} C^{7} v, C^{6} N^{3} v \& C^{7} N^{4} v$	
14	1317.5	1302.14	C^2H_3 τ & C^1H_2 ρ	10	1099	1116.97	C^2 N ¹ v, C^3 N ² v, (overall not symmetric) S ¹ H δ & S ⁴ H δ	
15	1346.5	1347.02	$C^3H\delta$	11	1124.5	1153.68	$C^2 C^3 v$, $C^2 N^1 v$ & $C^3 N^2 v$ (symmetric)	
16	1373	1420.36	Ring mode 8b, N^1H δ , N^2H δ , C^2H_3 δ_s , C^1H_2 ω & C^3H δ			1166.99	C ⁶ C ⁷ v, C ⁶ N ³ v & C ⁷ N ⁴ v	
		1430.44	$C^{2}H_{3} \delta_{s}, C^{4}H_{3} \delta_{s} \& C^{5}H_{3}$ δ_{s}	12	1224.5	1272.93	$C^2H_2\tau\;\&\;C^3H_2\tau$	
17	1446.5	1503.78	C ⁴ H ₃ τ & C ⁵ H ₃ τ			1288.84	$C^{6}H_{2} \tau \& C^{7}H_{2} \tau$	

		1512.93	$C^2H_3 au$	13	1289	1315.83	$C^2H_2\tau$ & $C^3H_2\tau$ (movement of
							only one H)
		1516.25	$C^2H_3 \; \delta_s, C^4H_3 \; \delta_s \; \& \; C^5H_3 \; \delta_s$	14	1352.5	1383.68	$C^2H_2~\omega,C^3~H~\delta$ (smaller), $C^1~C^2~\nu,$
							N^1 H δ,N^2 H δ,C^6H_2 ω,C^7H_2 ω,C^6
							$C^7\nu$ & N^3 H δ,N^4 H δ
18	1549	1564.81	$N^1 H \delta, N^2 C$ (of ring) v &			1385.53	$C^2H_2\:\omega,C^3H\:\delta,C^1\:C^2\:\nu,N^1\:H\:\delta,N^2$
			$C\ N\ \nu\ (on\ N^1\ side\ of\ ring)$				H δ , C^6H_2 ω , C^7H_2 ω , C^6 C^7 ν , N^3 H
							$\delta \ \& \ N^4 \ H \ \delta$
19	1599	1623.84	Ring mode 8b, $N^1H\delta$,			1413.45	$C^3H_2~\omega,C^2H~\delta,C^1~C^2~\nu,N^1~H~\delta$ &
			$N^2H\ \delta\ \&\ Ring\ mode\ 8b$				$N^2 H \delta$
						1413.64	C^6H_2 ω , C^7H_2 ω , C^6 C^7 v , N^3 H δ
							& N ⁴ H δ
				15	1438.5	1489.93	C^2H_2 δs (in plane), C^3H_2 δs (in
							plane) (smaller), $N^2H\delta$ & $N^1H\delta$
						1494.53	C^3H_2 δs (in plane), C^2H_2 δs (in
							plane) (smaller), $N^2H\;\delta\;\&\;N^1H\;\delta$
						1503.16	C6H2 os (in plane), C7H2 os (in
							plane), N2 H δ & N1 H δ
				16	1517.5	1553.35	N^3 H δ & N^4 H δ

6.2.3.3 Clofentezine

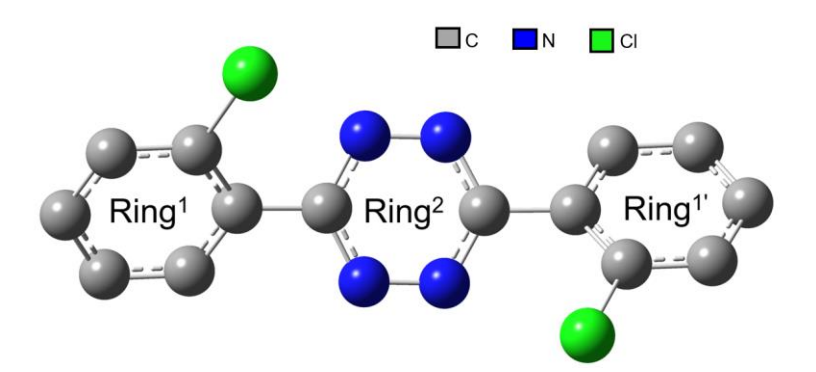


Figure 6.14 Optimized structure of Clofentezine

The structure of Clofentezine has 3 rings (as shown in Figure 6.14), a tetrazine ring and two chlorophenyl rings. Since, the structure is very symmetric, the majority of phenyl ring modes are also symmetric. The presence of the heavy chlorine atom has a major effect of the vibrational modes, the ring modes are imbalanced; however, the Wilson nomenclature still nicely describes all the vibrational modes [316]. The ring mode 4 which is an out of plane bending type vibration is present at 555.5 cm⁻¹ and 781.5 cm⁻¹ for ring 1 and 1'. Another type of out plane bending, ring mode 10a was seen for the ring 1 and 1' at 837.5 cm⁻¹ and 872 cm⁻¹. Coming to the stretching type vibrations, ring mode 6a in ring 1 and 1' was the major contributor for the Raman mode at 636.5 cm⁻¹, 660.5 cm⁻¹, and 822 cm⁻¹. The degenerate modes of the ring mode 18, i.e. ring mode 18a and 18b were present throughout the Raman spectrum of Clofentezine. The ring mode 18a was seen for ring 1 and ring 1' at 708.5 cm⁻¹ and 1255 cm⁻¹. The ring mode 18b was observed for both the rings at 1127 cm⁻¹, 1171.5 cm⁻¹, 1408 cm⁻¹, and 1482 cm⁻¹. The ring mode with stretching in the outward direction for all the components, ring mode 1, was

seen for ring 1 and 1' at 1044 cm⁻¹. The ring mode 19b was present at 1277 cm⁻¹ and 1305 cm⁻¹. Another ring mode which had two degenerate modes, 9a and 9b, was observed at 1550.5 cm⁻¹ and 1592.5 cm⁻¹. The mode in which the tetrazine ring (ring 2) was the major contributor was observed at 1437.5 cm⁻¹ and 1460 cm⁻¹, stretching of the N N bonds in ring 2 caused the Raman peaks, which is similar to the reported value of 1400 cm⁻¹ [330]. As expected, the symmetric nature of the molecule leads to a highly intense Raman response due to the increased polarizability. This phenomenon was observed both in the experimental and calculated Raman spectra. As observed in the previously discussed agrochemicals, the calculated spectra overestimation of the Raman peaks due to the unrestricted vibrations in the calculations. The most intense Raman mode was mode 21 for the experimental Raman spectra, while it was the second most intense for the calculated.

6.2.3.4 Chlorantraniliprole

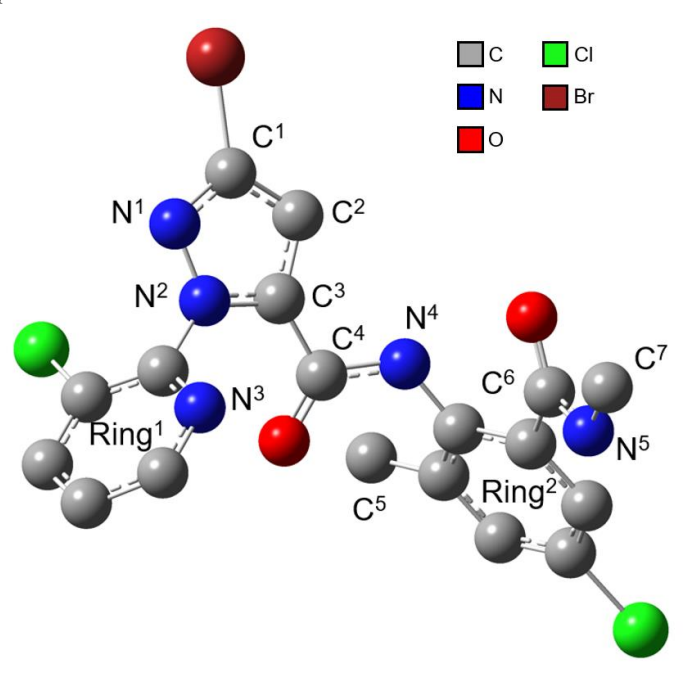


Figure 6.15 Optimized structure of Chlorantraniliprole

The insecticide Chlorantraniliprole has three rings: a dimethylbenzamide ring, a chloropyridine ring, and a 5 member pyrazole ring with a bromine atom. The Wilson nomenclature is generally used for 6 member rings, hence, it was not used for the pyrazole ring. The chloropyridine ring was named as ring 1 and dimethylbenzamide ring was named ring 2 to simplify the explanations. First discussing the modes dominated by ring 1. The ring mode 4, 6a, 11, 12, 1, 8a and 18a was observed at 563 cm⁻¹, 654.5 cm⁻¹, 798 cm⁻¹, 1009 cm⁻¹, 1041.5 cm⁻¹, 1076.5cm⁻¹, and 1463 cm⁻¹, respectively. All of the ring modes were inplane vibrations. Next, the vibrational modes dominated by ring 2. The degenerate modes of ring mode 9, 9a and 9b, were observed at 1646 cm⁻¹ and 526.5 cm⁻¹. Similarly, ring mode 19a and 19b were seen at 1108 cm⁻¹ and 1284 cm⁻¹. The ring mode 1 was observed at 591 cm⁻¹ and 763 cm⁻¹. Ring

mode 18b was located at 1307.5 cm⁻¹ and 1544 cm⁻¹. Ring mode 6a, 12, 8b and 13 was positioned at 930 cm⁻¹, 897 cm⁻¹, 1129.5 cm⁻¹ and 1214.5 cm⁻¹. The vibrational mode at 1298 cm⁻¹ was a combination of ring mode 18b of ring 1 and ring mode 2 of ring 2. After the ring modes, rest of the Raman peaks comprise of C C bond, CN bond, C H bond, N H bond and C Br bonds. The wagging mode of C² (at center) along with C¹ and C³ was seen at 637.5 cm⁻¹. The stretching of C² C³ bond dominated the mode at 1590.5 cm⁻¹. The antisymmetric stretch of C¹ (at center) along with N¹ and C² was present at 1355 cm⁻¹. Stretching of C (of ring 1) and N² was located at 1563.5 cm⁻¹. The bending of C² H bond was seen at 816 cm⁻¹. The N⁴H bending was present at 675 cm⁻¹ and 1579.5 cm⁻¹. The stretching of C¹ Br bond dominated the vibrational modes at 956 cm⁻¹ and 1344.5 cm⁻¹. This mode was the major vibrational mode the experimental Raman spectrum. The C=O vibrational modes seen in calculated spectrum beyond 1700 cm⁻¹, were not present in the experimental spectrum.

Table 6.7 Comparison of experimental and calculated wavenumbers of the main peaks of Clofentezine and Chlorantraniliprole with their vibrational mode assignment.

		Clofentez	tine	Chlorantraniliprole				
Mode	Experimental Raman shift (cm ⁻¹)	Calculated Raman shift (cm ⁻¹)	Assignment	Mode	Experimental Raman shift (cm ⁻¹)	Calculated Raman shift (cm ⁻¹)	Assignment	
1	555.5	552.1	Ring ¹ mode 4, Ring ¹ mode 4 & Ring ² mode 3	1	526.5	529.61	Ring ² mode 9b	
2	636.5	645.95	Ring ¹ mode 6a, Ring ¹ mode 6a & Ring ² mode 18a	2	563	585.77	Ring ¹ mode 4	
3	660.5	668.95	Ring ¹ mode 6a & Ring ¹ ' mode 6a	3	591	611.29	Ring ² mode 1 & Ring ¹ mode 4	
4	708.5	720.42	Ring ¹ mode 18a, Ring ¹ mode 18a & Ring ² mode 7a	4	637.5	649.4	$C^2 \; C^3 C^4 \; \omega$ & Ring1 mode 6a	
6	723			5	654.5	665.74	Ring1 mode 6a	
5	781.5	740.04	Ring ¹ mode 4 & Ring ¹ mode 4	6	675	711.62	N^4H δ	
7	822	842.24	Ring ¹ mode 6a, Ring ¹ mode 6a & Ring ² mode 6a	7	763	774.06	$Ring^2 \ mode \ 1, \ C^2H \ \delta \ \& \ Ring^1$ $mode \ 4$	
8	837.5	854.62	Ring ¹ mode 10a, Ring ¹ mode 10a & Ring ² mode 4	8	798	805.62	Ring ¹ mode 11	
9	872	880.68	Ring ¹ mode 10a & Ring ¹ mode 10a	9	816	813.29	$C^2H\delta$	
10	1044	1058.58	Ring ¹ mode 1 & Ring ^{1'} mode 1	10	897	882.55	Ring ² mode 12, C Cl v & C ⁷ H ₃ δ_{as}	
11	1127	1150.4	Ring ¹ mode 18b & Ring ¹ mode 18b			887.39	Ring ² mode 5	
12	1171.5	1184.32	Ring ¹ mode 18b & Ring ¹ mode 18b	11	930	944.01	Ring ² mode 6a, C^6 C (of Ring ²) v & C^7 H3 δ_{as}	
13	1255	1280.62	Ring ¹ mode 18a & Ring ¹ mode 18a	12	956	972.98	C^1 Br v & C^1 N^1C^2 δ_s	
14	1277	1314.58	Ring ¹ mode 19b, Ring ¹ mode 19b & Ring ² mode 1	13	1009	1033.66	$Ring^1\ mode\ 12\ \&\ C^3\ C^3N^2\ \delta_s$	
15	1305	1351.42	Ring ¹ mode 19b, Ring ¹ mode 19b, Ring ¹ Ring ² v & Ring ² Ring ¹ v	14	1041.5	1065.98	Ring ¹ mode 1	

16	1408	1451.99	Ring ¹ mode 18b, Ring ¹ mode 18b & Ring ² mode 8b	15	1076.5	1092.39	Ring ¹ mode 8a
17	1437.5	1496.12	N N v, Ring ¹ mode 9b & Ring ^{1'} mode 9b	16	1108	1138.25	Ring2 mode 19a
18	1460	1505.31	NN v, Ring ¹ Ring ² v, Ring ² Ring ^{1'} v, Ring ¹ mode 9b & Ring ^{1'} mode 9b	17	1129.5	1170.32	Ring ² mode 8b
19	1482	1512.93	Ring ¹ mode 18b, Ring ¹ mode 18b & Ring ² mode 8b	18	1214.5	1219.02	Ring 2 mode 13 & N 5 H δ
20	1550.5	1613.96	Ring ¹ mode 9a & Ring ^{1'} mode 9a	19	1284	1283.22	Ring ² mode 19b, N ⁴ H δ & N ⁵ H δ
21	1592.5	1642.79	Ring ¹ mode 9b & Ring ¹ ' mode 9b	20	1298	1307.51	Ring ² mode 2, Ring ¹ mode 18b, & N ⁵ H δ
						1308.92	Ring 1 mode 18b & N 5 H δ
				21	1307.5	1336.24	Ring 2 mode 18b & N 5 H δ
				22	1344.5	1376.02	C^1 Br v, C^1 N^1N^2 vs & C^2H δ
				23	1355	1386.23	$C^1~N^1C^2~\nu_{as},N^2~Ring1~\nu~\&~C^2H$ δ
				24	1463	1446.18	Ring ¹ mode 18b, N ² C ³ v, N ¹ C ¹ v & C ² H δ
				25	1544	1470.08	$Ring^2\ mode\ 18b\ \&\ C^5H_3\ \delta_s$
				26	1563.5	1500.89	C (of ring ¹) $N^2 v$, $C^5 H_3 \delta_s$, N^2 $C^3 v$, & $C^1 N^1 v$
				27	1579.5	1529.35	$N^4 H \; \delta \; \& \; C^5 H_3 \; \delta_s$
				28	1590.5	1553.23	$C^2 \ C^3 \ \nu, C^3 \ N^2 \ \nu, C^3 \ C^4 \ \nu, N^4 H$ $\delta \ \& \ N^5 H \ \delta$
				29	1646	1626.29	Ring ² mode 9a

6.2.3.5 Thiamethoxam

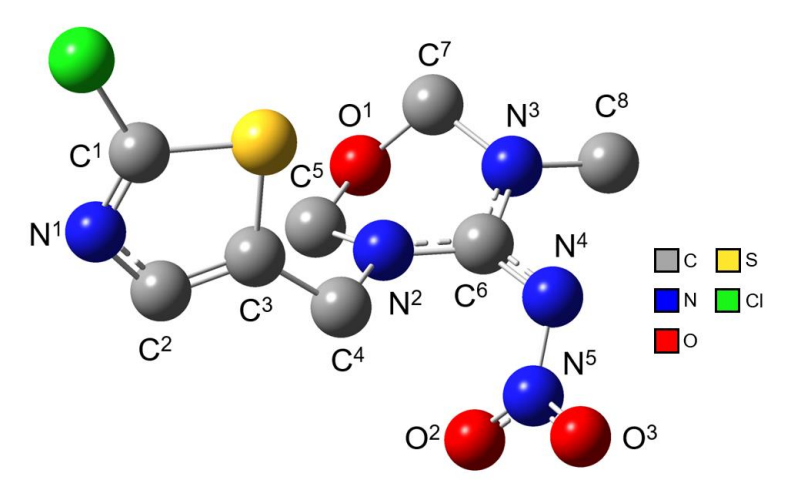


Figure 6.16 Optimized structure of Thiamethoxam

Thiamethoxam's structure has two types of rings, an ozadiazine and a 5 member chlorothiazol type. Since both these ring types do not have a symmetric benzene type structure, Wilson's nomenclature was not used to describe its vibrational modes. Starting with vibrations involving the Cl and S bond. The symmetric stretch of the S (at the centre) along with C¹ and C³ bond was the major vibrational mode at 632 cm⁻¹ and 670.5 cm⁻¹, similar to the reported value of 675 cm⁻¹ [331]. The antisymmetric stretch of

the C¹ (at centre) with Cl and S was seen at 1042 cm⁻¹. Next to the C O bonds, the symmetric bend and stretch of O¹ (at centre) along with C⁵ and C⁻ was located at 614 cm⁻¹ and 964 cm⁻¹, respectively. The stretching of C⁻ O¹ bond was the major vibration at 1108 cm⁻¹. The antisymmetric stretch of the N⁵ (at centre) along with O² and O³ was seen at 1598 cm⁻¹. The stretching of the C⁵ N² and C¹ N¹ bond was present at 1156 cm⁻¹ and 1494 cm⁻¹. The major Raman mode in the experimental spectrum was the in plane symmetric bend (scissoring mode) of C² (at center) along with N¹ and C³ at 760 cm⁻¹. The wagging of N⁴ (at centre) along with N⁵ and C⁶ was located at 778 cm⁻¹. The stretching of the N⁴ N⁵ bond was the major vibration at 694 cm⁻¹. The stretching of the C² C³ bond was seen at 1580 cm⁻¹. Rest of the vibrational modes involved the C H bonds and they dominated the Raman spectra beyond 950 cm⁻¹. The rocking of the C⁴H² bond was observed at 994 cm⁻¹. The twisting of C⁴H², C⁻H² and C⁵H³ were observed at 1244 cm⁻¹, 1312 cm⁻¹, and 1522 cm⁻¹. Wagging of C⁵H² and C⁴H² bond was seen at 1357.5 cm⁻¹ and 1416 cm⁻¹, respectively. The in plane symmetric bending (scissoring mode) of C⁵H² was present at 1534 cm⁻¹ and 1553.5 cm⁻¹.

Table 6.8 Comparison of experimental and calculated wavenumbers of the main peaks of Thiamethoxam and Flubendiamide with their vibrational mode assignment.

		Thiametho	xam		Flubendiamide		
Mode	Experimental Raman shift (cm ⁻¹)	Calculated Raman shift (cm ⁻¹)	Assignment	Mode	Experimental Raman shift (cm ⁻¹)	Calculated Raman shift (cm ⁻¹)	Assignment
1	614	612.01	$O^1 C^5 C^7 \delta_s \& C^6 N^2 N^4 \delta_s$	1	532.5	525.87	Ring ¹ mode 4 & C ⁸ H ₃ δ _{as}
2	632	629.02	$S C^1C^3 v_s, C^6 N^2 v \& C^7 N^3 v$	2	555.5	534.84	C^6 S v, N^1H \delta & N^2H δ
3	652			3	638	646.53	Ring ² mode 6a & Ring ¹ mode 4
4	670.5	670.06	$S \; C^1 C^3 \; \nu_s \; \& \; C^3 \; C^4 \; \nu$	4	703.5	702.33	C^3 S ν
5	694	696.09	$N^4 \; N^5 \; \nu \; \& \; N^5 \; O^2 O^3 \; \delta_s$	5	725	721.29	C ⁶ S v & Ring ¹ mode 6a
6	760	751.72	$C^2N^1C^3\delta_s$	6	752	746.09	Ring ² mode 4, $C^{10}F_3$ δ_s & $C^{11}F_3$ δ_s
7	778	761.68	$N^4C^6N^5\omega$	7	804.5	806.43	Ring ¹ mode 5, Ring ² mode 1 & $C^2C_3H_8 v_s$
8	964	996.83	$O^1 C^5 C^7 \nu_s$	8	881.5	886.15	$Ring^1\ mode\ 12\ \&\ C^3H_2\ \rho$
9	994	1011.03	$C^4 H_2 \rho \& N^4 N^5 \nu$	9	920.5	925.71	$C^2~C^3~\nu,C^4H_3~\delta_{as}~\&~C^5H3~\delta_{as}$
10	1042	1036.58	C^1 CIS ν_{as}	10	1065.5	1084.64	Ring ¹ mode 12
11	1108	1125.32	$C^7 O^1 \nu, C^7 H_2 \rho \& C^8 H_3 \tau$			1090.5	$SO_2 v_s$
12	1156	1165.4	$C^5~N^2~\nu,C^4H2~\tau$ & $C^8H_3~\tau$			1094.59	Ring ¹ mode 1
13	1244	1261.6	$C^4H_2\tau\;\&\;C^2H\delta$	11	1260.5	1269.25	$C^2~N^1~\nu,~S~O_2~\nu_{as},~C_4H_3~\&~C_5H_3$ δ_{as}
14	1312	1320.99	$C^7H_2 \tau \& C^5H_2 \tau$	12	1273	1286.89	N_2H δ , $C_9C_2F_6$ ν_s & Ring ² mode 18b
15	1357.5	1379.41	C^5H_2 ω & C^7H_2 ω	13	1294	1299.2	Ring ² mode 1, N ² H δ & C ⁹ C ₂ F ₆ v_s
16	1416	1412.73	C^4H_2 ω	14	1316	1356.19	Ring ² mode 18b & C ⁶ H ₃ δ_s
17	1436	1441.61	$C^{8}H_{3} \delta_{s}, C^{5}H_{2} \omega \& C^{6}H_{2} \omega$	15	1530	1556.13	N^2H δ & Ring ² mode 8a
18	1462	1457.91	$C^{8}H3 \delta_{s}, C^{5}H_{2} \omega \& C^{6}H_{2} \omega$	16	1585	1600.52	Ring ¹ mode 9a (I top)
19	1494	1486.49	$C^1 \ N^1 \ \nu, C^2 \ C^3 \ \nu \ \& \ C^4 H_2 \ \tau$	17	1613	1624.02	Ring ¹ mode 9a (I side)

20	1522	1519.06	$ m C^8H_3~ au$			1635.38	Ring ² mode 9a (N side) & N^2H δ
21	1534	1553.83	$C^5H_2 \; \delta_s, C^6 \; N^3 \; \nu \; \& \; C^8H_3 \; \delta_s$	18	1653	1665.05	Ring ² mode9a (N top)
22	1553.5	1570.98	$C^5H2~\delta_s,~C^6~N^4~\nu~\&~N^5~O^2O^3$				
			ν_{as}				
23	1580	1585.09	$C^2 \; C^3 \; \nu \; \& \; C^2 H \; \delta$				
24	1598	1592.09	$N^5~O^2O^3~\nu_{as}, C^6~N^3N^4~\nu_{as}, C^8H_2$				
			$\omega \& C^7H \delta$				

Table 6.9 Comparison of experimental and calculated wavenumbers of the main peaks of Taufluvalinate with its vibrational mode assignment.

	Tau-fluvalinate					
Mode	Experimental Raman shift (cm ⁻¹)	Calculated Raman shift (cm ⁻¹)	Assignment			
1	642	623.96	Ring ³ mode 3			
		642.87	Ring ² mode 3			
2	710	712.81	Ring ² mode 5 & Ring ¹ mode 3			
3	875	881.5	Ring ¹ mode 1 & Ring ² mode 5			
		890.96	Ring ² mode 5			
4	1001	1016.36	Ring ³ mode 12			
5	1023	1042.91	Ring ³ mode 19a			
6	1209	1230.95	Ring ³ mode 19a, Ring ² mode			
			19a & C ⁷ H δ			
7	1326	1334.22	$C^7H\delta$			
8	1614	1660.83	Ring ¹ mode 9a			

6.2.3.6 Tau-fluvalinate

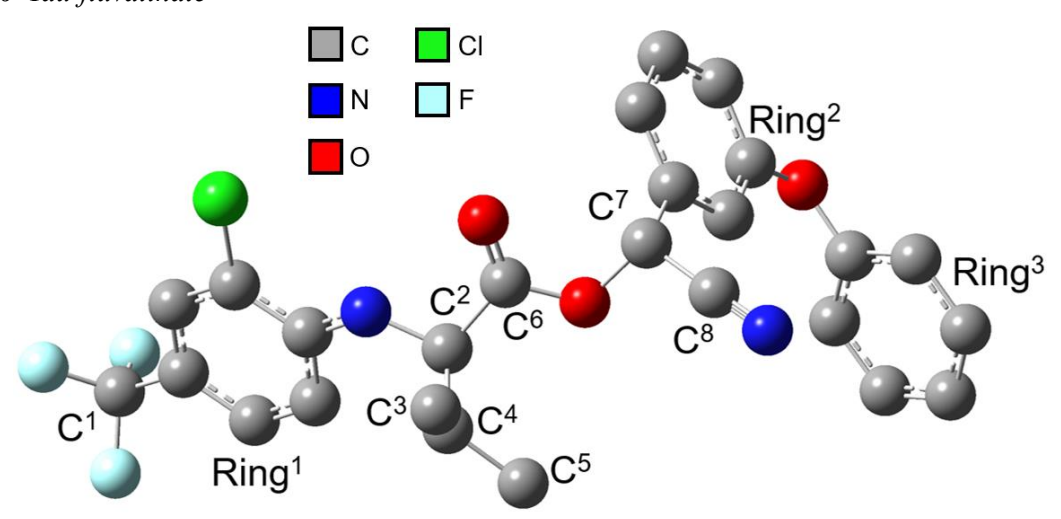


Figure 6.17 Optimized structure of Tau-fluvalinate

Tau-fluvalinate has 3 rings, an anilino ring (named ring 1) and 2 phenyl type rings in the phenoxyphenyl group (named ring 2 and ring 3). The ring modes dominate both the calculated and experimental Raman

spectra. The vibrational modes in ring 1, ring mode 1 and 9a were seen at 875 cm⁻¹ and 1614 cm⁻¹. The ring mode 5 in ring 2 also contributed to the vibrational mode at 875 cm⁻¹. The ring mode 5 for ring 2 was present at 710 cm⁻¹. Ring mode 3 for ring 2 and ring 3 contributed to the vibrational mode at 642 cm⁻¹. Also, ring mode 19a for ring 2 and ring 3 participated in the mode 1209 cm⁻¹. For the ring 3, the ring mode 12 and 19a were seen at 1001 cm⁻¹ and 1023 cm⁻¹. The ring mode 12 at 1001 cm⁻¹ was the dominant mode in the experimental Raman spectrum. The bending of the C⁷ H bond was observed at 1326 cm⁻¹.

6.2.3.7 Flubendiamide

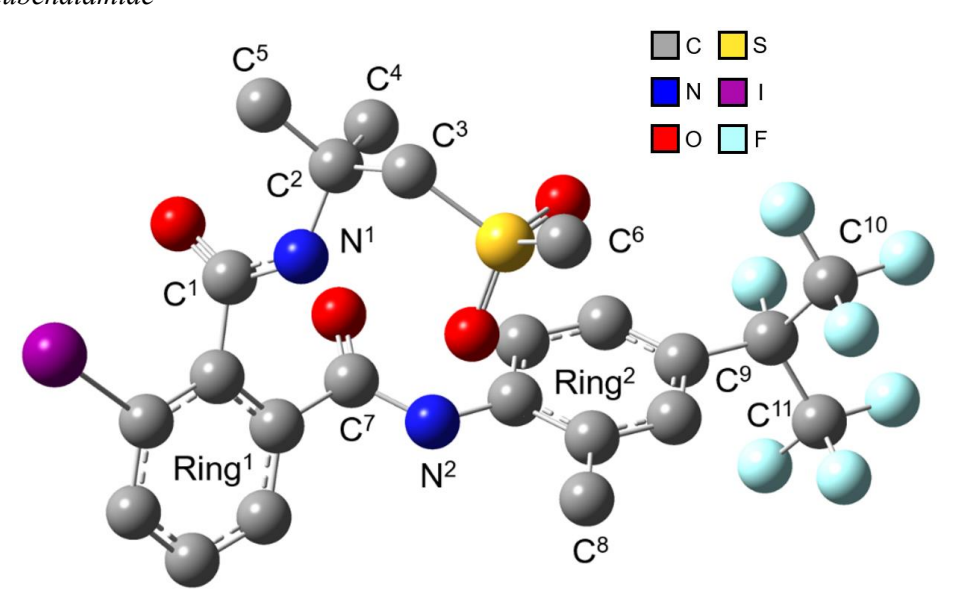


Figure 6.18 Optimized structure of Flubendiamide

Flubendiamide has two rings, a phenyl and a phthalimide type ring, which are labelled as ring 1 and ring 2 to simplify the discussion of the vibrational modes. The vibrational modes involving ring 1, ring mode 4 and ring mode 5 were seen at 532.5 cm⁻¹ and 804.5 cm⁻¹, respectively. Ring mode 12 was present at 881.5 cm⁻¹ and was a major component for the vibrational mode at 1065.5 cm⁻¹. The ring mode 1 and symmetric stretch of S (at centre) O₂ bond also contributed to mode at 1065.5 cm⁻¹. The ring mode 9a was seen at both 1585 cm⁻¹ and 1613 cm⁻¹, however, in the former, the iodine atom was at the top and at the side in the latter, as per Wilson's nomenclature. Ring 2 also contributed to the mode at 1613 cm⁻¹ with the ring mode 9a (with N² on the side). The ring mode 2 (with N² at the top) for ring 2 was present at 1653 cm⁻¹. Other contributions by the ring 2 were ring mode 6a, 1, and 18b at 638 cm⁻¹, 1294 cm⁻¹ and 1316 cm⁻¹, respectively. The ring mode 4 (of ring 2) and the symmetric bending (umbrella mode) of C¹⁰F₃ and C¹¹F₃ were the major Raman modes for the experimental spectrum at 752 cm⁻¹. The stretching of the C⁶ S bond was present at 555.5 cm⁻¹ and 725 cm⁻¹. Also, C³ S stretching was seen at 703.5 cm⁻¹. The stretching of C² C³ bond and C² N¹ bond was observed at 920.5 cm⁻¹ and 1260.5 cm⁻¹. The bending of N² H bond was present at 1273 cm⁻¹ and 1530 cm⁻¹. As seen for Chlorantraniliprole,

the vibrational modes of C=O bond were observed beyond 1700 cm⁻¹ in the calculated spectrum but were missing in the experimental.

6.2.4 Error analysis of the calculated wavenumbers

Fig 3 presents the error in Raman shift, the difference in the calculated and the experimental wavenumber. In general, the calculated wavenumbers were greater than the experimental, for the majority of the vibrational modes, as seen in Figure 6.19. However, the intensity of the calculated peaks had a higher discrepancy due to the overestimation caused due to unrestricted vibrations. The average error in the calculated and experimental wavenumbers was less than 35 cm⁻¹ as shown in Figure 6.20.

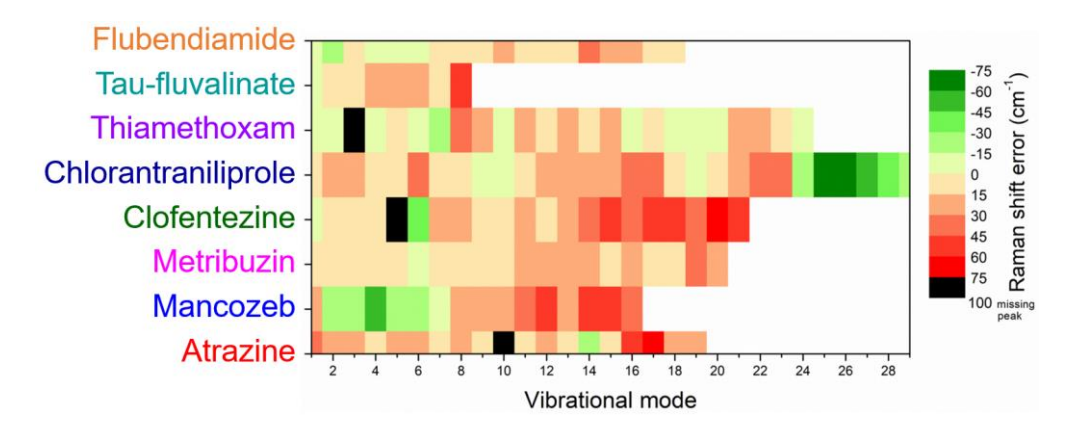


Figure 6.19 Comparison of the Raman shift error for the vibrational modes in the tested agrochemicals.

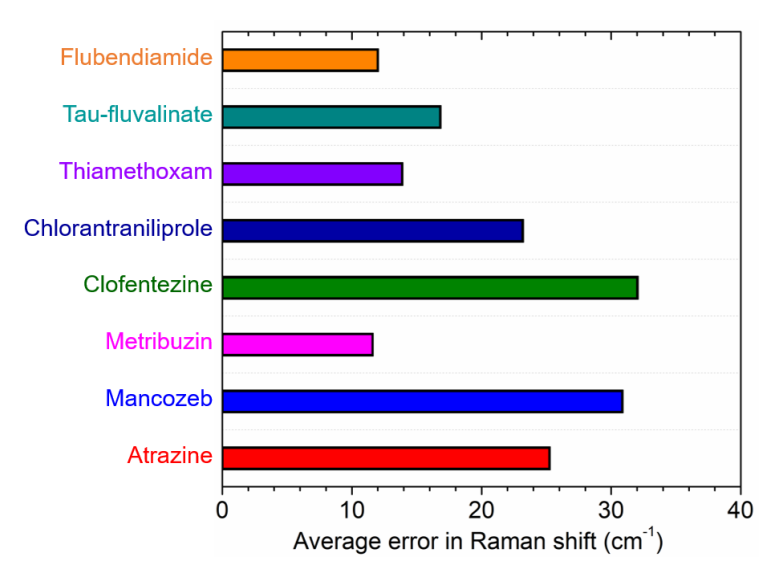


Figure 6.20 Comparison of the average of the absolute error in Raman shift for the tested agrochemicals.

6.3 Testing of various agrochemicals using the optimal substrate

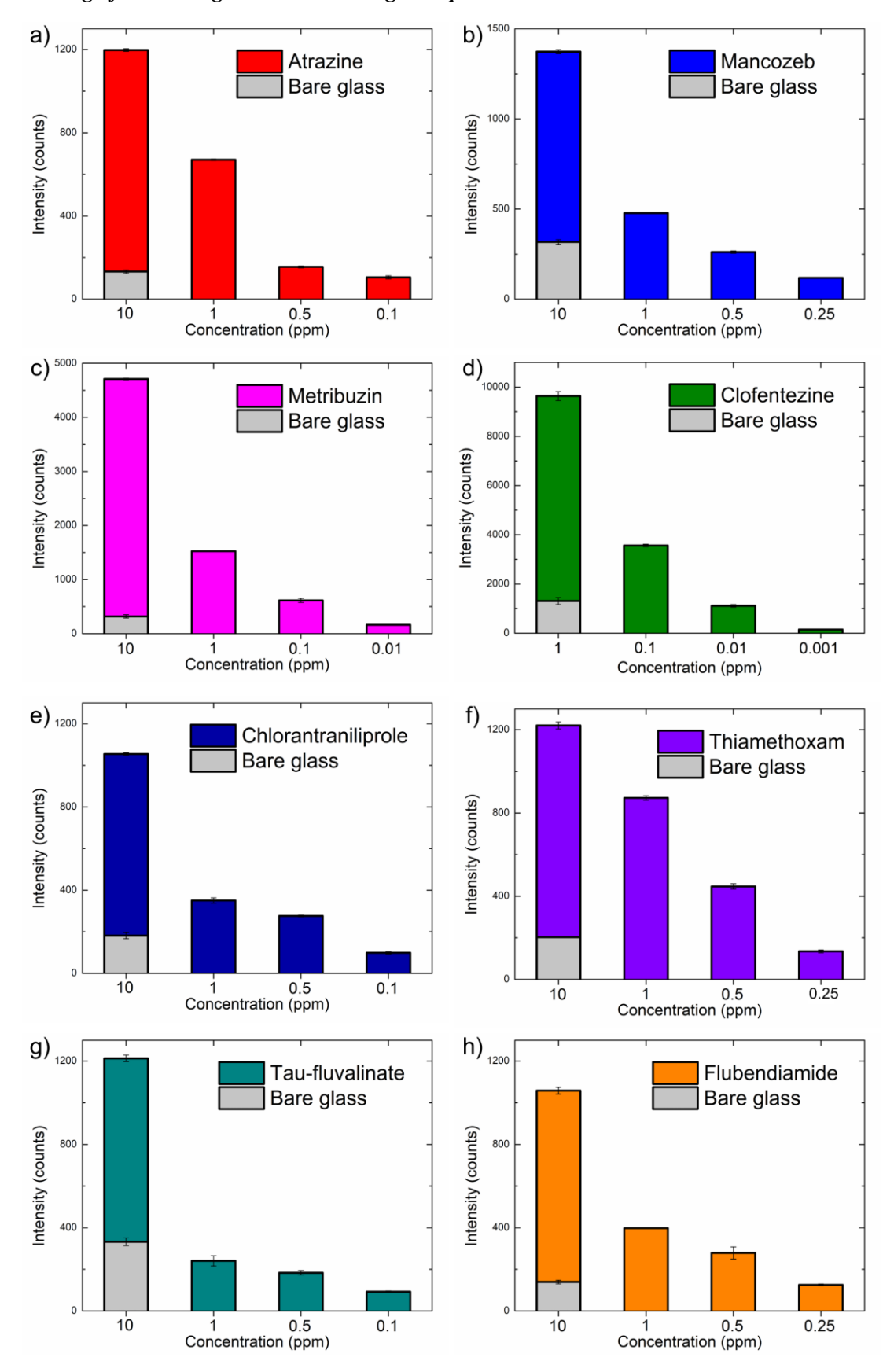


Figure 6.21 The limit of detection (LOD) of the agrochemicals testing using the optimal sample fabricated using LIL.

The optimal SERS substrate fabricated using LIL described in section 6.1 was used to detect the agrochemicals mentioned in section 6.2. The Raman measurements were performed using the Horiba LabRAM HR via a 633 nm laser (Melles Griot) and 100x objective lens with 0.8 numerical aperture. The measurements for all the agrochemicals were performed for an accumulation time of 18 seconds with 3 acquisitions. The power of the laser used for Atrazine and Mancozeb was 0.425 mW, and for the remaining agrochemicals was 1.7 mW. The reason is that at higher power, Atrazine and Mancozeb showed lower signals. Aqueous solutions with varying concentrations of the agrochemicals were prepared, and the concentration values were calculated according to the percentage of the major chemical present. 5 μ L of agrochemical solution was drop cased on bare glass substrate and 300 nm period gold nanodisk substrate, and was allowed to dry naturally.

Table 6.1 Comparison of the detection limit of the tested agrochemicals in the literature

Agrochemical	SERS substrate	LOD (ppm)	Ref
Atrazine	Gold nanorods	21.5	[329]
	Porous gold supraparticle surface	8	[330]
	Gold-coated nanosubstrates	0.1	[331]
	Gold nanodisk array	0.1	This work
	Silver nanorods	0.07	[326]
	Silver nanoparticle modified carbon dots	0.002	[332]
Mancozeb	Silver nanoparticles	500	[333]
	Silver colloids	0.5	[334]
	Gold nanodisk array	0.25	This work
	Silver@gold alloyed nanorods	0.05	[335]
Metribuzin	Gold nanodisk array	0.01	This work
Clofentezine	Gold nanodisk array	0.001	This work
Chlorantraniliprole	Gold nanodisk array	0.1	This work
Thiamethoxam	Self-Assembled gold Nanoparticle Array	3	[336]
	Silver nanoparticles (nanoparticles)	0.3	[337]
	Gold nanodisk array	0.25	This work
	Gold nanoparticles on an adhesive substrate	0.003	[194]
Tau-fluvalinate	Gold nanodisk array	0.1	This work
Flubendiamide	Gold nanodisk array	0.25	This work

The peaks marked with the star in the experimental Raman spectra in Figure 6.11 were used as the major peaks to experimentally check the LOD of the various agrochemicals. As shown in Figure 6.21, Clofentezine had the lowest LOD of 0.001 ppm due to the highly symmetric structure of the molecule leading to higher Raman signal compared to the other agrochemicals. Metribuzin also had a strong Raman signal in the calculated and experimental Raman spectra; hence, an LOD of 0.01 ppm was observed. Atrazine, Chlorantraniliprole, and Tau-fluvalinate had a similar detection limit of 0.1 ppm. Due to the lower excitation power being used, Mancozeb, Flubendiamide, and Thiamethoxam had a LOD of 0.25 ppm. The comparison of the agrochemicals of the current work and the literature is presented in Table 6.1. The substrates showing a higher LOD all had non periodic structures, which generally tend to have variable Raman signals across the sensing substrate. The vibrational modes and, therefore, Raman spectra of Metribuzin, Clofentezine, Chlorantraniliprole, Tau-fluvalinate, and Flubendiamide have not been reported in the literature.

6.4 Chapter summary

LIL is an easy and high throughput technique to fabricate nanostructured SERS substrates which can be reused multiple times. The LIL method was used to fabricate gold nanodisk arrays on glass with periods 250 nm, 300 nm, 344 nm, 395 nm, and 446 nm. The transmission response of the LIL substrates was used to compare their resonance wavelength. Furthermore, the resonance wavelength could be tuned by varying the period of the array. The SERS response of the LIL substrates was compared using the chemical Rhodamine 6G. The 300 nm period (diameter 140 nm) substrate displayed the highest enhancement because of the vicinity of the plasmonic peak wavelength to the excitation source wavelength and the target molecule wavelength, and an intense plasmonic response. The average EF for the 300 nm period LIL substrate was 2.3 x 10⁶. To verify its practical use as a SERS substrate, the Raman response of varying concentrations of urea was measured. The detection limit of urea was 0.05 mM (0.5 ppm) for the optimal LIL substrate.

The optimal LIL sample was intended to be used to detect agrochemicals. Various types of agrochemicals being used by the farmers were collected. One each of herbicide (Atrazine), fungicide (Mancozeb), acaricide (Clofentezine), and weedicide (Metribuzin) were analyzed. Four extremely harmful insecticides (Chlorantraniliprole, Thiamethoxam, Tau-fluvalinate, and Flubendiamide) were also studied. The vibrational analysis of the majority of the agrochemicals was lacking, which is essential for scientists and engineers to develop more efficient SERS based substrates. DFT calculations were used to verify the experimental spectra and assign vibrational modes to the major Raman peaks. The calculations were performed using GAUSSIAN software. Initially, the calculations were validated by comparing the experimental and calculated structure of Metribuzin. The Raman vibrational modes were assigned for the same, and a basis set comparison was performed to select the basis set with a good compromise between accuracy and computational cost. The DGDZVP basis set at the B3LYP level of theory was selected to calculate the Raman spectra of all the agrochemicals. The

vibrational theory was selected to calculate the Raman spectra of all the agrochemicals. The vibrational modes assignment and analysis was performed for all the agrochemicals. The calculated spectra showed good accuracy for the position (wavenumber) of the Raman peaks; however, there was discrepancy in the intensity of the peaks due to the unrestricted vibrations in the calculated molecules. The limit of detection (LOD) of the aforementioned agrochemicals was tested on the optimized LIL substrate. It was observed that Clofentezine had the lowest LOD of 0.001 ppm because of its symmetric structure. Metribuzin had a strong Raman signal in the calculated and experimental Raman spectra, hence, a LOD of 0.01 ppm was observed. Atrazine, Chlorantraniliprole, and Taufluvalinate had LOD close to 0.1 ppm. Lower excitation power was used for Mancozeb and Flubendiamide, hence, they had a lower LOD of 0.25 ppm. The LOD of the agrochemicals used in the literature was compared with the optimized gold nanodisk array substrate.

Chapter 7. Conclusion and Future Scope

7.1 Conclusion

The exciting properties and applications of plasmonic nanostructures for sensing agrochemicals were presented in the current thesis.

FEM simulations were used to analyse the effect of size, shape, material and surrounding environment on the plasmonic response of single nanoparticles and nanoarrays. The single nanoparticle simulations confirmed that silver and gold had an excellent plasmonic response. Although copper and aluminium have the potential to be used as economical plasmonic materials, the high losses in the visible region limited their practical use. Therefore, gold was selected for fabrication because of its strong plasmonic response, low losses, and high stability. The dipole resonance (LSPR) caused a massive increase in the electric field confinement of the region surrounding the nanoparticle. Arranging the single nanostructures into periodic arrays combined the near field (LSPR) and far field (grating resonance due to the array) resonances. The simulations of periodic nanoarrays showed that this coupling of resonances was strong in the visible wavelength range for nanodisk arrays of diameter greater than 100 nm. The sharpest resonance was observed at the optimal coupling condition, where the near field and far field resonance wavelengths overlapped.

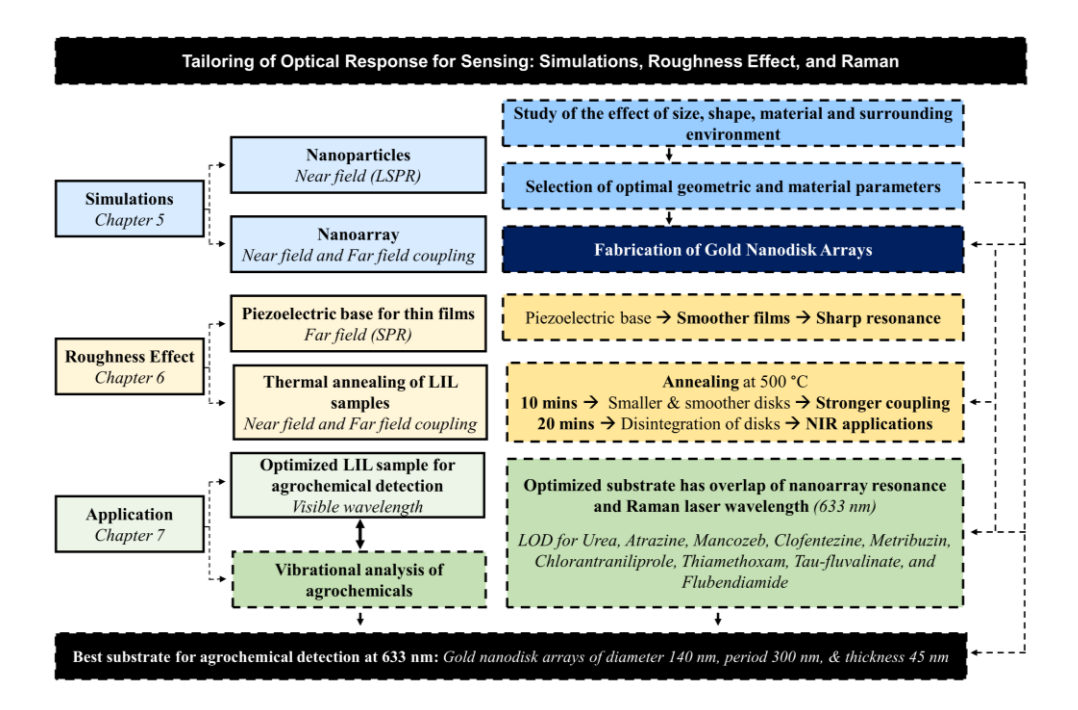


Figure 7.1 Conclusion of the thesis

Hence, gold nanodisk arrays with diameters 110 nm to 200 nm (period to diameter ratio ~2.2) were experimentally fabricated using laser interference lithography (LIL), which is a maskless and high throughput technique. To decrease the wavelength difference between the near field and far field resonances, thermal annealing was performed at 500 °C for 10 minutes and 20 minutes. It was observed

that annealing for 10 minutes significantly decreased the surface roughness and increased the grain size, which decreased scattering losses. Further, annealing causes the gold disk to conglomerate leading to a reduction in diameter and increase in thickness. The modification in the geometric parameters strengthens the coupling of the near and far field resonances by decreasing the wavelength difference between the two resonances. The resonance Q factor for the 187 nm diameter nanodisk array increased from 3.6 to 7.8, and for 220 nm diameter, it increased from 3.2 to 11.5. The improvement in the material properties was confirmed by lowering of the damping constant and increase in oscillator strength in the Lorentz-Drude model which was optimised to fit the simulated plot to the experimental plot.

The improvement in the plasmonic response for smoother surfaces was confirmed by studying the SPR dip of thin gold films. Gold films deposited with a piezoelectric base displayed a lower surface roughness. The smoother films had a lower FWHM of the SPR dip as compared to the film of larger surface roughness of the same thickness. The significant increase in the slope of the resonance angle and wavelength dependant curve established that smoother plasmonic films have a higher sensitivity.

Annealing the gold nanodisks for 20 minutes disintegrated them into much smaller pieces which increased the electric field confinement in the near field response, but due to the decreased size, the far filed resonance was drastically reduced. However, simulations were used to study the effect of disintegration of nanodisks for larger sizes (more than 280 nm) in the NIR wavelength range. Simulation results confirmed that disintegration of larger disks in a homogenous medium created very strong coupling because of the massive increase in far filed resonance. Therefore, annealing for longer time is an excellent technique for creating sharp resonances for large nanodisk arrays in a homogenous medium. A 30.2 times increase in Q factor was achieved for the simulated annealed (broken discs) nanoarray compared to the unannealed (unbroken discs) nanoarrays of diameter 360 nm.

The experimentally fabricated gold nanodisk arrays were indented to be used as surface enhanced Raman spectroscopy (SERS) substrates. The optimized SERS substrates was selected from the various nanodisk arrays by detecting the dye Rhodamine 6G (R6G). It was seen that 140 nm diameter (300 nm period) displayed the highest enhancement (EF of 2.3 x 10⁶) of the Raman signal due to the overlap of the resonance wavelength of the nanodisk array with the Raman excitation wavelength (633 nm). The practical use of the optimal LIL sample was confirmed by detecting the fertiliser urea; the LOD of urea in water was 0.05 mM (0.5 ppm). Therefore, the optimized LIL sample was used for sensing agrochemicals is water. Commonly used agrochemicals, herbicide (Atrazine), fungicide (Mancozeb), acaricide (Clofentezine), weedicide (Metribuzin) and insecticides (Chlorantraniliprole, Thiamethoxam, Tau-fluvalinate, and Flubendiamide) were collected for testing their LOD in water using the optimal LIL sample as a SERS substrate.

Density functional theory (DFT) was used to theoretically confirm the Raman spectra of the agrochemicals. The DGDZVP basis set at the B3LYP level of theory was selected to calculate the

spectra, which was confirmed to have good accuracy at a moderate computational cost. The calculated Raman spectra showed good accuracy for the position (wavenumber) of the Raman peaks; however, there was discrepancy in the intensity of the peaks due to the unrestricted vibrations in the calculated molecules. The assignment of Raman vibrational modes was performed for all the agrochemicals. For the optimized LIL sample, it was observed that Clofentezine had the lowest LOD of 0.001 ppm because of its symmetric structure. Metribuzin had a strong signal in both calculated and experimental Raman spectra; hence, an LOD of 0.01 ppm was observed. Atrazine, Chlorantraniliprole, and Tau-fluvalinate had similar LOD of 0.1 ppm. Mancozeb and Flubendiamide had a lower LOD of 0.25 ppm due to lower excitation power.

7.2 Future Scope

The improvement in nanofabrication techniques is enabling researchers to fabricate increasingly complicated shapes. In the current thesis, simulations were used to observe that increasing the complexity of the nanostructures in an array can improve their overall sensitivity. Furthermore, the coupling of the single structure resonance and the grating (array) resonance is also critical to determine the sensitivity. Due to the complexity of the shape, the potential sites for the formation of electric field hotspots increase, which allows greater confinement of light. A potential study can be to quantify the effect of shape complexity by counting the number of potential sites for hotspot formation and correlating it to the increase in sensitivity. Another potential study can be breaking the symmetry of the single structure of the array. For example, a dimer can be used as the repeating unit in an array, which can allow the control of the single structure resonance using the inter dimer distance (and not the size of the structures, as seen in the current thesis). Furthermore, the non symmetric single structure resonance and the array resonance can act as bright and dark modes to induce plasmonically induced transparency, which is at the heart of many new-age applications of nanostructures.

The systematic study of the effect of surface roughness on the optical response of thin films is essential for the development of advanced plasmonic devices. In the current thesis, it was established that the surface roughness significantly improves the plasmonic response of thin films. The surface roughness of the thin films was reduced by using an oscillating base of frequency 6 MHz during the deposition of gold on a glass substrate. An 18 nm decrease in roughness was observed. To systematically vary the roughness, various frequencies of oscillating base could be selected such that a frequency could be optimized to achieve a target roughness. Thereby, the detailed study could include the plasmonic response and sensitivity analysis of thin films of varying roughness. Hence, establishing a relationship between the roughness of the substrate and the SPR performance of the thin film.

The current thesis uses DFT calculation to establish the various vibrational modes of agrochemicals. The vibrational modes can be critical to determine the resonance frequency of the SERS substrates. The SERS substrate enhances the intensity of the vibrational modes of the target chemical, however, certain

substrates can also alter the Raman shift of the vibrational modes. DFT can be used to analyze both the increase in intensity and the Raman shift position of the substrate-chemical system. Since, metals and organic chemicals have to be included in the calculations, the basis set selection is critical for accurate results. The "Lan" type basis sets could be potentially used due to their ability to handle a wide range of materials. The DFT calculations of the substrate-chemical system provides an excellent base for researchers and engineers to select the optimal substrate to achieve the highest enhancement for the selected target chemical.

In the current thesis, an optimized SERS substrate is used to increase the Raman signal of target chemicals, which can harm the environment and/or the human body. However, Raman sensing is currently limited to laboratory testing with only a handful of portable options, which are very expensive. The research community is on the hunt for portable and economical Raman sensors. Despite the simple instrumentation of the Raman setup (a stable laser source, notch filter, collimating optics, and a spectrometer), it is difficult to achieve a commercially viable Raman sensor. Due to the extremely low Raman signal, very precise instrumentation is required which adds to the cost of the final product. The use of SERS substrates enhances the Raman signal and can be a critical part of commercial Raman sensors. Hence, the device development of an economical Raman sensor can potentially open up the market for highly precise and selective sensors that can be used for pollutant detection, onsite monitoring of products, medical diagnostics, etc.

Appendix

Appendix A.

MATALB codes

Appendix A.1.

Lorentz Drude model

function varargout = LD(lambda,material,model)

```
% LD: Drude-Lorentz model for the dielectric constant of metals and
    Debye-Lorentz model for the dielectric constant of pure water
%***
% Program author: Bora Ung
             Ecole Polytechnique de Montreal
             Dept. Engineering physics
%
%
             2500 Chemin de Polytechnique
%
             Montreal, Canada
             H3T 1J4
%
             boraung@gmail.com
        Date: January 31, 2012
                                ****************
% DESCRIPTION:
% This function computes the complex dielectric constant (i.e. relative
   permittivity) of various metals using either the Lorentz-Drude (LD) or
% the Drude model (D). The LD model is the default choice since it
% provides a better fit with the exact values. The dielectric function of
   pure water is calculated with a 2-pole Debye model valid for microwave
   frequencies and a 5-pole Lorentz model valid for higher frequencies.
   Reference [1] should be used to cite this Matlab code.
% The Drude-Lorentz parameters for metals are taken from [2] while the
% The Drude-Lorentz parameters for nuclear are from [3].
% Debye-Lorentz parameters for pure water are from [3].
% USAGE: epsilon = LD(lambda,material,model)
%
     OR: [epsilon_Re epsilon_Im] = LD(lambda,material,model)
     OR: [epsilon Re epsilon Im N] = LD(lambda,material,model)
   WHERE: "epsilon Re" and "epsilon_Im" are respectively the real and
%
       imaginary parts of the dielectric constant "epsilon", and "N"
%
%
       is the complex refractive index.
% INPUT PARAMETERS:
     lambda \  \, = = > wavelength \, (meters) \, of \, light \, excitation \, on \, material.
%
%
           Accepts either vector or matrix inputs.
%
     material ==> 'Au' = gold
     model ==> Choose 'LD' or 'D' for Lorentz-Drude or Drude model.
% REFERENCES:
% [1] B. Ung and Y. Sheng, Interference of surface waves in a metallic
     nanoslit, Optics Express (2007)
% [2] Rakic et al., Optical properties of metallic films for vertical-
     cavity optoelectronic devices, Applied Optics (1998)
% [3] J. E. K. Laurens and K. E. Oughstun, Electromagnetic impulse,
     response of triply distilled water, Ultra-Wideband /
     Short-Pulse Electromagnetics (1999)
if nargin < 3, model = 'LD'; end % Lorentz contributions used by default
if nargin < 2, return; end
% Physical constants
twopic = 1.883651567308853e+09; % twopic=2*pi*c where c is speed of light
omegalight = twopic*(lambda.^(-1)); % angular frequency of light (rad/s)
invsqrt2 = 0.707106781186547; % 1/sqrt(2)
ehbar = 1.51926751447914e+015; % e/hbar where hbar=h/(2*pi) and e=1.6e-19
% Drude-Lorentz and Debye-Lorentz parameters for dispersive medium [2,3]
```

```
switch material
  case 'Au'
     omegap = 9.03*ehbar;
          [0.62 0.024 0.010 0.071 0.601 4.384];
     Gamma = [0.04 0.241 0.345 0.870 2.494 2.214]*ehbar;
     omega = [0.000 \ 0.415 \ 0.830 \ 2.969 \ 4.304 \ 13.32]*ehbar;
     order = length(omega);
  otherwise
    error('ERROR! Not a valid choice of material in input argument.')
% Lorentz model (interband effects)
switch model
  case 'D' % Drude model
     epsilon = epsilon D;
  case 'LD' % Lorentz-Drude model
     epsilon L = zeros(size(lambda));
     % Lorentzian contributions
     for k = 2:order
       epsilon L = epsilon L + (f(k)*omegap^2)*...
          (((omega(k)^2)*ones(size(lambda)) - omegalight.^2) -...
          i*Gamma(k)*omegalight).^(-1);
     end
     % Drude and Lorentz contributions combined
     epsilon = epsilon D + epsilon L;
  otherwise
     error('ERROR! Invalid option. Choose "LD" or "D"')
end
% Output variables
switch nargout
  case 1 % one output variable assigned
     varargout\{1\} = epsilon;
  case 2 % two output variables assigned
     % Real part of dielectric constant
     varargout{1} = real(epsilon);
     % Imaginary part of dielectric constant
     varargout{2} = imag(epsilon);
  case 3 % three output variables assigned
     % Real part of dielectric constant
     varargout{1} = real(epsilon);
     % Imaginary part of dielectric constant
     varargout{2} = imag(epsilon);
     % Complex refractive index [2]: N = n + i*k
     varargout{3} = invsqrt2*(sqrt(sqrt((varargout{1}).^2 +...
       (varargout{2}).^2) + varargout{1}) + ...
       i*sqrt(sqrt((varargout{1}).^2 +...
       (varargout{2}).^2) - varargout{1});
  error('Invalid number of output variables; 1,2 or 3 output variables.')
end
```

Link for code: https://github.com/plasmon360/LD python/blob/master/LD bora ung code comparision/LD.m

Effective dielectric function using Bruggeman model

```
%BruggemanModel
syms eff
e1=1;
A=0.5;
f=0.1;
f0 = 1 - f;
gamma1=2300;
gamma2=940;
lambda1=468;
lambda2=331;
epsinfinity=1.53;
lambdap=145;
gammap=17000;
A1 = .94;
phi1=-pi/4;
A2=1.36;
phi2=-pi/4;
lambda=200:(1400-200)/340:1400;
for ii= 1:200
                              lambdaa(ii)=200+ii*(1400-200)/200;
                              lambda=lambdaa(ii);
                              epsilon(ii)=epsinfinity-1/lambdap^2/(1/lambda^2+sqrt(-1)/gammap/lambda)+A1/lambda1*((exp(sqrt(-1)/gammap/lambda)+A1/lambda1*((exp(sqrt(-1)/gammap/lambda)+A1/lambda1*((exp(sqrt(-1)/gammap/lambda)+A1/lambda1*((exp(sqrt(-1)/gammap/lambda)+A1/lambda1*((exp(sqrt(-1)/gammap/lambda)+A1/lambda1*((exp(sqrt(-1)/gammap/lambda)+A1/lambda1*((exp(sqrt(-1)/gammap/lambda)+A1/lambda1*((exp(sqrt(-1)/gammap/lambda)+A1/lambda1*((exp(sqrt(-1)/gammap/lambda)+A1/lambda1*((exp(sqrt(-1)/gammap/lambda)+A1/lambda1*((exp(sqrt(-1)/gammap/lambda)+A1/lambda1*((exp(sqrt(-1)/gammap/lambda)+A1/lambda1*((exp(sqrt(-1)/gammap/lambda)+A1/lambda1*((exp(sqrt(-1)/gammap/lambda)+A1/lambda1*((exp(sqrt(-1)/gammap/lambda)+A1/lambda1*((exp(sqrt(-1)/gammap/lambda)+A1/lambda1*((exp(sqrt(-1)/gammap/lambda)+A1/lambda1*((exp(sqrt(-1)/gammap/lambda)+A1/lambda1*((exp(sqrt(-1)/gammap/lambda)+A1/lambda1*((exp(sqrt(-1)/gammap/lambda)+A1/lambda1*((exp(sqrt(-1)/gammap/lambda)+A1/lambda1*((exp(sqrt(-1)/gammap/lambda)+A1/lambda1*((exp(sqrt(-1)/gammap/lambda)+A1/lambda1*((exp(sqrt(-1)/gammap/lambda)+A1/lambda1*((exp(sqrt(-1)/gammap/lambda)+A1/lambda1*((exp(sqrt(-1)/gammap/lambda)+A1/lambda1*((exp(sqrt(-1)/gammap/lambda)+A1/lambda1*((exp(sqrt(-1)/gammap/lambda)+A1/lambda1*((exp(sqrt(-1)/gammap/lambda)+A1/lambda1*((exp(sqrt(-1)/gammap/lambda)+A1/lambda1*((exp(sqrt(-1)/gammap/lambda)+A1/lambda1*((exp(sqrt(-1)/gammap/lambda)+A1/lambda1*((exp(sqrt(-1)/gammap/lambda)+A1/lambda1*((exp(sqrt(-1)/gammap/lambda)+A1/lambda1*((exp(sqrt(-1)/gammap/lambda)+A1/lambda1*((exp(sqrt(-1)/gammap/lambda)+A1/lambda1*((exp(sqrt(-1)/gammap/lambda)+A1/lambda1*((exp(sqrt(-1)/gammap/lambda)+A1/lambda1*((exp(sqrt(-1)/gammap/lambda)+A1/lambda1*((exp(sqrt(-1)/gammap/lambda)+A1/lambda1*((exp(sqrt(-1)/gammap/lambda)+A1/lambda1*((exp(sqrt(-1)/gammap/lambda)+A1/lambda1*((exp(sqrt(-1)/gammap/lambda)+A1/lambda1*((exp(sqrt(-1)/gammap/lambda)+A1/lambda1*((exp(sqrt(-1)/gammap/lambda)+A1/lambda1*((exp(sqrt(-1)/gammap/lambda)+A1/lambda1*((exp(sqrt(-1)/gammap/lambda)+A1/lambda1*((exp(sqrt(-1)/gammap/lambda)+A1/lam
1)*phi1)/(1/lambda1-1/lambda-sqrt(-1)/gamma1)+(exp(-sqrt(-1)*phi1)/(1/lambda1+1/lambda+sqrt(-1)*phi1)/(1/lambda1+1/lambda+sqrt(-1)*phi1)/(1/lambda1+1/lambda+sqrt(-1)*phi1)/(1/lambda1+1/lambda+sqrt(-1)*phi1)/(1/lambda1+1/lambda+sqrt(-1)*phi1)/(1/lambda1+1/lambda+sqrt(-1)*phi1)/(1/lambda1+1/lambda+sqrt(-1)*phi1)/(1/lambda1+1/lambda+sqrt(-1)*phi1)/(1/lambda1+1/lambda+sqrt(-1)*phi1)/(1/lambda1+1/lambda+sqrt(-1)*phi1)/(1/lambda+sqrt(-1)*phi1)/(1/lambda+sqrt(-1)*phi1)/(1/lambda+sqrt(-1)*phi1)/(1/lambda+sqrt(-1)*phi1)/(1/lambda+sqrt(-1)*phi1)/(1/lambda+sqrt(-1)*phi1)/(1/lambda+sqrt(-1)*phi1)/(1/lambda+sqrt(-1)*phi1)/(1/lambda+sqrt(-1)*phi1)/(1/lambda+sqrt(-1)*phi1)/(1/lambda+sqrt(-1)*phi1)/(1/lambda+sqrt(-1)*phi1)/(1/lambda+sqrt(-1)*phi1)/(1/lambda+sqrt(-1)*phi1)/(1/lambda+sqrt(-1)*phi1)/(1/lambda+sqrt(-1)*phi1)/(1/lambda+sqrt(-1)*phi1)/(1/lambda+sqrt(-1)*phi1)/(1/lambda+sqrt(-1)*phi1)/(1/lambda+sqrt(-1)*phi1)/(1/lambda+sqrt(-1)*phi1)/(1/lambda+sqrt(-1)*phi1)/(1/lambda+sqrt(-1)*phi1)/(1/lambda+sqrt(-1)*phi1)/(1/lambda+sqrt(-1)*phi1)/(1/lambda+sqrt(-1)*phi1)/(1/lambda+sqrt(-1)*phi1)/(1/lambda+sqrt(-1)*phi1)/(1/lambda+sqrt(-1)*phi1)/(1/lambda+sqrt(-1)*phi1)/(1/lambda+sqrt(-1)*phi1)/(1/lambda+sqrt(-1)*phi1)/(1/lambda+sqrt(-1)*phi1)/(1/lambda+sqrt(-1)*phi1)/(1/lambda+sqrt(-1)*phi1)/(1/lambda+sqrt(-1)*phi1)/(1/lambda+sqrt(-1)*phi1)/(1/lambda+sqrt(-1)*phi1)/(1/lambda+sqrt(-1)*phi1)/(1/lambda+sqrt(-1)*phi1)/(1/lambda+sqrt(-1)*phi1)/(1/lambda+sqrt(-1)*phi1)/(1/lambda+sqrt(-1)*phi1)/(1/lambda+sqrt(-1)*phi1)/(1/lambda+sqrt(-1)*phi1)/(1/lambda+sqrt(-1)*phi1)/(1/lambda+sqrt(-1)*phi1)/(1/lambda+sqrt(-1)*phi1)/(1/lambda+sqrt(-1)*phi1)/(1/lambda+sqrt(-1)*phi1)/(1/lambda+sqrt(-1)*phi1)/(1/lambda+sqrt(-1)*phi1)/(1/lambda+sqrt(-1)*phi1)/(1/lambda+sqrt(-1)*phi1)/(1/lambda+sqrt(-1)*phi1)/(1/lambda+sqrt(-1)*phi1)/(1/lambda+sqrt(-1)*phi1)/(1/lambda+sqrt(-1)*phi1)/(1/lambda+sqrt(-1)*phi1)/(1/lambda+sqrt(-1)*phi1)/(1/lambda+sqrt(-1)*phi1)/(1/lambda+sqrt(-1)*phi1)/(1/lambda+sqrt(-1)*phi1)/(1/lambda+sqrt(-1)*phi1)/(1/lambda+sqrt(-1)*phi1)/(1/l
1)/gamma1))))+A2/lambda2*((exp(sqrt(-1)*phi2)/(1/lambda2-1/lambda-sqrt(-1)/gamma2)+(exp(-sqrt(-1)*phi2)/(1/lambda2-1/lambda-sqrt(-1)/gamma2)+(exp(-sqrt(-1)*phi2)/(1/lambda2-1/lambda-sqrt(-1)/gamma2)+(exp(-sqrt(-1)*phi2)/(1/lambda2-1/lambda-sqrt(-1)/gamma2)+(exp(-sqrt(-1)*phi2)/(1/lambda2-1/lambda-sqrt(-1)/gamma2)+(exp(-sqrt(-1)*phi2)/(1/lambda2-1/lambda-sqrt(-1)/gamma2)+(exp(-sqrt(-1)*phi2)/(1/lambda2-1/lambda-sqrt(-1)/gamma2)+(exp(-sqrt(-1)*phi2)/(1/lambda2-1/lambda-sqrt(-1)/gamma2)+(exp(-sqrt(-1)*phi2)/(1/lambda2-1/lambda-sqrt(-1)/gamma2)+(exp(-sqrt(-1)*phi2)/(1/lambda2-1/lambda-sqrt(-1)/gamma2)+(exp(-sqrt(-1)*phi2)/(1/lambda2-1/lambda-sqrt(-1)/gamma2)+(exp(-sqrt(-1)*phi2)/(1/lambda2-1/lambda-sqrt(-1)/gamma2)+(exp(-sqrt(-1)*phi2)/(1/lambda2-1/lambda-sqrt(-1)/gamma2)+(exp(-sqrt(-1)*phi2)/(1/lambda2-1/lambda-sqrt(-1)/gamma2)+(exp(-sqrt(-1)*phi2)/(1/lambda2-1/lambda-sqrt(-1)/gamma2)+(exp(-sqrt(-1)*phi2)/(1/lambda2-1/lambda-sqrt(-1)/gamma2)+(exp(-sqrt(-1)*phi2)/(1/lambda-sqrt(-1)/gamma2)+(exp(-sqrt(-1)*phi2)/(1/lambda-sqrt(-1)/gamma2)+(exp(-sqrt(-1)*phi2)/(1/lambda-sqrt(-1)/gamma2)+(exp(-sqrt(-1)*phi2)/(1/lambda-sqrt(-1)/gamma2)+(exp(-sqrt(-1)*phi2)/(1/lambda-sqrt(-1)/gamma2)+(exp(-sqrt(-1)*phi2)/(1/lambda-sqrt(-1)/gamma2)+(exp(-sqrt(-1)*phi2)/(1/lambda-sqrt(-1)/gamma2)+(exp(-sqrt(-1)*phi2)/(1/lambda-sqrt(-1)/gamma2)+(exp(-sqrt(-1)*phi2)/(1/lambda-sqrt(-1)/gamma2)+(exp(-sqrt(-1)*phi2)/(1/lambda-sqrt(-1)/gamma2)+(exp(-sqrt(-1)*phi2)/(1/lambda-sqrt(-1)/gamma2)+(exp(-sqrt(-1)*phi2)/(1/lambda-sqrt(-1)/gamma2)+(exp(-sqrt(-1)*phi2)/(1/lambda-sqrt(-1)/gamma2)+(exp(-sqrt(-1)*phi2)/(1/lambda-sqrt(-1)/gamma2)+(exp(-sqrt(-1)*phi2)/(1/lambda-sqrt(-1)/gamma2)+(exp(-sqrt(-1)*phi2)/(1/lambda-sqrt(-1)/gamma2)+(exp(-sqrt(-1)*phi2)/(1/lambda-sqrt(-1)/gamma2)+(exp(-sqrt(-1)*phi2)/(1/lambda-sqrt(-1)/gamma2)+(exp(-sqrt(-1)*phi2)/(1/lambda-sqrt(-1)/gamma2)+(exp(-sqrt(-1)*phi2)/(1/lambda-sqrt(-1)/gamma2)+(exp(-sqrt(-1)*phi2)/(1/lambda-sqrt(-1)/gamma2)+(exp(-sqrt(-1)*phi2)/(1/lambda-sqrt(-1)/gamma2)+(exp(-sqrt(-1)*phi2)/(1/lambda-sqrt(-
1)*phi2)/(1/lambda2+1/lambda+sqrt(-1)/gamma2))));
                              e2(ii)=epsilon(ii);
                              ef1(ii) = -((A^2*e^{1/2}*f^{2} + 2*A^{2}*e^{1/2}*f^{2} + A^{2}*e^{1/2}*f^{2} + A^{2}*e^{1/2}*f^{2} - 2*A^{2}*e^{1/2}*f^{2})
4*A^2*e1*e2(ii)*f*f0 - 2*A^2*e1*e2(ii)*f0^2 + A^2*e2(ii)^2*f^2 + 2*A^2*e2(ii)^2*f*f0 + A^2*e2(ii)^2*f^2 + A^2*e2(ii)^2 + A^2*e2(ii)^
A^2 * e2(ii)^2 * f0^2 - 2*A*e1^2 * f^2 - 2*A*e1^2 * f^3 + 2*A*e1*e2(ii)*f^2 + 4*A*e1*e2(ii)*f^3 + 6*A*e1*e2(ii)*f^3 + 6*A*e1
2*A*e1*e2(ii)*f0^2 - 2*A*e2(ii)^2*f*f0 - 2*A*e2(ii)^2*f0^2 + e1^2*f^2 + 2*e1*e2(ii)*f*f0 + 2*e1*e2(ii)*f0^2 + e1^2*f^2 + 2*e1*e2(ii)*f0^2 + e1^2*f^2 + e
e2(ii)^2*f0^2(i)^2+f0^2(i)^2+f0^2(i)^2+f0^2(i)^2+f0^2(i)^2+f0^2(i)^2+f0^2(i)^2+f0^2(i)^2+f0^2(i)^2+f0^2(i)^2+f0^2(i)^2+f0^2(i)^2+f0^2(i)^2+f0^2(i)^2+f0^2(i)^2+f0^2(i)^2+f0^2(i)^2+f0^2(i)^2+f0^2(i)^2+f0^2(i)^2+f0^2(i)^2+f0^2(i)^2+f0^2(i)^2+f0^2(i)^2+f0^2(i)^2+f0^2(i)^2+f0^2(i)^2+f0^2(i)^2+f0^2(i)^2+f0^2(i)^2+f0^2(i)^2+f0^2(i)^2+f0^2(i)^2+f0^2(i)^2+f0^2(i)^2+f0^2(i)^2+f0^2(i)^2+f0^2(i)^2+f0^2(i)^2+f0^2(i)^2+f0^2(i)^2+f0^2(i)^2+f0^2(i)^2+f0^2(i)^2+f0^2(i)^2+f0^2(i)^2+f0^2(i)^2+f0^2(i)^2+f0^2(i)^2+f0^2(i)^2+f0^2(i)^2+f0^2(i)^2+f0^2(i)^2+f0^2(i)^2+f0^2(i)^2+f0^2(i)^2+f0^2(i)^2+f0^2(i)^2+f0^2(i)^2+f0^2(i)^2+f0^2(i)^2+f0^2(i)^2+f0^2(i)^2+f0^2(i)^2+f0^2(i)^2+f0^2(i)^2+f0^2(i)^2+f0^2(i)^2+f0^2(i)^2+f0^2(i)^2+f0^2(i)^2+f0^2(i)^2+f0^2(i)^2+f0^2(i)^2+f0^2(i)^2+f0^2(i)^2+f0^2(i)^2+f0^2(i)^2+f0^2(i)^2+f0^2(i)^2+f0^2(i)^2+f0^2(i)^2+f0^2(i)^2+f0^2(i)^2+f0^2(i)^2+f0^2(i)^2+f0^2(i)^2+f0^2(i)^2+f0^2(i)^2+f0^2(i)^2+f0^2(i)^2+f0^2(i)^2+f0^2(i)^2+f0^2(i)^2+f0^2(i)^2+f0^2(i)^2+f0^2(i)^2+f0^2(i)^2+f0^2(i)^2+f0^2(i)^2+f0^2(i)^2+f0^2(i)^2+f0^2(i)^2+f0^2(i)^2+f0^2(i)^2+f0^2(i)^2+f0^2(i)^2+f0^2(i)^2+f0^2(i)^2+f0^2(i)^2+f0^2(i)^2+f0^2(i)^2+f0^2(i)^2+f0^2(i)^2+f0^2(i)^2+f0^2(i)^2+f0^2(i)^2+f0^2(i)^2+f0^2(i)^2+f0^2(i)^2+f0^2(i)^2+f0^2(i)^2+f0^2(i)^2+f0^2(i)^2+f0^2(i)^2+f0^2(i)^2+f0^2(i)^2+f0^2(i)^2+f0^2(i)^2+f0^2(i)^2+f0^2(i)^2+f0^2(i)^2+f0^2(i)^2+f0^2(i)^2+f0^2(i)^2+f0^2(i)^2+f0^2(i)^2+f0^2(i)^2+f0^2(i)^2+f0^2(i)^2+f0^2(i)^2+f0^2(i)^2+f0^2(i)^2+f0^2(i)^2+f0^2(i)^2+f0^2(i)^2+f0^2(i)^2+f0^2(i)^2+f0^2(i)^2+f0^2(i)^2+f0^2(i)^2+f0^2(i)^2+f0^2(i)^2+f0^2(i)^2+f0^2(i)^2+f0^2(i)^2+f0^2(i)^2+f0^2(i)^2+f0^2(i)^2+f0^2(i)^2+f0^2(i)^2+f0^2(i)^2+f0^2(i)^2+f0^2(i)^2+f0^2(i)^2+f0^2(i)^2+f0^2(i)^2+f0^2(i)^2+f0^2(i)^2+f0^2(i)^2+f0^2(i)^2+f0^2(i)^2+f0^2(i)^2+f0^2(i)^2+f0^2(i)^2+f0^2(i)^2+f0^2(i)^2+f0^2(i)^2+f0^2(i)^2+f0^2(i)^2+f0^2(i)^2+f0^2(i)^2+f0^2(i)^2+f0^2(i)^2+f0^2(i)^2+f0^2(i)^2+f0^2(i)^2+f0^2(i)^2+f0^2(i)^2+f0^2(i)^2+f0^2(i)^2+f0^2(i)^2+f0^2(i)^2+f0^2(i)^2+f0^2(i)^2+f0^2(i)^2+f0^2(i)^2+f0^2(i)^2+f0^2(i)^2+f0^2(i)^2+f0^2(i)^2+f0^2(i)^2+f0^2(i)^2+f0^2(
A*f0));
                              ef2(ii) = -(A*e1*f - e2(ii)*f0 - (A^2*e1^2*f^2 + 2*A^2*e1^2*f^*f0 + A^2*e1^2*f0^2 - 2*A^2*e1*e2(ii)*f^2)
-4*A^2*e1*e2(ii)*f^*f0 - 2*A^2*e1*e2(ii)*f0^2 + A^2*e2(ii)^22*f^2 + 2*A^2*e2(ii)^22*f^*f0 + A^2*e2(ii)^22*f^2 + A^2*e2(ii)^2*f^2 + A^2*e2(ii)^2 + A^2
A^2 * e2(ii)^2 * f0^2 - 2*A*e1^2 * f^2 - 2*A*e1^2 * f^2 + 2*A*e1^2 * f^2 + 2*A*e1*e2(ii)*f^2 + 4*A*e1*e2(ii)*f^3 + 4*A*e1*e2
2*A*e1*e2(ii)*f0^2 - 2*A*e2(ii)^2*f*f0 - 2*A*e2(ii)^2*f0^2 + e1^2*f^2 + 2*e1*e2(ii)*f*f0 + e1^2*f^2 + e1^2*f
e2(ii)^2f0^2(1/2) - e1^f + A^e1^f0 + A^e2(ii)^f + A^e2(ii)^f0/(2^f + f0 - A^f - A^f0));
```

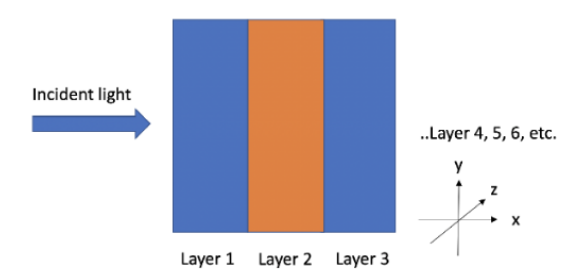
end

Toolbox to calculate angle resolved SPR plots

Link for toolbox: https://in.mathworks.com/matlabcentral/fileexchange/77636-transfer-matrix-methods-tmm-thin-film-tpv-optical-design

Transfer Matrix Methods (TMM) Thin-Film TPV Optical Design

If you have any questions please contact Zhewen Deng at jewden@umich.edu



This tutorial will give you an output of the reflectivity, absorptivity and transmissivity as a function of wavelength. The geometries of the films are considered to be semi-infinite in the y and z direction. Select layer composition and adjust your thickness. We currently only allow NORMAL incidence. i.e. Your incident light is perpendicular to the layers. You can also add more materials from https://refractiveindex.info/. Note that the wavelength from the website might be different from the axis limits we have below. You can reset the axis limits in last part of the file plot_TMM.m.

```
clear;clc;
                            → }; thickness(1) =
layers(1) = { Vac
                                                   0 🗢
                                                                       ;%in microns
layers(2) = { Au_b
                            ▼ }; thickness(2) = 0.4 🔽
layers(3) = { Au
                            ▼ }; thickness(3) = 0.4 🔽
                          ▼ }; thickness(4) = 1000 =
layers(4) = { Glass
                          ▼ }; thickness(5) = 0 🗁
layers(5) = { Vac
angle = 45.5;
% incident angle in degree NOT in radian
% If you have any thick film layer (i.e. when your thickness is >>> your wavelength) in your setting,
\ensuremath{\mathrm{\%}} please specify the layer number below.
thick film index = 4
% You can also save the output in csv. If you want an Excel document, instruction is at the
% eng of plot_TMM.m
% Example: filename = 'data.csv'
filename = Au.csv
clf;plot_TMM(layers, thickness, thick_film_index,angle,filename);
```

Additional parameters for FEM simulations

Common to both single nanoparticle and nanoarray			
Module	Electromagnetic wave frequency domain (ewfd) with parametric sweep		
Mesh			
Maximum size	75 nm		
Minimum size	2 nm		
Maximum element growth rate	1.15		
Curvature factor	0.5		
Resolution of narrow regions	0.5		

For single nanoparticle	For single nanoparticle simulation				
int_surf	Surface of nanoparticle				
in_vol	Volume of nanoparticle				
Background field	E0*exp(-i*k1*z)				
Symmetry	Perfect electric conductor				
	Perfect magnetic conductor				
nrelPoav	nx*up(ewfd.relPoavx) + ny*up(ewfd.relPoavy) + nz*up(ewfd.relPoavz)				
sigma_sc	int_surf(nrelPoav)/S0				
sigma_abs	in_vol(ewfd.Qh)/S0				
sigma_ext	sigma_sc+sigma_abs				
k1	ewfd.k0*sqrt(eps_ext)				
sigma_geom	int_surf(1)				
sigma_extOT	$-4*pi/(ewfd.k0*sqrt(eps_ext))*int_OT(imag(ewfd.Efarx*1[m]))/E0$				
M_ave	int_surf((up(ewfd.normE))^2)/sigma_geom/E0^2				
eps_ext	an1(lambda)+an2(lambda)*i				
S0	E0^2/(2*Z1)				
Z1	Z0_const/sqrt(eps_ext)				
S_in	E0^2/(2*Z0_const)				

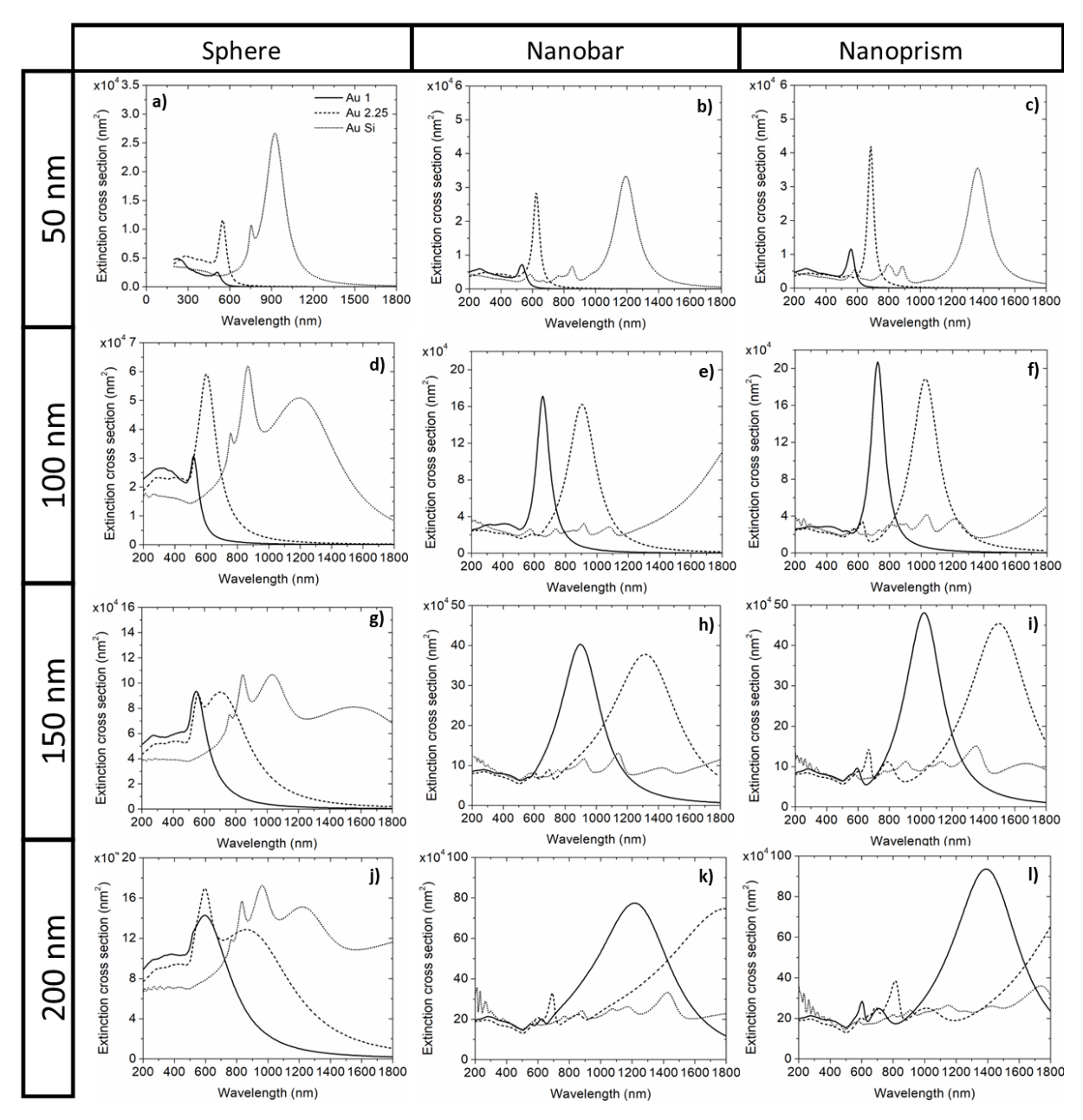


Figure C.1 Plots of the extinction cross-section for gold (black) in air (solid line), glass (dashed line), and a-Si (dotted line) environment, of spherical nanoparticles, nanobars and nanoprisms (left to right), and volumes equal to spheres of diameter 50 nm, 100 nm, 150 nm, and 200 nm (top to bottom).

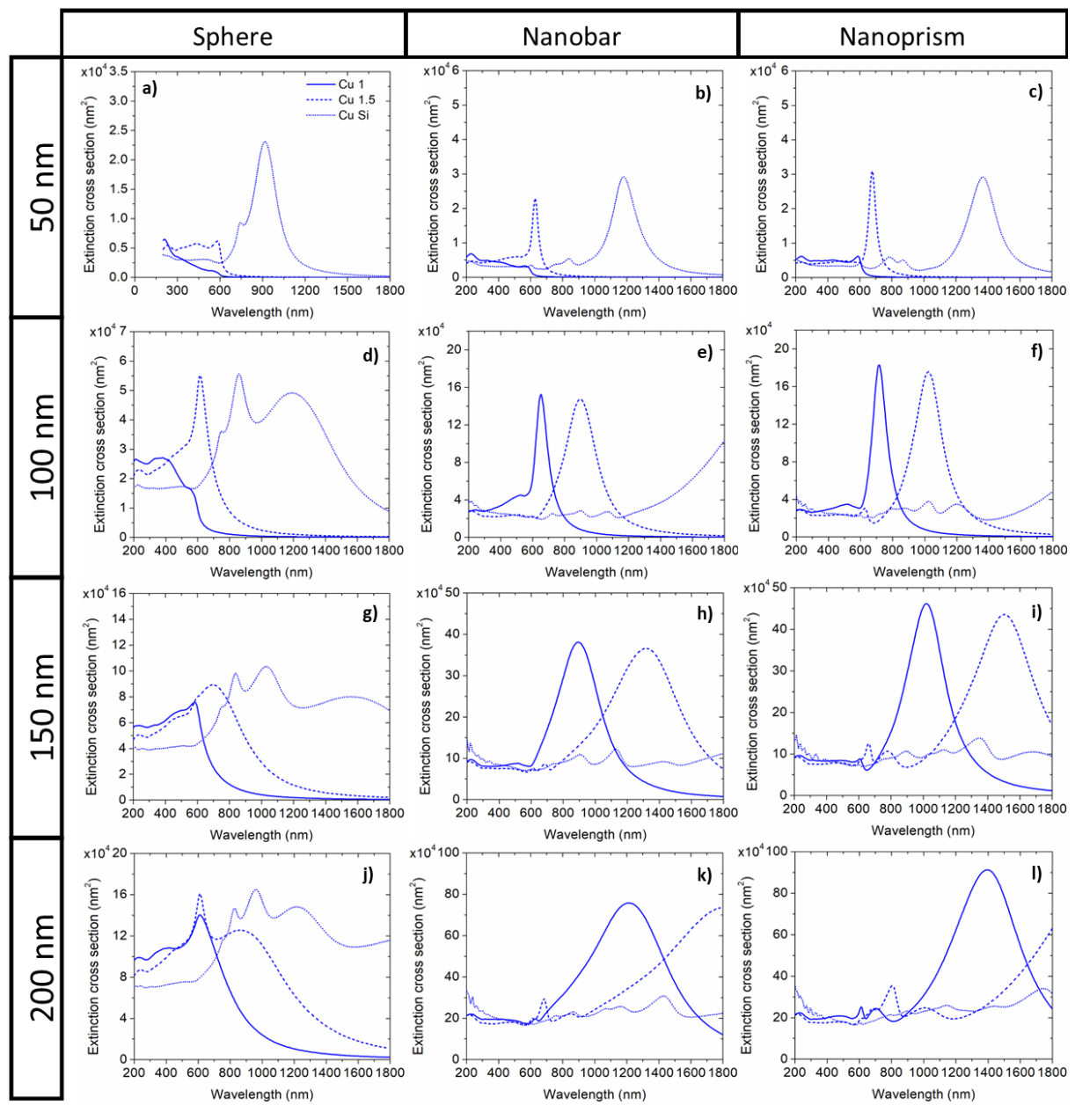


Figure C.2 Plots of the extinction cross-section for copper (blue) in air (solid line), glass (dashed line), and a-Si (dotted line) environment, of spherical nanoparticles, nanobars and nanoprisms (left to right), and volumes equal to spheres of diameter 50 nm, 100 nm, 150 nm, and 200 nm (top to bottom).

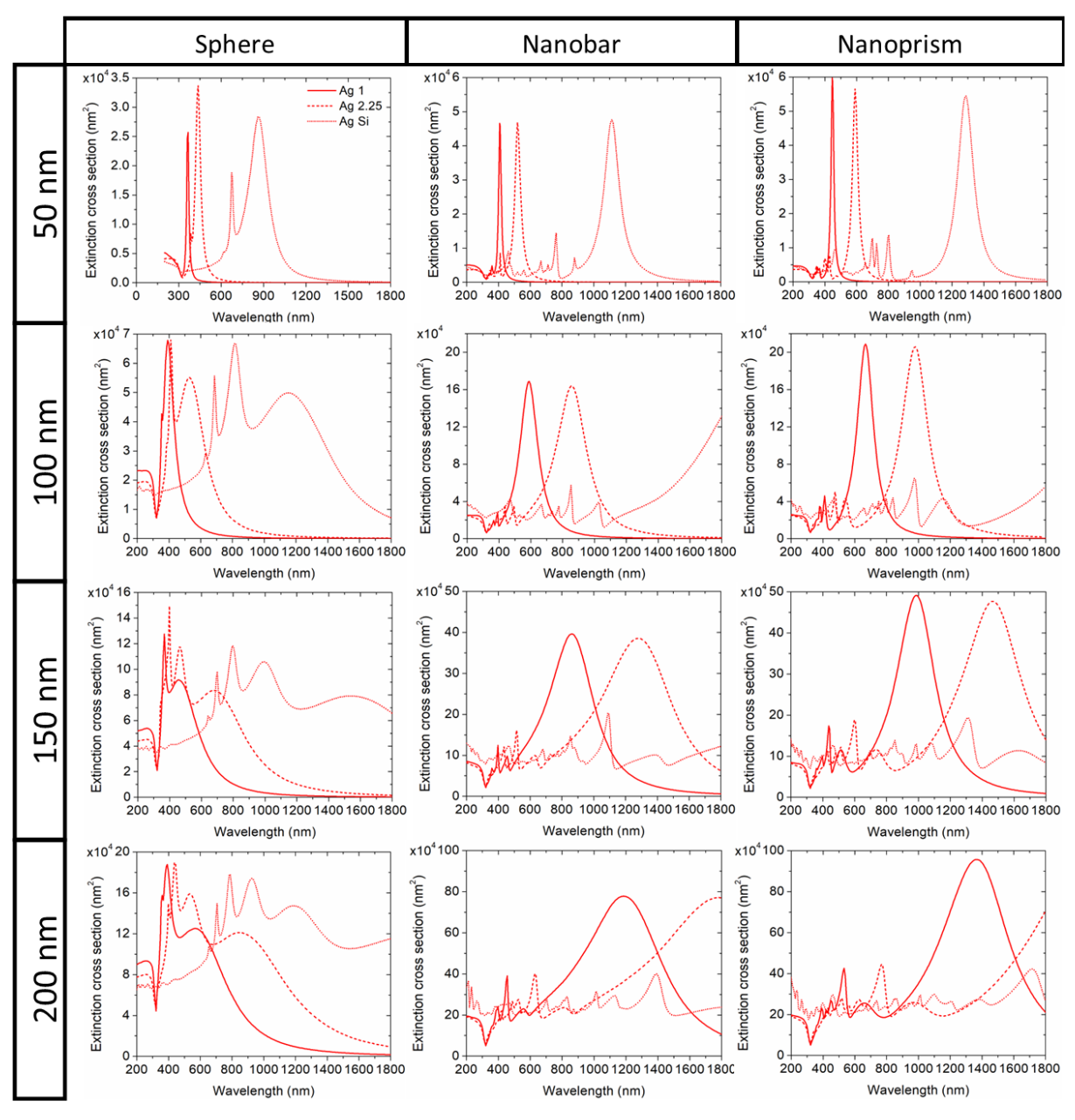


Figure C.3 Plots of the extinction cross-section for silver (red) in air (solid line), glass (dashed line), and a-Si (dotted line) environment, of spherical nanoparticles, nanobars and nanoprisms (left to right), and volumes equal to spheres of diameter 50 nm, 100 nm, 150 nm, and 200 nm (top to bottom).

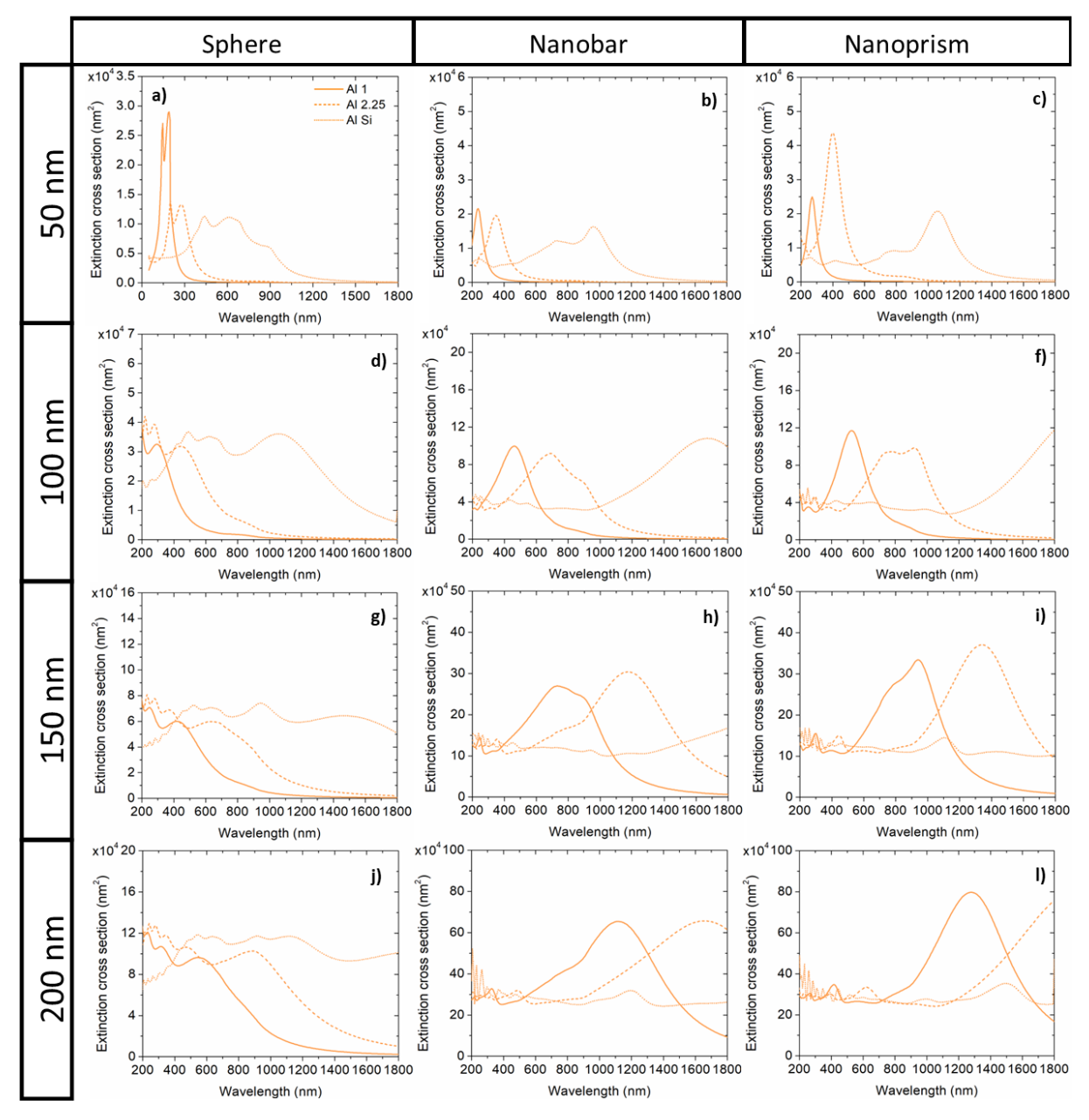


Figure C.4 Plots of the extinction cross-section for aluminium (orange) in air (solid line), glass (dashed line), and a-Si (dotted line) environment, of spherical nanoparticles, nanobars and nanoprisms (left to right), and volumes equal to spheres of diameter 50 nm, 100 nm, 150 nm, and 200 nm (top to bottom).

Transmission plots of nanoarrays calculated using FEM

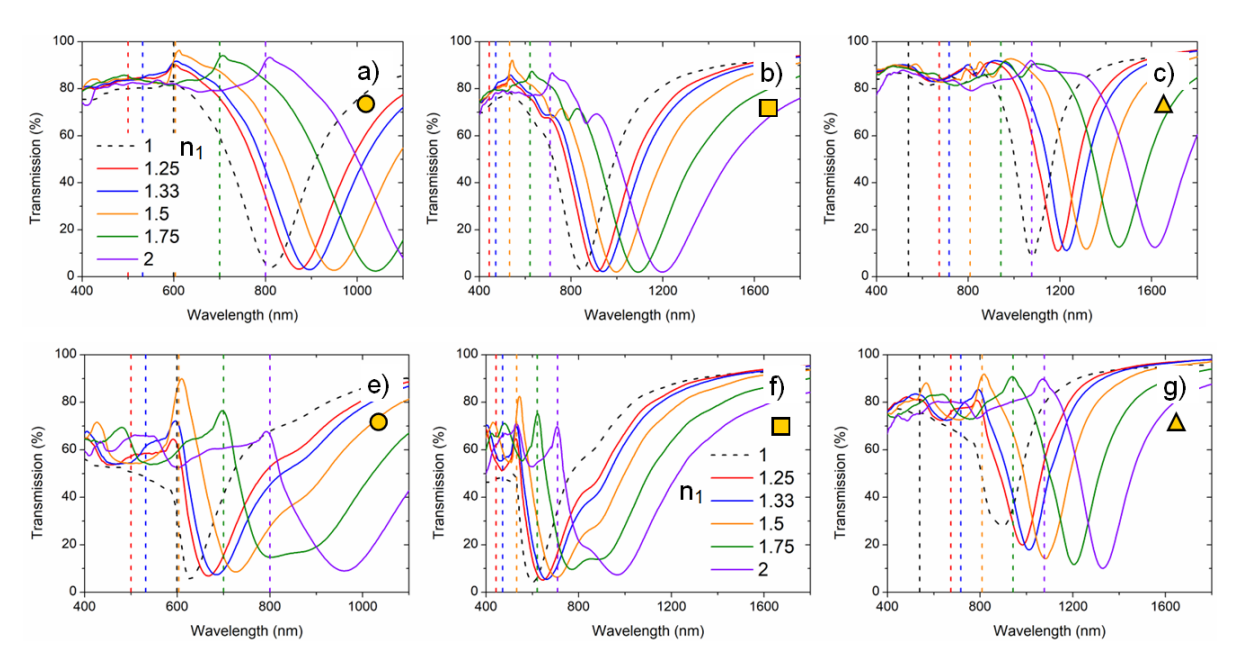


Figure D.1 Refractive index (n_1) variation in gold (a-c) and aluminium (a-c) nanoarray for disc (a, e), square, (b, f), and triangle (c, g) shapes. The dashed lines represent the lattice resonance due to n_1 . The side of square and triangle were kept as 177.25 nm and 269.35 nm to keep the volume equal to the disc of diameter 200 nm. The nanoarray was at air glass interface for $\theta = 0^{\circ}$.

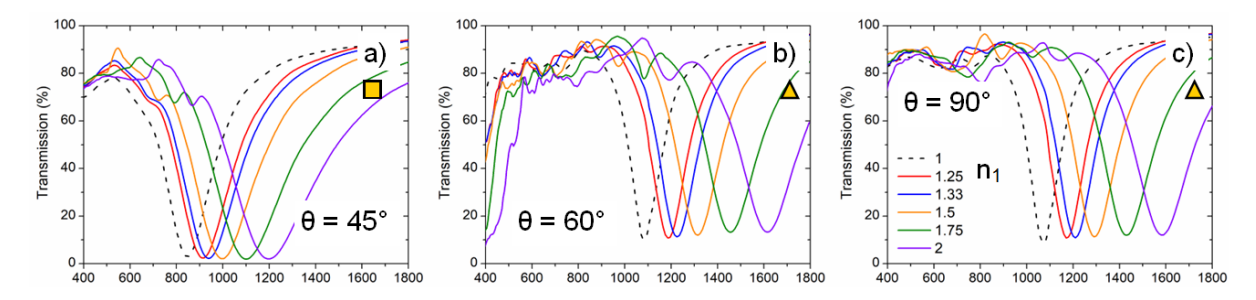


Figure D.2 Refractive index (n_1) variation in gold nanoarray for (a) square $\theta = 45^{\circ}$, and (b, c) triangle. $\theta = 60^{\circ}$ and $\theta = 90^{\circ}$.

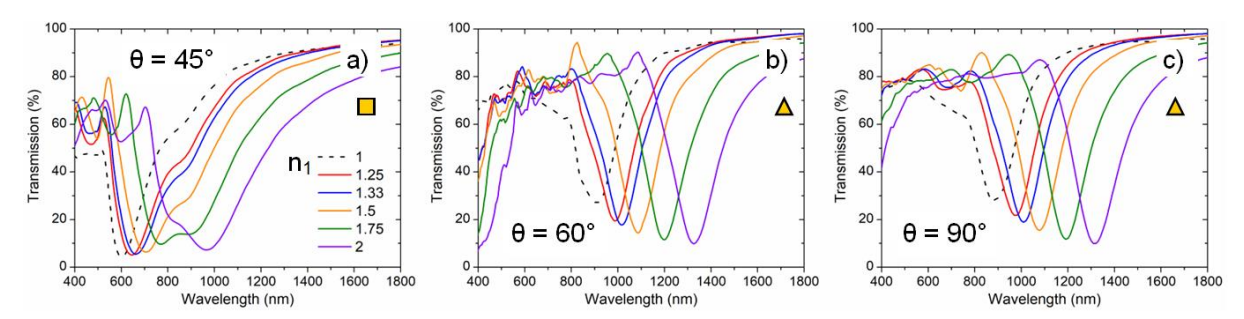


Figure D.3 Refractive index (n_1) variation in aluminium nanoarray for (a) square $\theta = 45^{\circ}$, and (b, c) triangle. $\theta = 60^{\circ}$ and $\theta = 90^{\circ}$.

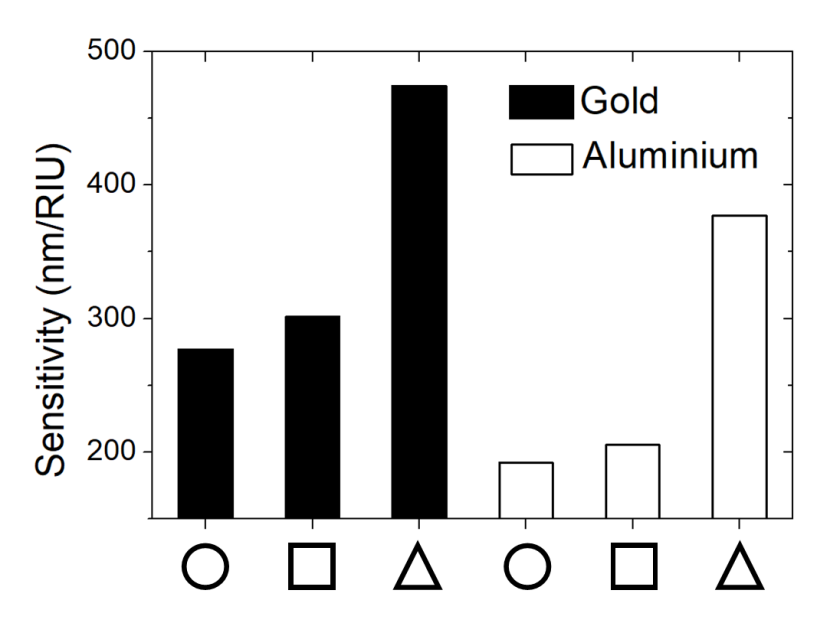
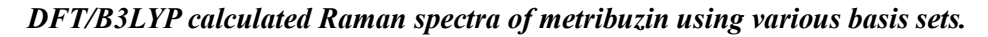


Figure D.4 Sensitivity comparison of gold and aluminium nanoarray of disc, square and triangle nanoarrays with p/D 0.5 (not at the optimal coupling condition). Volume equal to disk of diameter 200 nm and thickness 30 nm.



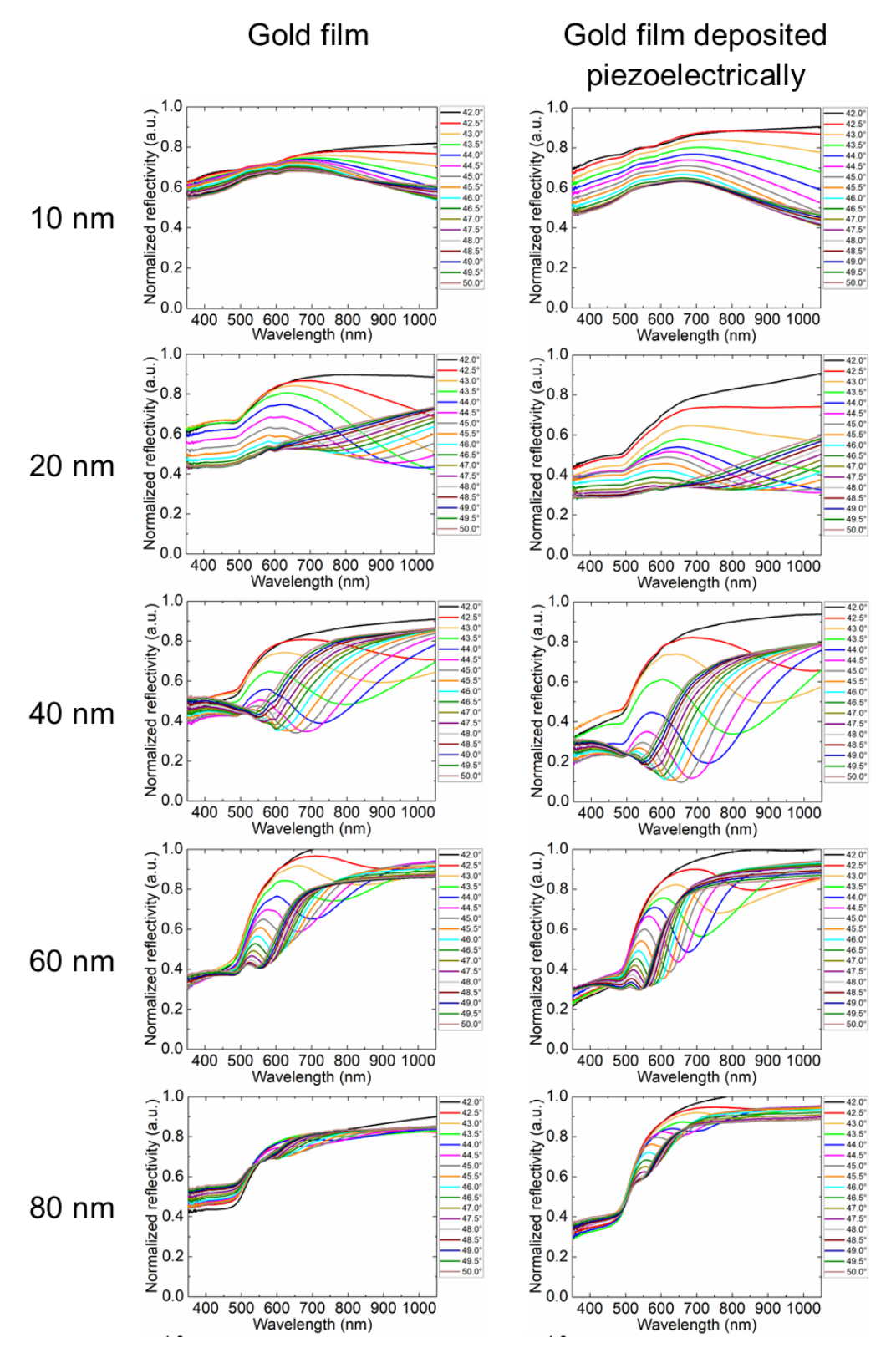
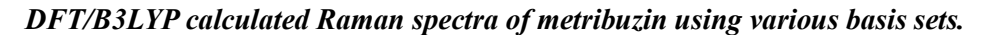


Figure E.1 Reflectivity plots for samples of various thicknesses deposited with and without a quartz base



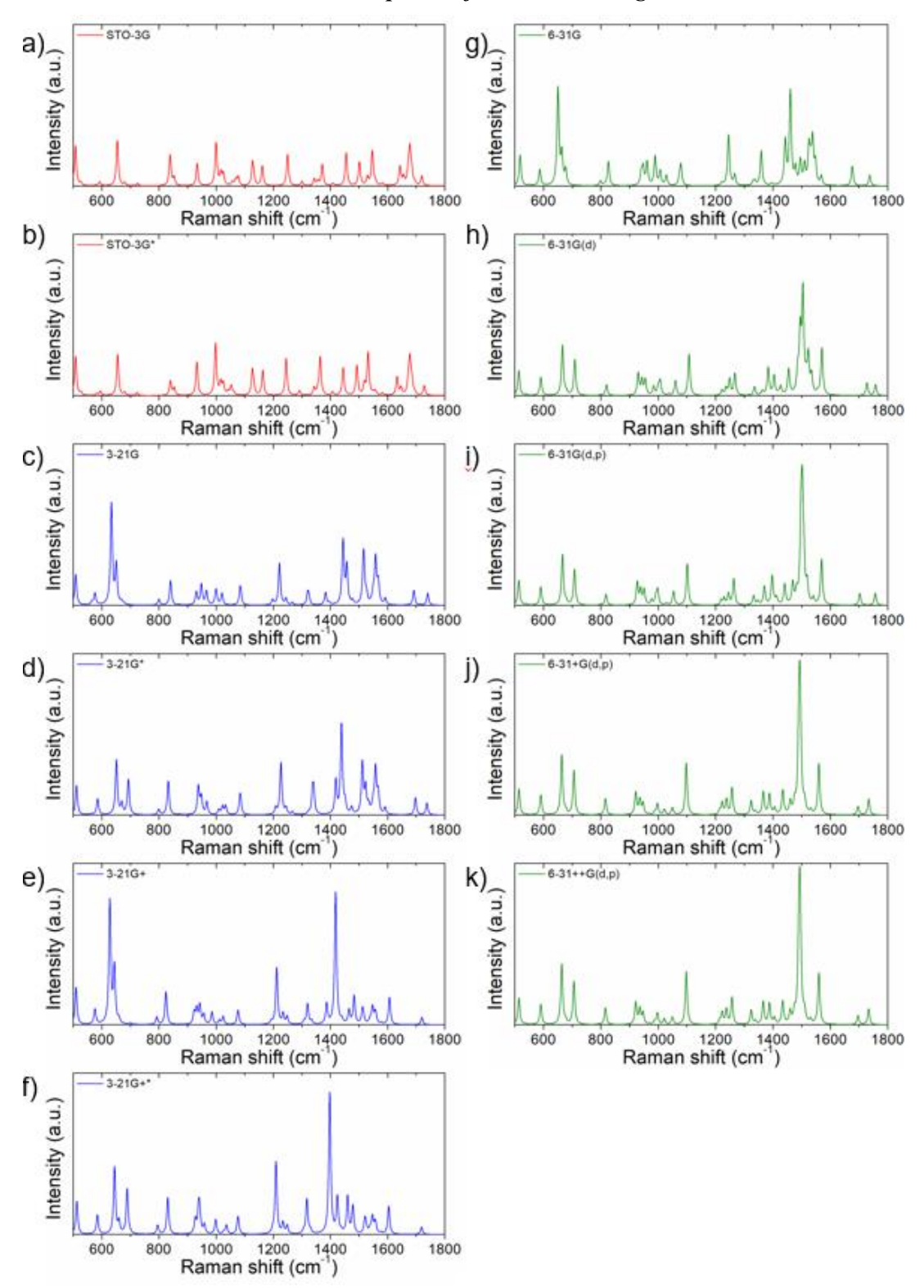


Figure F.1 DFT/B3LYP calculated Raman spectra of metribuzin using various basis sets.

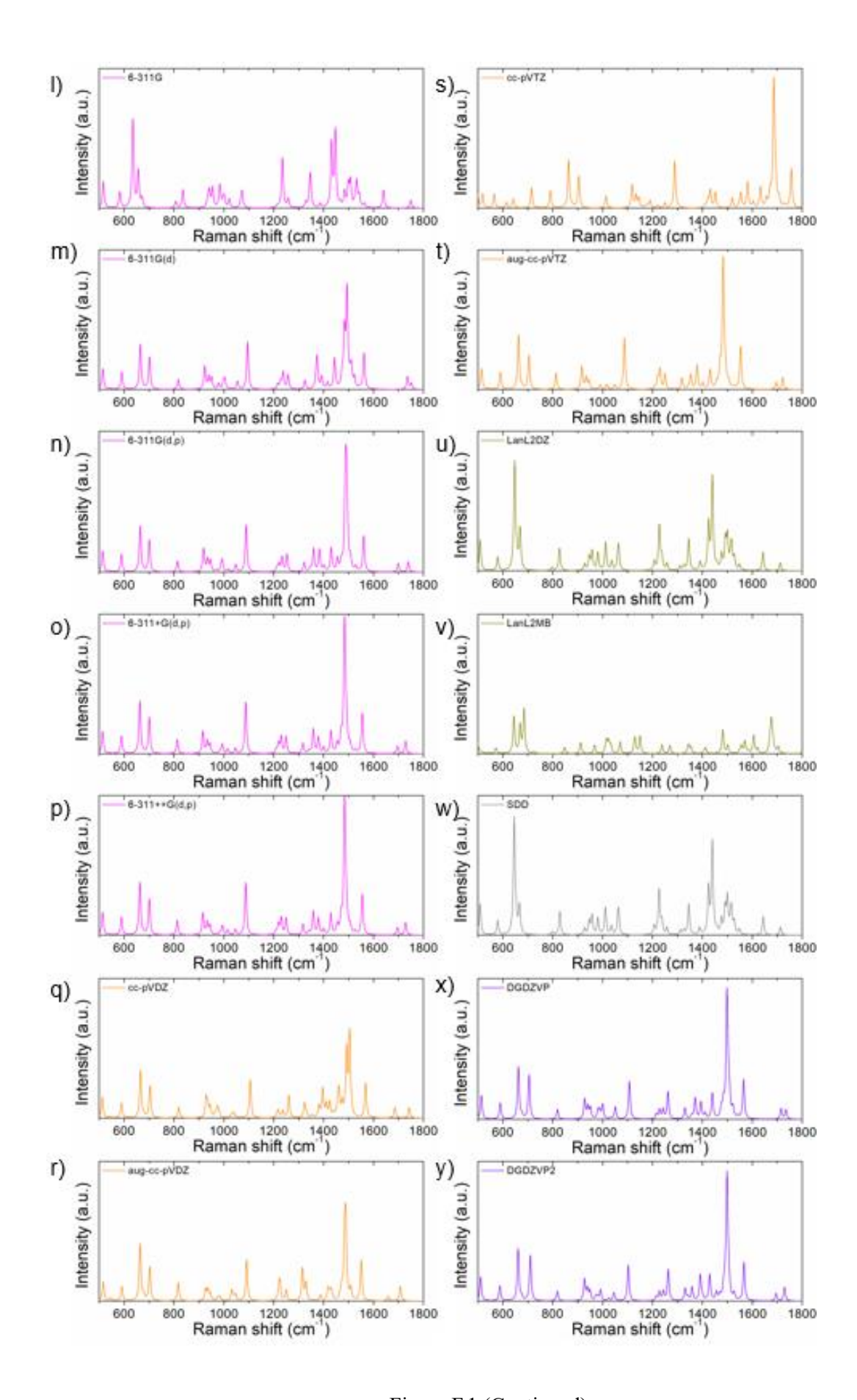


Figure F.1 (Continued)

Commercial agrochemicals tested in this thesis



Atrazine C₈H₁₄CIN₅



 $\begin{array}{c} \textbf{Mancozeb} \\ [C_8H_{12}MnN_4S_8]_x[C_8H_{12}ZnN_4S_8]_y \end{array}$



Metribuzin C₈H₁₄N₄OS



Clofentezine C₁₄H₈Cl₂N₄



 $\begin{array}{l} Chlorantraniliprole \\ C_{18}H_{14}BrCl_2N_5O_2 \end{array}$



Thiamethoxam $C_8H_{10}CIN_5O_3S$





 $\begin{array}{c} {\sf Flubendiamide} \\ {\sf C_{23}H_{22}F_7IN_2O_4S} \end{array}$

Agrochemical	Effect of structure on application		
Atrazine Herbicide	Chlorine atom enhances its ability to bind to the target enzyme (photosystem II) in plants,		
	while the alkyl groups increase its lipophilicity and soil persistence		
Mancozeb Fungicide	Zinc and manganese ions disrupt the cellular processes of fungi		
Clofentezine <i>Acaricide</i>	The tetrazine ring interferes with the cell division and growth of mite eggs leading to their		
	death. Chlorine atoms enhances the ability to bind to the target		
Thiamethoxam Insecticide	The nitro group enhances its ability to bind to the target site (nicotinic acetylcholine		
	receptors), while the thiazole ring contributes to its systemic movement within the plant		
Tau-fluvalinate Insecticide	Cyano group affects the nervous system of insects and mites by disrupting sodium channel		
	function. Fluorine atom increases its photostability and environmental persistence		

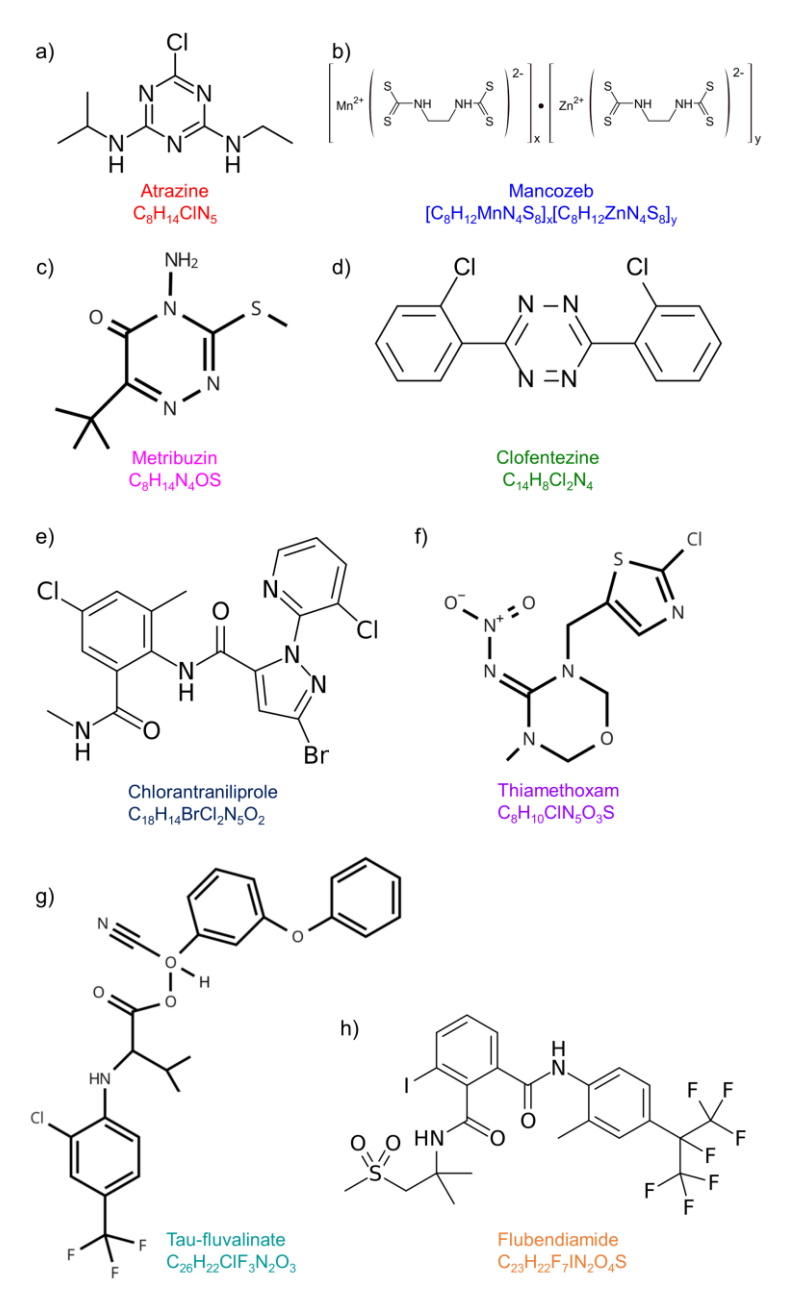


Figure G.1 Chemical structure of the agrochemicals tested in this thesis.

Appendix H. Nomenclature of vibrational modes (Wilson notation)

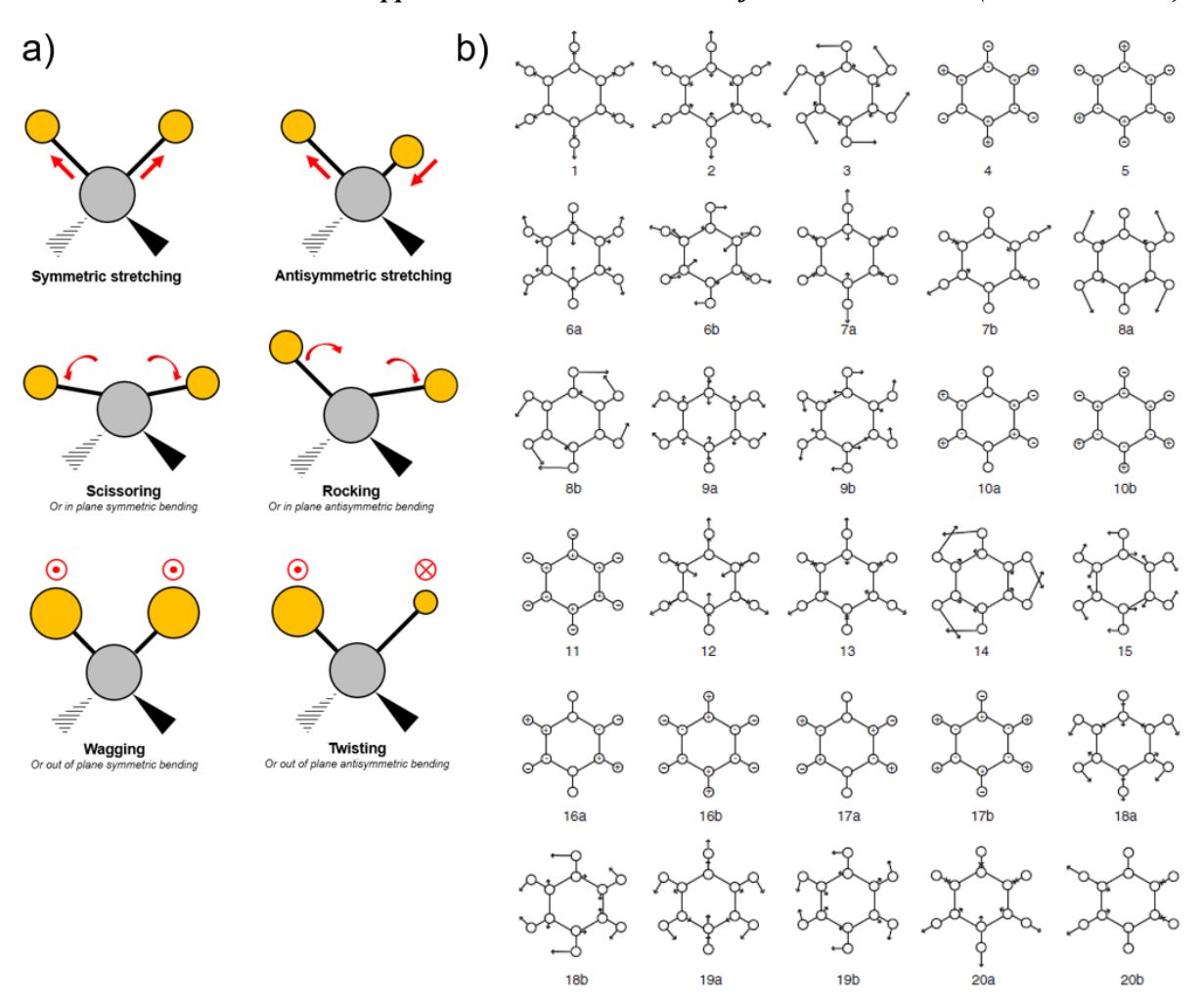


Figure H.1 a) Nomenclature used to describe the vibrational modes of a simple covalently bonded molecule. b) Wilson notation, which is used to describe the vibrational modes of benzene and other ring type organic molecules [316]. The degenerate modes are denoted by a and b components. Reprinted with permission from J. Chem. Phys. 2011, 135, 114305. Copyright 2011 AIP Publishing.

Appendix I. Permission for figures

Figure 2.6 Basic principle of Raman spectroscopy and Jablonski diagram along with Raman shifted response [170]. Reprinted with permission from Nanotechnol. Environ. Eng. 2023, 8, 41–48, Copyright 2018 Springer Nature.

SPRINGER NATURE LICENSE TERMS AND CONDITIONS

Apr 25, 2024

This Agreement between Indian Institute of Technology Ropar — Gaurav Pal Singh ("You") and Springer Nature ("Springer Nature") consists of your license details and the terms and conditions provided by Springer Nature and Copyright Clearance Center.

5776060986478 License Number

License date Apr 25, 2024

Licensed Content Publisher Springer Nature

Nanotechnology for Environmental Engineering Licensed Content Publication

Microplastic pollutant detection by Surface Enhanced Raman Spectroscopy (SERS): a mini-review Licensed Content Title

Licensed Content Author Tania Dey

Licensed Content Date Feb 10, 2022

Type of Use Thesis/Dissertation

Requestor type academic/university or research institute

Format print and electronic

figures/tables/illustrations Portion

Number of figures/tables/illustrations 1

Will you be translating?

Circulation/distribution 50000 or greater

Author of this Springer Nature

Tailoring of Optical Response for Sensing: Simulations, Roughness Effect, and Raman Title of new work

Expected presentation date Aug 2024

Portions FIgure 1

Indian Institute of Technology Ropar Bara Phool

Requestor Location

Rupnagar, Punjab 140001

Attn: Indian Institute of Technology Ropar

0.00 USD Total

Figure H.1 a) Nomenclature used to describe the vibrational modes of a simple covalently bonded molecule. b) Wilson notation, which is used to describe the vibrational modes of benzene and other ring type organic molecules [316]. The degenerate modes are denoted by a and b components. Reprinted with permission from J. Chem. Phys. 2011, 135, 114305. Copyright 2011 AIP Publishing.

AIP PUBLISHING LICENSE TERMS AND CONDITIONS Apr 20, 2024 This Agreement between Indian Institute of Technology Ropar -- Gaurav Pal Singh ("You") and AIP Publishing ("AIP Publishing") consists of your license details and the terms and conditions provided by AIP Publishing and Copyright Clearance Center. 5773271261332 License Number Apr 20, 2024 License date Licensed Content Publisher AIP Publishing Licensed Content Publication Journal of Chemical Physics Consistent assignment of the vibrations of monosubstituted Licensed Content Title Licensed Content Author Gardner, Adrian M.; Wright, Timothy G. Licensed Content Date Sep 19, 2011 Licensed Content Volume 135 Licensed Content Issue Thesis/Dissertation Type of Use Author (original article) Requestor type Format Print and electronic Figure/Table Portion Number of figures/tables Will you be translating? Tailoring of Optical Response for Sensing: Simulations, Roughness Effect, and Raman Title of new work Institution name IIT Ropar Expected presentation date Aug 2024 Figure 1 Indian Institute of Technology Ropar Bara Phool Requestor Location Rupnagar, Punjab 140001 India Attn: Indian Institute of Technology Ropar 0.00 USD

Total

Figure 2.7 Raman spectra of natural fingerprints of a human and fingerprints contaminated with aspirin, diclofenac, ketoprofen, ibuprofen and naproxen tablets in the "fingerprint" region of 500 cm-1 to 1800 cm-1 [176]. Reprinted with permission from *Sci. Rep.* 2022, 12, 3136. Copyright 2022 Springer Nature.

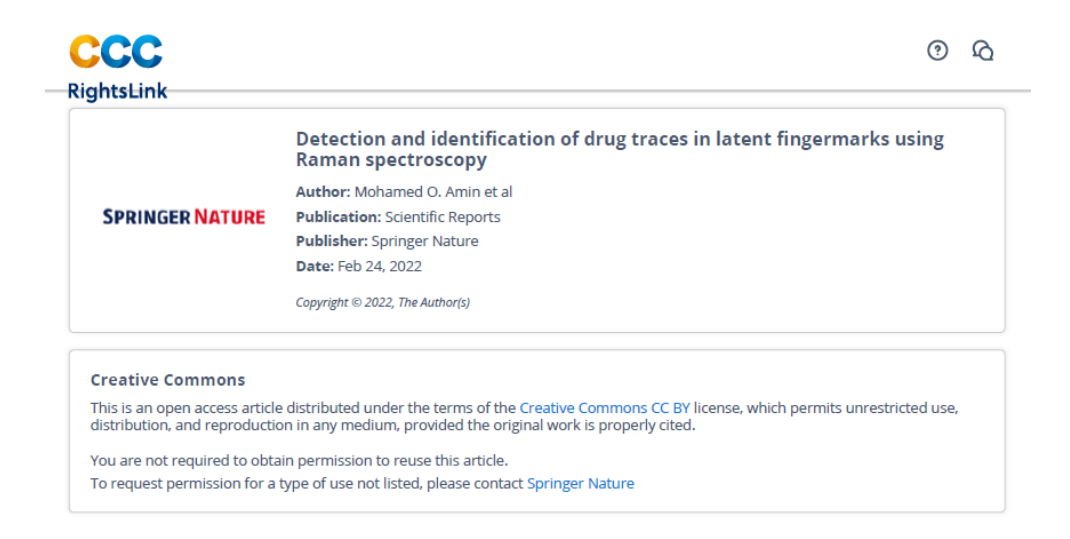
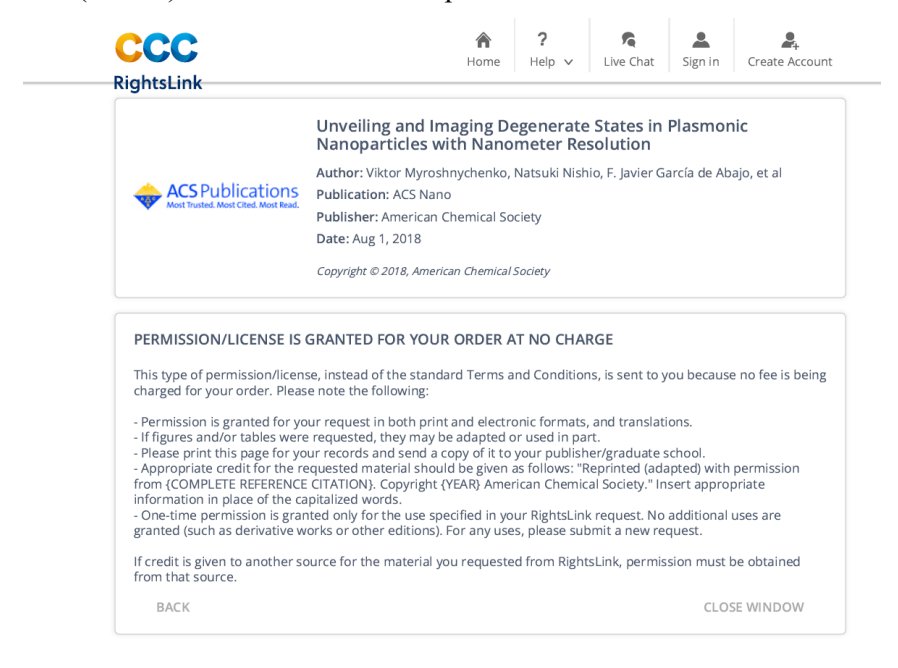


Figure 4.2 (a-d) Measured monochromatic photon maps for nanoprism of side 266 nm and height 50 nm for the dipole (D) (a and b) and quadrupole (Q) (c and d) modes at the peak energies for s (a and c) and p polarized (b and d) emission. Each pixel is associated with a different position of the electron beam [250]. (Figures adapted with permission from *ACS Nano* 2018, 12, 8436–8446. Copyright 2018 American Chemical Society). (e-f) The normalized electric field (V/m) using FEM simulation for the same nanoprism for the D (e and f) and Q (g and h) modes when the electric field is perpendicular (e and g) and parallel (f and h) to the side of the nanoprism.



References

- 1. (2024) Pesticides Use. In: Food Agric. Organ. United Nations. https://www.fao.org/faostat/en/#data/RP/visualize
- 2. Pimentel D (1996) Green revolution agriculture and chemical hazards. *Sci Total Environ* **188**:S86
- 3. Kaiser LL, Allen L (2002) Position of The American Dietetic Association. *J Am Diet Assoc* **102**:1479
- 4. Sabarwal A, Kumar K, Singh RP (2018) Hazardous effects of chemical pesticides on human health–Cancer and other associated disorders. *Environ Toxicol Pharmacol* **63**:103
- 5. (2003) Analysis of pesticide residues in bottled water
- 6. National Primary Drinking Water Regulations. In: U.S. Environ. Prot. Agency. https://www.epa.gov/ground-water-and-drinking-water/national-primary-drinking-water-regulations. Accessed 23 May 2024
- 7. (2023) Banning of Pesticides. In: Minist. Agric. Farmers Welf.
- 8. (2012) DRINKING WATER SPECIFICATION
- 9. (2024) List of pesticides which are banned, refused registration and restricted in use
- 10. Cupil-Garcia V, Strobbia P, Crawford BM, et al (2021) Plasmonic nanoplatforms: From surface-enhanced Raman scattering sensing to biomedical applications. *J Raman Spectrosc* **52**:541
- 11. Cialla D, März A, Böhme R, et al (2012) Surface-enhanced Raman spectroscopy (SERS): progress and trends. *Anal Bioanal Chem* **403**:27
- 12. Farcau C, Astilean S (2014) Periodically nanostructured substrates for surface enhanced Raman spectroscopy. *J Mol Struct* **1073**:102
- 13. Kitahama Y, Enogaki A, Tanaka Y, et al (2013) Truncated Power Law Analysis of Blinking SERS of Thiacyanine Molecules Adsorbed on Single Silver Nanoaggregates by Excitation at Various Wavelengths. *J Phys Chem C* **117**:9397
- 14. Sha MY, Xu H, Penn SG, Cromer R (2007) SERS nanoparticles: a new optical detection modality for cancer diagnosis. *Nanomedicine* **2**:725
- 15. Doherty MD, Murphy A, Pollard RJ, Dawson P (2013) Surface-Enhanced Raman Scattering from Metallic Nanostructures: Bridging the Gap between the Near-Field and Far-Field Responses. *Phys Rev X* **3**:011001
- 16. Ding T, Herrmann LO, de Nijs B, et al (2015) Self-Aligned Colloidal Lithography for Controllable and Tuneable Plasmonic Nanogaps. *Small* **11**:2139
- 17. Sharma B, Frontiera RR, Henry A-I, et al (2012) SERS: Materials, applications, and the future.

 Mater Today 15:16
- 18. Homola J (2006) Surface Plasmon Resonance Based Sensors. In: Springer Series on Chemical Sensors and Biosensors, 1st ed. Springer, Berlin, Heidelberg

- 19. Maier SA (2007) Plasmonics: Fundamentals And Applications. Springer US
- Mayer KM, Hafner JH (2011) Localized Surface Plasmon Resonance Sensors. Chem Rev 111:3828
- 21. Pandey PS, Raghuwanshi SK, Kumar S (2022) Recent Advances in Two-Dimensional Materials-Based Kretschmann Configuration for SPR Sensors: A Review. *IEEE Sens J* 22:1069
- 22. Maurer T, Adam P-M, Lévêque G (2015) Coupling between plasmonic films and nanostructures: from basics to applications. *Nanophotonics* **4**:363
- 23. Oates TWH, Wormeester H, Arwin H (2011) Characterization of plasmonic effects in thin films and metamaterials using spectroscopic ellipsometry. *Prog Surf Sci* **86**:328
- 24. Rycenga M, Cobley CM, Zeng J, et al (2011) Controlling the synthesis and assembly of silver nanostructures for plasmonic applications. *Chem Rev* **111**:3669
- 25. Singh GP, Sardana N (2022) Plasmonic response of metallic nanoparticles embedded in glass and a-Si. *Bull Mater Sci* **45**:241
- 26. Yaghubi F, Zeinoddini M, Saeedinia AR, et al (2020) Design of Localized Surface Plasmon Resonance (LSPR) Biosensor for Immunodiagnostic of E. coli O157:H7 Using Gold Nanoparticles Conjugated to the Chicken Antibody. *Plasmonics* 15:1481
- 27. Zhang D, Yan Y, Li Q, et al (2012) Label-free and high-sensitive detection of Salmonella using a surface plasmon resonance DNA-based biosensor. *J Biotechnol* **160**:123
- 28. D'Urso OF, Blasi MD De, Manera MG, et al (2008) Listeria monocytogenes detection with surface plasmon resonance and protein arrays. In: SENSORS, 2008 IEEE. pp 458–461
- Masdor NA, Altintas Z, Shukor MY, Tothill IE (2019) Subtractive inhibition assay for the detection of Campylobacter jejuni in chicken samples using surface plasmon resonance. *Sci Rep* 9:13642
- 30. Patel K, Halevi S, Melman P, et al (2017) A Novel Surface Plasmon Resonance Biosensor for the Rapid Detection of Botulinum Neurotoxins. *Biosensors* 7:
- 31. Kadota T, Takezawa Y, Hirano S, et al (2010) Rapid detection of nivalenol and deoxynivalenol in wheat using surface plasmon resonance immunoassay. *Anal Chim Acta* **673**:173
- 32. Gupta G, Singh PK, Boopathi M, et al (2010) Molecularly imprinted polymer for the recognition of biological warfare agent staphylococcal enterotoxin B based on Surface Plasmon Resonance. *Thin Solid Films* **519**:1115
- 33. Ertürk G, Özen H, Tümer MA, et al (2016) Microcontact imprinting based surface plasmon resonance (SPR) biosensor for real-time and ultrasensitive detection of prostate specific antigen (PSA) from clinical samples. Sensors Actuators B Chem 224:823
- 34. Chou T-H, Chuang C-Y, Wu C-M (2010) Quantification of Interleukin-6 in cell culture medium using surface plasmon resonance biosensors. *Cytokine* **51**:107
- 35. Yang C-Y, Brooks E, Li Y, et al (2005) Detection of picomolar levels of interleukin-8 in human saliva by SPR. *Lab Chip* 5:1017

- 36. Gnedenko O V, Mezentsev Y V, Molnar AA, et al (2013) Highly sensitive detection of human cardiac myoglobin using a reverse sandwich immunoassay with a gold nanoparticle-enhanced surface plasmon resonance biosensor. *Anal Chim Acta* **759**:105
- 37. Chen F, Wu Q, Song D, et al (2019) Fe3O4@PDA immune probe-based signal amplification in surface plasmon resonance (SPR) biosensing of human cardiac troponin I. *Colloids Surfaces B Biointerfaces* 177:105
- 38. Sharma PK, Kumar JS, Singh V V., et al (2020) Surface plasmon resonance sensing of Ebola virus: a biological threat. *Anal Bioanal Chem* **412**:4101
- 39. Estmer Nilsson C, Abbas S, Bennemo M, et al (2010) A novel assay for influenza virus quantification using surface plasmon resonance. *Vaccine* **28**:759
- 40. Wang X, Li Y, Wang H, et al (2010) Biosensors and Bioelectronics Gold nanorod-based localized surface plasmon resonance biosensor for sensitive detection of hepatitis B virus in buffer, blood serum and plasma. *Biosens Bioelectron* **26**:404
- 41. Omar NAS, Fen YW, Abdullah J, et al (2018) Development of an optical sensor based on surface plasmon resonance phenomenon for diagnosis of dengue virus E-protein. *Sens Bio-Sensing Res* **20**:16
- 42. Ke H, Du X, Wang L, et al (2020) Detection of morphine in urine based on a surface plasmon resonance imaging immunoassay. *Anal Methods* **12**:3038
- 43. Chuang T-LL, Chang C-CC, Chu-Su Y, et al (2014) Disposable surface plasmon resonance aptasensor with membrane-based sample handling design for quantitative interferon-gamma detection. *Lab Chip* **14**:2968
- 44. Fitzpatrick B, O'Kennedy R (2004) The development and application of a surface plasmon resonance-based inhibition immunoassay for the determination of warfarin in plasma ultrafiltrate. *J Immunol Methods* **291**:11
- 45. Park J-H, Byun J-Y, Yim S-Y, Kim M-G (2016) A Localized Surface Plasmon Resonance (LSPR)-based, simple, receptor-free and regeneratable Hg2+ detection system. *J Hazard Mater* **307**:137
- 46. Lokman NF, Bakar AAA, Suja F, et al (2014) Highly sensitive SPR response of Au/chitosan/graphene oxide nanostructured thin films toward Pb (II) ions. *Sensors Actuators B Chem* **195**:459
- 47. Agrawal H, Shrivastav AM, Gupta BD (2016) Surface plasmon resonance based optical fiber sensor for atrazine detection using molecular imprinting technique. *Sensors Actuators B Chem* **227**:204
- 48. Cakir O, Bakhshpour M, Yilmaz F, Baysal Z (2019) Novel QCM and SPR sensors based on molecular imprinting for highly sensitive and selective detection of 2,4-dichlorophenoxyacetic acid in apple samples. *Mater Sci Eng C* **102**:483
- 49. Estevez M-CC, Belenguer JJ, Gomez-Montes S, et al (2012) Indirect competitive immunoassay

- for the detection of fungicide Thiabendazole in whole orange samples by Surface Plasmon Resonance. *Analyst* **137**:5659
- 50. Hashim HS, Fen YW, Sheh Omar NA, et al (2020) Detection of phenol by incorporation of gold modified-enzyme based graphene oxide thin film with surface plasmon resonance technique.

 Opt Express 28:9738
- 51. Brulé T, Granger G, Bukar N, et al (2017) A field-deployed surface plasmon resonance (SPR) sensor for RDX quantification in environmental waters. *Analyst* **142**:2161
- 52. Cennamo N, D'Agostino G, Galatus R, et al (2013) Sensors based on surface plasmon resonance in a plastic optical fiber for the detection of trinitrotoluene. *Sensors Actuators B Chem* **188**:221
- 53. Kittel C (2004) Introduction to Solid State Physics, 8th ed. John Wiley & Sons, New York, NY
- 54. Chlebus R, Chylek J, Ciprian D, Hlubina P (2018) Surface Plasmon Resonance Based Measurement of the Dielectric Function of a Thin Metal Film. *Sensors (Basel)* **18**:3693
- 55. Citroni R, Di Paolo F, Di Carlo A (2018) Replacing noble metals with alternative metals in MID-IR frequency: A theoretical approach. In: AIP Conference Proceedings. p 020004
- 56. Hlaing M, Gebear-Eigzabher B, Roa A, et al (2016) Absorption and scattering cross-section extinction values of silver nanoparticles. *Opt Mater (Amst)* **58**:439
- 57. Rivera VAG, Ferri F, Marega E (2012) Localized Surface Plasmon Resonances: Noble Metal Nanoparticle Interaction With Rare-Earth Ions. In: Kim KY (ed) Plasmonics Principles and Applications, 1st ed. pp 283–312
- 58. Shabaninezhad M, Ramakrishna G (2019) Theoretical investigation of size, shape, and aspect ratio effect on the LSPR sensitivity of hollow-gold nanoshells. *J Chem Phys* **150**:144116
- 59. Zhuang Y, Liu L, Wu X, et al (2019) Size and Shape Effect of Gold Nanoparticles in "Far-Field" Surface Plasmon Resonance. *Part Part Syst Charact* **36**:1800077
- 60. Sonnefraud Y, Leen Koh A, McComb DW, Maier SA (2012) Nanoplasmonics: Engineering and observation of localized plasmon modes. *Laser Photon Rev* **6**:277
- 61. Kheirandish A, Sepehri Javan N, Mohammadzadeh H (2020) Modified Drude model for small gold nanoparticles surface plasmon resonance based on the role of classical confinement. *Sci Rep* **10**:6517
- 62. Vallée F (2007) Optical Properties of Metallic Nanoparticles. In: Nanomaterials and Nanochemistry. Springer Berlin Heidelberg, Berlin, Heidelberg, pp 197–227
- 63. Temple TL (2009) Optical properties of metal nanoparticles and their influence on silicon solar cells. University of Southampton
- 64. Stebunov Y V., Yakubovsky DI, Fedyanin DY, et al (2018) Superior Sensitivity of Copper-Based Plasmonic Biosensors. *Langmuir* **34**:4681
- 65. Soomro RA, Nafady A, Sirajuddin, et al (2014) 1-cysteine protected copper nanoparticles as colorimetric sensor for mercuric ions. *Talanta* **130**:415
- 66. Loos M (2015) Carbon Nanotube Reinforced Composites. Elsevier

- 67. Hao D, Hu C, Grant J, et al (2018) Hybrid localized surface plasmon resonance and quartz crystal microbalance sensor for label free biosensing. *Biosens Bioelectron* **100**:23
- 68. Mahmudin L, Wulandani R, Riswan M, et al (2024) Silver nanoparticles-based localized surface plasmon resonance biosensor for Escherichia coli detection. *Spectrochim Acta Part A Mol Biomol Spectrosc* **311**:123985
- 69. Moslemi A, Sansone L, Esposito F, et al (2024) Optical fiber probe based on LSPR for the detection of pesticide Thiram. *Opt Laser Technol* **175**:110882
- 70. Dissanayake NM, Arachchilage JS, Samuels TA, Obare SO (2019) Highly sensitive plasmonic metal nanoparticle-based sensors for the detection of organophosphorus pesticides. *Talanta* **200**:218
- 71. Kumar S, Singh R, Kaushik BK, et al (2019) LSPR-Based Cholesterol Biosensor Using Hollow Core Fiber Structure. *IEEE Sens J* **19**:7399
- 72. Li M, Singh R, Marques C, et al (2021) 2D material assisted SMF-MCF-MMF-SMF based LSPR sensor for creatinine detection. *Opt Express* **29**:38150
- 73. Feng B, Zhu R, Xu S, et al (2018) A sensitive LSPR sensor based on glutathione-functionalized gold nanoparticles on a substrate for the detection of Pb 2+ ions. *RSC Adv* **8**:4049
- 74. Li N, Lai Y, Lam SH, et al (2021) Directional Control of Light with Nanoantennas. *Adv Opt Mater* **9**:2001081
- 75. Patel SK, Argyropoulos C (2015) Plasmonic nanoantennas: enhancing light-matter interactions at the nanoscale. *EPJ Appl Metamaterials* **2**:4
- 76. Schumacher T, Kratzer K, Molnar D, et al (2011) Nanoantenna-enhanced ultrafast nonlinear spectroscopy of a single gold nanoparticle. *Nat Commun* **2**:333
- 77. Adato R, Yanik AA, Amsden JJ, et al (2009) Ultra-sensitive vibrational spectroscopy of protein monolayers with plasmonic nanoantenna arrays. *Proc Natl Acad Sci* **106**:19227
- 78. Liu Y, Cheng R, Liao L, et al (2011) Plasmon resonance enhanced multicolour photodetection by graphene. *Nat Commun* **2**:579
- 79. Chadha R, Das A, Lobo J, et al (2022) γ-Cyclodextrin capped silver and gold nanoparticles as colorimetric and Raman sensor for detecting traces of pesticide "Chlorpyrifos" in fruits and vegetables. *Colloids Surfaces A Physicochem Eng Asp* **641**:128558
- 80. Chadha R, Das A, Debnath AK, et al (2021) 2-thiazoline-2-thiol functionalized gold nanoparticles for detection of heavy metals, Hg(II) and Pb(II) and probing their competitive surface reactivity: A colorimetric, surface enhanced Raman scattering (SERS) and x-ray photoelectron spectroscopic (XPS). *Colloids Surfaces A Physicochem Eng Asp* **615**:126279
- 81. Chadha R, Das A, Kapoor S, Maiti N (2021) Surface-induced dimerization of 2-thiazoline-2-thiol on silver and gold nanoparticles: A surface enhanced Raman scattering (SERS) and density functional theoretical (DFT) study. *J Mol Liq* **322**:114536
- 82. Simovski C, Morits D, Voroshilov P, et al (2013) Enhanced efficiency of light-trapping

- nanoantenna arrays for thin-film solar cells. Opt Express 21:A714
- 83. Knight MW, King NS, Liu L, et al (2014) Aluminum for Plasmonics. ACS Nano 8:834
- 84. Sigle DO, Perkins E, Baumberg JJ, Mahajan S (2013) Reproducible Deep-UV SERRS on Aluminum Nanovoids. *J Phys Chem Lett* **4**:1449
- 85. Gokhale AA, Dumesic JA, Mavrikakis M (2008) On the Mechanism of Low-Temperature Water Gas Shift Reaction on Copper. *J Am Chem Soc* **130**:1402
- 86. Perelaer J, Smith PJ, Mager D, et al (2010) Printed electronics: the challenges involved in printing devices, interconnects, and contacts based on inorganic materials. *J Mater Chem* **20**:8446
- 87. Temple TL, Bagnall DM (2011) Optical properties of gold and aluminium nanoparticles for silicon solar cell applications. *J Appl Phys* **109**:084343
- 88. Kasani S, Curtin K, Wu N (2019) A review of 2D and 3D plasmonic nanostructure array patterns: fabrication, light management and sensing applications. *Nanophotonics* **8**:2065
- 89. Boltasseva A (2009) Plasmonic components fabrication via nanoimprint. *J Opt A Pure Appl Opt* 11:114001
- 90. Schade M, Fuhrmann B, Bohley C, et al (2014) Regular arrays of Al nanoparticles for plasmonic applications. *J Appl Phys* **115**:084309
- 91. Morarescu R, Shen H, Vallée RAL, et al (2012) Exploiting the localized surface plasmon modes in gold triangular nanoparticles for sensing applications. *J Mater Chem* **22**:11537
- 92. Takagi K, Nair S V., Watanabe R, et al (2017) Surface plasmon polariton resonance of gold, silver, and copper studied in the kretschmann geometry: Dependence on wavelength, angle of incidence, and film thickness. *J Phys Soc Japan* **86**:
- 93. Zhu H, Gao M, Pang C, et al (2022) Strong Faraday Rotation Based on Localized Surface Plasmon Enhancement of Embedded Metallic Nanoparticles in Glass. *Small Sci* 2100094
- 94. Bozzola A, Liscidini M, Andreani LC (2012) Photonic light-trapping versus Lambertian limits in thin film silicon solar cells with 1D and 2D periodic patterns. *Opt Express* **20**:A224
- 95. Yaseen MT, Chen M, Chang Y-C (2014) Partially embedded gold nanoislands in a glass substrate for SERS applications. *RSC Adv* **4**:55247
- 96. Chen Y, Karvonen L, Säynätjoki A, et al (2011) Ag nanoparticles embedded in glass by twostep ion exchange and their SERS application. *Opt Mater Express* **1**:164
- 97. Choudhury SA, Rifat RA, Fairooz F, et al (2017) On the possibility of using plasmonic metal nanoparticles embedded within the silicon substrate to enhance the energy conversion efficiency of silicon thin-film solar cells. In: 2017 IEEE Region 10 Humanitarian Technology Conference (R10-HTC). IEEE, pp 584–589
- 98. Mikac L, Ivanda M, Gotić M, et al (2015) Metal Nanoparticles Deposited on Porous Silicon Templates as Novel Substrates for SERS. *Croat Chem Acta* **88**:437
- 99. Pustovalov VK, Astafyeva LG (2021) Modeling of optical properties of plasmonic core-shell

- nanoparticles embedded in glass for filtering of solar radiation. *Nano-Structures & Nano-Objects* **27**:100776
- 100. Zhang Y, Wang Y (2017) Nonlinear optical properties of metal nanoparticles: a review. *RSC Adv* 7:45129
- 101. Kumar P, Chandra Mathpal M, Jagannath G, et al (2021) Optical limiting applications of resonating plasmonic Au nanoparticles in a dielectric glass medium. *Nanotechnology* **32**:345709
- 102. Kohlgraf-Owens DC, Kik PG (2009) Structural control of nonlinear optical absorption and refraction in dense metal nanoparticle arrays. *Opt Express* **17**:15032
- 103. Rao KS, Ganeev RA, Zhang K, et al (2019) Comparative analyses of optical limiting effects in metal nanoparticles and perovskite nanocrystals. *Opt Mater (Amst)* **92**:366
- 104. Koresawa H, Seki K, Hase E, et al (2022) Beam-angle-scanning surface plasmon resonance sensor for rapid, high-precision sensing of refractive index and bio-molecules. *Opt Contin* **1**:565
- 105. Wood RW (1902) XLII. On a remarkable case of uneven distribution of light in a diffraction grating spectrum. *London, Edinburgh, Dublin Philos Mag J Sci* **4**:396
- 106. Fano U (1941) The Theory of Anomalous Diffraction Gratings and of Quasi-Stationary Waves on Metallic Surfaces (Sommerfeld's Waves). *J Opt Soc Am* **31**:213
- 107. Otto A (1968) Excitation of nonradiative surface plasma waves in silver by the method of frustrated total reflection. *Zeitschrift für Phys A Hadron Nucl* **216**:398
- 108. Kretschmann E, Raether H (1968) Notizen: Radiative Decay of Non Radiative Surface Plasmons Excited by Light. *Zeitschrift für Naturforsch A* **23**:2135
- 109. Liedberg B, Nylander C, Lunström I (1983) Surface plasmon resonance for gas detection and biosensing. *Sensors and Actuators* **4**:299
- 110. Kegel LL, Boyne D, Booksh KS (2014) Sensing with prism-based near-infrared surface plasmon resonance spectroscopy on nanohole array platforms. *Anal Chem* **86**:3355
- 111. Liu J, Jalali M, Mahshid S, Wachsmann-Hogiu S (2020) Are plasmonic optical biosensors ready for use in point-of-need applications? *Analyst* **145**:364
- 112. Wujcik EK, Wei H, Zhang X, et al (2014) Antibody nanosensors: A detailed review. *RSC Adv* 4:43725
- 113. Samson R, Navale GR, Dharne MS (2020) Biosensors: frontiers in rapid detection of COVID-19. *3 Biotech* **10**:1
- 114. Zamora-Ledezma C, Clavijo DFC, Medina E, et al (2020) Biomedical science to tackle the COVID-19 pandemic: Current status and future perspectives. *Molecules* **25**:
- 115. Bhalla N, Pan Y, Yang Z, Payam AF (2020) Opportunities and Challenges for Biosensors and Nanoscale Analytical Tools for Pandemics: COVID-19. *ACS Nano* **14**:7783
- 116. Asif M, Ajmal M, Ashraf G, et al (2020) The role of biosensors in coronavirus disease-2019 outbreak. *Curr Opin Electrochem* **23**:174
- 117. Anderson GP, Liu JL, Zabetakis D, et al (2017) Label free checkerboard assay to determine

- overlapping epitopes of Ebola virus VP-40 antibodies using surface plasmon resonance. J Immunol Methods 442:42
- 118. Raether H (2006) Surface Plasmons on Smooth and Rough Surfaces and on Gratings. Springer Berlin Heidelberg
- 119. Snopok BA (2012) Theory and Practical Application of Surface Plasmon Resonance for Analytical Purposes. *Theor Exp Chem* **48**:283
- 120. Murray WA, Barnes WL (2007) Plasmonic materials. Adv Mater 19:3771
- 121. Zhang P, Chen Y-P, Wang W, et al (2016) Surface plasmon resonance for water pollutant detection and water process analysis. *TrAC Trends Anal Chem* **85**:153
- 122. Kedem O, Vaskevich A, Rubinstein I (2014) Critical issues in localized plasmon sensing. *J Phys Chem C* **118**:8227
- 123. Haes AJ, Van Duyne RP (2004) Preliminary studies and potential applications of localized surface plasmon resonance spectroscopy in medical diagnostics. *Expert Rev Mol Diagn* **4**:527
- 124. Kim N-H, Choi M, Kim TW, et al (2019) Sensitivity and Stability Enhancement of Surface Plasmon Resonance Biosensors based on a Large-Area Ag/MoS(2) Substrate. Sensors (Basel) 19:1894
- 125. Wang G, Wang C, Yang R, et al (2017) A Sensitive and Stable Surface Plasmon Resonance Sensor Based on Monolayer Protected Silver Film. *Sensors* 17:
- 126. Hayashi S, Nesterenko D V., Sekkat Z (2015) Fano resonance and plasmon-induced transparency in waveguide-coupled surface plasmon resonance sensors. Appl Phys Express 8:022201
- 127. Parrish T, Yang W (2020) Surface Plasmonic Resonance: The Underlying Fano Resonance Mechanism for the Attenuated Total Internal Reflection (ATIR). In: 2020 SoutheastCon. IEEE, pp 1–4
- 128. Agharazy Dormeny A, Abedini Sohi P, Kahrizi M (2020) Design and simulation of a refractive index sensor based on SPR and LSPR using gold nanostructures. *Results Phys* **16**:102869
- 129. Paliwal A, Tomar M, Gupta V (2016) Table top surface plasmon resonance measurement system for efficient urea biosensing using ZnO thin film matrix. *J Biomed Opt* **21**:087006
- 130. Homola J, Koudela I, Yee SS (1999) Surface plasmon resonance sensors based on diffraction gratings and prism couplers: sensitivity comparison. *Sensors Actuators B Chem* **54**:16
- 131. Polo J, Mackay T, Lakhtakia A (2013) Electromagnetic Surface Waves: A Modern Perspective. Elsevier Science
- 132. Qi H, Niu L, Zhang J, et al (2018) Large-area gold nanohole arrays fabricated by one-step method for surface plasmon resonance biochemical sensing. *Sci China Life Sci* **61**:476
- 133. Barnes WL, Murray WA, Dintinger J, et al (2004) Surface Plasmon Polaritons and Their Role in the Enhanced Transmission of Light Through Periodic Arrays of Subwavelength Holes in a Metal Film. *Phys Rev Lett* **92**:107401

- 134. Yurish S (2016) Advances in Sensors: Reviews, Vol. 3. IFSA Publishing
- 135. Gao H, McMahon JM, Lee MH, et al (2009) Rayleigh anomaly-surface plasmon polariton resonances in palladium and gold subwavelength hole arrays. *Opt Express* **17**:2334
- 136. Sinibaldi A, Danz N, Descrovi E, et al (2012) Direct comparison of the performance of Bloch surface wave and surface plasmon polariton sensors. *Sensors Actuators, B Chem* **174**:292
- 137. Zhang M, Wang J, Xiao T, et al (2018) Multispectral Plasmon-Induced Transparency Based on Asymmetric Metallic Nanoslices Array Metasurface. *Plasmonics* **13**:1535
- 138. Kuzmiak V, Maradudin AA (2015) Asymmetric transmission of surface plasmon polaritons on planar gratings. *Phys Rev A* **92**:053813
- 139. Vecchi G, Giannini V, Gómez Rivas J (2009) Shaping the Fluorescent Emission by Lattice Resonances in Plasmonic Crystals of Nanoantennas. *Phys Rev Lett* **102**:146807
- 140. Vecchi G, Giannini V, Gómez Rivas J (2009) Surface modes in plasmonic crystals induced by diffractive coupling of nanoantennas. *Phys Rev B* **80**:201401
- 141. Yang A, Hoang TB, Dridi M, et al (2015) Real-time tunable lasing from plasmonic nanocavity arrays. *Nat Commun* **6**:6939
- 142. Guan J, Sagar LK, Li R, et al (2020) Quantum Dot-Plasmon Lasing with Controlled Polarization Patterns. *ACS Nano* **14**:3426
- 143. Matricardi C, Hanske C, Garcia-Pomar JL, et al (2018) Gold Nanoparticle Plasmonic Superlattices as Surface-Enhanced Raman Spectroscopy Substrates. *ACS Nano* 12:8531
- 144. Hanske C, Hill EH, Vila-Liarte D, et al (2019) Solvent-Assisted Self-Assembly of Gold Nanorods into Hierarchically Organized Plasmonic Mesostructures. ACS Appl Mater Interfaces 11:11763
- 145. Plou J, García I, Charconnet M, et al (2020) Multiplex SERS Detection of Metabolic Alterations in Tumor Extracellular Media. *Adv Funct Mater* **30**:1910335
- 146. Yoon BK, Hwang W, Park YJ, et al (2005) Direct patterning of self assembled nano-structures of block copolymers via electron beam lithography. *Macromol Res* **13**:435
- 147. Keil M, Wetzel AE, Wu K, et al (2021) Large plasmonic color metasurfaces fabricated by super resolution deep UV lithography. *Nanoscale Adv* **3**:2236
- 148. Liu R, Cao L, Liu D, et al (2023) Laser Interference Lithography—A Method for the Fabrication of Controlled Periodic Structures. *Nanomaterials* **13**:1818
- 149. Zhao Z-J, Hwang S, Bok M, et al (2019) Nanopattern-Embedded Micropillar Structures for Security Identification. *ACS Appl Mater Interfaces* **11**:30401
- 150. Heltzel A, Theppakuttai S, Chen SC, Howell JR (2008) Surface plasmon-based nanopatterning assisted by gold nanospheres. *Nanotechnology* **19**:025305
- 151. Robatjazi H, Bahauddin SM, Macfarlan LH, et al (2016) Ultrathin AAO Membrane as a Generic Template for Sub-100 nm Nanostructure Fabrication. *Chem Mater* **28**:4546
- 152. Nishijima Y, Rosa L, Juodkazis S (2012) Surface plasmon resonances in periodic and random

- patterns of gold nano-disks for broadband light harvesting. Opt Express 20:11466
- 153. Hasan RMM, Luo X (2017) Nanolithography: Status and challenges. In: 2017 23rd International Conference on Automation and Computing (ICAC). IEEE, pp 1–6
- 154. Tassin P, Zhang L, Koschny T, et al (2009) Low-Loss Metamaterials Based on Classical Electromagnetically Induced Transparency. *Phys Rev Lett* **102**:053901
- 155. Zhao X, Huang R, Du X, et al (2024) Ultrahigh- Q Metasurface Transparency Band Induced by Collective–Collective Coupling. Nano Lett. https://doi.org/10.1021/acs.nanolett.3c04174
- 156. Yang Y, Wang W, Boulesbaa A, et al (2015) Nonlinear Fano-Resonant Dielectric Metasurfaces.

 Nano Lett 15:7388
- 157. Taubert R, Hentschel M, Kästel J, Giessen H (2012) Classical Analog of Electromagnetically Induced Absorption in Plasmonics. *Nano Lett* **12**:1367
- 158. Xie Q, Hong MH, Tan HL, et al (2008) Fabrication of nanostructures with laser interference lithography. *J Alloys Compd* **449**:261
- 159. Lasagni AF (2017) Laser interference patterning methods: Possibilities for high-throughput fabrication of periodic surface patterns. *Adv Opt Technol* **6**:
- 160. Hong KY, de Albuquerque CDL, Poppi RJ, Brolo AG (2017) Determination of aqueous antibiotic solutions using SERS nanogratings. *Anal Chim Acta* **982**:148
- 161. Hwang J, Yang M (2018) Sensitive and Reproducible Gold SERS Sensor Based on Interference Lithography and Electrophoretic Deposition. Sensors 18:4076
- 162. Chen Z, Chen Z, Feng K, et al (2022) Exploring SERS from two-dimensional symmetric gold array fabricated by double exposure laser interference lithography. *Opt Commun* **514**:128169
- 163. Xiang D, Liu Z, Wu M, et al (2020) Enhanced Piezo-Photoelectric Catalysis with Oriented Carrier Migration in Asymmetric Au–ZnO Nanorod Array. *Small* **16**:1907603
- 164. Kauranen M, Zayats A V. (2012) Nonlinear plasmonics. *Nat Photonics* **6**:737
- 165. Temple TL, Mahanama GDK, Reehal HS, Bagnall DM (2009) Influence of localized surface plasmon excitation in silver nanoparticles on the performance of silicon solar cells. *Sol Energy Mater Sol Cells* **93**:1978
- 166. Potejanasak P, Duangchan S (2020) Gold Nanoisland Agglomeration upon the Substrate Assisted Chemical Etching Based on Thermal Annealing Process. *Crystals* **10**:533
- 167. Hulteen JC, Patrissi CJ, Miner DL, et al (1997) Changes in the Shape and Optical Properties of Gold Nanoparticles Contained within Alumina Membranes Due to Low-Temperature Annealing. *J Phys Chem B* **101**:7727
- 168. Cesca T, Manca M, Michieli N, Mattei G (2019) Tuning the linear and nonlinear optical properties of ordered plasmonic nanoarrays by morphological control with thermal annealing. *Appl Surf Sci* **491**:67
- 169. Xu L, Tan LS, Hong MH (2011) Tuning of localized surface plasmon resonance of well-ordered Ag/Au bimetallic nanodot arrays by laser interference lithography and thermal annealing. *Appl*

- Opt **50**:G74
- 170. Dey T (2023) Microplastic pollutant detection by Surface Enhanced Raman Spectroscopy (SERS): a mini-review. *Nanotechnol Environ Eng* **8**:41
- 171. Prochazka M (2016) Surface-Enhanced Raman Spectroscopy. Springer International Publishing, Cham
- 172. Langer J, Jimenez de Aberasturi D, Aizpurua J, et al (2020) Present and Future of Surface-Enhanced Raman Scattering. *ACS Nano* **14**:28
- 173. Verma P (2017) Tip-Enhanced Raman Spectroscopy: Technique and Recent Advances. *Chem Rev* **117**:6447
- 174. Müller M, Zumbusch A (2007) Coherent anti-Stokes Raman Scattering Microscopy. ChemPhysChem 8:2156
- 175. Kögler M, Heilala B (2020) Time-gated Raman spectroscopy a review. *Meas Sci Technol* 32:012002
- 176. Amin MO, Al-Hetlani E, Lednev IK (2022) Detection and identification of drug traces in latent fingermarks using Raman spectroscopy. *Sci Rep* **12**:3136
- 177. Jiang L, Hassan MM, Ali S, et al (2021) Evolving trends in SERS-based techniques for food quality and safety: A review. *Trends Food Sci Technol* **112**:225
- 178. Li C, Huang Y, Li X, et al (2021) Towards practical and sustainable SERS: a review of recent developments in the construction of multifunctional enhancing substrates. *J Mater Chem C* 9:11517
- 179. Fleischmann M, Hendra PJ, McQuillan AJ (1974) Raman spectra of pyridine adsorbed at a silver electrode. *Chem Phys Lett* **26**:163
- 180. Angelini F, Colao F (2019) Optimization of laser wavelength, power and pulse duration for eye-safe Raman spectroscopy. *J Eur Opt Soc Publ* **15**:2
- 181. Cardinal MF, Vander Ende E, Hackler RA, et al (2017) Expanding applications of SERS through versatile nanomaterials engineering. *Chem Soc Rev* **46**:3886
- 182. Kumar S, Gahlaut SK, Singh JP (2022) Sculptured thin films: Overcoming the limitations of surface-enhanced Raman scattering substrates. *Appl Surf Sci Adv* **12**:100322
- 183. Tong L, Zhu T, Liu Z (2011) Approaching the electromagnetic mechanism of surface-enhanced Raman scattering: from self-assembled arrays to individual gold nanoparticles. *Chem Soc Rev* **40**:1296
- 184. Boyack R, Le Ru EC (2009) Investigation of particle shape and size effects in SERS using T-matrix calculations. *Phys Chem Chem Phys* **11**:7398
- 185. Lee D, Yoon S (2016) Effect of Nanogap Curvature on SERS: A Finite-Difference Time-Domain Study. *J Phys Chem C* **120**:20642
- 186. Feng J, Hu Y, Grant E, Lu X (2018) Determination of thiabendazole in orange juice using an MISPE-SERS chemosensor. *Food Chem* **239**:816

- 187. He L, Lamont E, Veeregowda B, et al (2011) Aptamer-based surface-enhanced Raman scattering detection of ricin in liquid foods. *Chem Sci* **2**:1579
- 188. He L, D. Deen B, Pagel AH, et al (2013) Concentration, detection and discrimination of Bacillus anthracis spores in orange juice using aptamer based surface enhanced Raman spectroscopy.

 Analyst 138:1657
- 189. Feng S, Hu Y, Ma L, Lu X (2017) Development of molecularly imprinted polymers-surfaceenhanced Raman spectroscopy/colorimetric dual sensor for determination of chlorpyrifos in apple juice. *Sensors Actuators B Chem* **241**:750
- 190. Pang S, Labuza TP, He L (2014) Development of a single aptamer-based surface enhanced Raman scattering method for rapid detection of multiple pesticides. *Analyst* **139**:1895
- 191. Liu P, Liu R, Guan G, et al (2011) Surface-enhanced Raman scattering sensor for theophylline determination by molecular imprinting on silver nanoparticles. *Analyst* **136**:4152
- 192. Hassan MM, Zareef M, Jiao T, et al (2021) Signal optimized rough silver nanoparticle for rapid SERS sensing of pesticide residues in tea. *Food Chem* **338**:127796
- 193. Feng S, Gao F, Chen Z, et al (2013) Determination of α-Tocopherol in Vegetable Oils Using a Molecularly Imprinted Polymers–Surface-Enhanced Raman Spectroscopic Biosensor. J Agric Food Chem 61:10467
- 194. Chen J, Huang Y, Kannan P, et al (2016) Flexible and Adhesive Surface Enhance Raman Scattering Active Tape for Rapid Detection of Pesticide Residues in Fruits and Vegetables. *Anal Chem* **88**:2149
- 195. Wang P, Pang S, Pearson B, et al (2017) Rapid concentration detection and differentiation of bacteria in skimmed milk using surface enhanced Raman scattering mapping on 4-mercaptophenylboronic acid functionalized silver dendrites. *Anal Bioanal Chem* **409**:2229
- 196. Ye C, He M, Zhu Z, et al (2022) A portable SERS sensing platform for the multiplex identification and quantification of pesticide residues on plant leaves. *J Mater Chem C* **10**:12966
- 197. Technique O, Technologies J, Clayton K, et al (2016) Encyclopedia of Nanotechnology. Springer Netherlands, Dordrecht
- 198. Sancho-Parramon J (2009) Surface plasmon resonance broadening of metallic particles in the quasi-static approximation: a numerical study of size confinement and interparticle interaction effects. *Nanotechnology* **20**:235706
- 199. Mie G (1908) Beiträge zur Optik trüber Medien, speziell kolloidaler Metallösungen. *Ann Phys* **330**:377
- 200. Zubko E, Petrov D, Grynko Y, et al (2010) Validity criteria of the discrete dipole approximation.
 Appl Opt 49:1267
- 201. Akbarzadeh Sharbaf A, Sarraf-Shirazi R (2010) An Unconditionally Stable Hybrid FETD-FDTD Formulation Based on the Alternating-Direction Implicit Algorithm. IEEE Antennas Wirel Propag Lett 9:1174

- 202. Chen Z, Taflove A, Backman V (2004) Photonic nanojet enhancement of backscattering of light by nanoparticles: a potential novel visible-light ultramicroscopy technique. *Opt Express* **12**:1214
- 203. Rakić AD, Djurišić AB, Elazar JM, Majewski ML (1998) Optical properties of metallic films for vertical-cavity optoelectronic devices. *Appl Opt* **37**:5271
- 204. Frezza F, Mangini F, Tedeschi N (2018) Introduction to electromagnetic scattering: tutorial. *J* Opt Soc Am A **35**:163
- 205. Grand J, Le Ru EC (2020) Practical Implementation of Accurate Finite-Element Calculations for Electromagnetic Scattering by Nanoparticles. *Plasmonics* **15**:109
- 206. Fantoni A, Fernandes M, Vygranenko Y, et al (2018) A Simulation Study of Surface Plasmons in Metallic Nanoparticles: Dependence on the Properties of an Embedding a-Si:H Matrix. *Phys status solidi* **215**:1700487
- 207. Xue X, Fan Y, Segal E, et al (2021) Periodical concentration of surface plasmon polaritons by wave interference in metallic film with nanocavity array. *Mater Today* **46**:54
- 208. Mäntynen H, Lipsanen H, Anttu N (2021) Symmetry Reduction in FEM Optics Modeling of Single and Periodic Nanostructures. *Symmetry (Basel)* **13**:752
- 209. Lv Z, Liu L, Zhangyang X, et al (2020) Enhanced absorptive characteristics of GaN nanowires for ultraviolet (UV) photocathode. *Appl Phys A* **126**:152
- 210. Braundmeier AJ, Arakawa ET (1974) Effect of surface roughness on surface plasmon resonance absorption. *J Phys Chem Solids* **35**:517
- 211. Mills DL (1975) Attenuation of surface polaritons by surface roughness. Phys Rev B 12:4036
- 212. Eagen CF, Weber WH (1979) Modulated surface-plasmon resonance for adsorption studies. *Phys Rev B* **19**:5068
- 213. Niklasson GA, Granqvist CG, Hunderi O (1981) Effective medium models for the optical properties of inhomogeneous materials. *Appl Opt* **20**:26
- 214. Dolan JA, Saba M, Dehmel R, et al (2016) Gyroid Optical Metamaterials: Calculating the Effective Permittivity of Multidomain Samples. *ACS Photonics* **3**:1888
- 215. Haddouche I, Cherbi L (2017) Comparison of finite element and transfer matrix methods for numerical investigation of surface plasmon waveguides. *Opt Commun* **382**:132
- 216. Lee C, Yang W, Parr RG (1988) Development of the Colle-Salvetti correlation-energy formula into a functional of the electron density. *Phys Rev B* **37**:785
- 217. Costa JCS, Ando RA, Sant'Ana AC, Corio P (2012) Surface-enhanced Raman spectroscopy studies of organophosphorous model molecules and pesticides. *Phys Chem Chem Phys* **14**:15645
- 218. Castillo M V., Iramain MA, Davies L, et al (2018) Evaluation of the structural properties of powerful pesticide dieldrin in different media and their complete vibrational assignment. J Mol Struct 1154:392
- 219. Joselin Beaula T, James C (2014) FT IR, FT-Raman spectra and chemical computations of herbicide 2-phenoxy propionic acid A DFT approach. *Spectrochim Acta Part A Mol Biomol*

- Spectrosc 122:661
- 220. Huang S, Yan W, Liu M, Hu J (2016) Detection of difenoconazole pesticides in pak choi by surface-enhanced Raman scattering spectroscopy coupled with gold nanoparticles. *Anal Methods* **8**:4755
- 221. Pietro WJ, Levi BA, Hehre WJ, Stewart RF (1980) Molecular orbital theory of the properties of inorganic and organometallic compounds. 1. STO-NG basis sets for third-row main-group elements. *Inorg Chem* 19:2225
- 222. Hehre WJ, Stewart RF, Pople JA (1969) Self-Consistent Molecular-Orbital Methods. I. Use of Gaussian Expansions of Slater-Type Atomic Orbitals. *J Chem Phys* **51**:2657
- 223. Hehre WJ, Ditchfield R, Pople JA (1972) Self—Consistent Molecular Orbital Methods. XII. Further Extensions of Gaussian—Type Basis Sets for Use in Molecular Orbital Studies of Organic Molecules. *J Chem Phys* **56**:2257
- 224. McLean AD, Chandler GS (1980) Contracted Gaussian basis sets for molecular calculations. I. Second row atoms, Z = 11-18. *J Chem Phys* **72**:5639
- 225. Dunning TH (1989) Gaussian basis sets for use in correlated molecular calculations. I. The atoms boron through neon and hydrogen. *J Chem Phys* **90**:1007
- 226. Collins JB, von R. Schleyer P, Binkley JS, Pople JA (1976) Self-consistent molecular orbital methods. XVII. Geometries and binding energies of second-row molecules. A comparison of three basis sets. *J Chem Phys* **64**:5142
- 227. Jensen JO (2003) Vibrational frequencies and structural determination of tetraethynylstannane. *J Mol Struct THEOCHEM* **640**:87
- 228. Godbout N, Salahub DR, Andzelm J, Wimmer E (1992) Optimization of Gaussian-type basis sets for local spin density functional calculations. Part I. Boron through neon, optimization technique and validation. *Can J Chem* **70**:560
- 229. Sosa C, Andzelm J, Elkin BC, et al (1992) A local density functional study of the structure and vibrational frequencies of molecular transition-metal compounds. *J Phys Chem* **96**:6630
- 230. Dalla Via A (2018) Density Functional Theory simulations of Raman and UV-VIS spectra of carbon atom wires. Politecnico di Milano
- 231. Sholl DS, Steckel JA (2009) Density Functional Theory. Wiley
- 232. Placzek G (1931) Intensität und Polarisation der Ramanschen Streustrahlung mehratomiger Moleküle. Zeitschrift für Phys **70**:84
- 233. Neugebauer J, Reiher M, Kind C, Hess BA (2002) Quantum chemical calculation of vibrational spectra of large molecules—Raman and IR spectra for Buckminsterfullerene. *J Comput Chem* 23:895
- 234. Moura JVB, Silveira JV, da Silva Filho JG, et al (2018) Temperature-induced phase transition in h-MoO3: Stability loss mechanism uncovered by Raman spectroscopy and DFT calculations. *Vib Spectrosc* **98**:98

- 235. Lloyd H (1831) On a New Case of Interference of the Rays of Light. Trans R Irish Acad 17:171
- 236. Titchmarsh PF (1941) Lloyd's single-mirror interference fringes. *Proc Phys Soc* **53**:391
- 237. Lu C, Lipson RH (2010) Interference lithography: a powerful tool for fabricating periodic structures. *Laser Photon Rev* **4**:568
- 238. Hassanzadeh A, Mohammadnezhad M, Mittler S (2015) Multiexposure laser interference lithography. *J Nanophotonics* **9**:093067
- 239. Shimizu Y (2021) Laser Interference Lithography for Fabrication of Planar Scale Gratings for Optical Metrology. *Nanomanufacturing Metrol* **4**:3
- 240. Lin T-H, Yang Y-K, Fu C-C (2017) Integration of multiple theories for the simulation of laser interference lithography processes. *Nanotechnology* **28**:475301
- 241. Najiminaini M, Vasefi F, Kaminska B, Carson JJL (2011) Optical resonance transmission properties of nano-hole arrays in a gold film: effect of adhesion layer. *Opt Express* **19**:26186
- 242. Ghosh PK, Debu DT, French DA, Herzog JB (2017) Calculated thickness dependent plasmonic properties of gold nanobars in the visible to near-infrared light regime. *PLoS One* **12**:1
- 243. Fu J, Park B, Zhao Y (2009) Limitation of a localized surface plasmon resonance sensor for Salmonella detection. *Sensors Actuators, B Chem* **141**:276
- 244. Alsawafta M, Wahbeh M, Truong V Van (2012) Plasmonic modes and optical properties of gold and silver ellipsoidal nanoparticles by the discrete dipole approximation. *J Nanomater* **2012**:
- 245. Raziman T V., Martin OJF (2013) Polarisation charges and scattering behaviour of realistically rounded plasmonic nanostructures. *Opt Express* **21**:21500
- 246. Mori T, Yamaguchi K, Tanaka Y, et al (2016) Optical characteristics of rounded silver nanoprisms. *Opt Rev* **23**:260
- 247. B. Johnson P, W. Christy R (1972) Optical Constants of Noble Metals. *Phys Rev B* 6:
- 248. Smith DY, Shiles E, Inokuti M (1997) The Optical Properties of Metallic Aluminum
- 249. Pierce DT, Spicer WE (1972) Electronic Structure of Amorphous Si from Photoemission and Optical Studies. *Phys Rev B* **5**:3017
- 250. Myroshnychenko V, Nishio N, García de Abajo FJ, et al (2018) Unveiling and Imaging Degenerate States in Plasmonic Nanoparticles with Nanometer Resolution. *ACS Nano* 12:8436
- 251. Jensen T, Kelly L, Lazarides A, Schatz GC (1999) Electrodynamics of Noble Metal Nanoparticles and Nanoparticle Clusters. *J Clust Sci* **10**:295
- 252. Palanisamy S, Zhang X, He T (2016) Simple colorimetric detection of dopamine using modified silver nanoparticles. *Sci China Chem* **59**:387
- 253. Liao PF, Wokaun A (1982) Lightning rod effect in surface enhanced Raman scattering. *J Chem Phys* **76**:751
- 254. Lermé J, Baida H, Bonnet C, et al (2010) Size Dependence of the Surface Plasmon Resonance Damping in Metal Nanospheres. *J Phys Chem Lett* **1**:2922
- 255. Kelly KL, Coronado E, Zhao LL, Schatz GC (2003) The optical properties of metal

- nanoparticles: The influence of size, shape, and dielectric environment. J Phys Chem B 107:668
- 256. Paris A, Vaccari A, Lesina AC, et al (2012) Plasmonic Scattering by Metal Nanoparticles for Solar Cells. *Plasmonics* 7:525
- 257. Gawad S, Valero A, Braschler T (2016) Encyclopedia of Nanotechnology. Springer Netherlands, Dordrecht
- 258. Tavakkoli Yaraki M, Daqiqeh Rezaei S, Tan YN (2020) Simulation guided design of silver nanostructures for plasmon-enhanced fluorescence, singlet oxygen generation and SERS applications. *Phys Chem Chem Phys* **22**:5673
- 259. Rang M, Jones AC, Zhou F, et al (2008) Optical Near-Field Mapping of Plasmonic Nanoprisms.

 Nano Lett 8:3357
- 260. Yu H, Zhang P, Lu S, et al (2020) Synthesis and Multipole Plasmon Resonances of Spherical Aluminum Nanoparticles. *J Phys Chem Lett* **11**:5836
- Kreibig U, Vollmer M (1995) Optical Properties of Metal Clusters. Springer Berlin Heidelberg,
 Berlin, Heidelberg
- 262. Grigorchuk NI (2012) Effect of Surface Plasmon Linewidth Oscillations on Optical Properties of Metal Nanoparticle Embedded in a Dielectric Media. *J Phys Chem C* **116**:23704
- 263. Bansal A, Verma SS (2014) Searching for Alternative Plasmonic Materials for Specific Applications. *Indian J Mater Sci* **2014**:1
- 264. Junhua Li 李俊华, Qiang Kan 阚强, Chunxia Wang 王春霞, Hongda Chen 陈弘达 (2011) Ef fect of shape, height, and interparticle spacing of Au nanoparticles on the sensing performance of Au nanoparticle array. *Chinese Opt Lett* **9**:090501
- 265. Sievers J, Below M, Reinhardt C, et al (2021) Periodic metal resonator chains for surface enhanced Raman scattering (SERS). *J Appl Phys* **130**:
- 266. Kravets VG, Kabashin A V., Barnes WL, Grigorenko AN (2018) Plasmonic Surface Lattice Resonances: A Review of Properties and Applications. *Chem Rev* 118:5912
- 267. Taylor AD, Ladd J, Yu Q, et al (2006) Quantitative and simultaneous detection of four foodborne bacterial pathogens with a multi-channel SPR sensor. *Biosens Bioelectron* **22**:752
- 268. Islam A, Haider F, Ahmmed Aoni R, Ahmed R (2022) Plasmonic photonic biosensor: in situ detection and quantification of SARS-CoV-2 particles. *Opt Express* **30**:40277
- 269. Nankali M, Einalou Z, Asadnia M, Razmjou A (2021) High-Sensitivity 3D ZIF-8/PDA Photonic Crystal-Based Biosensor for Blood Component Recognition. *ACS Appl Bio Mater* **4**:1958
- 270. Forzani ES, Zhang H, Chen W, Tao N (2005) Detection of Heavy Metal Ions in Drinking Water Using a High-Resolution Differential Surface Plasmon Resonance Sensor. *Environ Sci Technol* **39**:1257
- 271. Gouzy M-F, Keß M, Krämer PM (2009) A SPR-based immunosensor for the detection of isoproturon. *Biosens Bioelectron* **24**:1563

- 272. Päivänranta B, Merbold H, Giannini R, et al (2011) High Aspect Ratio Plasmonic Nanostructures for Sensing Applications. *ACS Nano* **5**:6374
- 273. Iqbal T, Noureen S, Afsheen S, et al (2020) Rectangular and sinusoidal Au-Grating as plasmonic sensor: A comparative study. *Opt Mater (Amst)* **99**:109530
- 274. Bukasov R, Ali TA, Nordlander P, Shumaker-Parry JS (2010) Probing the Plasmonic Near-Field of Gold Nanocrescent Antennas. *ACS Nano* 4:6639
- 275. Sun P, Zhou C, Jia W, et al (2020) Narrowband absorber based on magnetic dipole resonances in two-dimensional metal-dielectric grating for sensing. *Opt Commun* **459**:124946
- 276. Khan Y, Li A, Chang L, et al (2018) Gold nano disks arrays for localized surface plasmon resonance based detection of PSA cancer marker. *Sensors Actuators B Chem* **255**:1298
- 277. Cheng D, Cao S, Ding S, et al (2020) Ultrahigh absorption modulation in semiconductor/silvernanoarray hybrid metasurface. *Results Phys* **17**:103143
- 278. Lee S-W, Lee K-S, Ahn J, et al (2011) Highly Sensitive Biosensing Using Arrays of Plasmonic Au Nanodisks Realized by Nanoimprint Lithography. *ACS Nano* **5**:897
- 279. Hongyu W, Ni L (2024) Simulation research of localized surface plasmon sensor based on gold nanocone hexagonal array structure. *Chem Phys* **579**:112167
- 280. Im H, Sutherland JN, Maynard JA, Oh S-H (2012) Nanohole-Based Surface Plasmon Resonance Instruments with Improved Spectral Resolution Quantify a Broad Range of Antibody-Ligand Binding Kinetics. Anal Chem 84:1941
- 281. Nair R V., S. AT, Menon AU (2023) Orientation-Specific Plasmonic Biosensor for Alzheimer's Disease Detection Using Graphene-Wrapped Au Nano ellipsoids. Plasmonics. https://doi.org/10.1007/s11468-023-02006-5
- 282. Naguib M, Kurtoglu M, Presser V, et al (2011) Two-Dimensional Nanocrystals Produced by Exfoliation of Ti3AlC2. *Adv Mater* **23**:4248
- 283. P. B. Johnson and R. W. Christy (1972) Optical Constant of the Nobel Metals. *Phys L Re View B* **6**:4370
- 284. El-Gohary SH, Choi M, Kim YL, Byun KM (2016) Dispersion curve engineering of TiO2/silver hybrid substrates for enhanced surface plasmon resonance detection. *Sensors (Switzerland)* **16**:
- 285. Badilescu S, Raju D, Bathini S, Packirisamy M (2020) Gold nano-island platforms for localized surface plasmon resonance sensing: A short review. *Molecules* **25**:
- 286. Thompson C V. (2012) Solid-state dewetting of thin films. Annu Rev Mater Res 42:399
- 287. Siegel J, Lyutakov O, Rybka V, et al (2011) Properties of gold nanostructures sputtered on glass.

 Nanoscale Res Lett 6:1
- 288. Singh GP, Samanta S, Pegu A, et al (2023) Enhancement of plasmonic response by piezoelectrically deposited gold films. Indian J Phys. https://doi.org/10.1007/s12648-023-02974-8
- 289. Ercolessi F, Andreoni W, Tosatti E (1991) Melting of small gold particles: Mechanism and size

- effects. Phys Rev Lett 66:911
- 290. Yu X, Duxbury PM (1995) Kinetics of nonequilibrium shape change in gold clusters. *Phys Rev* B **52**:2102
- 291. Törmö P, Barnes WL (2015) Strong coupling between surface plasmon polaritons and emitters: A review. *Reports Prog Phys* **78**:
- 292. Auguié B, Barnes WL (2008) Collective Resonances in Gold Nanoparticle Arrays. *Phys Rev Lett* **101**:143902
- 293. Ray D, Wang H, Kim J, et al (2022) A Low-Temperature Annealing Method for Alloy Nanostructures and Metasurfaces: Unlocking a Novel Degree of Freedom. *Adv Mater* **34**:
- 294. Edlén B (1966) The Refractive Index of Air. Metrologia 2:71
- 295. RITLAND HN (1955) Relation Between Refractive Index and Density of a Glass at Constant Temperature. *J Am Ceram Soc* **38**:86
- 296. He XN, Gao Y, Mahjouri-Samani M, et al (2012) Surface-enhanced Raman spectroscopy using gold-coated horizontally aligned carbon nanotubes. *Nanotechnology* **23**:205702
- 297. Yan Y, Zhang J, Xu P, Miao P (2017) Fabrication of arrayed triangular micro-cavities for SERS substrates using the force modulated indention process. *RSC Adv* 7:11969
- 298. Li Z, Bai J, Tang J (2018) Micro-EDM method to fabricate three-dimensional surface textures used as SERS-active substrate. *Appl Surf Sci* **458**:810
- 299. Suresh V, Ding L, Chew AB, Yap FL (2018) Fabrication of Large-Area Flexible SERS Substrates by Nanoimprint Lithography. *ACS Appl Nano Mater* **1**:886
- 300. Li K, Wang Y, Jiang K, et al (2016) Large-area, reproducible and sensitive plasmonic MIM substrates for surface-enhanced Raman scattering. *Nanotechnology* **27**:495402
- 301. McFarland AD, Young MA, Dieringer JA, Van Duyne RP (2005) Wavelength-Scanned Surface-Enhanced Raman Excitation Spectroscopy. *J Phys Chem B* **109**:11279
- 302. Stiles PL, Dieringer JA, Shah NC, Van Duyne RP (2008) Surface-Enhanced Raman Spectroscopy. *Annu Rev Anal Chem* **1**:601
- 303. Ertell KG (2006) A Review of Toxicity and Use and Handling Considerations for Guanidine, Guanidine Hydrochloride, and Urea. Richland, WA (United States)
- 304. Keuleers R, Desseyn HO, Rousseau B, Van Alsenoy C (1999) Vibrational Analysis of Urea. *J Phys Chem A* **103**:4621
- 305. Li Y, Li Q, Sun C, et al (2018) Fabrication of novel compound SERS substrates composed of silver nanoparticles and porous gold nanoclusters: A study on enrichment detection of urea. *Appl Surf Sci* **427**:328
- 306. Leordean C, Gabudean A-M, Canpean V, Astilean S (2013) Easy and cheap fabrication of ordered pyramidal-shaped plasmonic substrates for detection and quantitative analysis using surface-enhanced Raman spectroscopy. *Analyst* **138**:4975
- 307. Choi CJ, Wu H-Y, George S, et al (2012) Biochemical sensor tubing for point-of-care

- monitoring of intravenous drugs and metabolites. Lab Chip 12:574
- 308. Wu H-Y, Choi CJ, Cunningham BT (2012) Plasmonic Nanogap-Enhanced Raman Scattering Using a Resonant Nanodome Array. *Small* **8**:2878
- 309. Stosch R, Yaghobian F, Weimann T, et al (2011) Lithographical gap-size engineered nanoarrays for surface-enhanced Raman probing of biomarkers. *Nanotechnology* **22**:105303
- 310. Das S, Saxena K, Goswami LP, et al (2022) Mesoporous Ag-TiO2 based nanocage like structure as sensitive and recyclable low-cost SERS substrate for biosensing applications. *Opt Mater* (Amst) 125:111994
- 311. Quinn A, You Y-H, McShane MJ (2019) Hydrogel Microdomain Encapsulation of Stable Functionalized Silver Nanoparticles for SERS pH and Urea Sensing. *Sensors* **19**:3521
- 312. Liu S-Y, Tian X-D, Zhang Y, Li J-F (2018) Quantitative Surface-Enhanced Raman Spectroscopy through the Interface-Assisted Self-Assembly of Three-Dimensional Silver Nanorod Substrates. *Anal Chem* **90**:7275
- 313. Mai QD, Nguyen HA, Phung TLH, et al (2022) Photoinduced Enhanced Raman Spectroscopy for the Ultrasensitive Detection of a Low-Cross-Section Chemical, Urea, Using Silver–Titanium Dioxide Nanostructures. *ACS Appl Nano Mater* **5**:15518
- 314. Juang R-S, Wang K-S, Cheng Y-W, et al (2019) Floating SERS substrates of silver nanoparticles-graphene based nanosheets for rapid detection of biomolecules and clinical uremic toxins. *Colloids Surfaces A Physicochem Eng Asp* **576**:36
- 315. Sammi H, Nair R V., Sardana N (2023) Fabrication of SERS substrates by laser restructuring of interconnected Au nanostructures for urea detection. *Opt Mater (Amst)* **146**:114539
- 316. Gardner AM, Wright TG (2011) Consistent assignment of the vibrations of monosubstituted benzenes. *J Chem Phys* **135**:
- 317. Lopez-Ramirez MR, Guerrini L, Garcia-Ramos J V., Sanchez-Cortes S (2008) Vibrational analysis of herbicide diquat: A normal Raman and SERS study on Ag nanoparticles. *Vib Spectrosc* **48**:58
- 318. Dhas DA, Joe IH, Roy SDD, Freeda TH (2010) DFT computations and spectroscopic analysis of a pesticide: Chlorothalonil. *Spectrochim Acta Part A Mol Biomol Spectrosc* 77:36
- 319. Mahalakshmi G, Balachandran V (2015) NBO, HOMO, LUMO analysis and vibrational spectra (FTIR and FT Raman) of 1-Amino 4-methylpiperazine using ab initio HF and DFT methods. Spectrochim Acta Part A Mol Biomol Spectrosc 135:321
- 320. Díaz-Mirón G, Sánchez MA, Chemes DM, Álvarez RMS (2018) SERS spectrum of imazalil. Experimental and quantum-chemical vibrational analysis. *J Raman Spectrosc* **49**:638
- 321. Creedon N, Lovera P, Moreno JG, et al (2020) Highly Sensitive SERS Detection of Neonicotinoid Pesticides. Complete Raman Spectral Assignment of Clothianidin and Imidacloprid. *J Phys Chem A* **124**:7238
- 322. Jurašeková Z, Jutková A, Kožár T, Staničová J (2022) Vibrational characterization of the

- pesticide molecule Tebuconazole. Spectrochim Acta Part A Mol Biomol Spectrosc 268:120629
- 323. Fleming GD, Villagrán J, Koch R (2013) IR, Raman and SERS spectral analysis and DFT calculations on the Herbicide O,S-Dimethyl phosphoramidothioate, metamidophos. Spectrochim Acta Part A Mol Biomol Spectrosc 114:120
- 324. Smith B (2018) Infrared Spectral Interpretation. CRC Press
- 325. Srivastava SK, Singh VB (2013) Ab initio and DFT studies of the structure and vibrational spectra of anhydrous caffeine. *Spectrochim Acta Part A Mol Biomol Spectrosc* **115**:45
- 326. Takei K, Takahashi R, Noguchi T (2008) Correlation between the Hydrogen-Bond Structures and the C=O Stretching Frequencies of Carboxylic Acids as Studied by Density Functional Theory Calculations: Theoretical Basis for Interpretation of Infrared Bands of Carboxylic Groups in Proteins. *J Phys Chem B* 112:6725
- 327. Irikura KK, Johnson RD, Kacker RN (2005) Uncertainties in Scaling Factors for ab Initio Vibrational Frequencies. *J Phys Chem A* **109**:8430
- 328. Umar Y, Abu-Thabit N, Jerabek P, Ramasami P (2019) Experimental FTIR and theoretical investigation of the molecular structure and vibrational spectra of acetanilide using DFT and dispersion correction to DFT. *J Theor Comput Chem* **18**:1950009
- 329. Costa JCS, Ando RA, Camargo PHC, Corio P (2011) Understanding the Effect of Adsorption Geometry over Substrate Selectivity in the Surface-Enhanced Raman Scattering Spectra of Simazine and Atrazine. *J Phys Chem C* **115**:4184
- 330. Anariba F, Viswanathan U, Bocian DF, McCreery RL (2006) Determination of the Structure and Orientation of Organic Molecules Tethered to Flat Graphitic Carbon by ATR-FT-IR and Raman Spectroscopy. *Anal Chem* **78**:3104
- 331. Wang H, Liu B, Zhao Y, Zheng X (2009) Resonance Raman spectra and excited state structural dynamics of ethylene trithiocarbonate in the A and B -band absorptions. *J Raman Spectrosc* **40**:1312
- 332. Albarghouthi N, MacMillan P, Brosseau CL (2021) Optimization of gold nanorod arrays for surface enhanced Raman spectroscopy (SERS) detection of atrazine. *Analyst* **146**:2037
- 333. Kang S, Wang W, Rahman A, et al (2022) Highly porous gold supraparticles as surface-enhanced Raman spectroscopy (SERS) substrates for sensitive detection of environmental contaminants. *RSC Adv* **12**:32803
- 334. Song X, Li H, Al-Qadiri HM, Lin M (2013) Detection of herbicides in drinking water by surface-enhanced Raman spectroscopy coupled with gold nanostructures. *J Food Meas Charact* 7:107
- 335. Tang J, Chen W, Ju H (2019) Sensitive surface-enhanced Raman scattering detection of atrazine based on aggregation of silver nanoparticles modified carbon dots. *Talanta* **201**:46
- 336. Atanasov PA, Nedyalkov NN, Fukata N, et al (2019) Surface-Enhanced Raman Spectroscopy (SERS) of Mancozeb and Thiamethoxam Assisted by Gold and Silver Nanostructures Produced by Laser Techniques on Paper. *Appl Spectrosc* **73**:313

- 337. Sánchez-Cortés S, Vasina M, Francioso O, García-Ramos J. (1998) Raman and surface-enhanced Raman spectroscopy of dithiocarbamate fungicides. *Vib Spectrosc* **17**:133
- 338. Tsen C-M, Yu C-W, Chen S-Y, et al (2021) Application of surface-enhanced Raman scattering in rapid detection of dithiocarbamate pesticide residues in foods. *Appl Surf Sci* **558**:149740
- 339. Wang P, Sun Y, Wang L, et al (2021) Facile Detection and Quantification of Acetamiprid Using a Portable Raman Spectrometer Combined with Self-Assembled Gold Nanoparticle Array. *Chemosensors* **9**:327
- 340. Gao Y, Xu ML, Xiong J (2019) Raman and SERS spectra of thiamethoxam and the Ag3–thiamethoxam complex: an experimental and theoretical investigation. *J Environ Sci Heal Part B Pestic Food Contam Agric Wastes* **54**:665

Curriculum vitae (CV)

Gaurav Pal Singh

Date of Birth: 12 February 1994 **Address:** 1671, Phase-1, Urban Estate Dugri, Ludhiana -141002 (INDIA)

Contact details:

+919878424311

gaurav12294@gmail.com linkedin.com/in/gaurav12294 Nationality: Indian

Marital Status: Unmarried

Languages Known: English, Hindi, and

Punjabi

EDUCATION / PROFESSIONAL DETAILS

DEGREE/ DESIGNATION	INSTITUTE	CGPA/10	YEAR
Assistant Professor	Punjab Engineering College Metallurgical and Materials Engineering	-	2024 - ongoing
Ph.D.	Indian Institute of Technology Ropar Metallurgical and Materials Engineering	8.85	2019 - 2024
Research Intern	ZIK SiLi-nano Martin Luther University Germany	-	Jul-Sept 2022
M.Tech.	Punjab Engineering College Industrial Materials and Metallurgy	9.38	2017 - 2019
B.Tech.	Manipal Institute of Technology Mechanical Engineering	8.35	2012 - 2016

EXPERIMENTAL SKILLS

- Nanofabrication
- Laser Interference Lithography at Martin Luther University Halle-Wittenberg, Germany
- Basic microbiological experiments

- Nanofabrication Raman spectroscopy
- Surface enhanced Raman spectroscopy (SERS)
- Optical setup for Transmission and Surface Plasmon Resonance (SPR)

SOFTWARE SKILLS

- COMSOL (Electromagnetics)
- ANSYS (Mechanical and CFD)
- Gaussian (DFT)
- Arduino and Raspberry Pi

- Android application development
- SolidWorks
- MATLAB
- ImageJ

Research Projects

PhD at Indian Institute of Technology Ropar (2019-2024)

- Fabrication, optimization and application of Gold Nanodisk Arrays
 - Gold nanodisk arrays were fabricated using Laser Interference Lithography (LIL) at the clean room facility at Matin Luther University, Germany, during my research internship. Gold nanodisk arrays with diameters 110 nm to 200 nm (period to diameter ratio ~2.2) were indented to be used as SERS substrates. It was seen that 140 nm diameter (300 nm period) displayed the highest enhancement (EF of 2.3 x 10⁶) of the Raman signal due to the overlap of the resonance wavelength of the nanodisk array with the Raman excitation wavelength (633 nm).
 - Thermal annealing of Gold nanodisk arrays for enhanced optical response The nanodisk arrays exhibited a strong plasmonic resonance in the visible and NIR regions, which was caused by the interaction of the single disk resonance and the (1 0) grating resonance.

Annealing for a short duration led to growth of gold grains and smoothening of the disk surfaces resulting in lower ohmic and radiative losses from the gold disks and **doubling of the Q-factor** of the resonances.

Annealing for a longer duration disintegrated the nanodisk into several smaller particles while maintaining the overall periodicity of the array. **Finite element method (FEM) simulations** predicted that for larger periods fragmented nanodisk arrays can exhibit extremely strong and sharp resonances whose **Q-factor increases more than 30 times**.

 Gold nanodisk arrays as Surface-enhanced Raman spectroscopy (SERS) substrates for pesticide sensing

Various types of agrochemicals being used by the farmers were collected. One each of herbicide (Atrazine), fungicide (Mancozeb), acaricide (Clofentezine), and weedicide (Metribuzin), and four extremely harmful insecticides (Chlorantraniliprole, Thiamethoxam, Tau-fluvalinate, and Flubendiamide) were tested. The limit of detection (LOD) of the pesticides was tested using a gold nanodisk array as a SERS substrate using Raman spectroscopy. It was observed that the pesticides showed a LOD much below the ppm level. Density Function Theory (DFT) calculations were used to verify the experimental spectra and assign vibrational modes to the major Raman peaks of the pesticides.

- Effect of roughness on Surface Plasmon Resonance (SPR) performance of gold thin films
 - Gold films deposited with an oscillating base displayed a lower surface roughness. The smoother films had a lower FWHM of the SPR dip as compared to the film of larger surface roughness of the same thickness.
 - The significant increase in the slope of the resonance angle and wavelength dependent curve established that smoother plasmonic films have a higher sensitivity.
- Simulation of plasmonic nanoparticles and nanoarrays for sensitivity enhancement
 - o FEM simulations were used to analyze the effect of size, shape, material and surrounding environment on the plasmonic response of single nanoparticles and nanoarrays.
 - Arranging the single nanostructures into periodic arrays combined the near field (Localized SPR) and far field (grating resonance due to the array) resonances. The highest sensitivity was observed at the optimal coupling condition, where the near field and far field resonance wavelengths overlapped.

• Theoretical study of MXenes coupled surface plasmon resonance (SPR) sensors for sensitivity enhancement

- MXenes are a new family of materials with exciting optical properties that have to the
 potential to replace conventional plasmonic materials. The finite element method (FEM)
 and transfer matrix method (TMM) were used to analyze the SPR response of various
 MXenes.
- A structured MXene layer, as well as, the combined effect of gold and MXene, both showed enhanced sensitivity as compared to conventional plasmonic sensing layers (an increase of more than 1.75 times).

Book chapters on Metamaterials

- Graphene metamaterials and their use as frequency selective and radar absorbing surfaces
- o Auxetic metamaterials for Biomedical and Tissue Engineering

Devices development

• Rapid sensing of bacterial growth on meat using optical device (Technology transfer for commercialization)

Conventional methods to detect bacterial contamination require the use of various chemicals and often take more than a day. An economical and portable device was developed for the rapid **detection of bacteria** in chicken meat in **15 to 30 minutes**. The sensing signal was the increased scattering from the meat surface due to bacterial colonies (10² to 10⁸ CFU/mL). The traditional **microbiological method of plate counting** was used to establish that the control samples did not have any significant bacterial colonies.

The smartphone based device is being **licensed** by a company for **commercialization**.

o **Economical optical sensing devices** (with undergraduate interns)

An economical **turbidity meter** was developed which could be operated using a **smartphone** using an **application** from the image feed from a camera via a **Raspberry Pi**. The prototype cost less than 80 USD and could detect **5 NTU** (Nephelometry Turbidity Unit), which was comparable to commercial devices.

An **economical transmission spectroscopy** setup was developed whose prototype cost less than 60 USD. The economical setup results were in good agreement with the laboratory grade equipment. The setup was used to measure the transmission response of various pesticides.

• An apparatus to measure burst pressure of an adhesive (Patent filed)

A burst pressure measuring apparatus with the provision for testing adhesives that require fluid flow to complete the adhesion process was developed, and the apparatus was specifically designed for **biological adhesives**. The apparatus created controlled fluid flow using a **peristaltic pump**, and the pressure was measured using a manometer. The fluid pressure in the testing chamber was increased using a plunger operated by a **stepper motor** via an **Arduino**.

o Affordable, Compact and Infection-Free BiPAP Machine

BiPAP (Bilevel Positive Airway Pressure) ventilation support can be used for the less critical COVID cases. An inexpensive BiPAP with an infection-free exhaust was developed using an air blower that was programmed using an **Arduino** via a speed controller. The cost of the mass produced device was approximated as 85 USD.

• A portable tent to prevent Electromagnetic Interference (EMI) (with undergraduate interns)

The **EMI shielding** performance of a 1 m² tent made using commonly available aluminum sheets and a commercial **conductive fabric** made of copper and nickel wires was compared.

- Shock Loading Response of Solid and Perforated Aluminum Sheets
 - Shock tube is an experimental apparatus used to impart shock loading for testing various materials and designs. CFD simulations of the shock tube were validated using the results of an experimental shock tube apparatus. Analytical equations were used to calculate the peak reflected pressure and energy. The maximum incident energy available at the end of the driven section using diaphragm thickness 4 mm was 46.72 KJ.
 - The shock tube analysis of **Aluminum alloy 6061-T6 sheets** of two configurations (solid and perforated) and two thicknesses (3 and 2 mm) were compared. **FEM simulations** of the shock loading impact on the sheets was performed. The simulation results were in close agreement with the experimentally tested sheets. It was observed that 2 mm thick perforated sheet experienced complete fracture and absorbed the highest energy (477 J).

Bachelors at Manipal Institute of Technology (2016)

Theoretical study on the effect of Trapezoidal Shaped Rib on Thermal Performance of Solar Air Heater

Solar air heaters generally exhibit lower levels of thermal performance due to thermal losses and poor heat transfer characteristics of air. **Computational fluid dynamics (CFD)** results revealed that the trapezoidal shape improved the conductive heat transfer, as indicated by the increased Nusselts number. The geometric parameters of the trapezoidal ribs were optimized to maximize the heat transfer at a reasonable pressure drop.

JOURNAL PUBLICATIONS

- **G. P. Singh**, A. Pandey, and N. Sardana "MXene coupled surface plasmon resonance (SPR) sensors for sensitivity enhancement: a theoretical study", *Submitted in Photonic Sensors*
- **G. P. Singh**, B. Fuhrmann, F. Syrowatka, J. Schilling, N. Sardana "Effect of Annealing on Plasmonic Response of Gold Nanopatterns" *Submitted in Physica Scripta*
- **G. P. Singh** and N. Sardana "Vibrational Modes of Metribuzin: A Theoretical and Experimental Comparison" *Accepted in ChemistrySelect*, doi: 10.1002/slct.202402793
- **G. P. Singh**, B. Fuhrmann, F. Syrowatka, J. Schilling, N. Sardana, "Tuning the Plasmonic Response of Periodic Gold Nanodisk Arrays for Urea Sensing" *J. Mater. Sci.* vol. 59, pp. 6497–6508, April 2024, doi: 10.1007/s10853-024-09599-0
- **G. P. Singh**, R. Harsh and N. Sardana "Tuning of the Plasmonic Response Gold and Aluminum Nanoarrays for Sensing Applications" *Indian J. Pure Appl. Phys.*, vol. 62, pp. 77-86, Feb. 2024, doi: 10.56042/ijpap.v62i2.7709
- **G. P. Singh**, R. Singh, J. D. Sharma, R. Arora, and I. S. Sandhu "Shock loading response of solid and perforated aluminium sheets." *J. of Materi Eng and Perform*, Jan. 2024, doi: 10.1007/s11665-023-08916-z
- **G. P. Singh**, S. Samanta, A. Pegu, S. S. Yadav, U. Singhal, A. Venkatesan and N. Sardana, "Enhancement of Plasmonic Response by Piezoelectrically Deposited Gold Films" *Indian J. Phys.*, Oct. 2023, doi: 10.1007/s12648-023-02974-8.
- **G. P. Singh** and N. Sardana, "Plasmonic response of metallic nanoparticles embedded in glass and a-Si," *Bull. Mater. Sci.*, vol. 45, no. 4, p. 241, Dec. 2022, doi: 10.1007/s12034-022-02812-3.
- **G. P. Singh** and N. Sardana, "Smartphone-based Surface Plasmon Resonance Sensors: a Review," *Plasmonics*, vol. 17, no. 5, pp. 1869–1888, Oct. 2022, doi: 10.1007/s11468-022-01672-1.
- **G. P. Singh** and N. Sardana, "Affordable, Compact and Infection-Free BiPAP Machine," *Trans. Indian Natl. Acad. Eng.*, vol. 5, no. 2, pp. 385–391, 2020, doi: 10.1007/s41403-020-00134-6.

CONFERENCE PUBLICATIONS

- S. Samanta, **G.P. Singh**, P. Jain, A. K. Singh, N. Sardana, "Arm angle dependence of X-shaped metamaterial resonator in the X-band Regime", *Springer Proc. Phys.*, vol. 308, pp. 183–190, 2024, doi: 10.1007/978-981-97-4557-9 19.
- **G. P. Singh**, J. D. Sharma, R. Arora, and I. S. Sandhu, "CFD analysis of shock tube for blast impact testing," *Mater. Today Proc.*, vol. 28, pp. 1872–1878, 2020, doi: 10.1016/j.matpr.2020.05.294.
- M. S. Manjunath, **G. P. Singh**, N. Akhil, and A. Singh, "Influence of shape factor and notch design of transverse trapezoidal shaped rib on thermal performance of solar air heater-a CFD study," *AIP Conf. Proc.*, vol. 2273, no. November, 2020, doi: 10.1063/5.0024515.

BOOK CHAPTERS

- **G. P. Singh** and N. Sardana, "Auxetic Materials for Biomedical and Tissue Engineering Materials for Biomedical Simulation: Design, Development and Characterization," Springer Nature Singapore, 2023, pp. 1–36.
- **G. P. Singh** and N. Sardana, "Graphene Metamaterials Recent Advances in Graphene and Graphene based technologies," IOP Publishing, 2023, pp. 17–38.
- **G. P. Singh** and N. Sardana, "Graphene-Based Tunable Metamaterial-FSS RAS BT Handbook of Metamaterial-Derived Frequency Selective Surfaces," Springer Nature Singapore, 2022, pp. 1–39.

PATENTS

G. P. Singh and N. Sardana, "A system and method for measuring burst pressure for an adhesive," 202111032081, *Indian patent filed*, 2021

TEACHING ASSISTANT ROLES

- Advanced Materials Characterization Techniques
- Electrical Optical and Magnetic Properties of Materials
- Tinkering Lab (Arduino based projects)
- Major and Minor Projects with B.Tech. Students

ACHIEVEMENTS

- Best oral presentation in International Conference on Advanced Functional Materials and Devices (AFMD-2024), SRMIST, Chennai
- Oral and Poster presentation at META 2022 12th International Conference on Metamaterials, Photonic Crystals and Plasmonics (19 July to 22 July 2022) at Torremolinos, Spain
- Best oral presentation at 14th Chandigarh Science Congress (CHASCON-2020), Chandigarh, 2020
- Qualified Graduate Aptitude Test in Engineering (GATE) in Mechanical Engineering in 2016 and 2019

References

Name	Institute	Email	Phone
Dr. Neha Sardana	Indian Institute of Technology Ropar	nsardana@iitrpr.ac.in	+91-1881-232406
Prof. Jörg Schilling	Martin Luther University, Germany	joerg.schilling@physik.uni-halle.de	+49-345-5528663
Dr. JD Sharma	Punjab Engineering College	jdsharma@pec.edu.in	+91-01722753954